



**HAL**  
open science

# ZnO nanoparticles as a luminescent down-shifting layer for solar cells

Yao Zhu

► **To cite this version:**

Yao Zhu. ZnO nanoparticles as a luminescent down-shifting layer for solar cells. Materials. INSA de Lyon, 2015. English. NNT : 2015ISAL0090 . tel-01339845

**HAL Id: tel-01339845**

**<https://theses.hal.science/tel-01339845>**

Submitted on 30 Jun 2016

**HAL** is a multi-disciplinary open access archive for the deposit and dissemination of scientific research documents, whether they are published or not. The documents may come from teaching and research institutions in France or abroad, or from public or private research centers.

L'archive ouverte pluridisciplinaire **HAL**, est destinée au dépôt et à la diffusion de documents scientifiques de niveau recherche, publiés ou non, émanant des établissements d'enseignement et de recherche français ou étrangers, des laboratoires publics ou privés.

2015ISAL0090

# THESE

## ZnO Nanoparticles as a Luminescent Down-Shifting Layer for Solar Cells

présentée devant  
L'Institut National des Sciences Appliquées de Lyon

pour obtenir  
le grade de docteur

Ecole doctorale: Matériaux de Lyon

par

**Yao ZHU**

Soutenance le 08 octobre 2015 devant la Commission d'examen

### Jury

---

Rapporteur	Gilles LEDOUX	Chargé de Recherche CNRS
Rapporteur	Fabrice GOURBILLEAU	Directeur de Recherche CNRS
Examineur	Hervé RINNERT	Professeur (Université de Lorraine)
Examineur	Stéphane DANIELE	Professeur (IRCE LYON-UCBL1)
Directeur de thèse	Bruno MASENELLI	Professeur (INSA-Lyon)
Co-Directeur de thèse	Alexandra APOSTOLUK	Maître de Conférences (INSA-Lyon)

Cette thèse a été préparée à l'Institut des Nanotechnologies de Lyon de l'INSA de LYON



# Acknowledgements

The research conducted during my thesis would not have been possible without the support of many people. First and foremost, I wish to express my deep sense of gratitude to Lyon Institute of Nanotechnology (INSA-Lyon), for providing the opportunity to join the lab with a good environment and facilities to carry out my research. I would like also to convey thanks to the members of the administration helping me through all the procedures required for the completion of the thesis.

I sincerely thank to my thesis supervisors Bruno Masenelli and Alexandra Apostoluk, for their patient guidance, enthusiastic encouragement, and for useful remarks and offering fascinating subject. My very great appreciation goes to Bruno Masenelli for his valuable and constructive suggestions during my Master research and the planning and development of the thesis that helped me tremendously in completing everything in time. I would like to gratefully acknowledge the motivating and energetic supervision of Alexandra Apostoluk during my Master research and thesis for her help on numerous optical measurements and discussions in many professional and personal matters.

Important part of this thesis related to high quality ZnO nanoparticles synthesis which would not have been possible without the collaboration with IRCE Lyon. My sincere thanks go to Prof. Stéphane DANIELE and his students Pierrick Gautier, Audrey Valette, Lama Omar and Thibaut Cornier for their professionalism and patience for providing us nice samples. I also appreciate the collaboration with Lodz University of Technology. My sincere thanks go to Maciej Sibiński, Katarzyna Znajdek and Zbigniew Lisik for preparing the solar cell samples, with which we can estimate the down-shifting effect of ZnO NPs layer.

I would like to show my greatest appreciation to Nicolas Chauvin, Jean-Marie Bluet, Bruno Canut, Dominique Vouagner and Laurence Burel for the invaluable assistance with physical, optical measurements and relevant discussions. I would like also thank Erwann Fourmond for his kind help in the ellipsometry measurement and the PFE student Victor Goutorbe for performing the simulations on the ZnO NPs effect on solar cells, which is a part of my thesis. Without his valuable contribution, the last chapter of my thesis would not be complete.

I wish to extend my thanks for the support given by all the technicians in our laboratory. A warm thank goes to Philippe Girard and Robert Perrin for their help. I also thank Joëlle Grégoire and Khaled Ayadi from NanoLyon team for their assistance in the chemistry lab.

Deepest gratitude is also due to people who enriched my thesis with their help and expertise. Roman Anufriev, Hajjaji Hamza, Trung-hieu Nguyen to give their time so generously during numerous measurements. An honourable mention goes to my colleagues in the same office with me, HU Xuan, LIU Huanhuan, WANG Lin and Mohamed-Khairi Hamza and all the colleagues in the lab for their kind help and encouragement.

Finally, I am forever indebted to my family and relatives for their understanding, endless patience and encouragement. I would like to express very great appreciation to my boyfriend XIE Zhongjian for his accompany, help and encouragement. I am grateful to all my friends in Lyon and in China for spending great times and their help.

### Résumé

Après plus d'une décennie de recherche intensive, les nanoparticules de ZnO deviennent des systèmes émetteurs de lumière visible compétitifs. Le but de cette thèse était de concevoir des matériaux à base de nanoparticules de ZnO qui puissent être utilisés de manière efficaces comme couche de « down-shifting » sur la face avant des cellules solaires photovoltaïques. La stratégie du « down-shifting » réside dans la conversion de photons UV-bleu qui sont inefficacement utilisés par les cellules solaires en photons visibles susceptibles d'être plus efficacement utilisés par ces dernières. Ainsi, notre but a été de concevoir un matériau mécaniquement stable, qui puisse être produit à grande échelle et déposé sur des cellules solaires standard à un coût modéré. Le critère le plus important concernait l'efficacité de conversion des photons UV en photon visible. Le défi principal a donc été d'obtenir des nanoparticules de ZnO avec un rendement de photoluminescence (PL QY) aussi élevé que possible. Le second défi a été de pouvoir disperser ces particules en matrice et en solution aqueuse (dispersion colloïdale) pour permettre leur utilisation ultérieure en milieu industriel. Notre choix s'est porté sur l'utilisation de matrice polymère.

Diverses méthodes ont été et comparées utilisées pour la synthèse de nanoparticules de ZnO. Nous avons en premier lieu étudié des particules synthétisées par voie physique (le dépôt par jet d'agrégats de basse énergie –LECBD- qui repose sur la détente adiabatique d'un plasma). Les particules résultantes n'ont pas démontré un PL QY suffisamment élevé pour être intéressant pour le « down-shifting ». Nous avons par la suite étudié des particules commerciales qui se sont comportées comme celles issues de la LECBD. Par conséquent, nous ne les avons pas retenues. Enfin, nous nous sommes concentrés sur des particules produites par voie chimique humide. Deux voies ont été explorées : la méthode conventionnelle de co-précipitation de l'acétate ou du sulfate de zinc en présence d'hydroxyde alcalin ainsi que l'hydrolyse de  $\text{ZnEt}_2$ . Pour chaque cas, les paramètres de synthèses ont été variés pour optimiser les propriétés optiques en vue de l'effet de « down-shifting ». Avec un choix approprié de la nature ( $\text{Li}^+$  au lieu de  $\text{K}^+$ ) et de la quantité d'ions alcalins, le rendement quantique de photoluminescence a été accru à 13 % par la méthode de co-précipitation. Nos résultats reproduisent l'état de l'art concernant cette technique. Cependant, la technique par hydrolyse s'est révélée bien plus intéressante. La seule réaction d'hydrolyse n'a pas initialement conduit à des particules très brillantes. Nous avons donc proposé une approche originale : l'ajout d'un acide faible, l'acide polyacrylique (PAAH), durant la synthèse. Alors que le PAAH a déjà été utilisé comme agent passivant de la surface de ZnO, son utilisation pendant la synthèse n'a jamais été tentée. Notre travail montre que en contrôlant la quantité et le poids moléculaire (longueur de chaîne) du PAAH introduit pendant la croissance,

un nanocomposite hybride très efficace à base de nanoparticules de ZnO et de PAAH peut être obtenu, avec un PL QY aussi élevé que 20 %. En mélangeant le PAAH avec son sel de sodium, PAANa, le nanocomposite présente un PL QY record de 50%, qui augmente jusqu'à 70 % après un mois. Les raisons physico-chimiques de cet accroissement sont discutées dans le manuscrit. Nos explications pointent vers un effet combiné de la taille, de la morphologie et de la composition.

Dans la partie suivante, des nanoparticules de ZnO pouvant être dispersées dans l'eau ont été obtenues avec succès tout en maintenant leur rendement quantique entre 20 % et 34 % ; ce en utilisant un mélange de PAAH/PAANa de ratio volumique, de concentration et de volume réactionnel optimaux. Nous insistons sur la nécessité d'obtenir un compromis entre une bonne capacité de dispersion et un fort PL QY. Cette partie de la thèse pave la voie vers des applications industrielles ultérieures.

Finalement, l'effet de « down-shifting » des nanoparticules luminescentes de ZnO a été simulé pour déterminer le gain potentiel de rendement de cellules photovoltaïques.

## Abstract

After more than a decade of extensive investigation, ZnO nanoparticles are becoming competing systems for visible light emission. The aim of this thesis was to design ZnO nanoparticle based materials that can be efficient as a down-shifting layer deposited on the front side of solar cells. The down-shifting strategy is to convert UV-blue photons that are not efficiently used by most of photovoltaic solar cells into visible photons which are more efficiently used. Thus we aimed at designing a material mechanically stable that can be processed on a scalable amount and deposited on standard solar cells at a reduced cost. The most important criterion regarded the efficiency of conversion of UV photons into visible ones. The main challenge was thus to get ZnO nanoparticles with as high photoluminescence quantum yield (PL QY) as possible. The second challenge was to be able to disperse them in a matrix and in an aqueous solution (colloidal dispersion) that allows further industrial processing. Our choice was set on the use of a polymer matrix.

Different methods have been used and compared to synthesize ZnO nanoparticles. We have first studied particles synthesized by a physical route (the Low Energy Cluster Beam Deposition relying on the adiabatic expansion of a plasma). The resulting particles did not exhibit a PL QY high enough to be interesting for down-shifting. We next investigated commercial particles which behaved as the LECBD ones. We consequently discarded them. Eventually, we concentrated on nanoparticles produced by wet chemistry. Two routes were explored: the conventional co-precipitation method of Zn acetate or sulfate in presence of an alkaline hydroxide and the hydrolysis of  $\text{ZnEt}_2$ . For both cases the synthesis parameters have been tuned to optimize the optical properties for down-shifting process. When appropriately choosing the alkaline ion ( $\text{Li}^+$  instead of  $\text{K}^+$ ) nature and amount, the PL QY has been increased to 13 % in the co-precipitation method. Our results reproduce the state-of-the-art knowledge concerning this technique. The hydrolysis route proved to be even more interesting. The sole hydrolysis reaction did not lead to very bright particles. We have thus proposed an original strategy: the addition of a weak acid, the polyacrylic acid (PAAH) during the synthesis. If PAAH has been used previously as a passivating capping agent of ZnO, its use during the synthesis has never been tempted. Our work shows that by tuning the amount and molecular weight (chain length) of PAAH introduced during the synthesis, a very efficient hybrid nanocomposite consisting of ZnO nanoparticles in a PAAH matrix can be obtained with PL QY as high as 20 %. When mixing PAAH to its sodium salt PAANa, the nanocomposite exhibits record values of PL QY of 50 %, increasing to 70 % over a month. The physico-chemical reasons for this enhancement are discussed in the manuscript. Our explanations point to a combined effect of the size, morphology and composition.

In the subsequent part, ZnO NPs dispersible in water have been successfully achieved while maintaining their PL QY high, between 20 % - 34 %, using a PAAH/PAANa mixture at the optimal volume ratio, concentration, lengths and volume. We highlight the need to get a

compromise between a good dispersibility and a high PL QY. This part of the thesis paves the way for the further industrial applications.

Finally, the down-shifting effect of luminescent ZnO nanoparticles on solar cells has been simulated to obtain a potential enhancement of solar cell efficiency by the ZnO NPs down-shifting layer.

**Keywords:** ZnO nanoparticles, Down-shifting, Photoluminescence quantum yield, dispersibility, solar cell efficiency.

# Contents

List of figures .....	V
Chapter 1 .....	1
Introduction .....	1
1.1. Structure of the thesis .....	1
1.2. Solar cells: state of the art.....	2
1.3. Down-shifting phenomenon .....	4
1.4. Technical challenges concerned in this thesis .....	7
1.5. References .....	8
Chapter 2 .....	9
Materials.....	9
2.1. Luminescent materials.....	9
2.2. An introduction to the zinc oxide .....	11
2.2.1. Crystalline structure of ZnO .....	11
2.2.2. Electrical characteristics of ZnO.....	15
2.2.3. Optical characteristics of ZnO .....	17
2.3. ZnO related material – Zinc hydroxide .....	27
2.4. Host materials .....	31
2.4.1. Poly(methyl methacrylate) (PMMA).....	32
2.4.2. Polyacrylic acid (PAAH) .....	34
2.5. Conclusions .....	36
2.6. References .....	37
Chapter 3 .....	47
Synthesis and characterization of ZnO nanoparticles .....	47
3.1. Synthesis methods of ZnO nanoparticles .....	47
3.1.1. Low Energy Cluster Beam Deposition (LECBD) method.....	47
3.1.2. Commercially available ZnO nanoparticles.....	49

3.1.3 Chemical synthesis methods .....	50
3.1.3.1 Co-precipitation method.....	50
3.1.3.2 Hydrolysis method .....	51
3.2. Characterization of ZnO NPs .....	51
3.2.1. Structural characterization .....	52
3.2.1.1. X-ray diffraction (XRD) analysis.....	52
3.2.1.2. Electron microscopy.....	53
3.2.1.3. Dynamic and electrophoretic light scattering.....	54
3.2.2. Chemical characterization.....	59
3.2.2.1. Fourier Transform Infrared Spectroscopy (FTIR) .....	59
3.2.2.2. Raman spectroscopy.....	60
3.2.2.3. Nuclear reaction analysis .....	62
3.2.3. Optical characterization .....	62
3.2.3.1. Photoluminescence spectroscopy.....	62
3.2.3.2. Quantum efficiency.....	68
3.3. Conclusions .....	73
3.4. References .....	74
Chapter 4 .....	77
Strategies for ZnO nanoparticles with a high PL QY .....	77
4.1. ZnO nanoparticles synthesized by LECBD method.....	77
4.2. Commercially available ZnO nanoparticles .....	83
4.3. Sol-gel methods .....	84
4.3.1. Co-precipitation method .....	85
4.3.1.1. Choice of the solvent.....	85
4.3.1.2. Crystalline structure characteristics .....	86
4.3.1.3. Morphology characteristics .....	89
4.3.1.4. Optical properties .....	90
4.3.1.5. Discussion .....	92
4.3.1.6. Conclusions .....	95
4.3.2. Hydrolysis method.....	96
4.3.2.1. Hydrolysis of Zn[N(SiMe <sub>3</sub> ) <sub>2</sub> ] <sub>2</sub> .....	96
4.3.2.2. Hydrolysis of ZnEt <sub>2</sub> .....	98
4.4. Conclusions .....	120
4.5. References .....	121
Chapter 5 .....	125

Dispersion of ZnO nanoparticles.....	125
5.1. ZnO nanoparticles dispersible in water .....	125
5.2. Effect of the mixture ratio of PAAH and PAANa.....	128
5.3. Effect of the mixture concentration of PAAH and PAANa .....	129
5.4. Effect of the length of individual chains of PAAH and PAANa.....	131
5.5. Effect of the type of the polyacrylate cation salt ( $\text{Li}^+/\text{Na}^+$ ) in the mixture.....	134
5.6. Effect of the volume of the reaction precursor and the added PAAH and PAANa (or PAALi) mixture.....	135
5.7. Conclusions .....	136
5.8. References .....	137
Chapter 6 .....	139
Simulation of the efficiency of solar cells with a luminescent down-shifting layer of ZnO nanoparticles.....	139
6.1. Determination of the optical indices of the down-shifting layer .....	139
6.1.1 Layer preparation – spin-coating technique.....	139
6.1.2. Spectroscopic ellipsometry measurement.....	141
6.1.3. Effective medium theory.....	145
6.1.3.1. Bruggeman model .....	145
6.1.3.2. Maxwell-Garnett model .....	145
6.1.3.3. Comparison with the ellipsometry results .....	147
6.2. Simulations .....	149
6.2.1. Anti-reflective behavior .....	149
6.2.1.1. Amorphous silicon solar cell.....	152
6.2.1.2. CIGS solar cell .....	154
6.2.2. Down-shifting effect .....	156
6.2.2.1. Amorphous Si solar cells.....	159
6.2.2.2. CIGS solar cells.....	160
6.3. Conclusions .....	162
6.4. References .....	163
General conclusions .....	165



## List of figures

<b>Figure 1.1:</b> Global solar emission spectrum at air mass (AM) 1.5 showing the fraction that is currently absorbed by a thick silicon (Si) solar cell and the additional regions of the spectrum that can contribute toward up- and down-conversion (UC and DC, respectively). $\lambda$ - wavelength.....	3
<b>Figure 1.2:</b> Processes of the (a) <b>up-conversion</b> , which permits the conversion of IR light to visible light by simultaneous absorption of two photons and emission of one photon with higher energy; (b) <b>down-conversion</b> , in which one photon with higher energy can be converted into two identical photons of equal energy, two times lower than the absorbed one and (c) <b>down-shifting</b> , a variant of the down-conversion technique, permits the conversion of a high-energy photon into one (or more) of lower-energy. ....	4
<b>Figure 1.3:</b> Structure of the solar cell with a down-shifting layer on the front side.....	4
<b>Figure 2.1:</b> Photoluminescence (PL) process in direct bandgap semiconductors. (①: UV radiative absorption; ②: band edge PL; ③: defect or impurity induced PL; ④: non-radiative recombination path.).....	10
<b>Figure 2.2:</b> Zinc oxide crystal structures: (a) hexagonal wurtzite structure, (b) cubic zinc blende structure and (c) cubic rock salt structure. ....	12
<b>Figure 2.3:</b> Phonon dispersion of wurtzite ZnO.....	14
<b>Figure 2.4:</b> GW correction Hybrid Density Functional Theory (HDFT) band structure of wurtzite ZnO in reciprocal space along high-symmetry directions of the crystal.....	16
<b>Figure 2.5:</b> Valence band structure of ZnO near the $\Gamma$ point.....	16
<b>Figure 2.6:</b> PL spectra of a bulk ZnO substrate measured at 5 K and 100 K, respectively.....	18
<b>Figure 2.7:</b> (a) Peak energies for the free (FX) and donor-bound (DX) excitons as a function of temperature; (b) Log plot of the free and donor-bound exciton peak intensities as a function of temperature.....	19
<b>Figure 2.8:</b> Quantum confinement phenomenon in the (a) absorption spectra of ZnO quantum dots of 2 nm, 5 nm and >10 nm in diameter and (b) in photoluminescence spectra of ZnO quantum dots of 2.1nm, 2.4 nm, 3 nm and 3.4 nm in diameter.....	19
<b>Figure 2.9:</b> Room-temperature PL spectra of different ZnO nanostructures: (1) tetrapods, (2) needles, (3) nanorods, (4) shells, (5) highly faceted rods, (6) ribbons/combs. ....	20
<b>Figure 2.10:</b> Formation energies as a function of the Fermi-level position for native point defects in ZnO for (a) Zn-rich and (b) O-rich conditions.....	21
<b>Figure 2.11:</b> Illustration of the calculated defect energy levels in ZnO from different literature sources.....	22
<b>Figure 2.12:</b> Schematic representation of an electron and hole pair creation and captured by an intrinsic defect or an impurity and a surface state, respectively .....	23
<b>Figure 2.13:</b> Maximum peaks position in PL spectrum of ZnO nanoparticles precipitated at different pH values of the precipitation solution of 12, 10, 8, 6, respectively, and the corresponding zeta potentials. The ZnO nanoparticles were dispersed in ethanol. The excitation	

wavelengths were 309, 325, 328 and 356 nm for the nanoparticles prepared at pH 12, 10, 8, and 6, respectively.....	23
<b>Figure 2.14:</b> Room temperature PL spectra with different excitation wavelengths for (a) needles, (b) rods, and (c) shells. ....	24
<b>Figure 2.15:</b> Maximum emission peak position with excitation wavelength of nano-colloidal ZnO of different sizes.....	25
<b>Figure 2.16:</b> Room temperature PL spectrum of ZnO nanoparticles under the excitation of 532 nm. The dashed lines are the Gaussian fitting of the broad PL peak showing two components at 660 nm and 701 nm. ....	25
<b>Figure 2.17:</b> (a) Numerical simulation of external quantum efficiency (marked as QE in the graph) for a standard Si cell, the CIGS cell and the CdTe cell in function of the incident solar light wavelength, simulated using the Solar Cell Capacitance Simulator (SCAPS) program. (b) Absorption and emission spectra of ZnO quantum dots. ....	27
<b>Figure 2.18 :</b> XRD pattern of pure Zn(OH) <sub>2</sub> . ....	28
<b>Figure 2.19:</b> Raman spectra of the ZnO and Zn(OH) <sub>2</sub> nanostructures mixture.....	29
<b>Figure 2.20:</b> PL spectrum of pure Zn(OH) <sub>2</sub> samples with thickness of 150 micron and 4mm diameter. ....	29
<b>Figure 2.21:</b> Photoconductivity of pure Zn(OH) <sub>2</sub> samples with thickness of 150 micron and 4mm diameter. ....	30
<b>Figure 2.22:</b> UV-visible spectra of pristine–Zn(OH) <sub>2</sub> . ....	30
<b>Figure 2.23:</b> Photoluminescence spectra of (a) pure Zn(OH) <sub>2</sub> , (b) Zn(OH) <sub>2</sub> –5 wt% of ANI, (c) Zn(OH) <sub>2</sub> –5 wt% of ANI + PVA and (d) pristine PVA. ....	31
<b>Figure 2.24:</b> Chemical formula of PMMA. ....	33
<b>Figure 2.25:</b> Normalized PL spectra of bare ZnO nanowires and nanowires embedded in PMMA. ....	33
<b>Figure 2.26:</b> Chemical formula of PAAH. ....	34
<b>Figure 2.27:</b> PL spectra of ZnO samples with different concentration of PAAH (0, 0.37, 1, 3 and 10 mg/mL) added after the synthesis and different surface charges (21.4, 11.1, 1.7, -11, -21.6 mV for 0, 0.37, 1, 3 and 10 mg/mL, respectively). ....	35
<b>Figure 3.1:</b> Schematic diagram of the LECBD experimental setup. ....	49
<b>Figure 3.2:</b> Operation principle of the XRD analysis. ....	52
<b>Figure 3.3:</b> X-ray diffraction pattern of zinc oxide nanoparticles. ....	53
<b>Figure 3.4:</b> Schematic diagram of the (a) SEM and (b) TEM principles. ....	54
<b>Figure 3.5:</b> An example showing the potential difference as a function of the distance from the negatively charged surface of a particle dispersed in a solution. ....	57
<b>Figure 3.6:</b> Schematic diagrams of the operational principles of the DLS and ELS techniques for the size and zeta potential measurements. ....	58
<b>Figure 3.7:</b> Schematic diagram of the operational principle of the Michelson interferometer. ....	59
<b>Figure 3.8:</b> Typical IR spectrum of bulk ZnO. ....	60
<b>Figure 3.9:</b> Room temperature first-order Raman spectra of wurtzite ZnO in different experimental configurations and allowed optical phonon modes. ....	61

<b>Figure 3.10:</b> The process of the photoluminescence (PL) including the above bandgap absorption ①, band edge PL ②, defect or impurity related PL ③ and non radiative recombination ④, under the excitation with energy higher than the bandgap.....	63
<b>Figure 3.11:</b> Schematic diagram of the setup for the steady-state PL measurement.....	64
<b>Figure 3.12:</b> PL spectrum of bulk ZnO. ....	64
<b>Figure 3.13:</b> PLE spectra of ZnO nanoparticle solution with an emission wavelength of 500 nm. Black dotted line: polymer was not added to the solution. Blue solid line: Polyethylene glycol (PEG) was added after synthesis. ....	65
<b>Figure 3.14:</b> Schematic diagrams of the TRPL measurement setup using the (a) real-time photoluminescence and (b) streak-camera-based measurement. ....	66
<b>Figure 3.15:</b> Time decay curve of 40 nm ZnO nanoparticles.....	67
<b>Figure 3.16:</b> Schematic diagram of the PL QY measurement setup. ....	69
<b>Figure 4.1:</b> AES spectra of $L_3M_{45}M_{45}$ transitions of aggregates of ZnO NPs synthesized by LECBD method with different oxygen pressures during the deposition and the target powder. ..	78
<b>Figure 4.2:</b> (a) TEM image of ZnO NPs synthesized by the LECBD method; (b) high-resolution TEM image of a particle; (c) Fourier transform of diffraction patterns taken at high-resolution and (d) size chart for NPs and the lognormal fit .....	78
<b>Figure 4.3:</b> Absorption spectrum of a 300 nm-thick ZnO NP layer fabricated using the LECBD method.....	79
<b>Figure 4.4:</b> PL spectra of ZnO NPs fabricated by the LECBD method with different contents of oxygen in the plasma. ....	80
<b>Figure 4.5:</b> PLE spectrum of ZnO NPs fabricated by the LECBD method. ....	80
<b>Figure 4.6:</b> External quantum efficiency (EQE) of the (a) Si photodiode with initially high quantum efficiency in the UV before (solid squares ■) and after (empty squares □) the 5 nm-thick ZnO layer deposition on the front side of the device; (b) Si photodiode with initially high quantum efficiency in the UV before (solid squares ■) and after (empty squares □) the 10 nm-thick ZnO layer deposition on the front side of the device and (c) Si photodiode with initially low quantum efficiency in the UV before (solid squares ■) and after (empty squares □) the 2 nm-thick ZnO layer deposition on the front side of the device. Inset of (c) is the zoom around 400 nm from (c).....	81
<b>Figure 4.7:</b> Spectral response measured on the monocrystalline Si solar cell, before and after the ZnO layer deposition on the front side of the solar cell. The inset is the picture of the solar cell: the black spot is the ZnO NPs deposited layer.....	83
<b>Figure 4.8:</b> PL spectrum of commercially available ZnO NPs from Iolitec Company (the excitonic emission is very weak). ....	83
<b>Figure 4.9:</b> PLE spectrum of commercially available ZnO NPs (Iolitec, Germany). ....	84
<b>Figure 4.10:</b> XRD diffractograms of ZnO NPs synthesized by the co-precipitation of the zinc acetate with KOH (4 KOH/Zn acetate) in ethanol (bottom) and in water (top). The curves are shifted along the y-axis for clarity.....	85

<b>Figure 4.11:</b> PL spectra of ZnO NPs synthesized by the co-precipitation of the zinc acetate with KOH (4 KOH/Zn acetate) in ethanol and in water.....	86
<b>Figure 4.12:</b> XRD diffractograms of ZnO NPs powders synthesized by the co-precipitation of the zinc acetate and zinc sulfate with KOH (4 KOH/Zn acetate and 4 KOH/Zn sulfate) and LiOH (4 LiOH/Zn acetate and 4 LiOH/Zn sulfate), from top to bottom. The curves are shifted along the y-axis for clarity.....	87
<b>Figure 4.13:</b> Raman spectra of ZnO nanoparticles synthesized by the co-precipitation of the zinc acetate with KOH (4 KOH/Zn acetate) and LiOH (2 and 4 LiOH/Zn acetate), from top to bottom. The curves are shifted along the y-axis for clarity. ....	88
<b>Figure 4.14:</b> Raman spectra of ZnO nanoparticles synthesized by the co-precipitation of the zinc sulfate with KOH (4 KOH/Zn sulfate) (top curve) and LiOH (4 LiOH/Zn sulfate) (bottom curve). The curves are moved along the y-axis for clarity. ....	88
<b>Figure 4.15:</b> TEM images of the ZnO nanoparticles synthesized by the co-precipitation of the zinc acetate and the zinc sulfate with: (a) 4 KOH/Zn acetate, (b) 4 LiOH/Zn acetate, (c) 4 KOH/Zn sulfate and (d) 4 LiOH/Zn sulfate. ....	89
<b>Figure 4.16:</b> Normalized PL spectra of ZnO nanoparticles synthesized by the co-precipitation of the zinc acetate with KOH (4 KOH/Zn acetate, bottom curve) and LiOH (2 LiOH/Zn acetate, middle curve and 4 LiOH/Zn acetate, top curve). The experimental curve is shown as a solid line and the dotted curves are the fits of the visible emission peak. The plots are shifted along the y-axis for clarity.....	91
<b>Figure 4.17:</b> Normalized PL spectra of ZnO nanoparticles synthesized by the co-precipitation of the zinc sulfate with KOH (4 KOH/Zn sulfate, bottom curve) and LiOH (2 LiOH/Zn sulfate, middle curve and 4 LiOH/Zn sulfate, top curve). The experimental curve is shown as a solid line and the dotted curves are the fits of the visible emission peak. The plots are shifted along the y-axis for clarity.....	91
<b>Figure 4.18:</b> PL spectrum of ZnO NPs under the excitation of 532 nm synthesized by the co-precipitation of the zinc acetate with LiOH (4 LiOH/Zn acetate), which has the optimum PL QY. ....	93
<b>Figure 4.19:</b> Diagram of the $O_i$ creation and diffusion mechanism after the $O_2$ adsorption on the ZnO NPs surface. ....	94
<b>Figure 4.20:</b> (a) Raman spectrum of ZnO NPs synthesized by the co-precipitation of the zinc sulfate with 4 LiOH/Zn sulfate and 1 % of PAAH in weight with respect to ZnO. The inset is the Raman spectrum of PAAH. (b) Zoom of Raman spectrum of ZnO NPs in the range 200-800 $cm^{-1}$ . ....	95
<b>Figure 4.21:</b> Normalized PL spectra of ZnO nanoparticles synthesized by the co-precipitation of the zinc sulfate with 4 LiOH/Zn sulfate with 1 % of PAAH in weight towards ZnO (top curve) and without PAAH addition (bottom curve). The plots are shifted along the y-axis for clarity. ....	95
<b>Figure 4.22:</b> PL spectrum of the ZnO NPs synthesized by the hydrolysis method (a) deposited on the indium foil by pressing and (b) dispersed in PU matrix and deposited on fused silica substrate. ....	97
<b>Figure 4.23:</b> PL spectrum of the PU matrix alone, without the ZnO NPs.....	97

<b>Figure 4.24:</b> PLE spectrum of ZnO NPs synthesized by the Zn[N(SiMe <sub>3</sub> ) <sub>2</sub> ] <sub>2</sub> hydrolysis.....	98
<b>Figure 4.25:</b> FTIR spectra of ZnO nanoparticles synthesized by the hydrolysis of ZnEt <sub>2</sub> with different concentrations of PAA (0 wt%, 0.063 wt%, 0.63 wt% and 6.3 wt% from bottom to top). Inset: the chemical structure of PAAH. The plots are shifted along the y-axis for clarity. ....	99
<b>Figure 4.26:</b> Raman spectrum of ZnO nanoparticles synthesized by the hydrolysis of ZnEt <sub>2</sub> with no PAAH. ....	100
<b>Figure 4.27:</b> XRD diffractograms of ZnO nanoparticles synthesized by the hydrolysis of ZnEt <sub>2</sub> with different concentrations of PAAH (0.063 wt%, 0.63 wt%, and 6.3 wt% from top to bottom). The plots are shifted along the y-axis for clarity. Peaks labeled with * refer the Zn(OH) <sub>2</sub> wulfingite phase. ....	100
<b>Figure 4.28:</b> TEM images of ZnO nanoparticles synthesized by the hydrolysis of ZnEt <sub>2</sub> (a) with 0.063 wt% of PAA and (b) with 0.63 wt% of PAAH (the inset is a zoom of the surface of a sphere). ....	101
<b>Figure 4.29:</b> PL spectra of ZnO nanoparticles synthesized by the hydrolysis of ZnEt <sub>2</sub> with different concentrations of PAAH (from bottom to top: 0 wt% of PAAH, 0.063 wt% of PAAH, 0.63 wt% of PAAH and 6.3 wt% of PAAH). The plots are shifted along the y-axis for clarity. ....	102
<b>Figure 4.30:</b> PL spectrum of PAAH. ....	102
<b>Figure 4.31:</b> TRPL decay curves of ZnO nanoparticles synthesized by the hydrolysis of ZnEt <sub>2</sub> with no PAAH, with 0.063 wt% and 0.63 wt% of PAAH. Corresponding biexponential fits (violet dash lines) results are summarized in <b>Table 4.4</b> . ....	103
<b>Figure 4.32:</b> PLE spectra of ZnO nanoparticles synthesized by the hydrolysis of ZnEt <sub>2</sub> with no PAAH and with 0.63 wt% of PAAH.....	104
<b>Figure 4.33:</b> Reflection spectrum (left) and the bandgap estimation via Kubelka-Monk approximation (right) of ZnO nanoparticles synthesized by the hydrolysis of the diethyl zinc with 0.63 wt% of PAAH. ....	104
<b>Figure 4.34:</b> PLE spectrum of pure PAAH. ....	105
<b>Figure 4.35:</b> Schematic diagram of the energy levels for ZnO/PAAH nanocomposites and supposed mechanism of the PL QY enhancement. ....	105
<b>Figure 4.36:</b> Adsorption of PAAH at the surface of ZnO NPs for various PAAH concentrations. ....	107
<b>Figure 4.37:</b> Scheme of the bidentate chelating structure of (a) COO <sup>-</sup> - Zn <sup>2+</sup> and (b) hydrogen bonding between ZnO NPs and PAAH layer.....	108
<b>Figure 4.38:</b> PL spectra of ZnO NPs under the excitation of 532 nm synthesized synthesized by the hydrolysis of ZnEt <sub>2</sub> with different concentrations of PAAH (from bottom to top: 0 wt% of PAAH, 0.063 wt% of PAAH and 0.63 wt% of PAAH).....	108
<b>Figure 4.39:</b> (a) SEM image and (b) XRD diffractogram of the ZnO NPs synthesized by the hydrolysis of ZnEt <sub>2</sub> with 0.63 wt% of PAAH and then washed with ethanol. ....	109
<b>Figure 4.40:</b> XRD diffractograms of ZnO nanoparticles synthesized by the hydrolysis of ZnEt <sub>2</sub> with different lengths of PAAH of 0.63 wt% (240 000, 100 000, 5000 and 2000 g·mol <sup>-1</sup> from top to bottom). The plots are shifted along the y-axis for clarity. Peaks labeled with * refer the Zn(OH) <sub>2</sub> wulfingite phase. ....	110

<b>Figure 4.41:</b> TEM images of ZnO nanoparticles synthesized by the hydrolysis of ZnEt <sub>2</sub> with PAAH of 0.63 wt% of (a) 2000 g·mol <sup>-1</sup> , (b) 5000 g·mol <sup>-1</sup> , (c) 100 000 g·mol <sup>-1</sup> and (d) 240 000 g·mol <sup>-1</sup> .	111
<b>Figure 4.42:</b> PL spectra of ZnO nanoparticles synthesized by the hydrolysis of ZnEt <sub>2</sub> with different lengths of PAAH of 0.63 wt% (240 000, 100 000, 5000 and 2000 g·mol <sup>-1</sup> from top to bottom). The plots are shifted along the y-axis for clarity.	112
<b>Figure 4.43:</b> (a) FTIR spectrum; (b) Raman spectrum and (c) PL spectrum of ZnO NPs synthesized by the hydrolysis of ZnEt <sub>2</sub> with 0.63 wt% of PAANa. Inset: chemical formula of PAANa.	113
<b>Figure 4.44:</b> (a) PL spectra of ZnO nanoparticles synthesized by the hydrolysis of ZnEt <sub>2</sub> with 0.63 wt% of PAAH only (bottom curve) and with PAAH and PAANa of 75:25 (middle curve) and after 1 month exposure to air (top curve). (b) XRD diffractograms of ZnO nanoparticles synthesized by the hydrolysis of ZnEt <sub>2</sub> with 0.63 wt% of PAAH only (bottom curve) and with PAAH and PAANa of 75:25 (top curve). The plots are shifted along the y-axis for clarity.	114
<b>Figure 4.45:</b> TRPL decay curves and corresponding biexponential fits (violet dash lines) results of ZnO nanoparticles synthesized by the hydrolysis of ZnEt <sub>2</sub> with the mixture of PAAH with PAANa (0.63 wt%, 75:25 in volume).	115
<b>Figure 4.46:</b> Zeta potential distribution spectrum of ZnO nanoparticles synthesized by the hydrolysis of ZnEt <sub>2</sub> with 0.63 wt% of PAAH and of M <sub>w</sub> = 2000 g·mol <sup>-1</sup> , dispersed in an aqueous solution containing 31.5 wt% of PAAH.	116
<b>Figure 4.47:</b> Diagram of the quantity of ZnO NPs dispersed in 10 mL suspension in function of PAAH concentration.	117
<b>Figure 4.48:</b> PL spectra of ZnO nanoparticles synthesized by the hydrolysis of ZnEt <sub>2</sub> with 0.63 wt% of PAAH at 2000 g·mol <sup>-1</sup> , dispersed in the solution with different concentrations of PAAH.	118
<b>Figure 4.49:</b> Diagram of the process of the deposition of one layer containing ZnO NPs in PAAH matrix and then another layer of PMMA on its top.	118
<b>Figure 4.50:</b> PL spectra of different parts of the structure shown in Figure 4.49, including the fused silica glass, the pure PMMA, the layer containing ZnO NPs in PAAH matrix and the PMMA layer on the top of the ZnO NPs layer.	119
<b>Figure 5.1:</b> Picture of ZnO NPs synthesized by the hydrolysis of ZnEt <sub>2</sub> with a mixture of PAAH and PAANa with the ratio of 50:50 in volume, the concentration of 0.63 wt% and the reaction time of 1h.	125
<b>Figure 5.2:</b> Size distribution measured by DLS measurement of ZnO NPs synthesized by the hydrolysis of ZnEt <sub>2</sub> with a mixture of PAAH and PAANa at the ratio of 50:50 in volume, the concentration of 0.63 wt% and the reaction time of 1h.	126
<b>Figure 5.3:</b> XRD diffractogram of ZnO nanoparticles synthesized by the hydrolysis of ZnEt <sub>2</sub> with a mixture of PAAH and PAANa at the ratio of 50:50 in volume, the concentration of 0.63 wt% and the reaction time of 1h. Peaks labeled with * are often present in XRD diffractograms of badly crystallized samples containing Zn hydroxide.	127

<b>Figure 5.4:</b> PL spectrum of ZnO nanoparticles synthesized by the hydrolysis of ZnEt <sub>2</sub> with a mixture of PAAH and PAANa at the ratio of 50:50 in volume, the concentration of 0.63 wt% and the reaction time of 1h.....	127
<b>Figure 5.5:</b> PL spectra of ZnO nanoparticles synthesized by the hydrolysis of ZnEt <sub>2</sub> with different ratios of PAAH and PAANa and the reaction time of 1h. The plots are shifted along the y-axis for clarity. ....	128
<b>Figure 5.6:</b> PL spectra of ZnO nanoparticles synthesized by the hydrolysis of ZnEt <sub>2</sub> with different concentrations of the mixture of PAAH and PAANa (50:50 in volume) and with the reaction time of 1h.....	129
<b>Figure 5.7:</b> TRPL decay curves of ZnO nanoparticles synthesized by the hydrolysis of ZnEt <sub>2</sub> with a mixture of PAAH (2000 g·mol <sup>-1</sup> ) and PAANa (4000 g·mol <sup>-1</sup> ) and a mixture of PAAH (240 000 g·mol <sup>-1</sup> ) and PAANa (2000 g·mol <sup>-1</sup> ) (50:50 in volume and the concentration of 0.63 wt%). Corresponding biexponential fits (violet dash lines) results are summarized in <b>Table 5.3</b> .....	133
<b>Figure 5.8:</b> Normalized PL spectra and PL QYs of ZnO nanoparticles synthesized by the hydrolysis of ZnEt <sub>2</sub> with 0.63 wt% of PAAH and 0.63 wt% of PAALi (50:50 in volume) and with 0.63 wt% of PAAH and 0.63 wt% of PAANa (50:50 in volume), with the reaction time of 1h. ....	134
<b>Figure 5.9:</b> Normalized PL spectra and PL QYs of ZnO nanoparticles synthesized by the hydrolysis of different volumes of ZnEt <sub>2</sub> with different volumes of 0.63 wt% of PAAH and 0.8 wt% of PAANa (or 0.63 wt% of PAALi) (50:50 in volume) mixture and with the reaction time of 1h. ....	135
<b>Figure 6.1:</b> Key stages of spin-coating process. ....	140
<b>Figure 6.2:</b> Schematic diagram of different components of an ellipsometric set up. ....	141
<b>Figure 6.3:</b> Model structures for samples: (left) the simple model and (right) the more elaborated model. ....	143
<b>Figure 6.4:</b> Comparison of optical indices of pure PAAH and of the mixture of PAAH + ZnO NPs (emitting in the green spectral range, PL QY of ~ 20 %). ....	143
<b>Figure 6.5:</b> Extrapolation of the refractive index in the range 730 - 1200 nm. ....	144
<b>Figure 6.6:</b> Schematic representation of the effective mediums by: (a) Bruggeman model and (b) Maxwell-Garnett model. ....	146
<b>Figure 6.7:</b> Comparison of refractive indices n obtained for the ZnO NPs + PAAH film experimentally and calculated theoretically using the Maxwell-Garnett model (with and without k for simplification) and the Bruggeman model, and the experimental values of n obtained for pure PAAH. The theoretical curves calculated using the Maxwell-Garnett model with and without k (k = 0) are superposed. ....	148
<b>Figure 6.8:</b> Comparison of extinction coefficients k between different materials (ZnO, PAAH and the ZnO NPs + PAAH mixture – marked as experimental in the legend) obtained by the ellipsometry measurement and the theoretical curves calculated using the Maxwell-Garnett model for ZnO NPs + PAAH mixture.....	149
<b>Figure 6.9:</b> Structure of the studied copper indium gallium selenide (CIGS) solar cell (left) and the amorphous Si (a-Si) solar cell (right). ....	150

<b>Figure 6.10:</b> Comparison of the EQE of the CIGS and amorphous silicon (a-Si) solar cells made by simulations with SCAPS software. ....	151
<b>Figure 6.11:</b> Schematic diagrams of different stack structures for amorphous silicon solar cells with a ZnO NPs+PAAH layer. ....	152
<b>Figure 6.12:</b> Evolution of the transmittance at 600 nm in function of the down-shifting layer thickness for different structures presented in <b>Figure 6.11</b> by simulations with SCAPS software. ....	152
<b>Figure 6.13:</b> Transmittance at 600 nm of the structure in <b>Figure 6.11</b> (a) in function of the down-shifting layer thickness. ....	153
<b>Figure 6.14:</b> Evolution of the transmittance at 600 nm in function of the thickness of the down-shifting layer for various thicknesses of the EVA layer. ....	154
<b>Figure 6.15:</b> Schematic diagrams of the different top layer stack structures to be applied to the CIGS solar cells. ....	155
<b>Figure 6.16:</b> Evolution of the transmittance at 600 nm in function of the down-shifting layer thickness for 3 different structures presented in <b>Figure 6.15</b> . ....	155
<b>Figure 6.17:</b> Evolution of the transmittance at 600 nm in function of the down-shifting layer thickness for various thicknesses of EVA layer. ....	156

# Chapter 1

## Introduction

### 1.1. Structure of the thesis

In this thesis, chapter 1 introduces the goal of this thesis, i.e. the increase of the solar cell efficiency via the application of the down-shifting phenomenon. The concept of the down-shifting is introduced and the main criteria which should be taken into account when choosing a proper down-shifting material is described. At last, the active down-shifting material used in the experimental part - ZnO nanoparticles - and the challenges related to the engineering of the luminescent down-shifting (LDS) layer is mentioned.

Chapter 2 presents the studied materials constituting the down-shifting layer (including the luminescent nanoparticles and the host materials). The physical, chemical and optical properties of ZnO NPs are presented in detail, with an emphasis on the optical properties. In the end, the host matrices - polymethyl methacrylate (PMMA) and polyacrylic acid (PAAH), in which ZnO nanoparticles were dispersed, are briefly introduced.

In chapter 3, the synthesis and characterization methods of ZnO nanoparticles are presented. Three fabrication methods of ZnO NPs are introduced: the purely physical method - Low Energy Cluster Beam Deposition (LECBD) method and two chemical synthesis methods: the co-precipitation method and the hydrolysis method. For comparison, some properties of commercially available ZnO nanoparticles are also presented. Then the characterization methods of the structural, chemical and optical properties of ZnO nanoparticles are introduced. The operational principles and setups of these characterization methods are also summed up in this chapter.

In chapter 4, the results of the structural, chemical and optical characterizations are shown, in function of the different ZnO NPs fabrication methods. The preliminary results obtained for some silicon photodiodes with the down-shifting layer on their top are also presented. Finally, the obtained results are discussed and some hypotheses for explaining them are introduced. The ZnO nanoparticles synthesized using the chemical methods turn out to have the best properties for the applications in the LDS layers.

In chapter 5, studies on the dispersible ZnO NPs synthesized with the mixture of PAAH and PAANa are shown. The influences of the mixture ratio, concentration, length of the surfactant mixture and the volume of the precursor  $\text{ZnEt}_2$  and the surfactant mixture on the dispersibility and visible light emission efficiency are presented and discussed.

In chapter 6, the results concerning the deposition of thin films containing ZnO nanoparticles in a matrix are presented. The deposition method used (spin-coating) is briefly introduced. Then the influence of the solvent on the dispersion of ZnO NPs in a matrix of PAAH is described. The results of the ellipsometry measurements performed on the down-shifting layer as a function of the matrix thickness and refractive index are presented. Finally, taking into account the results of the ellipsometry measurements, the simulation of the influence of the down-shifting layer containing ZnO NPs on the efficiency of various types of solar cells are presented.

### 1.2. Solar cells: state of the art

As the human population grows and the industry develops, the consumption of natural resources (among which coal, oil and gas) increases, resulting in the energy crisis and environmental pollution. The question of the accessibility of these resources on a long term and the pollution that their use induces are nowadays big issues for the whole humanity, so it is urgent to make progress of the research dedicated to the renewable energy sources such as sunlight, wind, water, tides, waves and geothermal heat. Solar energy, the most important source of renewable energy, is abundant, clean and its use has been widely studied. Many kinds of solar cells have been designed to collect the energy of the sunlight and transfer it into electricity. Among them, silicon (Si) solar cells occupy the majority of markets. Other materials such as copper indium gallium selenide (CIGS) and cadmium telluride (CdTe) cells are attracting more and more attention as an active layer in the thin film solar cells. However, the efficiency of solar cells is still to be improved, so that the cost of the energy can be competitive with fuel or nuclear energy sources, which are dominant today.

The solar cell efficiency is always lower than its theoretical value because it is limited by the surface reflection of the incident light and the photogenerated carrier collection. The largest proportion of losses in every developed photovoltaic (PV) technology originates from the mismatch between the spectral response (SR) of solar cells and the wideband of solar emission spectrum, as shown in **Figure 1.1**. The fundamental spectral losses limit the theoretical maximum efficiency ( $\eta$ ) of a single-junction solar cell having a bandgap of  $E_g = 1.1$  eV (like Si) to a value of  $\eta \approx 31$  %, called the Shockley-Queisser limit [1]. As a large part of sunlight is absorbed in the approximately first top micron of a semiconducting material (such as Si for example), an extensive laboratory research has been performed on the optimization of the front surface of PV devices. The potential increase in the solar cell SR passes through making better use of the short-wavelength ( $\lambda$ ) light (UV and blue spectral range) and long  $\lambda$  light (near infrared and infrared spectral range) of the solar emission spectrum which cannot be utilized efficiently by a single-junction solar cell. The short  $\lambda$  photons are often absorbed by the coating glass of the cell. Otherwise, once they are absorbed, hot carriers are generated. The excess hot carrier energy is released as heat (detrimental to the efficiency of the cell). On the other hand, the cell is transparent to long  $\lambda$  photons with energy below the bandgap of its active material. To improve the solar cell efficiency, these radiations should be transferred into the light spectrum which

overlaps better with the absorption spectrum of the solar cell's active material, i.e. in which the given solar cell has the highest SR.

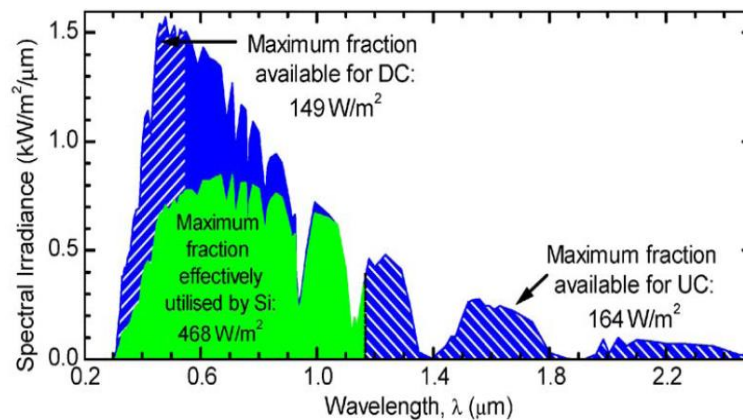


**Figure 1.1:** Global solar emission spectrum at air mass (AM) 1.5 showing the fraction that is currently absorbed by a thick silicon (Si) solar cell and the additional regions of the spectrum that can contribute toward up- and down-conversion (UC and DC, respectively).  $\lambda$  - wavelength. (Reprinted from reference [2]).

In what is called “the third generation solar cells”, different solutions are proposed to overcome this spectral mismatch, for example, multiple junction structures. In this kind of solar cells, several semiconductor materials with different bandgaps are used to form heterojunctions, composing the cell. It allows the absorption of a broader range of the solar spectrum. The up-conversion [3] and down-conversion [4] phenomena are also among those used to convert the incident solar light into the light spectrum that matches the absorption of the active layer in solar cells. Up-conversion permits the conversion of IR light to visible light by a simultaneous absorption of two photons for generation of one high-energy photon. This is a nonlinear process, hence the probability of such a transition is usually quite low. In down-conversion, the absorbed photon with higher energy (UV or blue) is converted into two identical photons of equal energy which is two times lower the bandgap (also called the quantum cutting). This concept is interesting since there is low energy loss. But it is only efficient for photons with the energy equal to the bandgap of the solar cell active material. Moreover, its efficiency is limited as it requires the existence of an intermediate energy level exactly in the middle of the bandgap of the material. The energy down-shifting [5, 6], which is a variant of the down-conversion technique, permits the conversion of a high-energy photon into one or more lower-energy ones, contributing to the generation of additional electron-hole pairs and thus to a potential increase in the overall solar cell efficiency. Moreover, it is less restricting compared to the down-conversion technique, as it does not require an intermediate energy level exactly in the middle of  $E_g$ , but can be located anywhere in the bandgap. **Figure 1.2** illustrates the energy levels involved in the up-conversion, down-conversion and down-shifting processes.

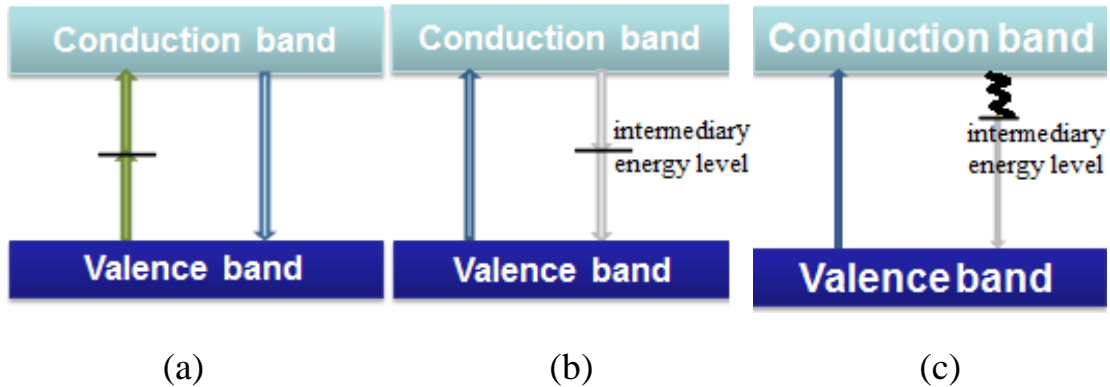


**Figure 1.2:** Processes of the (a) **up-conversion**, which permits the conversion of IR light to visible light by simultaneous absorption of two photons and emission of one photon with higher energy; (b) **down-conversion**, in which one photon with higher energy can be converted into two identical photons of equal energy, two times lower than the absorbed one and (c) **down-shifting**, a variant of the down-conversion technique, permits the conversion of a high-energy photon into one (or more) of lower-energy.

### 1.3. Down-shifting phenomenon

Luminescent down-shifting (LDS) is an approach that involves applying a luminescent species in a layer placed on the top of a solar cell. Such a supplementary layer is generically called an “add-on” module. The LDS layer absorbs photons, typically in the 300–500 nm spectral range, and re-emits at a longer wavelength, where the solar cell exhibits a significantly better spectral response. It should be mentioned that the application of the down-shifting technique will not permit to increase in a spectacular manner the solar cell efficiency, contrary to for example tandem solar cells, which theoretically aim at achieving a very high efficiency. Here, the goal of our strategy is to gain a few percents of the relative efficiency, and the most important point is that this should be made at low cost and based on standard cell structure.

The structure of the solar cell with a LDS layer on its top is shown in **Figure 1.3**. It has been demonstrated that the LDS layer can also act as an antireflection layer, by adjusting the layer thickness [7], further improving the solar cell efficiency.

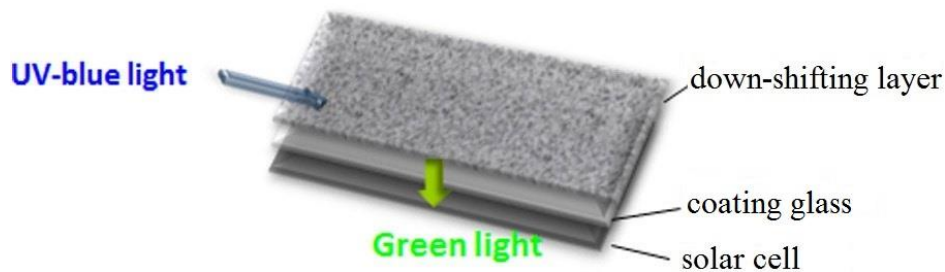


**Figure 1.3:** Structure of the solar cell with a down-shifting layer on the front side.

The solar cell efficiency improvement thanks to the presence of the luminescent down-shifting layer is determined by the optical properties of the luminescent material, including the absorption coefficient and the conversion efficiency and the LDS layer parameters (such as the thickness and the refractive index) as well as the transmission in other wavelength ranges. Kalytchuk S. *et al.* [8] have discussed the parameters that influence the solar cell efficiency having the LDS layer on its top and which should be optimized so that this efficiency is the highest, thanks to the down-shifting effect. In the following we introduce and define these parameters.

Two important characteristics of the luminescent materials which will permit to qualify them as good or bad down-shifters are the photoluminescence quantum yield (PL QY) and the overlap of their absorption and emission spectra.

**Photoluminescence quantum yield (PL QY).** For a given luminescent material, the PL QY is defined as the ratio between the number of emitted photons and the number of absorbed photons ( $N_{em}/N_{abs}$ ).

**Absorption and emission overlap.** The luminescent material absorption and emission overlap is controlled by the positions of the absorption and the emission band maxima (also called the Stokes shift) and the widths of these bands. The overlap between them should be minimized or even better avoided, in order to suppress the reabsorption of the emitted light in the LDS layer, which otherwise decreases the solar cell efficiency.

To obtain a good spectral matching between the emission spectrum of the luminescent down-shifting layer and the absorption spectrum of the active layer of the solar cell, the following criteria should be considered:

**Absorption spectral matching:** The absorption spectral matching characterizes the matching between the absorption spectrum of the luminescent material and the higher energy part of solar emission spectrum which is used inefficiently by a solar cell (i.e. SR of a given solar cell is low in this spectral range). The better the absorption matching, the broader the spectral range of the emitted sunlight which is expected to be converted efficiently into electricity by the solar cell thanks to the absorption in the LDS layer.

**Parasite absorption:** The parasite absorption is used to characterize the overlap between the absorption spectrum of the luminescent material and the solar spectrum which is efficiently used by a solar cell. Since the LDS layer is expected to emit light in the visible, it can also absorb in this spectral range. Thus, it can “take away” from the solar cell a part of the incident visible radiation from the sun. As this parasite absorption decreases the solar cell efficiency, it should be reduced as much as possible.

**Emission spectral matching:** The matching between the emission spectrum of the luminescent material and the spectral response of the solar cell without LDS on its top is characterized by the

emission spectral matching. The better the emission spectral matching, the higher the solar cell efficiency is expected to be when the LDS layer is deposited on its top.

The efficiency of a solar cell with a LDS layer on its front side can be defined by a simple model which takes the assumption that LDS layers emits only in one direction – to the inside of the cell. It is written as [9]:

$$\eta(\lambda) = [1 - A(\lambda)]\eta_b(\lambda) + A(\lambda) \cdot \eta_{LDS} \cdot \max(\eta_b) \quad (1.1)$$

where:

$\eta(\lambda)$  is the external quantum efficiency (EQE) of the complete solar cell with a LDS layer on its top,

$A(\lambda)$  is the fraction of the solar spectrum which is absorbed by the LDS layer,

$\eta_b(\lambda)$  is the EQE of the solar cell without the LDS layer,

$\eta_{LDS}$  is the luminescence efficiency of the LDS layer,

$\max(\eta_b)$  is the maximum EQE of the solar cell without the LDS layer.

The luminescence efficiency  $\eta_{LDS}$  is expressed by the formula [8]:

$$\eta_{LDS} = PL \text{ QY} \cdot CE \cdot ESM \quad (1.2)$$

where:

PL QY is the photoluminescence quantum yield of the active material of the LDS layer,

CE is the photogenerated carrier collection efficiency,

ESM is the emission spectral matching integral defined as:

$$\int \eta_b(\lambda)P_{em}(\lambda)d\lambda / \int P_{em}(\lambda)d\lambda \quad (1.3)$$

where,

$P_{em}$  is the normalized emission profile of the luminescent material in the LDS layer.

Through fine adjustment of the LDS layer refractive index, the CE can reach more than 80 % by decreasing the reflection on the top layer. The ESM can be increased as close as possible to unity through choosing the appropriate luminescent material for the LDS layer, depending on the considered kind of a solar cell. Indeed, several couples of LDS materials and solar cells have been considered. It has been predicted that ZnO nanoparticles (NPs) are more suitable down-shifters for CIGS and CdTe solar cells than for standard Si solar cells, with the relative efficiency increase of 5.1 % (CIGS) and 15.1 % (CdTe) [7, 8]. For standard Si solar cells with the LDSL

layer on their top, the efficiency growth is nearly negligible [7, 8]. For CdTe/CdS solar cells, CdTe QDs can possibly induce a maximum increase of 16 % in the value of the solar cell short circuit current [8]. CdSe/CdS quantum dots (QDs) and tetrapods appear to be more adapted down-shifters when compared to CdTe QDs, due to the smaller overlap between the absorption and emission spectrum [8]. For crystalline Si solar cells, the PbS QDs are better candidates for a down-shifting layer, while the Rhodamine 800 is not suitable [8]. The Rhodamine 800 has a low emission spectral matching with the crystalline Si solar cells [8]. With PbS QDs, a maximum possible increase of 50 % in the short circuit current can be obtained in crystalline Si solar cells [8]. Since the CE and ESM can be optimized through the layer fabrication process and the choice of the luminescent material, the PL QY has the most important effect on the improvement of the solar cell efficiency when the LDS layer is present. Thus, the main purpose of this thesis is to design a luminescent material with intense visible photoluminescence quantum yield under UV-blue excitation.

### 1.4. Technical challenges concerned in this thesis

In this thesis, we have designed LDS layer containing ZnO NPs acting as the luminescent material. There are several technical issues that must be addressed in order to obtain an efficient and optimized down-shifting layer. The first one is that a high PL QY in the visible spectral range seems difficult to achieve. The main reason for this is that the visible emission in the ZnO NPs originates from the intrinsic defects, without the introduction of any additional impurity [10, 11]. The introduction of the light emitting centers into the structure of the material often comes along with the introduction of the non-radiative (quenching) defects, the latter being generally more abundant than the former. Consequently, if the light originating from defect emission is to be adjusted, a very subtle defect engineering and fine tuning of their amount must be achieved. This is all the more important as the size of the active material reaches the nanoscale (like in the case of ZnO NPs): the fraction of surface states increases as the size decreases. The presence of these surface states often leads to the luminescence quenching. Nevertheless, generally speaking, efficient defect engineering can be done via the controlled introduction of point defects, as for instance in nanodiamonds [12] or nanoparticles of SiC [13] (N-V centers in carbon diamond or the carbon antisite-vacancy in SiC). Moreover, the complete understanding of the origins of this visible emission in ZnO is still lacking, though several reviews provide the state-of-the-art knowledge [10, 11]. Another challenge is related to the choice of a good matrix protecting the ZnO NPs. The ZnO NPs should be easily dispersed in the matrix and the matrix itself should be transparent in the visible spectral range, not affecting the photoluminescence of the ZnO NPs.

## 1.5. References

---

1. Shockley W., Queisser H. J., Detailed balance limit of efficiency of p-n junction solar cells. *Journal of Applied Physics*, 1961, vol. 32, no. 3, p. 510-519.
2. Richards B. S., Enhancing the performance of silicon solar cells via the application of passive luminescence conversion layers. *Solar Energy Materials and Solar Cells*, 2006, vol. 90, no. 15, p. 2329-2337.
3. Trupke T., Green M. A., Würfel P., Improving solar cell efficiencies by up-conversion of sub-bandgap light. *Journal of Applied Physics*, 2002, vol. 92, no. 7, p. 4117-4122.
4. Kim H. J., Song J. S., Efficiency enhancement of solar cell by down-conversion effect of  $\text{Eu}^{3+}$  doped  $\text{LiGdF}_4$ . *Journal of the Korean Physical Society*, 2004, vol. 45, no. 3, p. 609-613.
5. Klampaftis E., Ross D., McIntosh K. R., Richards B. S., Enhancing the performance of solar cells via luminescent down-shifting of the incident spectrum. *Solar Energy Materials and Solar Cells*, 2009, vol. 93, no. 8, p. 1182-1194.
6. Apostoluk A., Zhu Y., Canut B., Masenelli B., Delaunay J.-J., Znajdek K., Sibiński M., Investigation of luminescent properties of ZnO nanoparticles for their use as a down-shifting layer on solar cells. *Physica Status Solidi C*, 2013, vol. 10, no. 10, p. 1301-1307.
7. Apostoluk A., Zhu Y., Masenelli B., Delaunay J.-J., Sibiński M., Znajdek K., Focsa A., Kaliszewska I., Improvement of the solar cell efficiency by the ZnO nanoparticle layer via the down-shifting effect. *Microelectronic Engineering*, 2014, vol. 127, p.51-56.
8. Kalytchuk S., Gupta S., Zhovtiuk O., Vaneski A., Kershaw S. V., Fu H. Y., Fan Z. Y., Kwok E. C. H., Wang C.-F., Teoh W. Y., Rogach A. L., Semiconductor nanocrystals as luminescent down-shifting layers to enhance the efficiency of thin-Film CdTe/CdS and crystalline Si solar cells. *The Journal of Physical Chemistry C*, 2014, vol. 118, no. 30, p. 16393–16400.
9. Geyer S. M., Scherer J. M., Moloto N., Jaworski F. B., Bawendi M. G., Efficient luminescent down-shifting detectors based on colloidal quantum dots for dual-band detection applications. *ACS Nano*, 2011, vol. 5, no. 7, p. 5566–5571.
10. Djurišić A. B., Leung Y. H., Optical properties of ZnO nanostructures. *Small*, 2006, vol. 2, p. 944-961.
11. Willander M., Nur O., Sadaf J. R., Qadir M. I., Zaman S., Zainelabdin A., Bano N., Hussain I., Luminescence from zinc oxide nanostructures and polymers and their hybrid devices. *Materials*, 2010, vol. 3, p. 2643-2667.
12. Ampem-Lassen E., Simpson D. A., Gibson B. C., Trpkovski S., Hossain F. M., Huntington S. T., Ganesan K., Hollenberg L. C. L., Praver S., Nano-manipulation of diamond-based singlephoton sources. *Optics Express*, 2009, vol. 14, p. 11287-11293.
13. Castelletto S., Johnson B. C., Ivády V., Stavrias N., Umeda T., Gali A., Ohshima T., A silicon carbide room-temperature single-photon source. *Nature Materials*, 2014, vol.13, p.151-156.

## Chapter 2

### Materials

In most of the current studies the LDS layer consists of a luminescent species, which is the active material performing the down-shifting process, embedded in a host material. As was mentioned in the introduction, the active material for the down-shifting is the most important component of a LDS layer. A material adapted to different types of solar cells, in terms of absorption and emission band positions and widths and having an intense visible photoluminescence quantum yield (PL QY) is required for an efficient down-shifting layer. An appropriate host material is crucial not only to ensure the high efficiency of the LDS layer, but also if the production of the LDS layer at the industrial scale is considered. Apart from the nature of both the luminescent and the host material, the mutual influence of one on another should also be considered. To make a layer, a solution being a mixture of the luminescent and the host material should be prepared. So a good dispersion of the luminescent material in the host material is important for obtaining a LDS layer of good optical quality. The basis to obtain an enhancement of the solar cell efficiency using the LDS layer stands obviously in the materials.

#### 2.1. Luminescent materials

The aim of a LDS layer is to absorb photons in the UV-blue range and to emit photons of lower energy (at longer wavelengths). Wide bandgap materials are necessary, as the excitation wavelengths are in the UV-blue spectral range. **Figure 2.1** presents the possible emission pathways following the absorption of a photon having the energy above the material bandgap. Following this UV absorption (marked as ① in **Figure 2.1**), the excited electron or hole first thermalizes to the minimum of the conduction band or maximum of the valence band, respectively. On one hand, the electron can relax directly to the valence band by photon emission, giving rise to the band edge emission which is marked as ② in **Figure 2.1**. On the other hand, the electron can de-excite through an intermediate level (in the bandgap) induced by an intrinsic defect or an impurity, which is marked as ③ in **Figure 2.1**. Thus photons with lower energy are emitted. Of course, these luminescent processes are in competition with non-radiative ones, marked as ④, related to impurities or defects and which often prevail over the photoluminescent emission. A large number of luminescent materials have been investigated for LDS and they can be separated into three main categories: organic dyes, rare-earth ions/complexes and quantum dots.

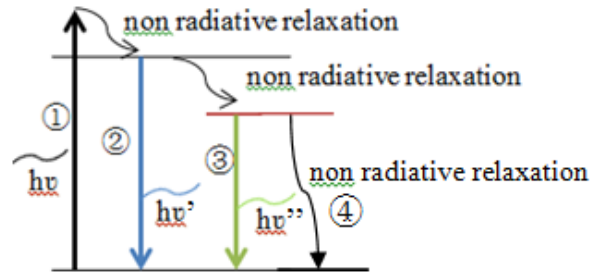


**Figure 2.1:** Photoluminescence (PL) process in direct bandgap semiconductors. (①: UV radiative absorption; ②: band edge PL; ③: defect or impurity induced PL; ④: non-radiative recombination path.)

**Organic dyes.** Organic dyes are organic compounds (or their complexes) which can be used as luminescent materials, exhibit relatively high absorption coefficients [1], close to unity photoluminescence quantum yield (PL QY) [2, 3] and are easy to process in polymeric matrices [1, 2]. The Rhodamine 6G [3], Lumogen Violet dye [4], Lumogen yellow 083 [5] and the mixture of Lumogen dyes violet (V570) and yellow (Y083) [6] have been commonly used to obtain the enhancement of the photocurrent in the photovoltaic (PV) modules in the short wavelength range. The main limitations of organic dyes for their use as a down-shifter are the narrow absorption bandwidth and a small Stokes shift. Their photostability over prolonged periods of exposure to the UV remains questionable in many cases, which can also be problematic if they are applied in a LDS layer on the PV devices [7].

**Rare-earth ions.** A rare earth element (REE) or rare earth metal is one of a set of seventeen chemical elements in the periodic table, specifically the fifteen lanthanides, together with scandium and yttrium. Rare-earth ions can be used as down-shifters via doping in other materials such as the  $\text{Ln}^{3+}$  [8],  $\text{Eu}^{3+}$  [9] doped  $\text{YVO}_4$  nanoparticles,  $\text{Sm}^{3+}$  and  $\text{Eu}^{3+}$  (emitting in red spectral range) or  $\text{Tb}^{3+}$  (emitting in green spectral range) doped borate glasses [10]. Rare-earth ions exhibit high PL QY [11, 12], but have extremely low absorption coefficients [12]. Additionally they are expensive materials with rather complicated processing procedures.

**Quantum dots (QDs).** QDs are nanosize semiconducting crystals with tunable absorption and emission bands, according to their size. They exhibit a wide absorption band, high emission intensity and a relatively good photostability [13]. Materials like PbS/CdS core/shell QDs [14], CdS QDs [15], CdSe/CdS core/shell QDs [16],  $\text{CdS}_x\text{Se}_{1-x}/\text{ZnS}$  core/shell QDs [17] and Si QDs [18] have been reported as a LDS layer for different types of solar cells. Application of QDs as down-shifter resulted in the average improvements in the solar cells external quantum efficiency (EQE) across the near UV ranging from 1.7 % to 21 % and in the increase of the short circuit current from 16 % to 50 %. However, there are high re-absorption losses due to the large overlap of the QDs absorption and emission bands and their use remains generally expensive [11]. Furthermore, it is widely known that cadmium (Cd) and sulfur (S), the elements often used for

the QDs fabrication, are very harmful both to nature and human beings. Additionally, there are serious recycling problems on the long-term concerning the Cd-based solar cells. Thus another material which will be used to replace CdS-based QDs should be considered. We propose the use of zinc oxide, ZnO, an environmental friendly and abundant (thus cheap) material.

### 2.2. An introduction to the zinc oxide

Zinc oxide (ZnO) is a direct bandgap semiconductor with great potential for a variety of applications, such as optical waveguides [19], phosphors [20], transparent conductive oxides [21], chemical gas sensors [22] and spin functional devices [23], UV-light emitters [24] and piezoelectric transducers [25]. Its wide bandgap (3.37 eV at room temperature [26]) makes ZnO a promising material for optoelectronic and photonic applications in the UV or blue spectral range, while the high exciton binding energy (60 meV), which is much larger than that of GaN (25 meV) and which can ensure an efficient exciton emission even at room temperature (RT). As a direct and wide bandgap material, ZnO has many advantages: higher breakdown voltages, ability to sustain large electric noise, high-temperature and high-power operation. It is also stable under UV exposure (UV eg. blocker applications). The semiconducting and piezoelectric properties of ZnO make it appealing for energy harvesting systems such as the piezoelectric generators [27]. The semiconducting property also makes ZnO sensitive to the doping. The Al doped ZnO is a highly conductive n-type material [28]. The doping (Al, In, etc.) of ZnO also influences its optical properties [29, 30] which can be used to tune emission colors.

There exist various forms of ZnO nanostructures such as nanoparticles, nanowires, nanorods, nanobelts and nanotubes [31, 32, 33]. It is easy to tune the ZnO nanostructures properties by controlling their size and morphology. Due to excellent optical and electrical properties and the easy synthesis control of the shape of ZnO nanostructures, they are potential candidates for photovoltaic (PV) applications. Some have a low reflectivity, which increases the light absorption, thus ZnO nanostructures are usually introduced as the anti-reflection layer in PV devices. Al/ZnO nanostructures are also attractive as transparent conductive oxides (TCO) for the application in solar cells [28]. ZnO based catalysts, such as Cu–ZnO or Cu-ZnO/Al<sub>2</sub>O<sub>3</sub>, have found extensive industrial applications in methanol synthesis from CO<sub>2</sub> [34]. Methanol-based polysulfide electrolyte has been used in quantum dot sensitized solar cells resulting in a particularly dramatic enhancement in photocurrent and reduced series resistance [35].

#### 2.2.1. Crystalline structure of ZnO

Zinc oxide is one of the most important II – VI semiconductor materials. Like bigger part of II-VI binary compound semiconductors, ZnO can crystallize in the form of hexagonal wurtzite structure or cubic zinc blende structure or cubic rock salt structure, as shown in **Figure 2.2** [25]. For ZnO, the cubic rock salt structure may be obtained at relatively high temperature and pressure and the cubic zinc blende structure can be stabilized only on cubic substrates. They are not common structures for ZnO in ambient conditions. In both hexagonal wurtzite structure and

cubic zinc blende structure, each Zn atom is surrounded by four O atoms at the corners of a tetrahedron, and vice versa. This tetrahedral coordination is typical of  $sp^3$  covalent bonding, which is eclipsed for hexagonal wurtzite structure and staggered for cubic zinc blende structure [36]. ZnO also has an ionic character, which tends to increase the bandgap beyond the one expected from the purely covalent bonding.

The wurtzite structure has a hexagonal unit cell with two lattice constants  $\mathbf{a}$  and  $\mathbf{c}$  as marked in **Figure 2.2** (a). The ratio of  $c/a$  in an ideal hexagonal wurtzite structure is 1.633. It belongs to the space group  $C_{6v}^4$  in the Schoenflies notation and  $P6_3mc$  in the Hermann-Mauguin notation. The structure is composed of two interpenetrating hexagonal close packed (hcp) sublattices. One of the sublattices consists of Zn atoms and another one consists of O atoms. They interpenetrate with respect to each other along the  $c$ -axis by the amount of  $\mathbf{u}$  of 0.375 in an ideal hexagonal wurtzite structure.  $\mathbf{u}$  is defined as the Zn-O bond length parallel to the  $c$ -axis, which is equal to  $u = \frac{1}{3} \cdot \left(\frac{a}{c}\right)^2 + \frac{1}{4}$ . The lattice constants are commonly measured at room temperature by X-ray diffraction (XRD) or observed through a high-resolution transmission electron microscopy (HRTEM). The lattice constants mostly range from 3.2475 to 3.2501 Å for  $\mathbf{a}$  and from 5.2042 to 5.2075 Å for  $\mathbf{c}$ , which is consistent with each other and close to the ideal data [35]. Some measured lattice constants  $\mathbf{a}$ ,  $\mathbf{c}$ ,  $\mathbf{c/a}$  ratio and  $\mathbf{u}$  parameters are listed in **Table 2.1**. This polar structure is characterized by the absence of mirror planes that are perpendicular to  $c$ -axis. This creates a  $c$ -axis oriented electronic dipole moment in each tetrahedron. Thus the asymmetric wurtzite structure leads to a large piezoelectric coefficient in ZnO [ 37 ].

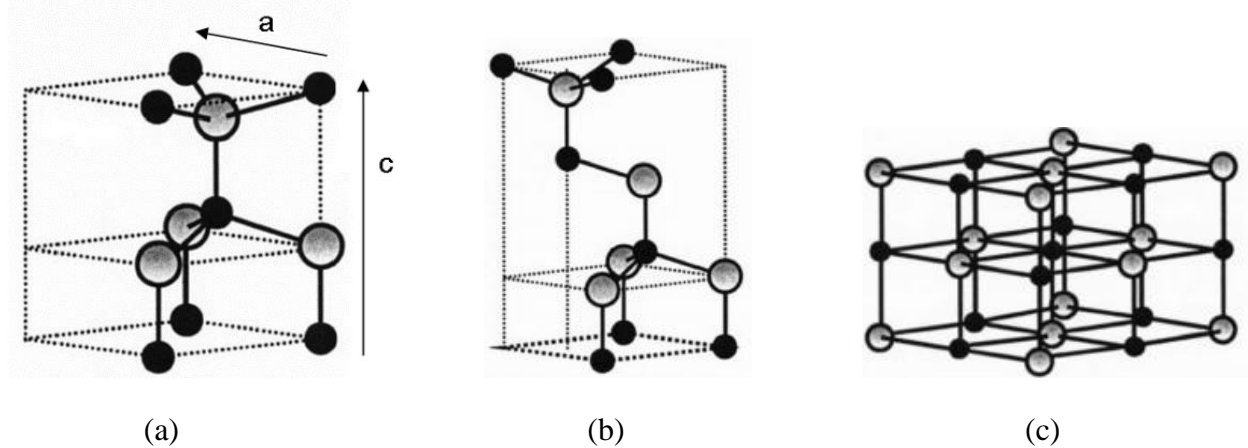


**Figure 2.2:** Zinc oxide crystal structures: (a) hexagonal wurtzite structure, (b) cubic zinc blende structure and (c) cubic rock salt structure.

**Table 2.1:** Measured lattice constants  $a$ ,  $c$ ,  $c/a$  ratio and  $u$  parameter of wurtzite ZnO.

$a$ (Å)	$c$ (Å)	$c/a$	$u$	Reference
3.2496	5.2042	1.6018	0.3819	38
3.2501	5.2071	1.6021	0.3817	39
3.2475	5.2075	1.6035		40

The lattice dynamics of ZnO are reflected in its phonon dispersion curve, as shown in **Figure 2.3** [41], in which the energy of a lattice vibration (in frequency) is plotted versus its wave vector in the reciprocal space along high-symmetry directions of the crystal. Due to the translational symmetry, the phonon dispersion is conventionally displayed within the Brillouin zone. The wurtzite ZnO possesses  $n = 4$  atoms in a unit cell (2 Zn-O molecular units). Each atom occupies the  $C_{3v}$  site, resulting in  $3n = 12$  phonon branches, with 3 acoustic modes (1 longitudinal acoustic (LA), 2 transverse acoustic (TA) modes) and  $3n - 3 = 9$  optical modes (3 longitudinal optical (LO), 6 transverse optical (TO) modes) [42]. At the Brillouin zone center (wave vector  $k = 0$ ), the acoustic phonon energy tends to zero while the optical phonons have the irreducible representation [43]  $\Gamma = A_1 + 2B_1 + E_1 + 2E_2$ , whereas the E modes are twofold degenerate. The  $A_1$  and  $E_1$  branches are polar, they split into LO and TO modes with different frequencies due to the macroscopic electric field which is associated with the LO phonons. These phonon modes can be detected by Infrared (IR) spectroscopy or Raman spectroscopy, except  $B_1$  mode which is inactive to both of them. The IR spectroscopy is active when there exists a molecule dipole change while the Raman spectroscopy is active when the polarization of the molecule changes. **Table 2.2** lists all the phonon modes and in which spectroscopy they are active.

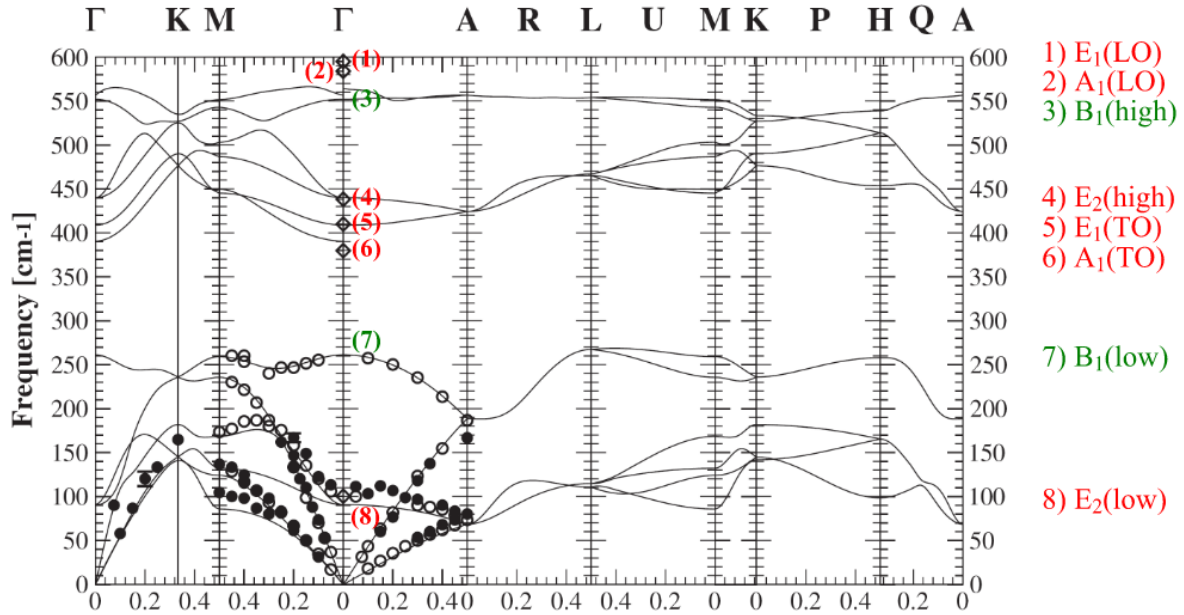


**Figure 2.3:** Phonon dispersion of wurtzite ZnO from [40]. The experimental results were derived from Raman scattering (diamond symbols in the Brillouin zone center [44]) and from inelastic neutron scattering (circles, [45, 46]). The solid lines are calculated results obtained by *ab initio* calculations [40].

**Table 2.2:** Phonon modes with different frequencies [42] and their active spectroscopy methods.

Optical phonon modes	Frequency (cm <sup>-1</sup> )	Active to the spectroscopy
A <sub>1</sub> (LO)	574	active to IR and Raman
A <sub>1</sub> (TO)	380	active to IR and Raman
B <sub>1</sub>	–	inactive to IR or Raman
E <sub>1</sub> (LO)	583	active to IR and Raman
E <sub>1</sub> (TO)	407	active to IR and Raman
E <sub>2</sub> <sup>low</sup>	101	only Raman active
E <sub>2</sub> <sup>high</sup>	437	only Raman active

### 2.2.2. Electrical characteristics of ZnO

The electronic band structure is very important if the applications of a given material are considered. Several studies of the full band structure of the wurtzite ZnO have been published such as the theoretical band structure simulation using the Korringa-Kohn-Rostoker (KKR) method [47], or the experimental studies by the Angle-Resolved Photoemission Spectroscopy (ARPES) [26] or by the Resonant X-ray Photoemission Spectroscopy (RXES) [48]. An example of the electronic band structure calculated using the GW correction Hybrid Density Functional Theory (HDFT) compared with the RXES experimental results is presented in **Figure 2.4** [48]. The GW correction is an approximation made in order to calculate the self-energy of a many-body system of electrons. The approximation is the expansion of the self-energy  $\Sigma$  in terms of the single particle Green's function  $G$  and the screened Coulomb interaction  $W$ . In the band structure, the energy states in the conduction band and in the valence band are characterized by a certain crystal momentum ( $k$ -vector) in the Brillouin zone. From this band structure, we can observe that the minimal energy state in the conduction band and the maximum energy state in the valence band are located at the same location, i.e. Brillouin zone center ( $\Gamma$  point), so ZnO is defined as a direct bandgap semiconductor. That is very important for ZnO applications in light-emitting devices. The bandgap is calculated to be 3.2 eV in [47], which is close to the experimental value (3.37 eV at room temperature [25]). The wide bandgap makes ZnO an interesting material for photoelectric applications in the UV range.

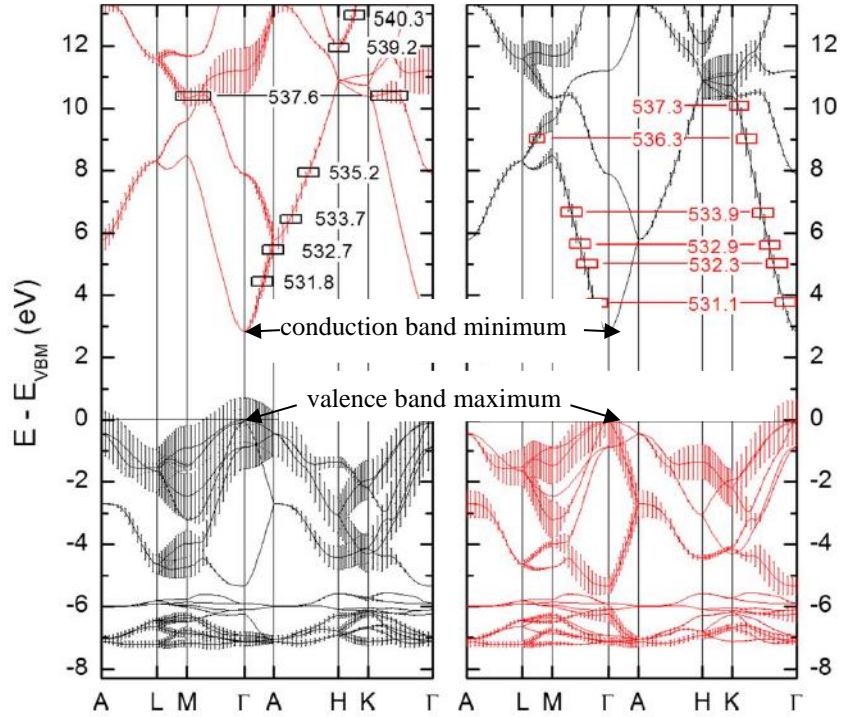


**Figure 2.4:** GW correction Hybrid Density Functional Theory (HDFT) band structure of wurtzite ZnO in reciprocal space along high-symmetry directions of the crystal. Calculation is orbitally resolved into  $p_{xy}$  (black) and  $p_z$  (red) contributions. Error bars represent the strength of contribution. Labels indicate RXES excitation energies [48].

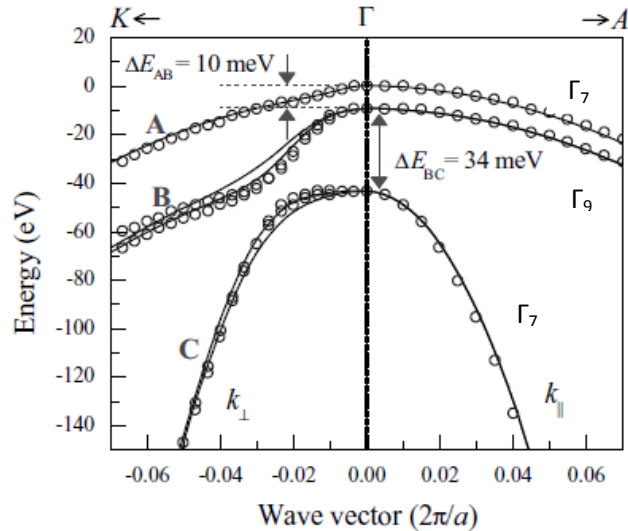


**Figure 2.5:** Valence band structure of ZnO near the  $\Gamma$  point. The open circles represent the calculation results using the atomic sphere approximation – linearized muffin-tin orbital (ASA-LMTO) method including spin-orbit coupling. The solid lines are fits to the Rashba–Sheka–Pikus effective Hamiltonian [49].

The band structure of ZnO shown in **Figure 2.4** also reveals that there are three very closely spaced valence bands. They result from the spin-orbit coupling and the crystal field splitting near the zone center ( $\Gamma$  point), which are usually referred to as the A, B, and C bands from top to bottom, or the heavy-hole, light-hole, and crystal field split-off bands, respectively. **Figure 2.5** [49] shows the details of the valence band structure of ZnO near the  $\Gamma$  point. The sequence of  $\Gamma_7$ ,  $\Gamma_9$ ,  $\Gamma_7$  of the valence band in decreasing energy order in wurtzite ZnO is attributed to a negative spin-orbit splitting parameter as a result of hybridization with the Zn-3d states.

The bandgap value of ZnO is between conductors and insulators, so an ideally pure ZnO cannot conduct the current, but because of several reasons ZnO is intrinsically the n-type material. First, it is scarcely stoichiometric [50]. The oxygen vacancy ( $V_O$ ) or the Zn interstitial ( $Zn_i$ ) have been shown to give rise to the n-type conductivity [51]. Second, the unintentional hydrogen incorporation also induces an excess of donors [52]. Eventually, the presence of ZnO fabrication by-products, such as aluminum, also induces an n-type doping [49]. Because of the low solubility of p-type dopants and the self-compensation by the abundant n-type defects and impurities, the achievement of the p-type doping has been a major problem. The achievement of a stable p-n junction in ZnO, the cornerstone of ZnO based UV optoelectronics, still remains a pending issue.

### 2.2.3. Optical characteristics of ZnO

In a perfect direct bandgap semiconductor, the electron in the valence band can be excited to the conduction band by a photon with energy higher than the bandgap, leaving a hole in the valence band. The excited electron relaxes to the conduction band minimum with the excess energy released as heat in the crystal network. Due to the Coulomb interaction, the electron-hole pair forms a free exciton (FX) with the energy lower than the bandgap. The FX electron de-excites radiatively to the ground state, emitting a photon. FX has an electric dipole moment and it is able to couple with incident light, resulting in the formation of a polariton in certain conditions. Moreover, the scatterings between the carriers, excitons and phonon vibrations also influence the optical properties of semiconductors. In a nonpolar material, the deformation potential scattering is the dominant carrier or exciton-phonon scattering mechanism. It is based on the deformation of the atomic lattice induced by both the acoustic and optical phonons [53]. In a polar and wide bandgap material like ZnO, Fröhlich interaction is the most prominent carrier or exciton-phonon scattering mechanism, which is induced by the longitudinal-optical (LO) phonons [51]. The coupling of excitons and LO-phonons results in the phonon replicas of excitonic emissions. The LO phonon energy in ZnO is 72 meV. LO phonon replicas with different orders ( $n = 1, 2, \dots$ ) exist with energy of  $n$  times 72 meV lower than the excitonic emission (zero phonon line). In an ideal bulk crystalline ZnO, there exist no intermediary energy levels in the bandgap. As a consequence, FX and FX-nLO replicas contributions dominate in the photoluminescence (PL) spectrum at room temperature. As there are three valence bands in ZnO, three kinds of excitons, noted  $FX_A$ ,  $FX_B$  and  $FX_C$  excitons, correspondingly, can be formed. Due to the different natures of these excitons, they have different dipole polarization orientations and oscillator strengths. They can only be coupled with light having the same orientation.

If crystalline defects or impurities are present, extra energy levels will be introduced in the bandgap, the FX can be captured on these levels at low temperature, creating the bound exciton (BX), which are different from the FXs by a localization of their energy level. The main types of the BX are the exciton bound to a donor center (DX) and the exciton bound to an acceptor center (AX). Whether the donors and acceptors are neutral or ionized, the DX and AX are denoted  $D^0X$  or  $D^+X$ , respectively, and  $A^0X$  or  $A^-X$ , respectively. If the donor electron is excited after the recombination, a two-electron-satellite is formed. Due to the n-type conductivity of ZnO, the acceptor in ZnO is rare and the existence of acceptor bound excitons (AXs) in ZnO has not yet been proven. Now all the studies on BXs focus on donor bound excitons (DXs).

The PL spectra of a bulk ZnO under 266 nm continuous-wave (CW) laser at 100 K and at low temperature 5 K are shown in **Figure 2.6** [54]. The FX and BX energies decrease with temperature according to the Varshni law expressed in equation (2.1).

$$E(T) = E(0) - \frac{\alpha T^2}{T + \theta_D} \quad (2.1)$$

where:

$E(0)$  is the exciton energy at temperature  $T = 0$  K,

$\alpha$  is a parameter,

$\theta_D$  is the Debye temperature of ZnO which is assumed to be 920 K.

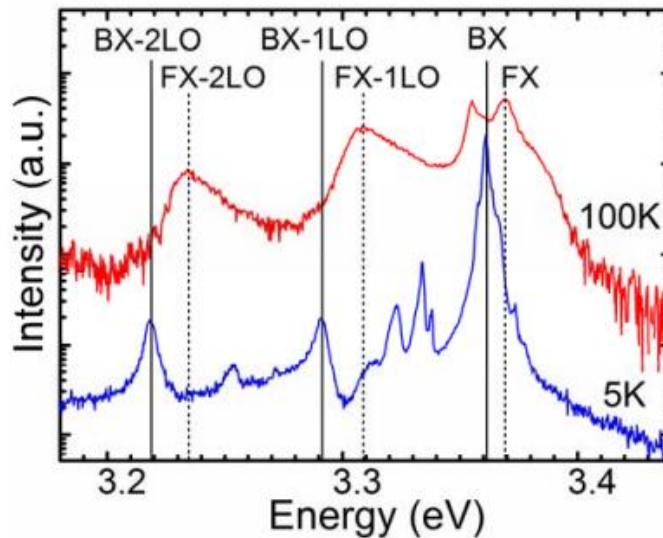


**Figure 2.6:** PL spectra of a bulk ZnO substrate measured at 5 K and 100 K, respectively. The zero-phonon BX (FX) transition and its phonon replicas are marked by the solid (dotted) lines.

Both of the peak energies and intensities of the FX and BX emission decrease with temperature. This is presented in **Figure 2.7** [55].

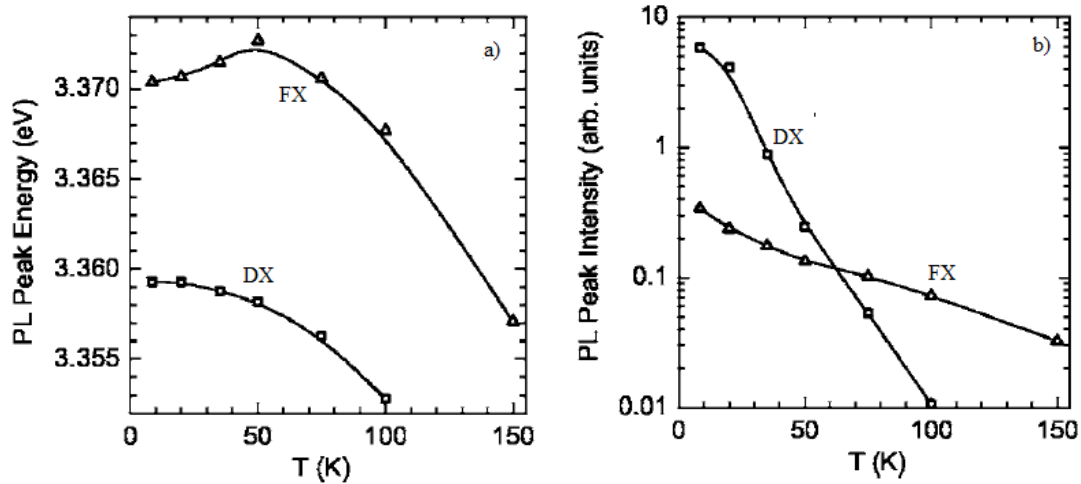


**Figure 2.7:** (a) Peak energies for the free (FX) and donor-bound (DX) excitons as a function of temperature; (b) Log plot of the free and donor-bound exciton peak intensities as a function of temperature.

The dielectric constant of ZnO is large (8.91 [56]), so the electric field screening tends to reduce the Coulomb interaction between electrons and holes, resulting in an exciton Bohr radius ( $a_B$ ) of about 2 nm [57], larger than the lattice spacing. The resulting exciton is defined as a Wannier exciton. When the size of the material approaches a few  $a_B$  (we deal with a nanostructure), the quantum confinement may occur. As a consequence, discrete energy levels instead of continuous one (like in bulk ZnO) arise at the band-edges of both the conduction band and valence band. Consequently, the bandgap of ZnO increases as the size decreases, as shown in **Figure 2.8** (a) [58] and (b) [59].

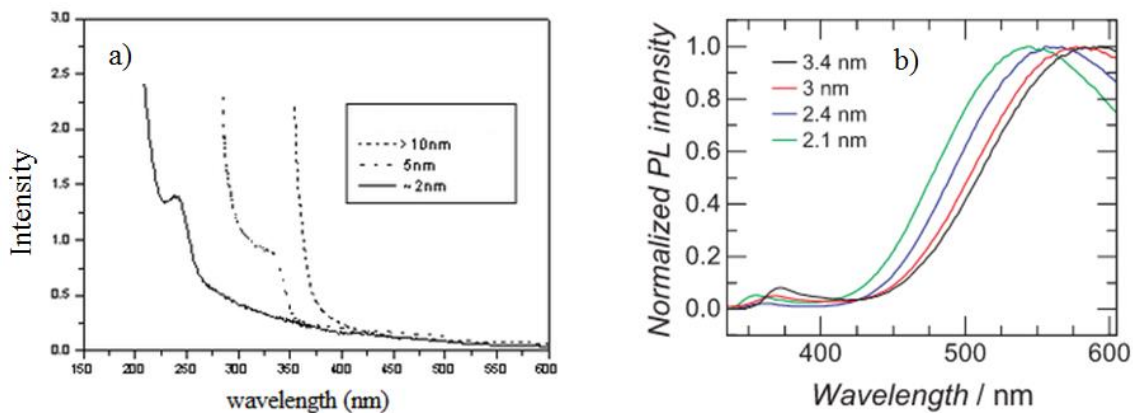


**Figure 2.8:** Quantum confinement phenomenon in the (a) absorption spectra of ZnO quantum dots of 2 nm, 5 nm and >10 nm in diameter [58] and (b) in photoluminescence spectra of ZnO quantum dots of 2.1 nm, 2.4 nm, 3 nm and 3.4 nm in diameter [59].

There exist many forms of ZnO nanostructures, such as tetrapods, needles, nanoparticles, nanoplatelets, nanorods, shells and so on. Different shapes possess peculiar emission properties. An example of emissions (normalized PL spectra) from different ZnO nanostructures is shown in **Figure 2.9** [34]. The nanostructures can be synthesized by many methods: vapor transport method, electrodeposition, solution-gelatin (sol-gel), polymer assisted growth method and so on [60]. The gaseous phase method requires high temperature, while the solution methods permit to synthesize ZnO at low temperature. The ZnO nanostructure properties are sensitive to the synthesis conditions (the nature of the reactants, temperature, pressure, reaction time and the presence of the additives and of the surfactants). Since all these synthesis parameters play a major role in the introduction of defects into the structure of ZnO nanostructures, the emission spectrum and the luminescence efficiency can be controlled, (see **Figure 2.9** [61]).

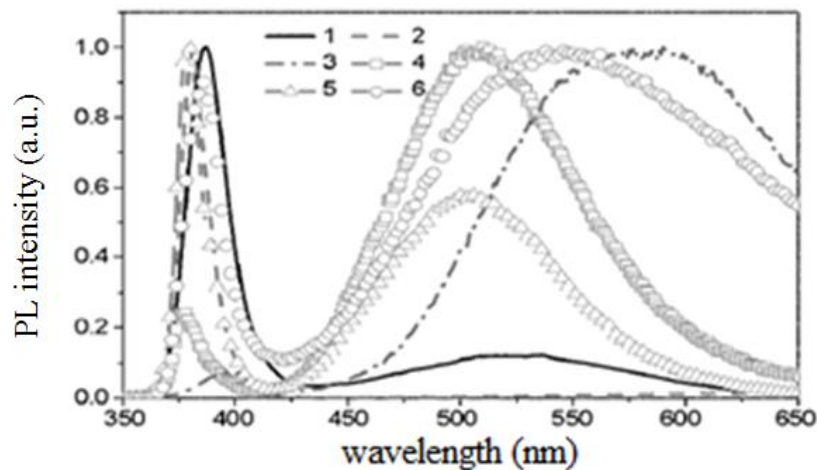


**Figure 2.9:** Room-temperature PL spectra of different ZnO nanostructures: (1) tetrapods, (2) needles, (3) nanorods, (4) shells, (5) highly faceted rods, (6) ribbons/combs [61].

With excitonic emission and defect- or impurity-related emission, room-temperature PL spectra of ZnO typically consist of a UV emission and possibly one or more visible bands. At RT the band-edge UV emission has its maximum at around 382 nm. As exposed in Chapter 1, the goal of this study is to convert UV photons into visible ones. We will thus focus particularly on the defect emission in the visible spectral range, which should be maximized in order to obtain a high down-shifting efficiency in ZnO nanoparticles.

In direct gap semiconductors, the presence of luminescent defects is perceived as a problem and much research has been devoted to its suppression, since this “parasitic” emission competes with the band edge radiative recombination. The introduction of the light emitting defect centers is often accompanied by the introduction of non-radiative defect centers, with the latter more abundant than the former, thus the light emission efficiency is decreased. However, on further examination, it can turn out to be an advantage, since it provides new possibilities to generate a wide spectrum of light wavelengths. From this point of view, ZnO is one of the most interesting semiconductors, since it possesses a variety of intrinsic defects. They can provide a visible emission from blue to IR. Depending on the partial pressure of Zn, the two most common defects

in ZnO are likely to be oxygen vacancy ( $V_O$ ) and zinc vacancy ( $V_{Zn}$ ) [63]. In addition to these two types of defects, oxygen interstitial ( $O_i$ ), zinc interstitial ( $Zn_i$ ), oxygen antisite ( $O_{Zn}$ ) and zinc antisite ( $Zn_O$ ) defects are also observed in ZnO, as well as their complexes which are more complicated [63]. The formation energies as a function of the Fermi-level position for these intrinsic point defects in ZnO for both Zn-rich and O-rich conditions are presented in **Figure 2.10** (a) and (b) [62]. It can be seen that in Zn-rich conditions,  $V_O$ ,  $Zn_i$  and  $Zn_O$  have lower formation energies, hence should be more abundant, while in O-rich conditions,  $V_{Zn}$ ,  $O_i$  and  $O_{Zn}$  should be more favored. Several calculations of the native defect levels in ZnO have been reported [63, 64, 65,66], as summarized in **Figure 2.11** [67].

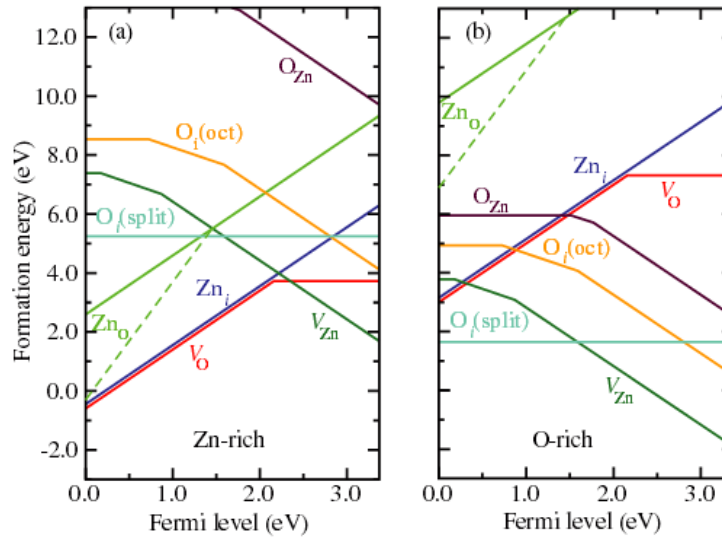


**Figure 2.10:** Formation energies as a function of the Fermi-level position for native point defects in ZnO for (a) Zn-rich and (b) O-rich conditions, from [62]. The zero of Fermi level corresponds to the valence-band maximum. Only segments corresponding to the lowest energy charge states are shown. The slope of these segments indicates the charge state. Kinks in the curves indicate transitions between different charge states.

RT PL spectra of ZnO can exhibit a number of different peaks in the visible spectral region, which have been attributed to the defect emission. Emission lines at 405, 420, 446, 466, 485, 510, 544, 583 and 640 nm have been reported (see Ref [68] and references therein). Different peaks may be related to different types of defects. However, the structure size is also the reason of the shift of some peaks in the PL spectrum. Indeed, the quantum confinement introduced previously for the FX emission of small quantum dots is also valid to a certain extent for the defect emission. While the bandgap increases as the size is reduced, the level positions depicted in **Figure 2.11** are shifted accordingly. The observed PL emission in blue, green and red spectral ranges and the corresponding defects are summed up in **Table 2.3**.

The reduction of the size of the ZnO structure results in the increase of the surface area/volume ratio. This is of prime importance since, whatever the defects responsible for the visible emission, there exists a consensus about their prominence at the surface of the NPs and

their influence on the visible emission of these ZnO NPs. Thus these surface defects are more abundant in ZnO with smaller size, resulting in the defect emission PL QY dramatically enhanced [58, 69, 70].

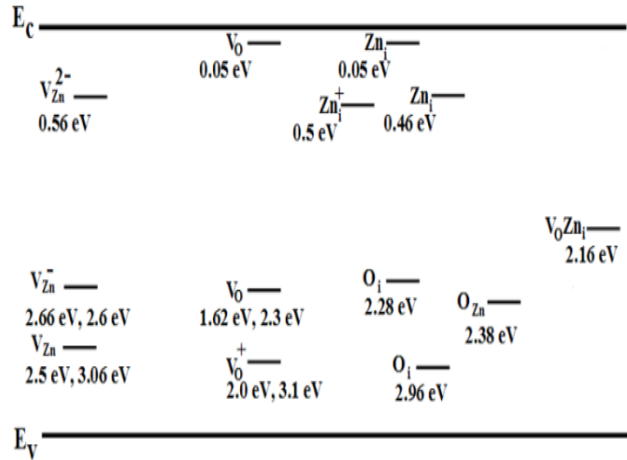


**Figure 2.11:** Illustration of the calculated defect energy levels in ZnO from different literature sources, from [67].  $V_{Zn}$ ,  $V_{Zn}^-$  and  $V_{Zn}^{2-}$  denote neutral, singly charged, and doubly charged zinc vacancies, respectively.  $Zn_i$  indicates neutral zinc interstitials, while  $Zn_i^+$  denotes singly charged zinc interstitial.  $V_o$  denotes neutral oxygen vacancies, while  $V_o^+$  denotes a singly charged oxygen vacancy.  $O_i$  represents oxygen interstitial.  $V_oZn_i$  denotes a complex of an oxygen vacancy and zinc interstitial.  $O_{Zn}$  indicates an oxygen antisite.

**Table 2.3:** Some reported visible emission of ZnO and the proposed associated defects. The conduction and valence bands are abbreviated as CB and VB, respectively.

Emission spectral range	Corresponding defects and transitions
Blue emission	$Zn_i$ and extended $Zn_i$ states to VB [71]
	$Zn_i$ to $V_{Zn}$ [72]
	CB to $V_{Zn}$ [73]
Green emission	$V_{Zn}$ on non-polar surface [74]
	CB to $V_o$ [75]
	$V_{Zn}$ contained complex [76, 77]
Red emission	$Zn_i$ [78]

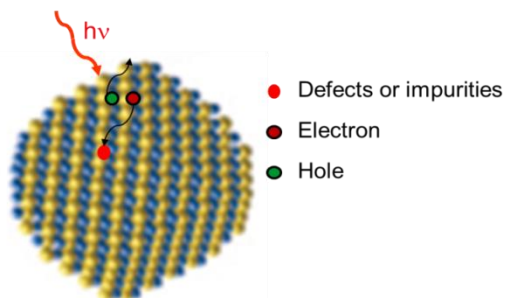


**Figure 2.12:** Schematic representation of an electron and hole pair creation (the red and green circle with a black edge representing the electron and hole, respectively) and captured by an intrinsic defect or an impurity and a surface state, respectively (presented by the black arrows, the red circle representing a defect or an impurity).

In addition to the intrinsic defects, the surface states also have an important influence on the defect emission. The adsorbed molecules, like ethanol and oxygen, catch holes and electrons, respectively [58]. When a radiation with energy higher than the bandgap is absorbed, it will generate an electron-hole pair. The electron then will quickly be captured by an intrinsic defect or an impurity, while the hole will be captured by a surface state as depicted in **Figure 2.12**. These captured electron and hole can recombine radiatively to emit a photon in the visible spectral range, once the hole has tunneled back to the trapped electron. Among the surface states, the OH group is a very important one. It acts as a surface trap for photogenerated charge carriers, enhancing visible emissions when the material is exposed to air [58, 79] and inducing additional peaks in the UV range [80]. When excess OH anions exist on the surface, they induce blue emission from ZnO quantum dots, which is attributed to the facilitation of  $O_i$  formation [81] and the Zn-OH linkage formation causing local structure change from wurtzite ZnO [82]. The influence of the OH bonds on the defect emission of ZnO quantum dots can also be explained by the effect of pH value and zeta potential. It has been reported [83] that when synthesized by the ethanol-based precipitation method, at a high pH value of the precipitation solution, ZnO nuclei are formed faster and in a larger amount than those at a low pH value. At a high pH value, the competition in the growth of ZnO nanoparticles occurs and results in the smaller particle size. Hence via controlling the pH value of the precipitation solution, the size of ZnO nanoparticles can be tuned and thus the emission color and the PL quantum yield of the obtained ZnO nanoparticles can be controlled. Concomitantly, the zeta potential can be tuned. It shifts from positive to negative values and the PL spectra blue shift from orange to blue spectral range as the pH value increases, as shown in **Figure 2.13** [83]. Therefore, the state of the surface (charge, traps, etc.) is of prime importance to permit the tuning and the control of the visible emission.

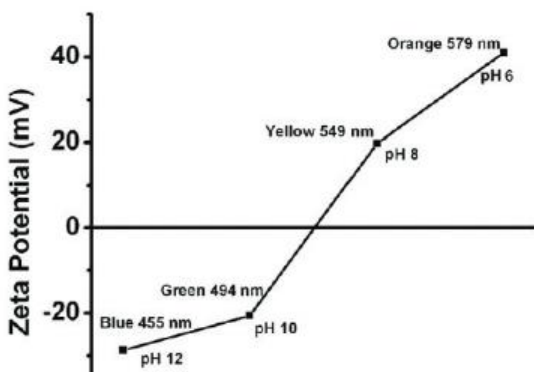


**Figure 2.13:** Maximum peaks position in PL spectrum of ZnO nanoparticles precipitated at different pH values of the precipitation solution of 12, 10, 8, 6, respectively, and the corresponding zeta potentials. The ZnO nanoparticles were dispersed in ethanol. The excitation wavelengths were 309, 325, 328 and 356 nm for the nanoparticles prepared at pH 12, 10, 8, and 6, respectively [83].

The time resolved photoluminescence (TRPL) has been used to analyze the phenomena that determine fast charge carrier dynamics in ZnO. It provides information about the exciton lifetime, which is related to the radiative and non-radiative decay phenomena [84]. It indicates the material quality and the radiative recombination efficiency. The enhancement of the radiative recombination efficiency is indicated by the improvement of the emission lifetime. The band edge emission decay time of ZnO nanostructures is typically shorter than the one of high quality bulk ZnO. The reported UV emission of ZnO quantum dots is 65 ps at 4.3 K, while that of bulk ZnO is reported to be of the order of 1 ns [83]. The reported visible emission lifetime ranges between 25 ns [85] and 1  $\mu$ s [86]. The decay time in ZnO nanostructures is dependent on the size, bigger size normally resulting in longer decay time [83]. It is consistent with the model shown in **Figure 2.12**, i.e. with bigger size, the charge carriers need more time to be captured by the defects and surface states and the overlap of the hole and the trapped electron wavefunctions is lower, leading to a reduced tunneling rate. The decay time is also influenced by the presence of the defects. The more numerous trapping centers induced by defects, the longer the decay time [87]. Different morphologies of ZnO nanostructures have different decay times. It is thus extremely difficult to attribute a specific decay time component to a specific de-excitation process.

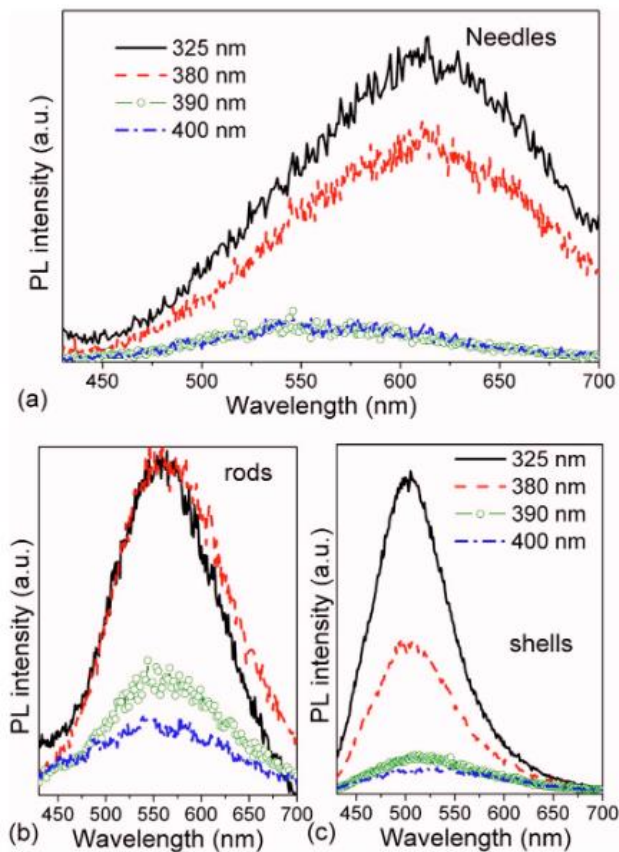


**Figure 2.14:** Room temperature PL spectra with different excitation wavelengths for (a) needles, (b) rods, and (c) shells, from [90].

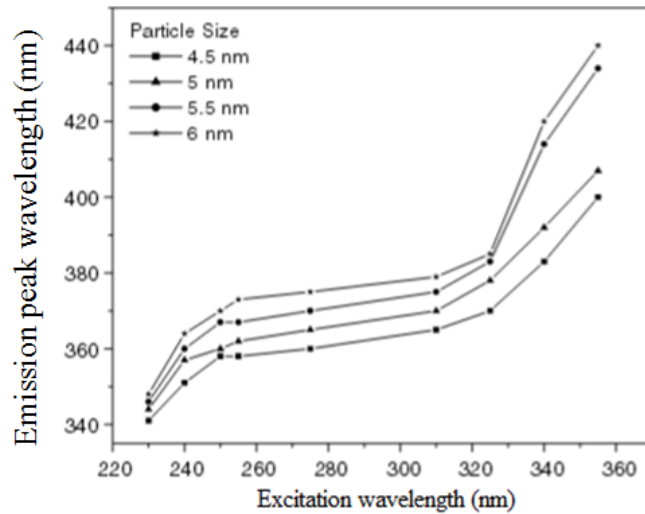


**Figure 2.15:** Maximum emission peak position with excitation wavelength of nano-colloidal ZnO of different sizes, from [92].

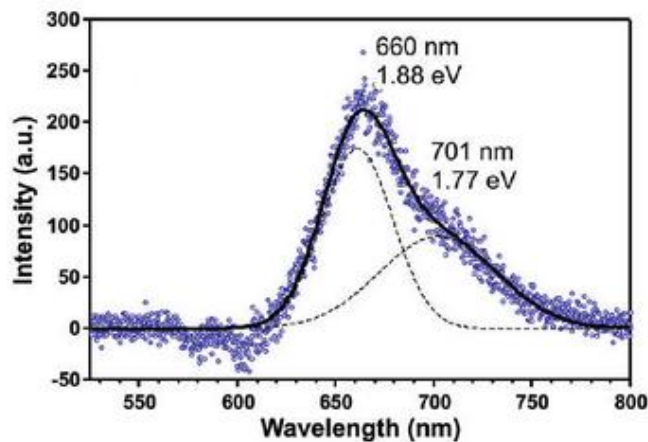


**Figure 2.16:** Room temperature PL spectrum of ZnO nanoparticles under the excitation of 532 nm, from [95]. The dashed lines are the Gaussian fitting of the broad PL peak showing two components at 660 nm and 701 nm.

Several researchers have suggested that the PL peak of crystalline ZnO does not exhibit a dependence on the excitation wavelength [88, 89]. However, the changes of PL spectra of crystalline ZnO with excitation wavelengths were observed for different morphologies and it turned out that the emission intensity decreases with increasing excitation wavelength, as illustrated in **Figure 2.14** [90]. It has been explained by the fact that the excitation wavelength variation results in different PL peaks and thus the PL spectrum changes [90, 91]. Another example of the change of the PL spectra with the excitation wavelength is the one observed in colloidal ZnO at the tail of the absorption band, as shown in **Figure 2.15** [92]. However, a different explanation was given to the observed phenomenon than that in the case of the

crystalline ZnO. The red shift of PL spectra with the increased excitation wavelength was explained by the presence of different forms of the constituent ZnO molecules associated with different energy levels and a slow rate of the relaxation process from the excited state.

Efficient defect engineering can be done, as was demonstrated for instance in nanodiamonds [93] or nanoparticles of SiC [94] with the controlled introduction of point defects (N-V centers in carbon diamond or carbon antisite-vacancy in SiC). The resulting light source can be so intense that it can be used as a single photon source. Sub-bandgap absorption and red emission has been observed in ZnO which is attributed to single defect -  $V_{Zn}$  [95].  $V_{Zn}$  in ZnO can be excited with energy  $\sim 2.4$  eV and emits at  $\sim 1.8$  eV, as shown in **Figure 2.16** [95]. This makes ZnO another interesting candidate for the single photon sources like SiC.

Until now, many researchers have reported high visible efficiency of ZnO QDs. It has been demonstrated in previous publications that ZnO QDs fabricated by the sol-gel method permitted to achieve luminescence quantum yield of about 26 % [82]. The synthesis of ZnO QDs in a non-thermal plasma reactor has been reported to result in a luminescence quantum yield of as high as 60 % [96]. Even higher emission quantum efficiency (76 %) has been obtained using oleic acid as a capping agent, but the PL QY drastically decreases after several days [97]. These high PL QYs have been obtained with an excitation close to the bandgap. Another major result is that the PL QY is highly dependent on the quantum dot size: the smaller the size, the larger the QY, as mentioned previously. Thus, very high QY have only been reached for very small ( $\sim 2$  nm in diameter) ZnO quantum dots. The major drawback when relying on defect emission is that the introduction of the light emitting centers into the structure of the material often comes along with the introduction of the non-radiative (quenching) defects. This process is hard to control as it is sensitive to the fabrication conditions. Consequently, if one wants to harness the light originating from defects, one has to achieve a very subtle defect engineering and finely tune the defect amount. This is all the more important as the size of the material reaches the nanoscale: the fraction of surface states increases and these states often lead to the luminescence quenching. Complete understanding of the causes of this visible emission is still lacking, but several reviews have summed up the state-of-the-art knowledge [61, 98]. The critical challenge is to get the PL QY of the visible emission as high as possible.

When using ZnO nanoparticles as down-shifters in solar cells, another important parameter to consider is the spectral matching between emission of the ZnO nanoparticles and the spectral response of solar cells. The simulated spectral response of three common solar cells (CIGS, CdS/CdTe and Si solar cells) is presented in **Figure 2.17** (a) [99]. An example of the absorption and emission spectra of ZnO QDs are also shown in **Figure 2.17** (b) [100]. It can be seen that, ZnO QDs absorb in the UV range with a high absorption below 400 nm, especially in the range below 350 nm. It emits in the visible range with a wide emission peak which can be tuned from blue to IR. ZnO QDs also show a low overlap of absorption and emission spectra which is important for down-shifters. In addition to the potential efficiency enhancement, the introduction of a down-shifting layer to the structure of a solar cell creates additional interactions with the

light resulting in extra loss mechanisms. Therefore, any potential gains to be made by the down-shifting of the solar spectrum will have to compensate for these losses, before offering an overall solar cell efficiency improvement. For CIGS and CdS/CdTe solar cells, the external quantum efficiency (EQE) is low in the range below 350 nm due to the inefficient change of the UV light to electrons, where ZnO has a high absorption. They have a high EQE in the range between 500-800 nm, in which range ZnO re-emits visible light. CIGS and CdS/CdTe solar cells have a good spectral matching with ZnO QDs, so it is expected to obtain their efficiency enhancement via a ZnO down-shifting layer. For crystalline Si solar cells, in the range below 350 nm, it already has a high EQE, so the efficiency improvement with ZnO down-shifting layer is not expected.

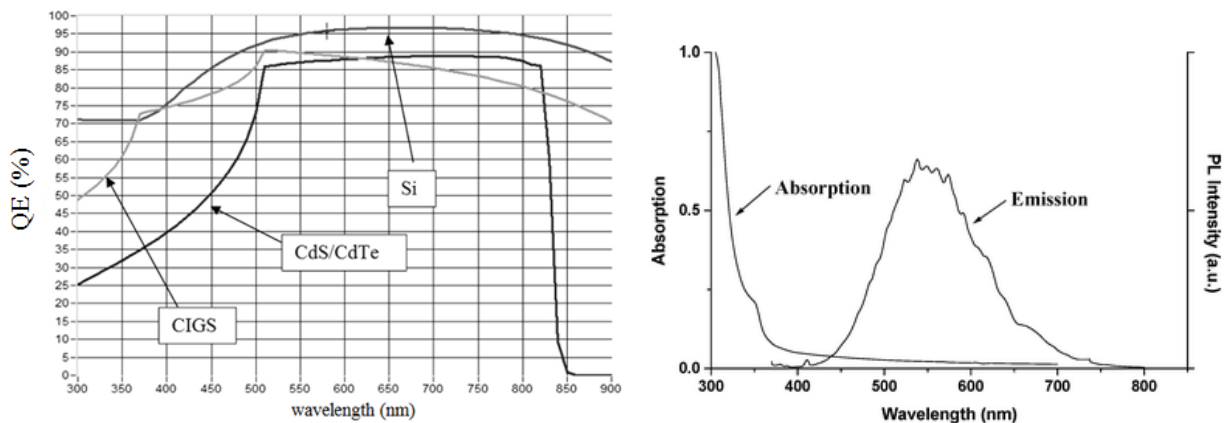


**Figure 2.17:** (a) Numerical simulation of external quantum efficiency (marked as  $QE$  in the graph) for a standard Si cell, the CIGS cell and the CdTe cell in function of the incident solar light wavelength, simulated using the Solar Cell Capacitance Simulator (SCAPS) program. (b) Absorption and emission spectra of ZnO quantum dots [100].

### 2.3. ZnO related material – Zinc hydroxide

During the fabrication of ZnO, there exists many parasite products like the zinc hydroxide ( $Zn(OH)_2$ ) and oligomeric  $Zn(OH)_x(Oac)_y$  species. Among them, orthogonal  $\epsilon$ - $Zn(OH)_2$  (wulfingite) is the major intermediate in ZnO production by the sol-gel process. Tetragonal sweetite  $Zn(OH)_2$  also exists but it is not a common structure which is rarely studied. The abundant hydroxyl groups on  $Zn(OH)_2$  afford strong coordination ability with cations and help to the coating of a shell layer [101].  $Zn(OH)_2$  has attracted a lot of interest during the last years due to its important role in the development of II–VI based semiconductor nanomaterials, in particular as a precursor in the synthesis of nanocrystalline ZnO [102, 103]. Zinc hydroxide can be also formed on the surface of ZnS/ZnSe/ZnO nanocrystals (NCs), either during their preparation by crystallization from a high pH solution, resulting in a core–shell structure [104, 105], or in a later stage by atmospheric corrosion [106, 107]. Monitoring of the formation and structure of the  $Zn(OH)_2$  surface layers by the usual structural X-ray diffraction (XRD) and transmission electron microscopy (TEM) techniques is a difficult task, as one needs to distinguish

the  $\text{Zn(OH)}_2$  present in the atomic surface layers from other possible compounds such as zinc oxide, zinc carbonate or zinc carbonate hydroxide (also known as hydrozincite  $[\text{Zn}_5(\text{CO}_3)_2(\text{OH})_6]$ ), the last two expected to be produced by atmospheric corrosion as well [103, 105, 106].

According to JCPDS 89-0138, in XRD diffractograms,  $\epsilon\text{-Zn(OH)}_2$  has distinct diffraction peaks at  $27^\circ$ ,  $33^\circ$ ,  $35.1^\circ$  and  $59.5^\circ$ , corresponding to the (102), (112), (002), (124) planes of  $\epsilon\text{-Zn(OH)}_2$ , which is shown in **Figure 2.18**. The other peaks at  $20^\circ$ ,  $37.5^\circ$ ,  $41^\circ$ ,  $45^\circ$  and  $50^\circ$  can also be seen in the XRD pattern of  $\epsilon\text{-Zn(OH)}_2$ . However, for tetragonal sweetite phase  $\text{Zn(OH)}_2$ , there exists only one file (JCPDS file no. 00-38-0356) for the sweetite phase and none established structure. The diffraction peaks at  $25^\circ$  and  $30.5^\circ$  of sweetite  $\text{Zn(OH)}_2$  has also been detected in this thesis study.

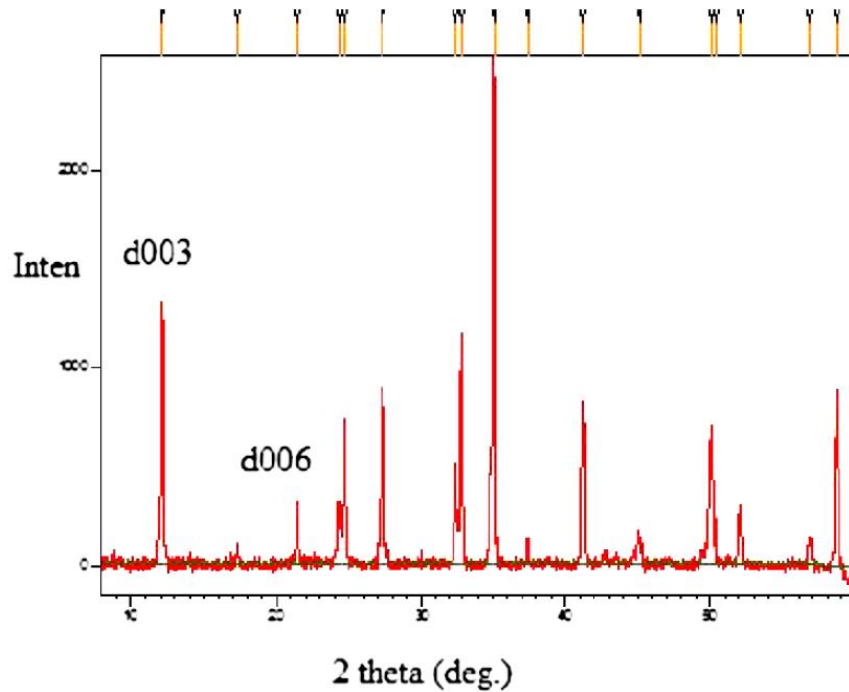


**Figure 188** : XRD pattern of pure  $\text{Zn(OH)}_2$  [108].

The  $\epsilon\text{-Zn(OH)}_2$  phase can also be detected by Raman spectroscopy. As shown in **Figure 2.19**, besides the characteristic  $\text{A}_1(\text{TO})$  mode of wurtzite  $\text{ZnO}$ , there appeared five more peaks, located at about 220, 266, 486, 554 and  $725\text{ cm}^{-1}$ , which corresponds to  $\text{Zn(OH)}_2$  phase [109].

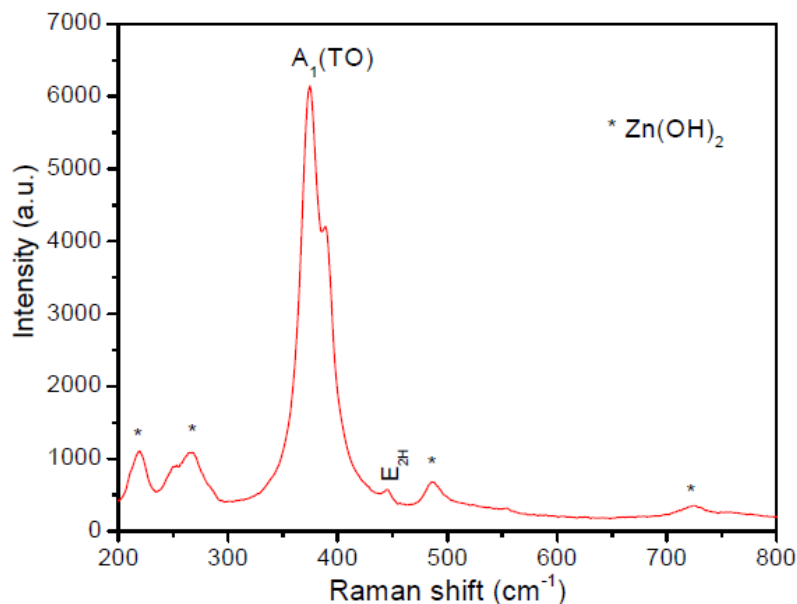


**Figure 199:** Raman spectra of the ZnO and Zn(OH)<sub>2</sub> nanostructures mixture [109].

Zn(OH)<sub>2</sub> is investigated to decompose in the 110–140 °C temperature range [101] while some found a minor weight loss in the thermogravimetric analysis (TGA) profile of Zn(OH)<sub>2</sub> around 550 °C due to the de-hydroxylation of the OH group of Zn(OH)<sub>2</sub> [108]. The thermal stability of Zn(OH)<sub>2</sub> is found to be improved above 750 °C by forming the Zn(OH)<sub>2</sub>- Aniline (ANI) hybrid system [108].

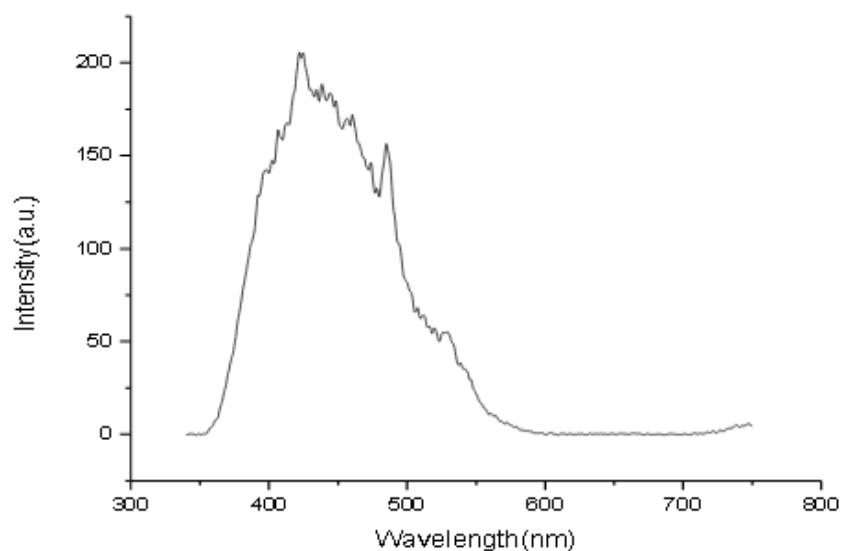


**Figure 200:** PL spectrum of pure Zn(OH)<sub>2</sub> samples with thickness of 150 micron and 4mm diameter [110].

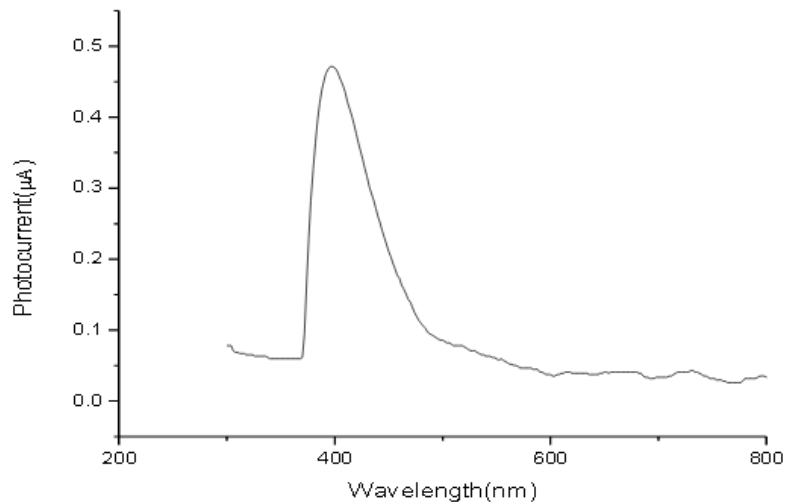


**Figure 211:** Photoconductivity of pure  $Zn(OH)_2$  samples with thickness of 150 micron and 4mm diameter [110].

Some researchers have observed the fluorescent emission of the bulk  $Zn(OH)_2$  at around 400 nm, as shown in **Figure 2.20**. They also found its photoconductivity thus indicating the absorbing of  $Zn(OH)_2$  starts at 405 nm, as shown in **Figure 2.21**. According to these results and some other techniques, they have obtained the bandgap of  $Zn(OH)_2$ , which is 3.01 eV [110].

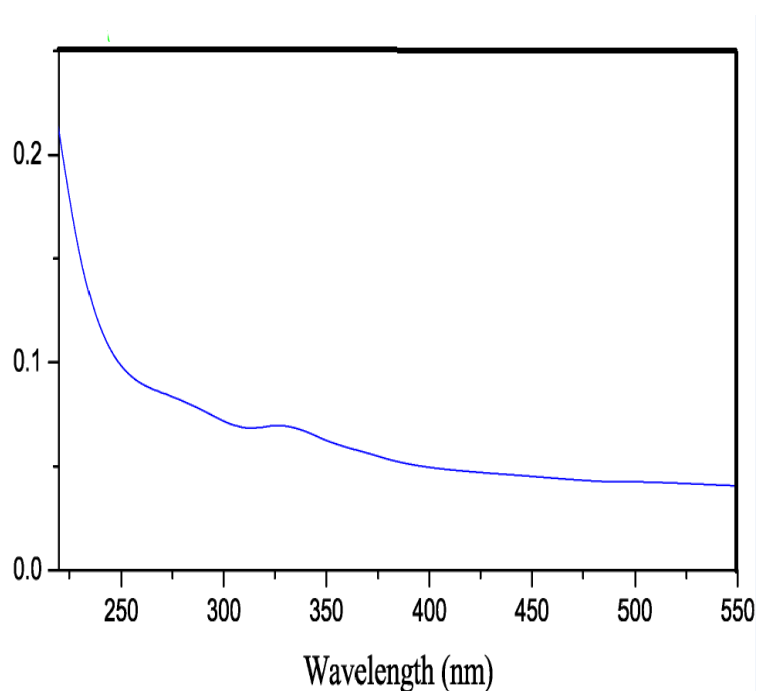


**Figure 222:** UV-visible spectra of pristine- $Zn(OH)_2$  [108].

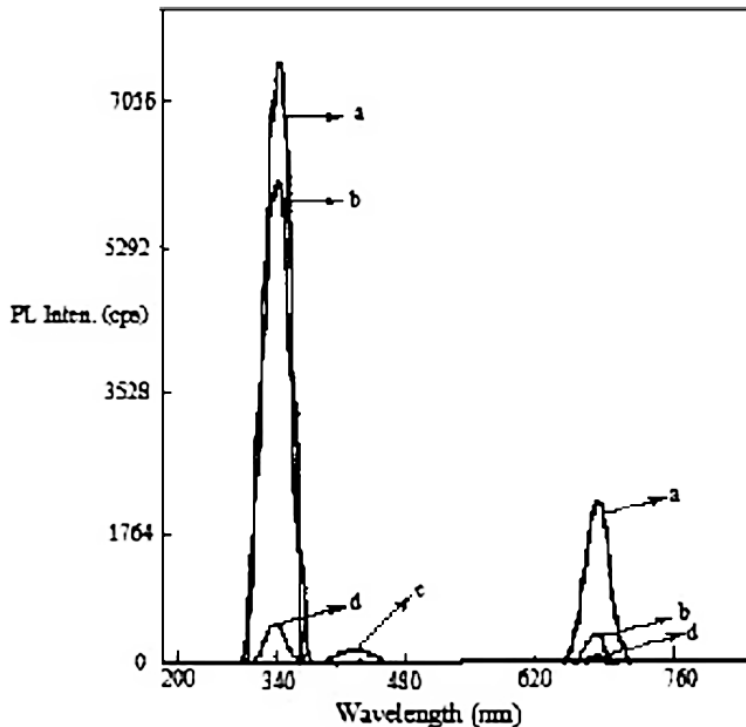


**Figure 233:** Photoluminescence spectra of (a) pure  $\text{Zn(OH)}_2$ , (b)  $\text{Zn(OH)}_2$ -5 wt% of ANI, (c)  $\text{Zn(OH)}_2$ -5 wt% of ANI + PVA and (d) pristine PVA [108].

The absorption of nano-sized  $\text{Zn(OH)}_2$  (40 nm) and Aniline (ANI) intercalated  $\text{Zn(OH)}_2$  nano-composite with poly(vinylalcohol) (PVA) of different concentrations have also been studied [108]. The UV-VIS absorption spectrum is shown in **Figure 2.22** and the PL spectrum is shown in **Figure 2.23**. It is found that the pure  $\text{Zn(OH)}_2$  shows an absorption peak at 330 nm and two emission bands peaking at 340 nm and 630 nm, respectively.

The observations of strong UV luminescence from surface capped OH free ZnO QDs have been reported in literatures [111]. Contrarily, a core/shell structure formed with the presence of large amount of  $\text{Zn(OH)}_2$  on the surface of ZnO, resulting in the weak UV emission and high visible emission, confirms that the excitonic emission quenching of  $\text{Zn(OH)}_2$ . However, the details of the bonding of the  $\text{Zn(OH)}_2$  shell to the ZnO core, leading to this quenching effect are not clear yet [112]. Thus it is important for improving the PL QY in the visible spectral range with a  $\text{Zn(OH)}_2$  shell to the ZnO NPs core also in this study since that is our goal.

## 2.4. Host materials

For an industrial application and fabrication, the luminescent materials should be dispersed in host materials to make the LDS layer. The host materials not only act as a dispersion milieu, but also protect the luminescent species [47]. Some of the host materials can also react with the luminescent material forming composites [113, 114] to increase the PL intensity. The host

materials used in the LDS layer must satisfy specific requirements in order to maximize the benefits from their introduction into the structure of the PV module. The host materials must exhibit high transmittance, particularly in the region where the solar cell spectral response is high, as well as a low scattering. It should be also optically matched to transparent emitter contacts or antireflective layer of the cell. At the same time it needs to provide an optimum environment for the luminescent species which are dispersed in the host material. Finally, it will have to endure a thermal treatment to which solar cells are subjected during their manufacturing and exhibit prolonged photostability over the extended periods of 20–25 years, the average lifetime of a solar cell.

Silica has proven to be an excellent matrix, providing good mechanical and optical properties and conferring a high stability to quantum dots (QDs) used as luminescent species. Many researchers have incorporated ZnO [115, 116] and other QDs like Si [18] and CdS [15] into a transparent silica matrix. However, the studies making use of the QD-silica composite film as a luminescent down-shifter for solar cells are still few, although some researchers have studied the optical performance of QD-silica composite films for their possible application in luminescent solar concentrators.

Inorganic crystalline materials, such as  $\text{Al}_2\text{O}_3$  [117] or  $\text{CaF}_2$  [118], exhibit high transparency over the whole solar spectrum and are photostable. They are, however, expensive and difficult to process and thus unlikely to be considered as a reliable option for the fabrication of the PV modules on a commercial basis.

Nowadays polymers find application in the PV industry. Studied polymeric materials exhibit high transparency in the UV and visible region of the solar spectrum, an adequate resistance to heat and humidity variations, and a high mechanical resistance [119]. They also provide a very good host environment for organic dye molecules [51]. Poly(methyl methacrylate) (PMMA) and polyvinyl alcohol (PVA) are the most used polymers as a host material in the LDS layers due to their highly transparency in the UV and visible spectral range and their good dissolubility in organic solvents and water, respectively [16].

The parasitic absorption from the host material is an additional loss mechanism introduced by the application of the LDS layer. The extent of this loss mechanism is strongly dependent on the material and the thickness of the host matrix layer. Given that highly transparent materials are naturally desirable for PV applications, the thickness of the luminescent layer is critical. In our work, we used or no host material at all, or the polyurethane (PU) or poly(methyl methacrylate) (PMMA) and polyacrylic acid (PAAH) as the matrix for the luminescent species for preliminary studies.

### 2.4.1. Poly(methyl methacrylate) (PMMA)

PMMA is the most commonly used polymer for the surface modification of ZnO NPs. Its chemical formula is shown in **Figure 2.24**. It exhibits very good optical properties – it is highly

transparent in the visible spectral range and has low reflectivity. It transmits more visible light (up to 93 %) than glass and gives a reflection of about 4 % from each of its surfaces on account of its refractive index (1.4905 at 589.3 nm) [120]. It transmits light in the spectral range as low as about 300 nm. The surface of ZnO NPs can be capped and passivated by PMMA, leading to an efficient UV emission with quenching visible emission after the synthesis [121, 122], as shown in **Figure 2.25** [110]. PMMA is one of the polymers that are most resistant to a direct exposure to sunshine. It exhibits fairly small change under the UV radiation, as well as in the presence of ozone. These properties make PMMA suitable for PV devices intended for open air operation over long periods of time. ZnO NPs embedded in PMMA have been more stable [123], and thus more suitable for device fabrication and application. In PMMA, ZnO NPs can be homogeneously dispersed, which is important to make an LDS layer of good optical quality [124].

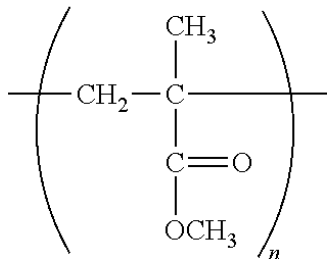


**Figure 2.24:** Chemical formula of PMMA.

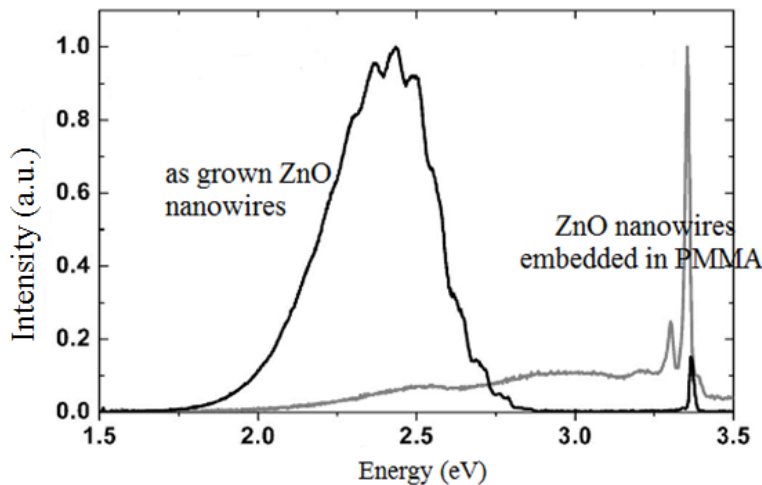


**Figure 2.25:** Normalized PL spectra of bare ZnO nanowires and nanowires embedded in PMMA.

## 2.4.2. Polyacrylic acid (PAAH)

Polyacrylic acid is a weak acid with the chemical formula presented in **Figure 2.26**. It shows a high transmittance in the visible region up to the near IR region. It has been used as a macroligand for the binding of the metal ions [125]. PAAH is known to have a significant effect on the PL emission of ZnO nanostructures. It has been observed that coating of nanowires with PAAH after the synthesis enhances the excitonic emission while decreasing the visible emission [110], like PMMA. It is also observed that coating the nanoparticles with PAAH after the synthesis decreases the positive surface charge, decreasing the PL intensity of the excitonic emission, however if the concentration of the PAAH in the NPs solution increases the surface charge changes from positive to negative and a slow increase of the intensity of the excitonic emission is observed, as shown in **Figure 2.27** [126]. The hypothesis evoked to explain these observations relies on the modification of the ZnO surface charge. Not only does the PAAH passivate the surface defects but it is also expected to screen the surface hole traps (by controlling the zeta potential) that are thought to play a major role in the subsequent recombination of holes with electrons at defects close to the ZnO surface. Nanocomposites containing PAAH in its cadmium carboxylate form resulted in an overall 50 % enhancement in the PL quantum yield compared with nanocomposites containing PAAH in its acid form [127]. PAAH has also been reported to increase the dispersion stability [128], which is essential for the homogeneous dispersion of the DS material, ZnO NPs, in order to get a transparent film, without aggregation of the NPs.

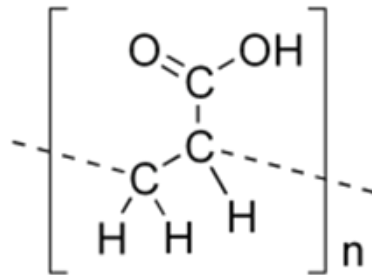


**Figure 2.26:** Chemical formula of PAAH.

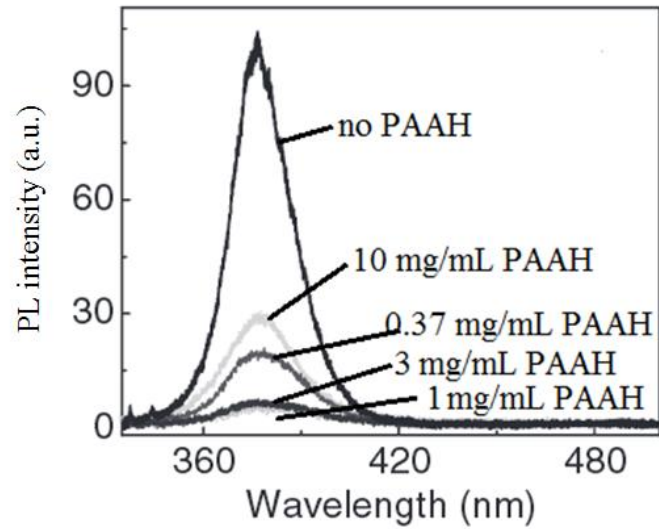


**Figure 2.27:** PL spectra of ZnO samples with different concentration of PAAH (0, 0.37, 1, 3 and 10 mg/mL) added after the synthesis and different surface charges (21.4, 11.1, 1.7, -11, -21.6 mV for 0, 0.37, 1, 3 and 10 mg/mL, respectively).

## 2.5. Conclusions

In this chapter, the state of the art concerning several types of luminescent materials and host materials used for the fabrication of luminescent down-shifting layers has been presented. Their advantages and drawbacks have been discussed. Among the possible materials reported in the literature as down-shifters, ZnO and its nanostructures are presented in detail. It is a cheap, abundant and environmentally friendly material which exhibits a visible emission related to crystal defects, which is suitable for down-shifting. The optical properties of luminescence, in conjunction with the crystal structure and chemical quality, have been presented and discussed. The commonly accepted model of a defect-related visible emission from ZnO nanocrystals has been introduced. Eventually, the two main polymer materials used in this study as a host matrix for the ZnO NPs have been briefly presented.

## 2.6. References

---

1. Viehmann W., Thin-film scintillators for extended ultraviolet (UV) response silicon detectors. *Measurements of Optical Radiations*, 1979, vol. 196, no. 15, p. 90–95.
2. Seybold G., Wagenblast G., New perylene and violanthrone dyestuffs for fluorescent collectors. *Dyes and Pigments*, 1989, vol. 11, p. 303-317.
3. Hong B. -C., Kawano K., Organic dye-doped thin films for wavelength conversion and their effects on the photovoltaic characteristics of CdS/CdTe solar cells. *Japanese Journal of Applied Physics*, 2004, vol. 43, p. 1421–1426.
4. Ahmed H., Kennedy M., Doran J., McCormack S. J., Della P. M., Gutiérrez-Tauste D., Aubouy L., Characterization of Luminescent Down-Shifting Materials and Applications for PV Devices. *Proceeding 8th Photovoltaic Science Application and Technology*, 2012.
5. Maruyama T., Kitamura R., Transformations of the wavelength of the light incident upon solar cells. *Solar Energy Materials and Solar Cells*, 2001, vol. 69, p. 207–216.
6. Danos L., Parel T., Markvart T., Barrioz V., Brooks W. S. M., Irvine S. J. C., Increased efficiencies on CdTe solar cells via luminescence down-shifting with excitation energy transfer between dyes. *Solar Energy Materials and Solar Cells*, 2012, vol. 98, p. 486-490.
7. Klampaftisa E., Rossa D., McIntosh K. R., Richards B. S., Enhancing the performance of solar cells via luminescent down-shifting of the incident spectrum: A review. *Solar Energy Materials and Solar Cells*, 2009, vol. 93, no. 8, p. 1182–1194.
8. Li L. P., Zhao M. L., Tong W. M., Guan X. F., Li G. S., Yang L. S., Preparation of cereal-like  $\text{YVO}_4:\text{Ln}^{3+}$  (Ln = Sm, Eu, Tb, Dy) for high quantum efficiency photoluminescence. *Nanotechnology*, 2010, vol. 21, no. 19, p. 195601/1-8.
9. Huang C. K., Chen Y. C., Hung W. B., Chen T. M., Sun K. W., Chang W. L., Enhanced light harvesting of Si solar cells via luminescent down-shifting using  $\text{YVO}_4:\text{Bi}^{3+}, \text{Eu}^{3+}$  nanophosphors. *Progress in Photovoltaics: Research and Applications*, 2013, vol. 21, no. 7, p. 1507–1513.
10. Steudel F., Loos S., Ahrens B., Schweizer S., Trivalent rare-earth ions as photon down-shifter for photovoltaic applications. *Proceedings of SPIE*, 2014, vol. 9140, p. 914001/1-7.
11. Rowan B. C., Wilson L. R., Richards B. S., Advanced Material Concepts for Luminescent Solar Concentrators. *IEEE Journal of Selected Topics in Quantum Electronics*, 2008, vol. 14, no. 5, p. 1312-1322.
12. Strumpel C., Mc Cann M., Beaucarne G., Arkhipov V., Slaoui A., Svrcek V., del Canizo C., Tobias I., Modifying the solar spectrum to enhance silicon solar cell efficiency—An overview of available materials. *Solar Energy Materials and Solar Cells*, 2007, vol. 91, no. 4, p. 238–249.
13. van Sark W. G. J. H. M., Meijerink A., Schropp R. E. I., van Roosmalen J. A. M., Lysen E. H., Enhancing solar cell efficiency by using spectral converters. *Solar Energy Materials and Solar Cells*, 2005, vol. 87, p. 395–409.
14. Geyer S. M., Scherer J. M., Moloto N., Jaworski F. B., Bawendi M. G., Efficient Luminescent Down-Shifting Detectors Based on Colloidal Quantum Dots for Dual-Band Detection Applications. *ACS Nano*, 2011, vol. 5, no. 7, p. 5566–5571.

15. Cheng Z. J., Su F. F., Pan L. K., Cao M. L., Sun Z., CdS quantum dot-embedded silica film as luminescent down-shifting layer for crystalline Si solar cells. *Journal of Alloys and Compounds*, 2010, vol. 494, p. L7–L10.
16. Kalytchuk S., Gupta S., Zhovtiuk O., Vaneski A., Kershaw S. V., Fu H. Y., Fan Z. Y., Kwok E. C. H., Wang C.-F., Teoh W. Y., Rogach A. L., Semiconductor nanocrystals as luminescent down-shifting layers to enhance the efficiency of thin-Film CdTe/CdS and crystalline Si solar cells. *The Journal of Physical Chemistry C*, 2014, vol. 118, no. 30, p. 16393–16400.
17. Hodgson S. D., Brooks W. S. M., Clayton A. J., Kartopu G., Barrioz V., Irvine S. J. C., The impact of quantum dot concentration on the optical properties of QD/PMMA luminescent down-shifting films applied to CdTe photovoltaic devices. *Nano Energy*, 2014, vol. 4, p. 1-6.
18. Sgrignuoli F., Paternoster G., Marconi A., Ingenhoven P., Anopchenko A., Pucker G., Pavese L., Modeling of silicon nanocrystals based down-shifter for enhanced silicon solar cell performance. *Journal of Applied Physics*, 2012, vol. 111, p. 034303/1-7.
19. Chen B. G., Meng C., Yang Z. Y., Li W., Lin S. S., Gu T. Y., Guo X., Wang D. L., Yu S. L., Wong C. W., Tong L. M., Graphene coated ZnO nanowire optical waveguides. *Optics Express*, 2014, vol. 22, no. 20, p. 24276-24285.
20. Wang Z. L., Lin C. K., Liu X. M., Li G. Z., Luo Y., Quan Z. W., Xiang H. P., Lin J., Tunable photoluminescent and cathodoluminescent properties of ZnO and ZnO:Zn phosphors. *The Journal of Physical Chemistry B*, 2006, vol. 110, no. 9, p. 9469–9476.
21. Stadler A., Transparent conducting oxides—an up-to-date overview. *Materials*, 2012, vol. 5, p. 661-683.
22. Park J. Y., Choi S. -W., Kim S. S., Fabrication of a highly sensitive chemical sensor based on ZnO nanorod arrays. *Nanoscale Research Letters*, 2010, vol. 5, no. 2, p. 353–359.
23. Absor M. A. U., Kotaka H., Ishii F., Saito M., Tunable Rashba effect on strained ZnO: First-principles density-functional study. *Applied Physics Express*, 2014, vol. 7, no. 5, p. 053002/1-4.
24. Chen M. -J., Yang J. -R., Shiojiri M., ZnO-based ultra-violet light emitting diodes and nanostructures fabricated by atomic layer deposition. *Semiconductor Science and Technology*, 2012, vol. 27, no. 7, p. 074005/1-15.
25. Hsu Y.-H., Lin J., Tang W. C., RF sputtered piezoelectric zinc oxide thin film for transducer Applications. *Journal of Materials Science: Materials in Electronics*, 2008, vol. 19, p. 653–661.
26. Özgür Ü., Alivov Y. I., Liu C., Teke A., Reshchikov M. A., Doğan S., Avrutin V., Cho S. -J., Morkoç H., A comprehensive review of ZnO materials and devices. *Journal of Applied Physics*, 2005, vol. 98, no. 4, p. 041301/1-103.
27. Kumar B., Kim S. -W., Energy harvesting based on semiconducting piezoelectric ZnO nanostructures. *Nano Energy*, 2012, vol. 1, p. 342–355.
28. Nickel N. H., Terukov E., Zinc oxide—a material for micro- and optoelectronic applications. *Proceedings of the NATO Advanced Research Workshop on Zinc Oxide as a Material for Micro- and Optoelectronic Applications*, 2004, vol. 194, p. 197–209.
29. Wang R. -C., Liu C. -P., Huang J. -L., Single-crystalline AlZnO nanowires/nanotubes synthesized at low temperature. *Applied Physics Letters*, 2006, vol. 88, p. 023111/1-3.

30. Bae S. Y., Na C. W., Kang J. H., Park J., Comparative structure and optical properties of Ga-, In-, and Sn-doped ZnO nanowires synthesized via thermal evaporation. *The Journal of Physical Chemistry B*, 2005, vol. 109, no. 7, p. 2526-2531.
31. Xu S., Wang Z. L., One-dimensional ZnO nanostructures: Solution growth and functional properties. *Nano Research*, 2011, vol. 4, p. 1013–1098.
32. Wang Z. L., Self-assembled nanoarchitectures of polar nanobelts/nanowires. *Journal of Materials Chemistry*, 2005, vol. 15, p. 1021–1024.
33. Zhang B. P., Binh N. T., Wakatsuki K., Segawa Y., Yamada Y., Usami N., Kawasaki M., Koinuma H., Formation of highly aligned ZnO tubes on sapphire (0001) substrates. *Applied Physics Letters*, 2004, vol. 84, p. 4098-4100.
34. Wang C. J., Ranasingha O., Natesakhawat S., Ohodnicki J. P. R., Andio M., Lewis J. P., Matranga C., Visible light plasmonic heating of Au–ZnO for the catalytic reduction of CO<sub>2</sub>. *Nanoscale*, 2013, vol. 5, p. 6968-6974.
35. McDaniel H., Fuke N., Makarov N. S., Pietryga J. M., Klimov V. I., An integrated approach to realizing high-performance liquid-junction quantum dot sensitized solar cells. *Nature Communications*, 2013, vol. 4, p. 2887/1-10.
36. Morkoç H., Özgür Ü., Zinc oxide: fundamentals, materials and device technology. 1st edition, Wiley-VCH, Berlin, 2009, p. 1-76.
37. Lee J. -H., Lee W. -J., Lee S. -H., Kim S. M., Kim S. J., Jang H. M., Atomic-scale origin of piezoelectric in wurtzite ZnO. *Physical Chemistry Physical Physics*, 2015, vol. 17, p.7857-7863.
38. Karzel H., Potzel W., Köfferlein M., Schiessl W., Steiner M., Hiller U., Kalvius G. M., Mitchell D. W., Das T. P., Blaha P., Schwarz K., Pasternak M. P., Lattice dynamics and hyperfine interactions in ZnO and ZnSe at high external pressures. *Physical Review B: Condensed Matter*, 1996, vol.53, p. 11425-11438.
39. Kisi E. H., Elcombe M. M., u parameters for the wurtzite structure of ZnS and ZnO using powder neutron diffraction. *Acta Crystallographica Section C. Crystal Structure Communications*, 1989, vol. 45, p.1867-1870.
40. Gerward L., Olsen J. S., The high-pressure phase of zincite. *Journal of synchrotron radiation*, 1995, vol. 2, p. 233-235.
41. Serrano J., Romero A. H., Manjón F. J., Lauck R., Cardona M., Rubio A., Pressure dependence of the lattice dynamics of ZnO: An ab initio approach. *Physical Review B*, 2004, vol. 69, p. 094306/1-14.
42. Soni B. H., Deshpande M. P., Bhatt S. V., Chaki S. H., Sathe V., X-ray diffraction, X-ray photoelectron spectroscopy, and Raman spectroscopy of undoped and Mn-doped ZnO nanoparticles prepared by microwave irradiation. *Journal of Applied Spectroscopy*, 2013, vol. 79, no. 6, p. 901-906.
43. Damen T. C., Porto S. P. S., Tell B., Raman effect in zinc oxide. *Physical Review*, 1966, vol. 142, no. 2, p. 570-574.

44. Serrano J., Widulle F., Romero A. H., Rubio A., Lauck R., Cardona M., Dependence of phonons widths on pressure and isotopic mass: ZnO. *Physica Status Solidi (b)*, 2003, vol. 235, no. 2, p. 260-266.
45. Hewat A. W., Lattice dynamics of ZnO and BeO. *Solid State Communications*, 1970, vol. 8, p. 187-189.
46. Thoma K., Dorner B., Duesing G., Wegener W., Lattice dynamics of ZnO. *Solid State Communications*, 1974, vol. 15, p. 1111-1114.
47. Rössler U., Energy bands of hexagonal II-VI semiconductors. *Physical Review*, 1969, vol. 184, no. 3, p. 733-738.
48. Preston A. R. H., Ruck B. J., Piper L. F. J., DeMasi A., Smith K. E., Schleife A., Fuchs F., Bechstedt F., Chai J., Durbin S. M., Band structure of ZnO from resonant X-ray emission spectroscopy. *Physical Review B*, 2008, vol. 78, p. 155114/1-4.
49. Lambrecht W. R. L., Rodina A. V., Limpijumngong S., Segall B., Meyer B. K., Valence-band ordering and magneto-optic exciton fine structure in ZnO. *Physical Review B: Condensed Matter*, 2002, vol. 65, no. 7, p. 075207/1-12.
50. Look D. C., Hemsley J. W., Szelove J. R., Residual native shallow donor in ZnO. *Physical Review Letters*, 1999, vol. 82, no. 12, p. 2552-2555.
51. Look D. C., Claflin B. B., Cantwell G., Park S.-J., Renlund G. M., Electrical properties of ZnO. N. H. Nickel and E. Terukov (eds.), *Zinc Oxide – A Material for Micro- and Optoelectronic Applications*, 2004, vol. 194, p. 37–46.
52. Janotti A., Van De Walle C. G., Hydrogen multicentre bonds. *Nature Materials*, 2007, vol. 6, no. 1, p. 44–47.
53. Chernikov A., Bornwasser V., Koch M., Chatterjee S., Böttge C. N., Feldtmann T., Kira M., Koch S. W., Wassner T., Lautenschläger S., Meyer B. K., Eickhoff M., Phonon-assisted luminescence of polar semiconductors: Fröhlich coupling versus deformation-potential scattering. *Physical Review B*, 2012, vol. 85, p. 035201/1-8.
54. Chen S. L., Excitonic effects and energy upconversion in bulk and nanostructured ZnO [D]. Linköping University, Department of Physics, Chemistry and Biology Division of Functional Electronic Materials, 2014, Dissertation No. 1560.
55. Fonoberov V. A., Alim K. A., Balandin A. A., Photoluminescence investigation of the carrier recombination processes in ZnO quantum dots and nanocrystals. *Physical Review B*, 2006, vol. 73, p. 165317/1-9.
56. Ashkenov N., Mbenkum B. N., Bundesmann C., Riede V., Lorenz M., Spemann D., Kaidashev E. M., Kasic A., Schubert M., Grundmann M., Infrared dielectric functions and phonon modes of high-quality ZnO films. *Journal of Applied Physics*, 2003, vol. 93, no. 1, p. 126-133.
57. Haranath D., Sahai S., Joshi A. G., Gupta B. K., Shanker V., Investigation of confinement effects in ZnO quantum dots. *Nanotechnology*, 2009, vol. 20, p. 425701/1-7.

58. Cao L., Su X. Y., Wu Z. Y., Zou B. S., Dai J. H., Xie S. S., Quantum confinement effect of ZnO nano-particles. *Chemical Journal on Internet*, 2002, vol. 4, no. 9, p. 45. DOI: <http://www.chemistrymag.org/cji/2002/049045ne.htm>.
59. Felbier P., Yang J. H., Theis J., Liptak R. W., Wagner A., Lorke A., Bacher G., Kortshagen U., Highly luminescent ZnO quantum dots made in a nonthermal plasma. *Advance Functional Materials*, 2014, vol. 24, p. 1988-1993.
60. Fan Z. Y., Lu J. G., Zinc oxide nanostructures: synthesis and properties. *Journal of Nanoscience and Nanotechnology*, 2005, vol. 5, no. 10, p. 1561-1573.
61. Djurišić A. B., Leung Y. H., Optical properties of ZnO nanostructures. *Small*, 2006, vol. 2, p. 944-961.
62. Janotti A., Van de Walle C. G., Native point defects in ZnO. *Physical Review B*, 2007, vol. 76, p. 165202/1-22.
63. Lin B., Fu Z., Jia Y., Green luminescent center in undoped zinc oxide films deposited on silicon substrates. *Applied Physics Letters*, 2001, vol. 79, p. 943-945.
64. Xu P. S., Sun Y. M., Shi C. S., Xu F. Q., Pan H. B., The electronic structure and spectral properties of ZnO and its defects. *Nuclear Instruments and Methods in Physics Research Section B: Beam Interactions with Materials and Atoms*, 2003, vol. 199, p. 286-290.
65. Lima S. A. M., Sigoli F. A., Jafellici Jr M., Davolos M. R., Luminescent properties and lattice defects correlation on zinc oxide. *International Journal of Inorganic Materials*, 2001, vol. 3, no. 7, p. 749-754.
66. Kobayashi A., Sankey O. F., Dow J. D., Deep energy levels of defects in the wurtzite semiconductors AlN, CdS, CdSe, ZnS, and ZnO. *Physical Review B*, 1983, vol. 28, p. 946-956.
67. Willander M., Nur O., Sadaf J. R., Qadir M. I., Zaman S., Zainelabdin A., Bano N., Hussain I., Luminescence from zinc oxide nanostructures and polymers and their hybrid devices. *Materials*, 2010, vol. 3, p. 2643-2667.
68. Djurišić A. B., Choy W. C. H., Roy V. A. L., Leung Y. H., Kwong C. Y., Cheah K. W., Gundu Rao T. K., Chan W. K., Lui H. F., Surya C., Photoluminescence and EPR of ZnO tetrapod structures. *Advanced Functional Materials*, 2004, vol. 14, p. 856-864.
69. Samanta P. K., Patra S. K., Ghosh A., Chaudhuri P. R., Visible emission from ZnO nanorods synthesized by a simple wet chemical method. *International Journal of NanoScience and Nanotechnology*, 2009, vol. 1, no. 1-2, p. 81-90.
70. Lv Y., Xiao W., Li W., Xue J. and Ding J., Controllable synthesis of ZnO nanoparticles with high intensity visible photoemission and investigation of its mechanism. *Nanotechnology*, 2013, vol. 24, p. 175702/1-10.
71. Zeng H. B., Duan G. T., Li Y., Yang S. K., Xu X. X., Cai W. P., Blue luminescence of ZnO nanoparticles based on non-equilibrium processes: defect origins and emission controls. *Advanced Functional Materials*, 2010, vol. 20, p. 561-572.
72. Ahn H. A., Kim Y. Y., Kim D. C., Mohanta S. K., Cho H. K., A comparative analysis of deep level emission in ZnO layers deposited by various methods. *Journal of Applied Physics*, 2009, vol. 105, p. 013502/1-5.

73. Fang Z., Wang Y., Xu D., Tan Y., Liu S., Blue luminescent centers in ZnO deposited on Si substrates. *Optical Materials*, 2004, vol. 26, p. 239–242.
74. Fabbri F., Villani M., Catellani A., Calzolari A., Cicero G., Calestani D., Calestani G., Zappettini A., Dierre B., Sekiguchi T., Salviati G., Zn vacancy induced green luminescence on non-polar surfaces in ZnO nanostructures. *Scientific Reports*, 2014, vol. 4, no. 5158, p. 1-6.
75. Vanheusden K., Seager C. H., Warren W. L., Tallant D. R., Voigt J. A., Correlation between photoluminescence and oxygen vacancies in ZnO phosphors. *Applied Physics Letters*, 1996, vol. 15, p. 403–405.
76. Leung Y. H., Chen X. Y., Ng A. M. C., Guo M. Y., Liu F. Z., Djurišić A. B., Chan W. K., Shi X. Q., Van Hove M. A., Green emission in ZnO nanostructures---examination of the roles of oxygen and zinc vacancies. *Applied Surface Science*, 2013, vol. 271, p. 202-209.
77. Li M. J., Xing G. C., Xing G. Z., Wu B., Wu T., Zhang X. H. Sum T. C., Origin of green emission and charge trapping dynamics in ZnO nanowires. *Physical Review B*, 2013, vol. 87, 115309/1-8.
78. Gomi M., Oohira N., Ozaki K., Koyano M., Photoluminescence and structural properties of precipitated ZnO fine particles. *Japanese Journal of Applied Physics*, 2003, vol. 42, p. 481–485.
79. Norberg N. S., Gamelin D. R., Influence of surface modification on the luminescence of colloidal ZnO nanocrystals. *The Journal of Physical Chemistry B*, 2005, vol. 109, p. 20810-20816.
80. Tainoff D., Masenelli B., Mélinon P., Belsky A., Ledoux G., Amans D., Dujardin C., Fedorov N., Martin P., Competition between exciton-phonon interaction and defects states in the 3.31 eV band in ZnO. *Physical Review B*, 2010, vol. 81, p. 115304/1-8.
81. Han L. L., Cui L., Wang W. H., Wang J. L., Du X. W., On the origin of blue emission from ZnO quantum dots synthesized by a sol–gel rout. *Semiconductor Science and Technology*, 2012, vol. 27, p. 065020/1-8.
82. John T. T., Priolkar K. R., Bessière A., Sarode P. R., Viana B., Effect of [OH<sup>-</sup>] linkages on luminescent properties of ZnO nanoparticles. *The Journal of Physical Chemistry C*, 2011, vol. 15, no. 37, p. 18070–18075.
83. Tang X. S., Choo E. S. G., Li L., Ding J., Xue J. M., Synthesis of ZnO nanoparticles with tunable emission colors and their cell labeling applications. *Chemistry of Materials*, 2010, vol. 22, p. 3383-3388.
84. Zhong Y. C., Djurišić A. B., Hsu Y. F., Wong K. S., Brauer G., Ling C. C., Chan W. K., Exceptionally Long Exciton Photoluminescence lifetime in ZnO tetrapods. *The Journal of Physical Chemistry C*, 2008, vol. 112, p. 16286–16295.
85. Layek A., Manna B., Chowdhury A., Carrier recombination dynamics through defect states of ZnO nanocrystals: from nanoparticles to nanorods. *Chemical Physics Letters*, 2012, vol. 539–540, p. 133–138.
86. Rodnyi P. A., Khodyuk I. V., Optical and luminescence properties of zinc oxide (Review). *Optics and Spectroscopy*, 2011, vol. 111, p. 776-785.

87. Mishra S. K., Srivastava R. K., Prakash S. G., Yadav R. S., Panday A. C., Photoluminescence and photoconductive characteristics of hydrothermally synthesized ZnO nanoparticles. *Opto-Electronics Review*, 2010, vol. 18, no. 4, p. 467–473.
88. Nyffenegger R. M., Craft B., Shaaban M., Gorer S., Erley G., Penner R. M., A hybrid electrochemical/chemical synthesis of zinc oxide nanoparticles and optically intrinsic thin films. *Chemistry of Materials*, 1998, vol. 10, p. 1120–1129.
89. Kim S. W., Fujita S., Self-organized ZnO quantum dots on SiO<sub>2</sub>/Si substrates by metalorganic chemical vapor deposition. *Applied Physics Letters*, 2002, vol. 81, no. 26, p. 5036-5038.
90. Djurišić A. B., Leung Y. H., Tam K. H., Green, yellow, and orange defect emission from ZnO nanostructures: influence of excitation wavelength. *Applied Physics Letters*, 2006, vol. 88, p. 103107/1-3.
91. Zhang D. H., Wang Q. P., Xue Z. Y., Photoluminescence of ZnO films excited with light of different wavelength. *Applied Surface Science*, 2003, vol. 207, p. 20-25.
92. Irimpan L., Krishnan B., Deepthy A., Nampoori V. P. N., Radhakrishnan P., Excitation wavelength dependent fluorescence behaviour of nano colloids of ZnO. *Journal of Physics D: Applied Physics*, 2007, vol. 40, p. 5670–5674.
93. Ampem-Lassen E., Simpson D. A., Gibson B. C., Trpkovski S., Hossain F. M., Huntington S. T., Ganesan K., Hollenberg L. C. L., Praver S., Nano-manipulation of diamond-based single photon sources. *Optics Express*, 2009, vol. 14, p. 11287-11293.
94. Castelletto S., Johnson B. C., Ivády V., Stavrias N., Umeda T., Gali A., Ohshima T., A silicon carbide room-temperature single-photon source. *Nature Materials*, 2014, vol. 13, p. 151-156.
95. Morfa A. J., Gibson B. C., Karg M., Karle T. J., Greentree A. D., Mulvaney P., Tomljenovic-Hanic S., Single-photon emission and quantum characterization of zinc oxide defects. *Nano Letters*, 2012, vol. 12, p. 949-954.
96. Xiong H.-M., Ma R.-Z., Wang S.-F., Xia Y.-Y., Photoluminescent ZnO nanoparticles synthesized at the interface between air and triethylene glycol. *Journal of Materials Chemistry*, 2011, vol. 21, p. 3178-3182.
97. Fu Y. S., Du X. W., Kulinich S. A., Qiu J. S., Qin W. J., Li R., Sun J., Liu J., Stable aqueous dispersion of ZnO quantum dots with strong blue emission via simple solution route. *Journal of the American Chemical Society*, 2007, vol. 129, no. 51, p. 16029-16033.
98. Willander M., Nur O., Sadaf J. R., Qadir M. I., Zaman S., Zainelabdin A., Bano N., Hussain I., Luminescence from zinc oxide nanostructures and polymers and their hybrid devices. *Materials*, 2010, vol. 3, p. 2643-2667.
99. Apostoluk A., Zhu Y., Masenelli B., Delaunay J. -J., Sibiński M., Znajdek K., Focsa A., Kaliszewska I., Improvement of the solar cell efficiency by the ZnO nanoparticle layer via the down-shifting effect. *Microelectronic Engineering*, 2014, vol. 127, p.51-56.
100. Moussodia R. -O., Balan L., Schneider R., Synthesis and characterization of water-soluble ZnO quantum dots prepared through PEG-siloxane coating. *New Journal of Chemistry*, 2008, vol. 32, p. 1388-1393.

101. Nistor S. V., Ghica D., Stefan M., Vlaicu I., Barascu J. N., Bartha C., Magnetic defects in crystalline Zn(OH)<sub>2</sub> and nanocrystalline ZnO resulting from its thermal decomposition. *Journal of Alloys and Compounds*, 2013, vol. 548, p. 222-227.
102. Shaporev A. S., Ivanov V. K., Baranchikov A. E., Polezhaeva O. S., Tretyakiv Yu. D., ZnO Formation under Hydrothermal Conditions from Zinc Hydroxide Compounds with Various Chemical Histories. *Russian Journal of Inorganic Chemistry*, 2007, vol. 52, no. 12, p. 1925–1931.
103. Wu. D. P., Jiang Y., Liu J. L., Yuan Y. F., Wu. J. S., Jiang K., Xue D. F., Template Route to Chemically Engineering Cavities at Nanoscale: A Case Study of Zn(OH)<sub>2</sub> Template. *Nanoscale Research Letters*, 2010, vol. 5, p. 1779–1787.
104. Dinsmore A. D., Hsu D. S., Quadri S. B., Cross J. O., Kennedy T. A., Gray H. F., Ratna B. R., Structure and luminescence of annealed nanoparticles of ZnS:Mn. *Journal of Applied Physics*, 2000, vol. 88, no. 90, p. 4985–4993.
105. Porambo M. W., Marsh A. L., Synthesis and photoluminescent properties of doped ZnS nanocrystals capped by poly(vinylpyrrolidone). *Optical Materials*, 2009, vol. 31, p. 1631–1635.
106. Sawada Y., Murakami M., Nishide T., Thermal analysis of basic zinc carbonate. Part 1. Carbonation process of zinc oxide powders at 8 and 13°C. *Thermochimica Acta*, 1996, vol. 273, p. 95–102.
107. Zhengwei. Pan, Jing. Tao, Yimei. Zhu, Jingfang. Huang, M. Parnas Parantham, Spontaneous Growth of ZnCO<sub>3</sub> Nanowires on ZnO Nanostructures in Normal Ambient Environment: Unstable ZnO Nanostructures. *Chemistry of Materials*, 2010, vol. 22, p. 149–154.
108. Fathima Parveen M., Umopathy S., Dhanalakshmi V., Anbarasan R., Synthesis and Characterization of Nano-sized Zn(OH)<sub>2</sub> and Zn(OH)<sub>2</sub>/PVA Nano-composite. *Composite Interfaces*, 2010, vol. 17, p. 757–774.
109. Morales-Flores N., Galeazzi R., Rosendo E., Díaz T., Velumani S., Pal U., Morphology control and optical properties of ZnO nanostructures grown by ultrasonic synthesis. *Advances in Nano Research*, 2013, vol. 1, no. 1, p. 59-70.
110. Islam S. M. Z., Seredych M., Bandosz T. J., Alfano R., Energy band gap of Zinc(Hydr)oxide using absorption, fluorescence and photoconductivity. *FiO/LS Technical Digest © OSA*, 2012.
111. Guo L., Yang S., Yang C., Yu P., Wang J., Ge W., Wong G. K. L., Highly monodisperse polymer-capped ZnO nanoparticles: Preparation and optical properties. *Applied Physics Letters* 2000, vol.76, p. 2901-2903.
112. Zhou H., Alves H., Hofmann D. M., Kriegseis W., Meyer B. K., Behind the weak excitonic emission of ZnO quantum dots: ZnO/Zn(OH)<sub>2</sub> core-shell structure. *Applied Physics Letters*, vol. 80, no. 2, p. 210-212.
113. Wang G., Ji J. W., Zhang X. W., Zhang Y., Wang Q. B., You X. Z., Xu X. X., Colloidal nanocrystals fluoresced by surface coordination complexes. *Scientific Reports*, 2014, vol. 4, no. 5480, p. 1-8.
114. Xiong H. -M., Wang Z. -D., Liu D. -P., Chen J. -S., Wang Y. -G., Xia Y. -Y., Bonding polyether onto ZnO nanoparticles: an effective method for preparing polymer nanocomposites with tunable luminescence and stable conductivity. *Advanced Functional Materials*, 2005, vol. 15, p. 1751-1756.

115. Sharma P. K., Dutta R. K., Kumar M., Singh P. K, Pandey A. C., Luminescence studies and formation mechanism of symmetrically dispersed ZnO quantum dots embedded in SiO<sub>2</sub> matrix. *Journal of Luminescence*, 2009, vol. 129, no. 6, p. 605–610.
116. Bouguerra M., Samah M., Belkhir M. A., Chergui A., Gerbous L., Nouet G., Chateigner D., Madelon R., Intense photoluminescence of slightly doped ZnO-SiO<sub>2</sub> matrix. *Chemical Physics Letters*, 2006, vol. 425, p. 77–81.
117. Hovel H. J., Hodgson R. T., Woodall J. M., The effect of fluorescent wavelength shifting on solar cell spectral response. *Solar Energy Materials*, 1979, vol. 2, no. 1, p. 19–29.
118. Kawano K., Hashimoto N., Nakata R., Effects on solar cell efficiency of fluorescence of rare-earth ions. *Materials Science Forum*, 1997, vol. 239-241, p. 311-314.
119. Richards B. S., Shalav A., The role of polymers in the luminescence conversion of sunlight for enhanced solar cell performance. *Synthetic Metals*, 2005, vol. 154, p. 61-64.
120. Refractive index and related constants – Poly(methyl methacrylate) (PMMA, Acrylic glass). *Refractiveindex.info*. Retrieved 2015-03-20.
121. Du X. -W., Fu Y. -S., Sun J., Han X., Liu J., Complete UV emission of ZnO nanoparticles in a PMMA matrix. *Semiconductor Science and Technology*, 2006, vol. 21, p. 1202–1206.
122. Richters J. -P., Voss T., Wischmeier L., Rückmann I., Gutowski J., Influence of polymer coating on the low-temperature photoluminescence properties of ZnO nanowires. *Applied Physics Letters*, 2008, vol. 92, p. 011103/1-3.
123. Sreeja R., John J., Aneesh P. M., Jayaraj M. K., Linear and nonlinear optical properties of luminescent ZnO nanoparticles embedded in PMMA matrix. *Optics Communications*, 2010, vol. 283, no. 14, p. 2908–2913.
124. Sun D. Z., Miyatake N., Sue H. -J., Transparent PMMA/ZnO nanocomposite films based on colloidal ZnO quantum dots. *Nanotechnology*, 2007, vol. 18, 215606/1-6.
125. Pomogailo A. D., Dzhardimalieva G. I., Kestelman V. N., Macromolecular metal carboxylates and their nanocomposites. *Springer Series in Materials Science*, 2010, vol. 138, p. 7-25. DOI: 10.1007/978-3-642-10574-6\_2.
126. Zhang J. H., Dong G. J., Thurber A., Hou Y. Y., Gu M., Tenne D. A., Hanna C. B., Punnoose A., Tuning the properties of ZnO, Hematite, and Ag nanoparticles by adjusting the surface charge. *Advanced Materials*, 2012, vol. 24, p. 1232-1237.
127. Wang C. W., Moffitt M. G., Surface-tunable photoluminescence from block copolymer-stabilized cadmium sulfide quantum dots. *Langmuir*, 2004, vol. 20, p. 11784-11796.
128. Ikono R., Maulana N. N., Dewinggih T., Effendi M., Widayanto W. B., Sukarto A., Rochman N. T., Effect of polyacrylic acid addition to improve nano zinc oxide dispersion stability. *International Journal of Engineering & Technology*, vol. 12, no. 6, p. 95-99.



## Chapter 3

### Synthesis and characterization of ZnO nanoparticles

ZnO nanostructures can be synthesized via different methods such as the Low Energy Cluster Beam Deposition (LECBD) [1] or laser ablation (in vacuum or liquid) [2, 3], ultrasonic synthesis [4], hydrothermal method [5] and sol-gel synthesis [6]. It turns out that the defect emission is influenced strongly by the synthesis conditions and it is difficult to control it in a precise manner. Moreover, the mechanisms of these defect emissions are still controversial as mentioned in Chapter 2 [7, 8], making it more difficult to attain a high defect luminescent emission efficiency.

A physical method (LECBD method) was chosen to synthesize ZnO nanoparticles (NPs) because the stoichiometry and the size of ZnO NPs can be tuned without capping their surface. On the other hand, wet chemistry synthesis routes were also used as they can provide scalable amounts of ZnO NPs powders for further envisaged industrial applications. Moreover, using chemical methods, the surface states of the NPs can be controlled by adding a suitable capping agent. This is of prime importance, since whatever the defects responsible for the visible emission, there exists a consensus in the scientific community about their prominence at the surface of the dots and their influence on the visible emission of the ZnO NPs.

For comparison with the ZnO NPs fabricated in the laboratory, the commercially available ZnO NPs were also studied in this work.

In this chapter, the methods of the physical fabrication and of the chemical synthesis of ZnO NPs used will be described in details. Next, operation principles and experimental setup of the characterization techniques, including structural, chemical and optical analyses will be presented.

#### 3.1. Synthesis methods of ZnO nanoparticles

##### 3.1.1. Low Energy Cluster Beam Deposition (LECBD) method

The Low Energy Cluster Beam Deposition (LECBD) method was developed for the fabrication of well-defined nanostructured materials composed of clusters. A cluster is an ideal nanometric building block to assemble the nanostructures which exhibit particular physical properties related to the cluster size. Based on this technique, various cluster-assembled films were prepared successfully such as metal, oxide, alloys and composite films, which demonstrate properties different from the bulk films prepared by the usual methods such as pulse laser deposition (PLD), magnetron sputtering (MS), metal-organic chemical vapor deposition (MOCVD), sol-gel, etc. Cluster-generated solids differ from both the amorphous and crystalline structures, in the sense

that the short range order in them is controlled by the grain size and the long range order does not exist due to random stacking of nanograins.

The schematic diagram of the LECBD experimental setup is shown in **Figure 3.1**. The synthesis technique used here has been detailed in several articles [9, 10]. A ZnO target made from a sintered powder (99.99 % pure) is ablated by a pulse YAG:Nd laser (10 Hz repetition rate, 10 ns pulse duration). The ablation creates plasma of Zn and O species which is first cooled by the continuous injection of a buffer gas at 20 mbars. The buffer gas is a mixture of He and O<sub>2</sub>. While cooling the plasma, the buffer gas induces the formation of nucleation embryos (dimers and trimers). The plasma subsequently undergoes a supersonic adiabatic expansion while moving from the nucleation chamber at 20 mbars to the high vacuum deposition chamber at 10<sup>-7</sup> mbars through a micrometric nozzle. During the expansion, the formation of clusters is achieved by the accretion of embryos and atoms. The typical quenching rate is ~ 10<sup>8</sup> K/s. The preformed clusters are then deposited on any given substrate without being destroyed, for their kinetic energy per atom is about one order of magnitude lower than the binding energy per atom when they are in the clusters. It should be mentioned that up till now this technique used to synthesize clusters of metallic and covalent materials has always led to nanostructured films whose building blocks are the individual “preformed” clusters. This fact is referred to as the “memory effect”.

In the nucleation stage, the reactions taking place in the plasma can be written in equations as following:



The coefficients a, b, c, and d here correspond to the creation rate of the formed dimers that can be dissociated according to the coefficients a', b', c', and d', in verse direction of the creation. The problem encountered in the physical synthesis of ZnO nanostructures is that the O<sub>2</sub> is a very stable molecule that does not dissociate (d = 1; d' = 0) and will be pumped out of the reaction chamber, while the Zn<sub>2</sub> molecule is weakly bound, having a very short lifetime and will dissociate (a = 0, a' = 1), introducing an excess Zn in the subsequent reaction. At this stage, the reaction involves two Zn and two ZnO and is therefore non-stoichiometric. The binding energies of these complexes are too small (Zn<sub>2</sub>) and too high (O<sub>2</sub>) to be significantly modified through collisions with buffer gas, but it is not the case for ZnO molecules having intermediate binding energies. The bonding of Zn and O atoms cooled by collisions with buffer gas in LECBD is irreversible, i.e. b' = c' = 0, which works at non-thermodynamic equilibrium state. Indeed, at thermodynamic equilibrium, both ZnO created molecules can dissociate with probability b = b' = c = c' = 0.5. The balance of the equilibrium reaction is 3 Zn, 1 O and 1 ZnO, reintroducing an

oxygen atom which is able to combine with another oxygen atom and thus be pumped out of the reaction chamber. The balance of the non-equilibrium reaction in LECBD is  $2 \text{ Zn}$  and  $2 \text{ ZnO}$ , which saves a part of the oxygen involved in each step. The stoichiometry is then logically improved. We are able to control the stoichiometry of the ZnO clusters by controlling the  $\text{O}_2$  pressure in the nucleation chamber. Subsequently, the stoichiometry can be measured using the X-ray Photoelectron Spectroscopy (XPS) setup connected to the deposition chamber. The ZnO cluster size can be controlled to some extent by changing the size of the nozzle. Indeed, as the nozzle size is small, the probability of accretion of embryos and atoms is increased. The typical deposition rate is  $\sim 1 \text{ nm/min}$ , as measured by a quartz microbalance and the achievable thickness is  $\sim 100 \text{ nm}$ .

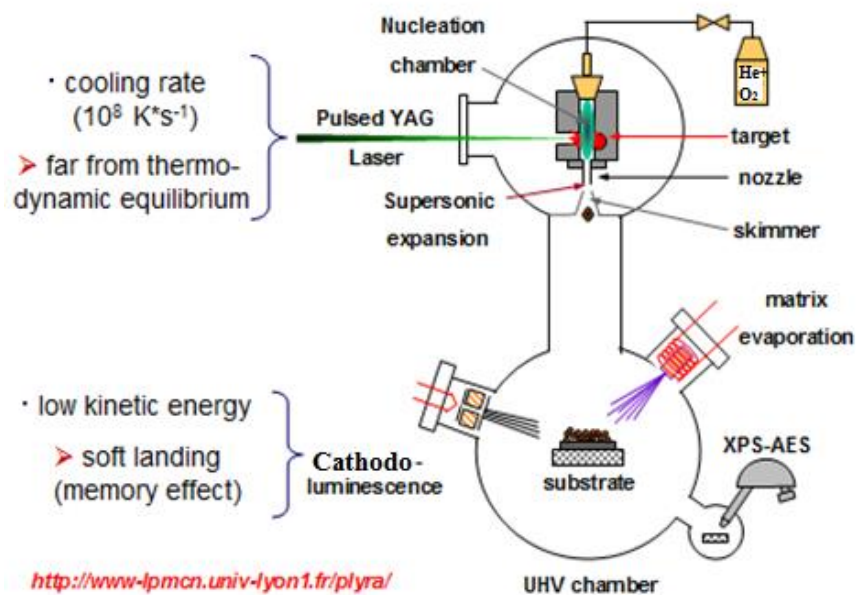


**Figure 3.1:** Schematic diagram of the LECBD experimental setup.

### 3.1.2. Commercially available ZnO nanoparticles

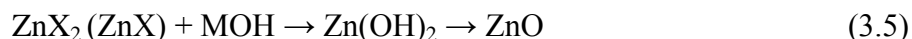
The commercially available ZnO nanoparticles used in this study as test samples were purchased from Iolitec Company (<http://www.iolitec.de/en/>) from Germany. The description of their fabrication method is not available, protected by the manufacturer. Despite our repeated requests, the manufacturer did not provide us with the purity of the sample or did not indicate the presence of any capping agent. We deposited these ZnO NPs on the indium foil just by a simple pressing and studied their photoluminescent characteristics.

### 3.1.3 Chemical synthesis methods

The development of these methods has been done in close collaboration with Prof. Daniele's team from the IRCE Lyon where the chemical syntheses have been performed. Wet chemistry synthesis routes have been developed because they can provide scalable amounts of ZnO NPs powders for further industrial applications. Moreover, using chemical synthesis methods, the surface states of the NPs can be controlled. This is of prime importance as we have mentioned in Chapter 2, these surface states have an important effect on the visible emission efficiency. Two chemical methods have been studied in the frame of this thesis. The first one is the co-precipitation method, a widely used sol-gel synthesis technique, requiring moderate conditions (ambient environment and room temperature) and is cost-effective. It allows an easy control of the synthesis parameters and various surfactants can be added to protect the as-prepared nanoparticles (NPs). It can be performed in polar (water) and non-polar (ethanol) solutions. The other method is the hydrolysis, which is less studied in the literature, but possibly more interesting, as the surface can be modified easily through the surfactants added.

#### 3.1.3.1 Co-precipitation method

The reaction equation of the co-precipitation synthesis used in this study can be described by the following equation:



where,

$\text{ZnX}_2$  ( $\text{ZnX}$ ) is zinc acetate dihydrate ( $\text{Zn}(\text{OAc})_2 \cdot 2\text{H}_2\text{O}$ ) or zinc sulfate,

$\text{MOH}$  is the alkaline hydroxide ( $\text{LiOH}$  or  $\text{KOH}$ ).

In the co-precipitation method, 20 mmol (4.400 g) of zinc acetate dihydrate ( $\text{Zn}(\text{OAc})_2 \cdot 2\text{H}_2\text{O}$ ) or zinc sulfate ( $\text{ZnSO}_4$ ) were dissolved in 70 ml of ethanol or water with vigorous stirring. Next, 80 mmol (4.488 g) of potassium hydroxide ( $\text{KOH}$ ) were dissolved in 10 ml of ethanol with vigorous stirring, and then cooled to room temperature. The  $\text{KOH}$  solution was then added into zinc acetate solution drop wise using a syringe. The reaction medium was further stirred for 1 hour and then centrifuged at 4000 turns/min for 10 minutes, so as to isolate the formed solid ZnO. Two steps of washing with 20 ml of water followed by washing with 20 ml of ethanol were performed before placing the resulting white solid in an oven at  $70^\circ\text{C}$  for 4 hours. For some syntheses, the precursor  $\text{Zn}(\text{OAc})_2 \cdot 2\text{H}_2\text{O}$  was replaced by zinc sulfate ( $\text{ZnSO}_4$ ) and  $\text{KOH}$  was replaced with different quantities of  $\text{LiOH}$  (the ratios of the mole of  $\text{LiOH}$  solution to the zinc acetate being either 2:1 or 4:1), so as to compare the role of the precursor and alkaline ion on the emission of the resulting ZnO nanoparticles. 1 % of PAAH, (with molecular weight of  $2000 \text{ g} \cdot \text{mol}^{-1}$ ) in weight with respect to ZnO was added during the synthesis of ZnO NPs by the co-precipitation of the zinc sulfate with 4  $\text{LiOH}/\text{Zn}$  sulfate to examine the effect of the surfactant on the synthesized ZnO NPs.

### 3.1.3.2 Hydrolysis method

The reaction equation of hydrolysis synthesis presented in this study is described by the following equation:



where,

$\text{ZnX}_2$  is diethyl zinc ( $\text{ZnEt}_2$ ) or zinc bis(trimethylsilyl)amide ( $\text{Zn}[\text{N}(\text{SiMe}_3)_2]_2$ ).

In the hydrolysis method with zinc bis(trimethylsilyl)amide ( $\text{Zn}[\text{N}(\text{SiMe}_3)_2]_2$ ), 1.54 g of  $\text{Zn}[\text{N}(\text{SiMe}_3)_2]_2$  ( $4 \times 10^{-3}$  mol) in 4 mL of hexane ( $1 \text{ mol} \cdot \text{L}^{-1}$ ) was added dropwise to 50 mL water under vigorous stirring. The mixture was stirred for 2 h and was then centrifuged to give a white solid (242 mg, 74 % based on the Zn content). The as-prepared precipitate was washed with 50 mL of ethanol and dried at  $70^\circ\text{C}$  for ca. 12 h, yielding 74 % of ZnO. The powder was dispersed in the polymer matrix (polyurethane (PU)) solution and then deposited on the fused silica substrate or was deposited on indium foil by a simple pressing. In the hydrolysis method with diethyl zinc ( $\text{ZnEt}_2$ ), 2.6 mmol of the  $\text{ZnEt}_2$  (1.8 ml of commercial solution, 15 % weight in toluene) were added drop wise in a Schlenk tube containing 25 ml water, with vigorous stirring. The resulting ethane was removed via a bubbler.  $\text{ZnEt}_2$  being pyrophoric, the reaction was carried out in an inert atmosphere [11]. Stirring was continued overnight for 24 hours at room temperature. The zinc oxide formed was subsequently isolated by centrifugation at 4000 turns/min for 10 minutes and then the isolated white powder was washed with 20 ml of ethanol and rinsed in water twice. Finally, the compound was placed at  $70^\circ\text{C}$  for 4 hours. Different hydrolytic conditions were tested. In order to control the surface state of the fabricated nanoparticles in terms of both the crystalline quality and zeta potential, a capping agent - polyacrylic acid (PAAH) - was added to the solution at different concentrations (0.063 wt%, 0.63 wt% and 6.3 wt%, respectively) during the synthesis of ZnO NPs.

## 3.2. Characterization of ZnO NPs

In order to obtain ZnO NPs emitting visible luminescence as high as possible and to control the spectral shape of this emission, the influence of the synthesis conditions on the optical properties of ZnO NPs should be identified. In order to identify the impact of each parameter of the synthesis of ZnO NPs on their properties, different characterization techniques have been used, including the structural, chemical and optical ones. The structural properties were characterized with the observation techniques such as X-ray diffraction (XRD) analysis, transmission electron microscopy (TEM), scanning electron microscopy (SEM) and dynamic/electrophoretic light scattering (DLS/ELS). These techniques permitted to estimate the size, shape and crystallinity of NPs. Moreover, Fourier Transform Infra-Red spectroscopy (FTIR), Raman spectroscopy and Nuclear Reaction Analysis (NRA) provided insight into the chemical composition of ZnO NPs. All these characterizations help to understand the effects of the physical and chemical properties

on the optical properties of ZnO NPs, thus a fine control on ZnO NPs synthesis conditions can be attained and the optimum visible emission efficiency can be reached. Finally, the photoluminescence (PL) spectra and PL quantum yield (PL QY) of each batch of synthesized ZnO NPs were measured in order to check the spectral range and the efficiency of the PL emission.

### 3.2.1. Structural characterization

#### 3.2.1.1. X-ray diffraction (XRD) analysis

The crystalline structure was probed by X-ray diffraction (XRD) analysis. The operation principle of XRD analysis is presented in **Figure 3.2**. The sample is irradiated with a beam of monochromatic X-rays (produced by bombarding a metal target (Cu or Mo for example) with a beam of electrons emitted from a hot filament) with an angle of  $\theta$ . After interacting with the atoms, the diffracted X-rays are collected by the X-ray detector. There will be constructive interference each time Bragg's law is satisfied. This law can be written as:  $2d \sin\theta = n\lambda$ , where  $d$  is the interplanar distance of the lattice planes from which X-rays are scattered,  $\theta$  is the angle of incidence of the X-ray,  $n$  is an integer and  $\lambda$  is the wavelength of the incident X-rays. The collection of the diffracted beam yield as a function of  $2\theta$  builds up a diffractogram. By comparing the diffractogram to standard files (JCPDS files), one can determine the type of the crystalline network.

The Bruker (Siemens) D5005 diffractometer was used to acquire the XRD diffractograms using the K-alpha radiation of Cu ( $1.54184 \text{ \AA}$ ) in the  $\theta$ - $2\theta$  geometry. The crystalline domain size of the nanoparticles can be estimated crudely from X-ray diffraction (XRD) analysis using the Scherrer's formula. The formula writes as:  $d = k\lambda/(\beta \cos \theta)$ , where  $k$  is a constant (equal to 0.89),  $\lambda$  is the wavelength of the X-rays,  $\theta$  is the incident angle of X-ray and  $\beta$  is the full width at half-maximum (FWHM) of the diffraction peak.

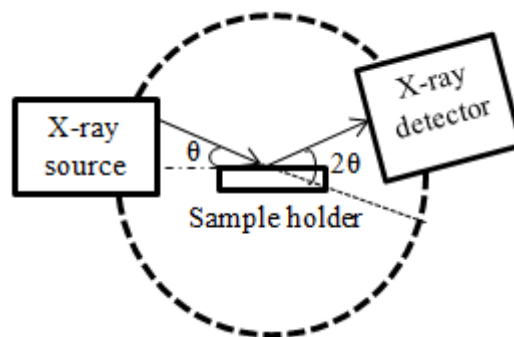


**Figure 3.2:** Operation principle of the XRD analysis.

The normally obtained XRD pattern is shown in **Figure 3.3** [12]. The peaks of crystalline hexagonal wurtzite ZnO normally observed at  $2\theta = 31.67^\circ, 34.31^\circ, 36.14^\circ, 47.40^\circ, 56.52^\circ, 62.73^\circ, 66.28^\circ, 67.91^\circ, 69.03^\circ,$  and  $72.48^\circ$  are assigned to (100), (002), (101), (102), (110), (103), (200), (112), (201), and (004) plane of ZnO NPs.

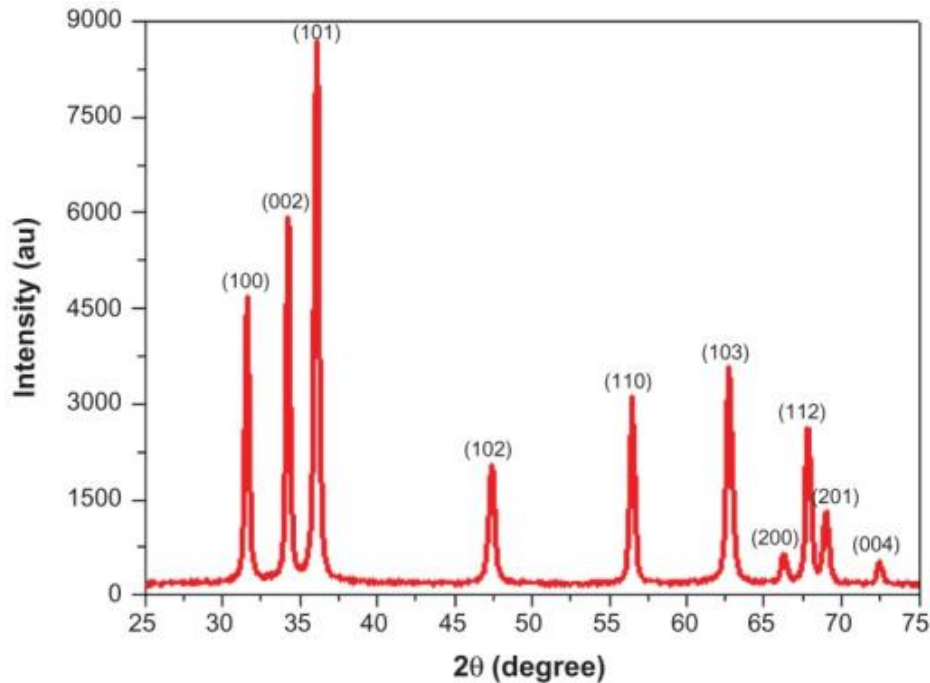


**Figure 3.3:** X-ray diffraction pattern of zinc oxide nanoparticles [12].

### 3.2.1.2. Electron microscopy

The electron microscope is a type of microscope that uses a beam of electrons to create an image of the specimen. Interactions of the electron beam and the studied matter produce backscattered electrons, secondary electrons, transmitted electrons or X-ray. Focusing the beam of electrons is ensured by means of electrostatic or electromagnetic (EM) lenses. It is capable of much higher magnifications and has a greater resolving power than a traditional optical microscope. It allows seeing much smaller objects in finer detail, because electrons have wavelengths shorter than visible light used as a light source in an optical microscope. The structure, composition and morphology can be determined using electron microscopy.

**Scanning electron microscopy (SEM).** In SEM, a beam of electrons accelerated by a high voltage (2-25 kV) is used to scan the surface of the specimen. Different signals are generated via the reaction with the electron beam which strikes the sample surface, including the secondary electrons (SE), the backscattered electrons (BSE), Auger electrons, characteristic X-rays, X-ray continuum and cathodoluminescence. As the energetic electrons produced and accelerated by the electron gun arrive on the specimen, they will penetrate in the specimen over a given distance and produce the mentioned different signals instead of bouncing off on the surface. As the acceleration voltage increases, the penetration length increases at the expense of the detailed surface information of the specimen. The SE and BSE signals are usually used to obtain the topologic information of the specimen since they are produced near the surface. The scanning coils deflect the primary electron beam along the x-axis or y-axis to probe the specimen surface spot by spot. The BSE signals are detected by solid state BSE detectors, while the Everhart-

Thornley (ET) detector is used to capture the SE and BSE signals to form a three dimensional (3D) image of the specimen. The schematic diagram of the SEM principles is shown in **Figure 3.4 (a)**.

In the present study, we have used SEM TESCAN MIRA 3 equipped with a field emission gun with a spot size of 2.5 nm.

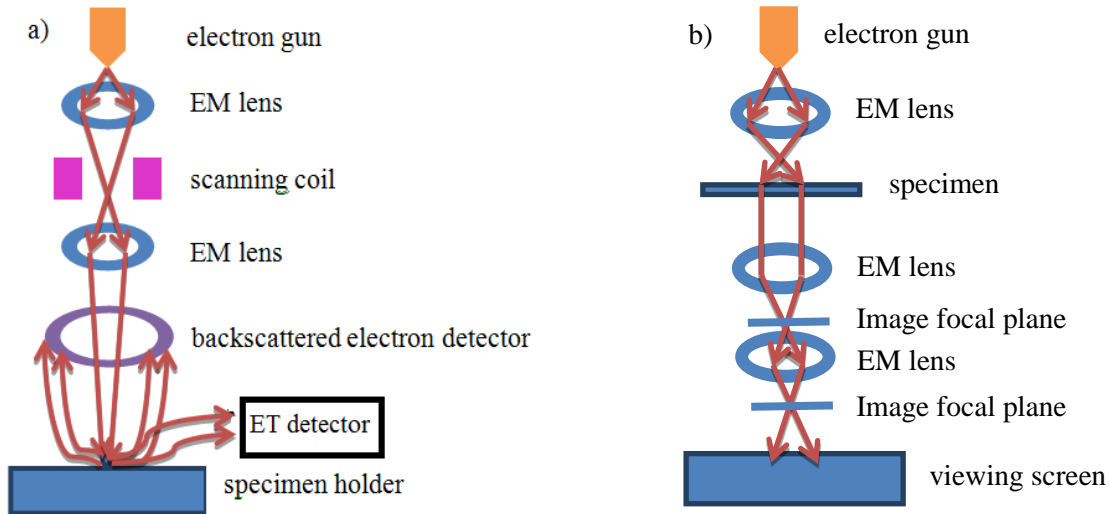


**Figure 3.4:** Schematic diagram of the (a) SEM and (b) TEM principles.

**Transmission electron microscopy (TEM).** Unlike the SEM, in TEM, ultra-thin specimen is required. The beam of electrons accelerated with a high voltage (50-400 kV) is transmitted through the specimen, interacting with it as it passes through. An image of the specimen is formed from the electrons transmitted directly through the specimen. The image is magnified and focused onto an imaging device, such as a fluorescent screen. Two dimensional (2D) images with more detailed morphology information can be obtained by TEM compared to SEM. The schematic diagram of the TEM is shown in **Figure 3.4 (b)**. There are two operation modes: the contrast mode (either in dark or bright field) usually for low magnification, and the high resolution mode (for high magnification) which allows the direct observation of the crystal network. The high resolution mode is based on the diffraction of the e-beam by the crystal lattice.

For the needs of this thesis, the morphologies and images of the synthesized ZnO nanoparticles were made using the transmission electronic microscope TEM JEOL 2010F (200KV).

### 3.2.1.3. Dynamic and electrophoretic light scattering

In a colloidal system containing particles dispersed in a liquid solution, the particle size distribution can be determined using dynamic light scattering (DLS). The information about the

nanoparticle surface charge can be obtained by zeta potential measurement using electrophoretic light scattering (ELS).

**Dynamic light scattering (DLS).** The particles dispersed in the liquid move randomly due to the collision with the surrounding solvent molecules, the so called Brownian motion. Dynamic light scattering (also known as photon correlation spectroscopy) measures Brownian motion and relates it to the size of the particles. As the particle is illuminated by a light source (here we used a laser), the light will be scattered in all directions. When the light scattered by the particles arrive to the detector with the same phase, constructive interference takes place and a bright area is formed. Otherwise, when the phase additions are mutually destructive and cancel each other out, dark spaces are formed. Since the particles move, the dark and light areas will change both in position and intensity. For the Brownian motion, the small particles move quickly in a liquid, while large particles move slowly. So the rates of intensity fluctuations are quicker for small particles than larger ones. The correlations are created between the signals of the intensity at a specific time (t) and the randomly fluctuating signal after the sample time ( $\tau$ ) of the correlator in the Zetasizer setup (at time equals to  $t + \tau$ ).

For a large number of monodisperse particles in Brownian motion, the correlation function is given by an exponential decay [13]:

$$G(\tau) = A[1 + B \exp(-2\Gamma\tau)] \quad (3.7)$$

where:

A is the baseline of the correlation function

B is the intercept of the correlation function

$$\Gamma = Dq^2$$

where:

D is the translational diffusion coefficient, determined from the measurement of G, with

$$q = (4 \pi n / \lambda_0) \sin (\theta/2) \quad (3.8)$$

where:

n is the refractive index of dispersant

$\lambda_0$  is the wavelength of the laser

$\theta$  is the scattering angle

For polydisperse samples, the equation can be written as [10]:

$$G(\tau) = A[1 + B \cdot (g_1(\tau))^2] \quad (3.9)$$

where:

$g_1(\tau)$  is the sum of all the exponential decays contained in the correlation function.

The relationship between the size of a particle and its speed due to Brownian motion is defined in the Stokes-Einstein equation:

$$d = kT/3\pi\eta D \quad (3.10)$$

where:

$d$  is the diameter of the spheres representing the particles,

$k$  is Boltzmann's constant,

$T$  is the absolute temperature,

$\eta$  is the viscosity of the dispersant.

The particle size measured with DLS is the diameter of the sphere that diffuses at the same speed as the particle being measured. The size distribution obtained is originally a plot of the intensity-size distribution and it can be converted into volume-weighted and number-weighted distribution. This technique is more sensitive to small sizes than bigger ones, since the relative intensity of the scattered light from the big nanoparticles is higher, the intensity-size distribution plot cannot reflect the relative number or volume of the big nanoparticles accurately.

**Electrophoretic light scattering (ELS).** The particles dispersed in the liquid acquire surface charges due to the surface ions or the adsorption of the solvent ions. The ions carrying the opposite charge will be attracted to bind strongly on the surface of the particles, forming the inner Stern layer. An outer, diffuse region where the ions are less firmly attached is also formed, combined with the Stern layer creating a double electrical layer surrounding the particle. The electrical double layer and the particle form a stable entity, the ions inside the layer move together with the particle while the ions outside do not. This boundary is the slipping plane. The potential at this boundary is called zeta potential. An example showing the different potential at different boundaries in the entity as a function of the distance from the charged surface of a particle is shown in **Figure 3.5** [10].

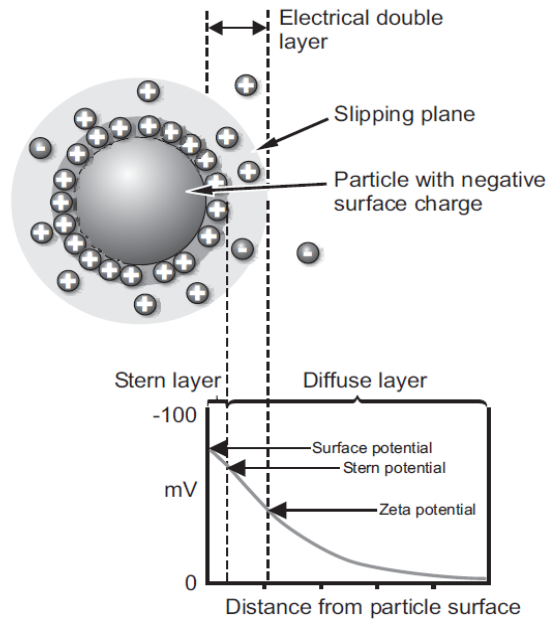


**Figure 3.5:** An example showing the potential difference as a function of the distance from the negatively charged surface of a particle dispersed in a solution.

Zeta potential can be measured using electrophoretic light scattering (ELS), that is to say: when an electric field is applied across the solution containing the charged particles, the charged particles are attracted towards the electrode of opposite charge. Viscous forces acting on the particles tend to oppose to this movement. When equilibrium is reached between these two opposing forces, the particles move with constant velocity, which is commonly referred to as electrophoretic mobility. Zeta potential of the particle can be obtained by applying the Henry equation if the electrophoretic mobility is known:

$$U_e = 2\varepsilon \cdot z \cdot f(Ka) / 3\eta \quad (3.11)$$

where:

$U_e$  is the electrophoretic mobility of the charged particles,

$\varepsilon$  is the dielectric constant of the dispersant,

$z$  is zeta potential of the particles,

$f(Ka)$  is the Henry function (two values are generally used 1.5 or 1.0 for Smoluchowski approximation or Huckel approximation respectively),

$\eta$  is the viscosity of the dispersant.

The Laser Doppler Velocimetry (LDV) technique is used to measure the electrophoretic mobility. As the DLS technique, when the particles are illuminated by a light source, the light is scattered by them. Since the particles move, the frequency of the scattered light will be Doppler

shifted in frequency when compared to the incident light. The electrophoretic mobility ( $U_e$ ) of the particle can be calculated from the Doppler frequency shift:

$$\Delta\nu = 2U_e \cdot \sin(\theta/2)/\lambda \quad (3.12)$$

where:

$\Delta\nu$  is the Doppler shift between the light scattered by the particles in motion,

$\theta$  is the scattering angle of the incident light,

$\lambda$  is the wavelength of the incident light.

Then zeta potential can be calculated from the formula (3.11) and (3.12):

$$z = 3\eta \cdot \lambda \cdot \Delta\nu / 4\epsilon \sin(\theta/2) f(Ka) \quad (3.13)$$

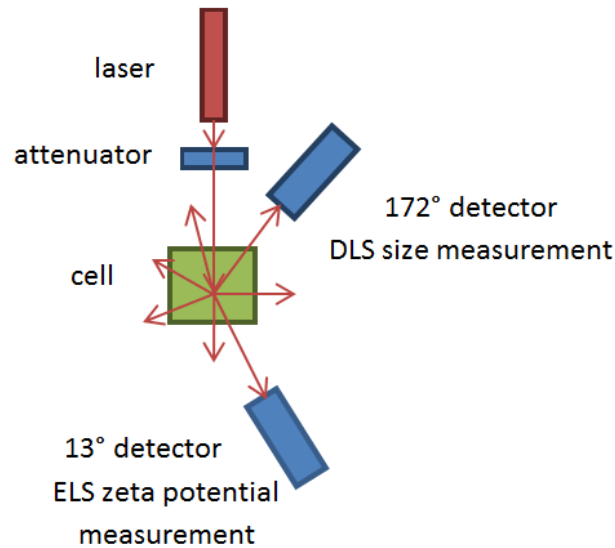


**Figure 3.6:** Schematic diagrams of the operational principles of the DLS and ELS techniques for the size and zeta potential measurements.

Both DLS and ELS measurements were performed using Zetasizer Nano ZS apparatus (Malvern, UK). The schematic diagrams of their operational principles are described in **Figure 3.6**. A laser with the emission wavelength at 633 nm is used as the light source to illuminate the sample particles within a cell. The photodiode detector in 13° (forward scattering) and in 172° (back scattering) geometry are used to detect the scattered light in the zeta potential and size distribution measurement, respectively. To avoid that too much scattered light enters the detector damaging the setup, an “attenuator” is used to reduce the intensity of the laser and hence reduce the intensity of the scattered light. The scattered intensity signal from the detector is then passed

to a correlator. This correlator information is then transmitted to a computer, where the size or zeta-potential information is derived from the measurement.

### 3.2.2. Chemical characterization

Vibrational spectroscopies (Infrared Spectroscopy (IR) and Raman spectroscopy) probe the vibrations of atoms in molecules or solids so as to identify the chemical compositions of the sample. The crystalline structure can also be analyzed from vibrational spectroscopies to a certain extent. The IR spectroscopy measures the absorption spectrum of photons directly, while the Raman spectroscopy measures the inelastic scattering of photons.

#### 3.2.2.1. Fourier Transform Infrared Spectroscopy (FTIR)

Each chemical bond, in solids or molecules, has specific (quantized) vibrational modes. These modes, acting as oscillators, can absorb photons of energy corresponding to the oscillator transition. The absorption spectrum is thus “a picture” of the chemical bonds present in the sample, provided that they are IR active, i.e. having a dipole moment, capable of absorbing the electromagnetic radiation.

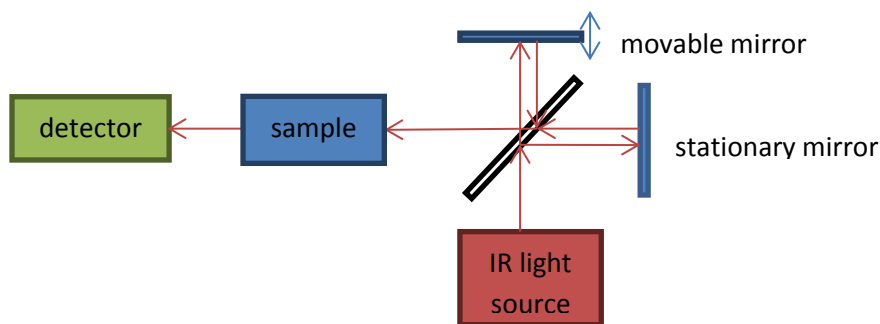


**Figure 3.7:** Schematic diagram of the operational principle of the Michelson interferometer.

IR absorption spectroscopy can be performed using either a monochromatic source or a broad spectrum IR source. Before the incident light arrives at the sample, it is divided by a beam splitter into two light beams and reflected by a stationary and a movable mirror, respectively. The two reflected light beams then recombine and undergo interference which is normally called the Michelson interferometer, as shown in **Figure 3.7**. The recombined light illuminates the studied samples, and the transmitted or deflected light is detected. The transmittance spectrum can be obtained from the collected signal and the interferogram is treated by the Fourier transform. The absorption spectrum can also be converted from the transmittance spectrum using programs integrated in the FTIR instrument.

The method using the broad band IR source has the advantage of being faster and more sensitive than the simpler one using a monochromatic source.

A common Fourier Transform Infrared Spectroscopy (FTIR) is able to cover a long range of electromagnetic spectrum regions: the near-infrared (0.8–2.5  $\mu\text{m}$ ), mid-infrared (2.5–25  $\mu\text{m}$ ) and far infrared (25–1000  $\mu\text{m}$ ). A typical IR spectrum of bulk ZnO is shown in **Figure 3.8** [14]. Metal oxides generally give transmission bands in the fingerprint region below 1000  $\text{cm}^{-1}$ , arising from inter-atomic vibrations [15]. Peaks in the range 400–700  $\text{cm}^{-1}$  have been observed in IR spectra of ZnO and they are attributed to wurzite crystalline Zn-O stretching mode [14, 16].

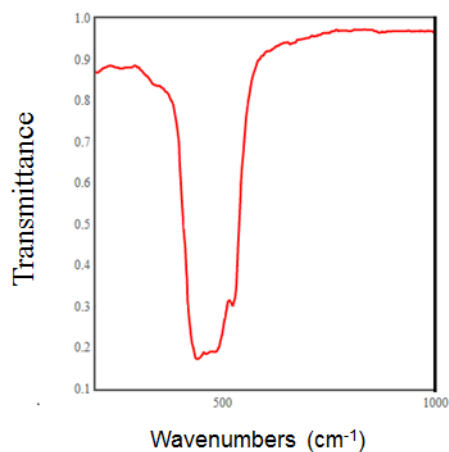


**Figure 3.8:** Typical IR spectrum of bulk ZnO, from [13].

The FTIR measurements were performed by a Vertex 80 (Bruker Optics) apparatus. The mid-infrared (2.5–25  $\mu\text{m}$ ) light source and the transmittance detection mode were used. For measurements, two KBr pellets were used to make an ultra-thin film of the ZnO sample powder.

#### 3.2.2.2. Raman spectroscopy

In general the strong bands in the IR spectrum of a compound correspond to weak bands in the Raman spectrum and vice versa. This complimentary nature is due to the electrical properties of the vibration. If a bond is strongly polarized, a small change in its length occurs during a vibration and will have a limited effect on the polarization. Vibrations involving polar bonds (C-O, N-O, O-H) are therefore comparatively weak Raman scatterers. Such polarized bonds, however, carry their charges during the vibrational motion, (unless neutralized by symmetry factors), which results in a large net dipole moment change and produce strong IR absorption band. Conversely, relatively neutral bonds (C-C, C-H, C=C) undergo large changes in the polarizability during a vibration. But the dipole moment is not affected in the same manner. Vibrations that predominantly involve relatively neutral bond are strong Raman scatterers, but weak in the IR. The IR spectroscopy is active when there exists a molecule dipole change, while the Raman spectroscopy is active when the polarization of the molecule changes. Raman scattering is thus highly sensitive to the symmetry of the crystal network. It can give complementary information on the samples, besides the IR spectroscopy.

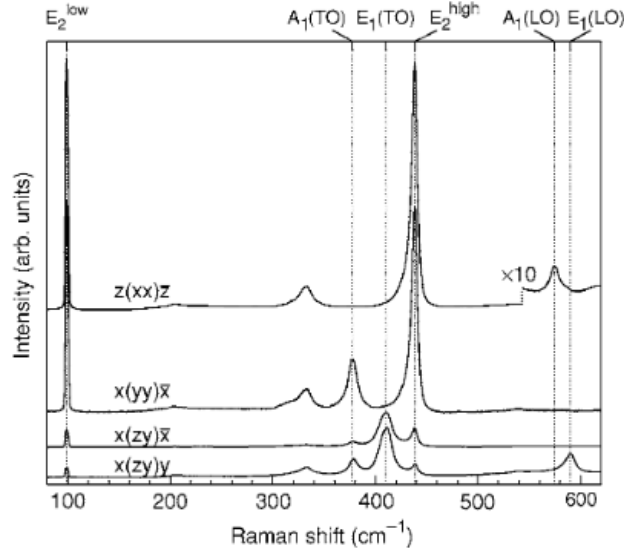


**Figure 3.9:** Room temperature first-order Raman spectra of wurtzite ZnO in different experimental configurations and allowed optical phonon modes, from [16].

**Table 3.1:** Optical phonon modes and their corresponding Raman shift, from [16].

Optical phonon modes	Raman shift (cm <sup>-1</sup> )
E <sub>2</sub> (low)	99
A <sub>1</sub> (TO)	378
E <sub>1</sub> (TO)	410
E <sub>2</sub> (high)	438
A <sub>1</sub> (LO)	574
E <sub>1</sub> (LO)	590
E <sub>2</sub> (high)- E <sub>2</sub> (low)	330

When the sample is excited by a laser, scattering will occur. Two kinds of scattering can be distinguished: the Rayleigh scattering and Raman scattering. For Rayleigh scattering, the scattering light has the same frequency as the incident one, as the elastic interaction happens between the incident photons and the atoms in the sample system. On the contrary, for the Raman scattering, the energy of the scattered light is different from the incident one. If the light beam loses energy during the interaction, the phenomenon is called Stokes scattering, whereas it is referred to as anti-Stokes scattering in the inverse case. The difference between the scattered and incident light can be used to identify the sample in terms of the characteristic vibrational modes. A typical Raman spectrum of bulk ZnO is presented in **Figure 3.9** [17]. The Raman peaks and the corresponding vibration modes are listed in **Table 3.1**.

The Raman spectroscopy measurements were performed using a Raman spectrometer (Raman Thermo-Fisher DXR) with the laser excitation at 532 nm and intensity of 10 mW, at the CECOMO platform of the University Lyon 1.

### 3.2.2.3. Nuclear reaction analysis

The Nuclear reaction analysis (NRA) is an effective method for the detection of the concentration and depth profile of light elements in a heavy matrix. When an energetic particle (typically protons or alpha particles) hits a nucleus of a target element, depending on the mass of the particle and target element and the energy of the particle, a variety of final products may be formed. Rutherford Backscattering Spectrometry (RBS) corresponds to the case where the reaction products are the same in type and energy as those before reaction (elastic scattering). In cases where the incident beam energy exceeds a certain threshold value, other energetic particles appear in the spectrum. This case corresponds to the NRA. The detection of these particles usually provides information about the elements in the sample. The NRA can detect light elements which are inaccessible to RBS analysis.

The content of lithium (Li) in some of the studied samples was investigated using the nuclear reaction analysis (NRA) based on the nuclear reaction of  ${}^7\text{Li} (p, \alpha) \alpha$ . A proton beam with 1.5 MeV energy was used and the quantity of the formed  $\alpha$  particles was measured to determine the Li content in the samples. The sensitivity is limited when the element concentration is below 0.5 %.

### 3.2.3. Optical characterization

#### 3.2.3.1. Photoluminescence spectroscopy

Photoluminescence (PL) is a process in which a material absorbs photons and then re-emits photons. The material is irradiated by an external light source and if the excitation energy is higher than the bandgap of the material, the electrons originally in the valence band have the opportunity to transit to a higher energy level situated in the conduction band, leaving a hole in the valence band, so that an electron-hole pair is formed. This electron will then de-excite to the ground state and recombine with the hole, emitting a photon through de-excitation which might be also accompanied by the emission of heat, as shown in the **Figure 3.10**, or lead to a non-radiative de-excitation from defect energy levels.

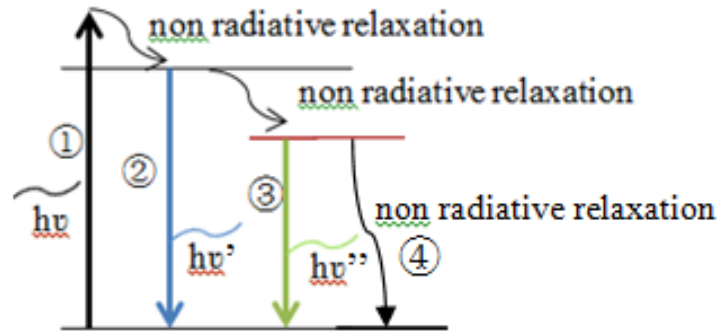


**Figure 3.10:** The process of the photoluminescence (PL) including the above bandgap absorption ①, band edge PL ②, defect or impurity related PL ③ and non radiative recombination ④, under the excitation with energy higher than the bandgap.

#### 3.2.3.1.1. Steady-state photoluminescence spectroscopy

From the steady-state PL spectrum measurements, the emission features of materials can be characterized. As mentioned in Chapter 2, in ZnO bulk material, we can expect two bands in the steady-state PL spectrum: one band at about 380 nm due to the band edge emission and another wide band located in the visible range, from blue to IR spectral range due to the defects or impurities. The position and intensity of the emission band in the visible spectral range are usually used to evaluate the nature and intensity of the intrinsic defects or impurities in the materials. From the steady-state PL spectrum the ratio of the intensities of the visible and UV emission is readily obtained. This is a usual way to estimate the crystalline quality of ZnO. In our case, it is a tool to estimate whether the down-shifting effect is efficient, since we want to maximize the visible emission to the detriment of the UV one. As the steady-state PL spectroscopy is a qualitative technique, the ratio is only indicative and is meant to give a hint about which ZnO nanoparticles could be the most efficient down-shifter.

The steady-state photoluminescence (PL) experiments at room temperature were performed in the preliminary studies with a continuous wave frequency doubled argon laser operating at 244 nm (Lexel 95 SHG). The PL signal of ZnO NPs was dispersed using a Jobin–Yvon HR 640 monochromator and then detected with a GaAs (Hamamatsu H5701–50) photomultiplier tube. The PL setup is shown in **Figure 3.11**. Afterwards, the experimental setup was modified and the PL measurement has been carried out with a continuous laser excitation at 266 nm (1.2 mW, Crylas FQCW 266-10). The emission from the nanoparticles was collected by an optic fiber located close to the sample, dispersed by a spectrometer (iHR Triax 320 Jobin-Yvon) and detected by a liquid-nitrogen cooled Si CCD detector. In all cases the spectra were corrected from the spectral response of the system and normalized to their maximum.

With our UV laser operating at 266 nm, only a thin layer of NPs is probed. In a bulk ZnO, the absorption coefficient at 266 nm is about  $2 \cdot 10^5 \text{ cm}^{-1}$ . Thus most of the light is absorbed in the top 100 nm layer.

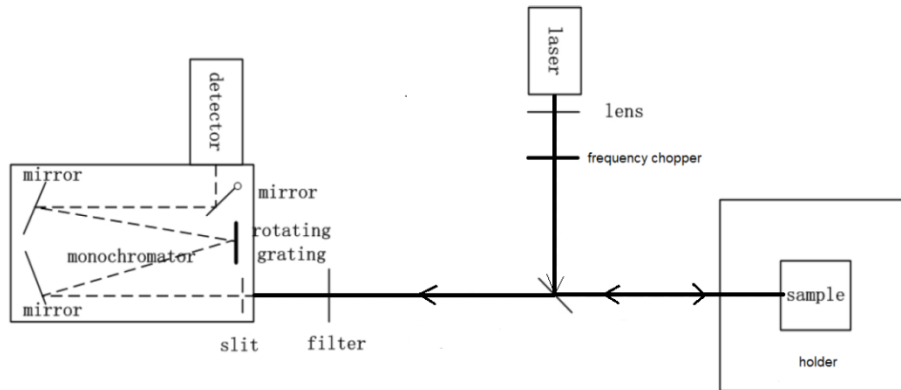


**Figure 3.11:** Schematic diagram of the setup for the steady-state PL measurement.

The steady-state PL spectrum of bulk ZnO has two distinct peaks with the excitonic one in UV range at around 380 nm and the other wide emission band in the visible range from blue to infrared. One example of the PL spectrum of bulk ZnO is shown in **Figure 3.12** [18].

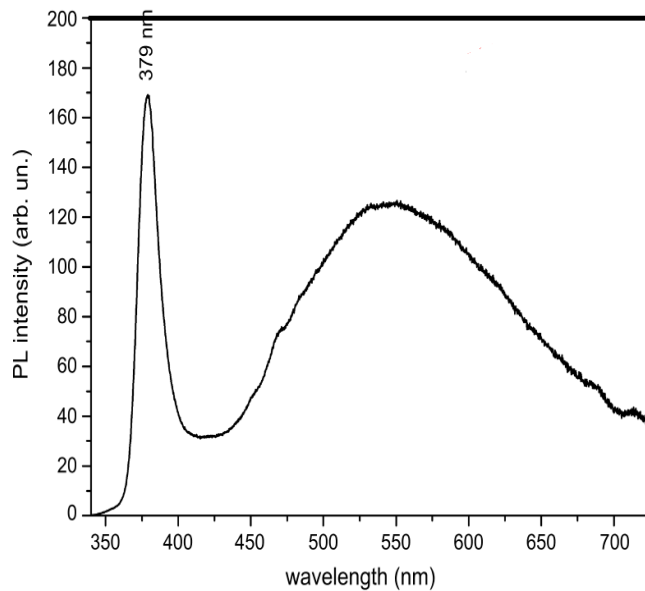


**Figure 122:** PL spectrum of bulk ZnO [18].

### 3.2.3.1.2. Photoluminescence excitation spectroscopy

Photoluminescence excitation (PLE) is a specific type of photoluminescence used for characterization of the optical transitions in materials. In this process, the wavelength of the

emitted radiation is set and the excitation wavelength is scanned. The PLE thus provides the information about the resonant excitation paths corresponding to the considered emission.

In this work, we have used two setups to measure the PLE spectra. In the first method, the PL setup described above (**Figure 3.11**) was used. A continuous xenon white light lamp was used as the light source. The light wavelength was monitored by a Jobin–Yvon HR 640 monochromator. The monochromatic light was varied from 350–400 nm with the step of 2 nm. The emission in the spectral range of 400–800 nm was collected by an optic fiber located near the sample, dispersed by a spectrometer (iHR Triax 320 Jobin-Yvon) with a grating groove density of 600 lines/mm and detected by a liquid-nitrogen cooled Si CCD detector. The spectra were corrected from the spectral response of the system and the integrated area under the emission profile was plotted with the excitation wavelength to obtain the PLE spectra at room temperature. In the second setup, a FLS920 Series fluorescence spectrometer (Edinburgh Instruments, Livingston, UK) was used to measure the PLE spectra. A 450-W Xe900 continuous xenon arc lamp with spectral range varying from 280 to 450 nm with the interval of 1 nm was used as the excitation source. The excitation beam light was dispersed by a single-grating monochromator blazed at 500 nm. All spectra were corrected automatically by the transfer function of the instrument. The wavelength of the emission maximum intensity was chosen as the detection wavelength. The emission intensity at this specific wavelength was plotted as a function of the excitation wavelength to obtain the PLE spectra. The temperature was varied using a Peltier module between 303 and 383 K.

A commonly obtained PLE spectrum of ZnO nanoparticles is shown in **Figure 3.13**. The peak around 340 nm could be attributed to the bandgap of ZnO nanoparticles [19].

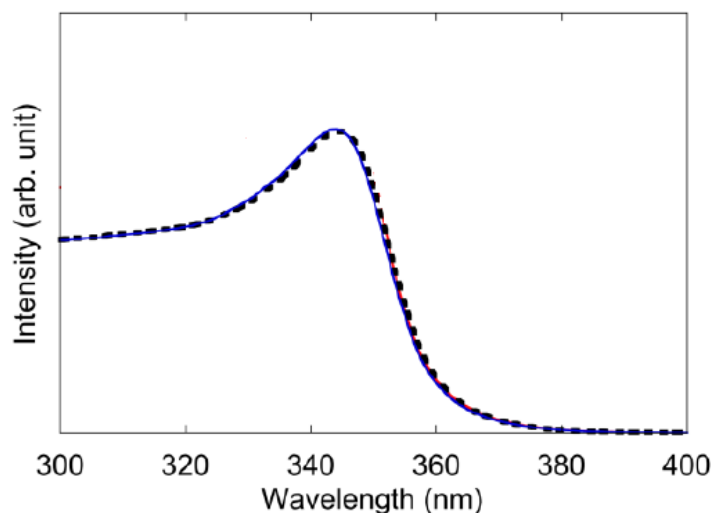


**Figure 133:** PLE spectra of ZnO nanoparticle solution with an emission wavelength of 500 nm [19]. Black dotted line: polymer was not added to the solution. Blue solid line: Polyethylene glycol (PEG) was added after synthesis.

## 3.2.3.1.3. Time Resolved Photoluminescence (TRPL)

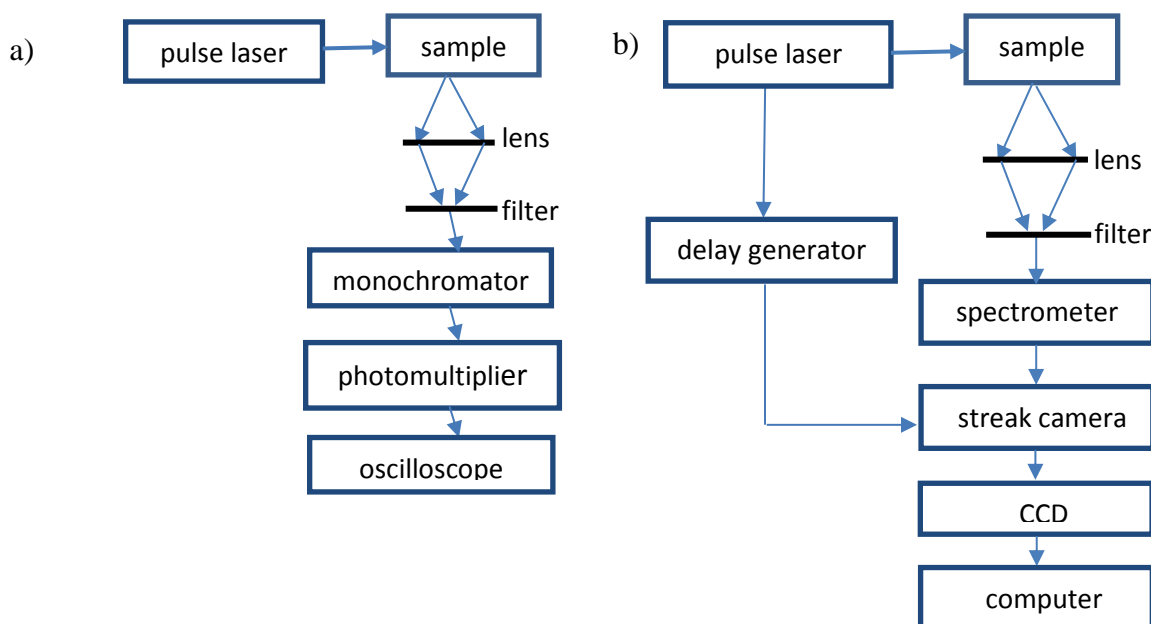


**Figure 3.14:** Schematic diagrams of the TRPL measurement setup using the (a) real-time photoluminescence and (b) streak-camera-based measurement.

The dynamics of the light emission decay is an important parameter, since it provides information on the nature of the radiative channels as well as the non-radiative ones. The TRPL consists in exciting the material with a pulsed light source and measuring the subsequent PL decay in function of time. The characteristic charge carrier lifetime is highly dependent on the nature and size of the studied materials and the interfaces involved. Furthermore, surface effects, passivation and the energy transfer efficiency of sensitizers as well as the presence of dopants, impurities and defect sites can introduce significant variations of this parameter. Depending on the experimental conditions, the mechanisms that determine the charge carrier dynamics within a particular system can be characterized directly by the TRPL down to the sub-nanosecond time scale. The decay time components can be determined for a specific wavelength of emission from the TRPL spectra, providing details concerning the specific de-excitation channels.

There are many techniques to measure the TRPL spectra: real time photoluminescence, time-correlated single photon counting, multi-channel scaler/photon counter, streak-camera measurement and so on. In this work, real time photoluminescence and streak-camera based measurement was used to measure TRPL spectra. The schematic diagrams of both setups are shown in **Figure 3.14** (a) and (b), respectively. For the real time photoluminescence measurement, a laser emitting at 266 nm (10 mW average power with 10 ns pulse duration and 20 Hz repetition rate) was used as the excitation source. A 385 nm filter was used to remove the laser signal. The PL signal of ZnO NPs was dispersed using a Jobin–Yvon HR 640 monochromator and then detected with a GaAs (Hamamatsu H8567–03) photomultiplier tube. This photomultiplier was chosen because it gave a fast and direct output. The TRPL spectra were

then collected and plotted by the oscilloscope (LeCroy Wavepro 954) with a temporal resolution of 500 ps. For the streak-camera measurement, a pulsed laser emitting at 343 nm (with 300 ps pulse duration and 50 MHz repetition rate) was used. The time-resolved photoluminescence of the samples were analyzed by a synchronized streak camera with a temporal resolution of 20 ps and maximum detection time of 2000 ps and collected by a liquid nitrogen cooled CCD camera.

An example of the TRPL spectrum of ZnO nanoparticles is shown in **Figure 3.15** [20].

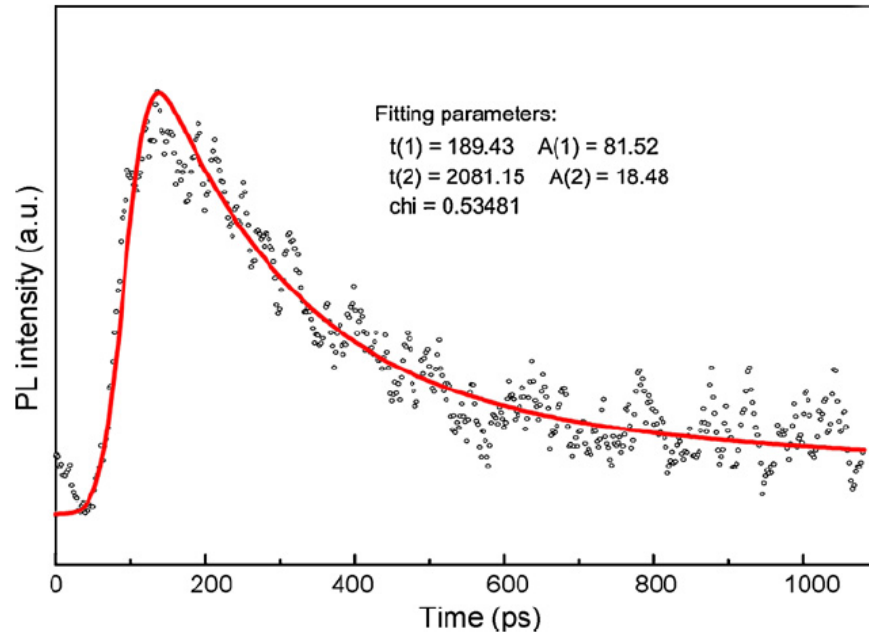


**Figure 155:** Time decay curve of 40 nm ZnO nanoparticles [20].

In general, the de-excitation behavior of an excited charge carrier population in a given material can be described by the rate equation:

$$dN/dt = G(t) - N/\tau \quad (3.14)$$

where,

$N$  is the population density of the excited state,

$G$  is an arbitrary function of the time, describing the temporal evolution of the excitation,

$\tau$  is the lifetime or time constant of all the de-excitation processes which is defined as the time it takes for the population density to decay to  $1/e$  of the original value. The decay rate  $1/\tau$  can be decomposed into the sum of decay rates of independent phenomena, such as radiative and non-radiative processes, according to:

$$1/\tau = 1/\tau_r + 1/\tau_{nr} \quad (3.15)$$

where,

$\tau_r$  is the time constant of the radiative de-excitation process,

$\tau_{nr}$  is the time constant of the non-radiative de-excitation process.

When the excitation is stopped at  $t = 0$ , i.e.  $G = 0$ , equation (3.14) becomes

$$dN/dt = - N/\tau \quad (3.16)$$

Integrating equation (3.16), it can be obtained that:

$$N(t) = N^0 \cdot e^{-t/\tau} \quad (3.17)$$

The intensity of the photoluminescence can be written as:

$$I(t) = (1/\tau_r) \cdot N^0 \cdot e^{-t/\tau} \quad (3.18)$$

The photoluminescence quantum yield (PL QY, the intensity ratio of the emitted photons to the absorbed photons) of the material can be determined by the time constants:

$$PL\ QY = \frac{1/\tau_r}{1/\tau_r + 1/\tau_{nr}} \quad (3.19)$$

When there are defect or impurity energy levels in the bandgap of the materials, the number of the decay rates will increase, corresponding to the number of these energy levels. The decay time constants are normally determined by fitting the TRPL spectra with exponential decay equations, with a model containing an appropriate number of components.

### 3.2.3.2. Quantum efficiency

For the materials, the photoluminescence quantum yield (PL QY) is used to evaluate the quality. It determines the capacity of an exciton to relax via radiative routes, i.e. to emit light. For the solar cells, the external quantum efficiency (EQE) determines the conversion capacity of solar light to electricity.

#### 3.2.3.2.1. Photoluminescence quantum yield

The PL spectra deliver information about the collected fraction of light emitted by the material, and give a qualitative analysis of the emission properties of the sample. However, the PL does not give much information about the non-radiative relaxation routes, they just measure the radiative emission.

The measurement of the absolute quantum yield is valid to probe the down-shifting efficiency. The photoluminescence quantum yield (PL QY) is defined as the ratio of the number of emitted photons to the number of absorbed photons (PL QY = Number of emitted photons / Number of absorbed photons). Usually, there are two ways to measure the PL QY: the

comparative method and the absolute method. The comparative method is based on the comparison between the studied sample and a reference sample with a known PL QY. The integrated absorption and emission signals of the reference are measured and compared with the signals of the studied sample under the same conditions. The PL QY value is then calculated as follows:

$$PL\ QY_s = PL\ QY_r \cdot \frac{(I_e/I_a)_s}{(I_e/I_a)_r} \quad (3.20)$$

where,

$PL\ QY_s$  is the PL QY of the studied sample,

$PL\ QY_r$  is the PL QY of the reference sample with the known PL QY,

$(I_e/I_a)_s$  is the intensity ratio of the measured emission and the absorption of the studied sample,

$(I_e/I_a)_r$  is the intensity ratio of the measured emission and the absorption of the reference sample under the same conditions as the measurement of the studied sample.

The absolute measurement of the PL QY consists in measuring the emission and absorption signals directly using an integrating sphere. According to de Mello *et al.* [21], the PL QY can be measured as shown in **Figure 3.16**.

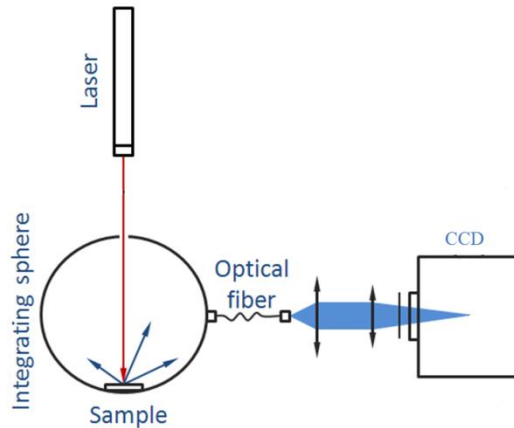


**Figure 3.16:** Schematic diagram of the PL QY measurement setup.

The measurement is made in three steps: first, the measurement is done without a sample, with the area under the laser profile referred as  $L_a$ ; second, the measurement is done with the sample present inside the sphere, but the incident laser does not shine on the sample directly, with the area under the laser profile referred as  $L_b$  and the area under the emission profile referred as  $P_b$ ; third, the measurement is also made with sample and the laser shines on the sample directly, with the area under the laser profile referred as  $L_c$  and the area under the emission profile referred

as  $P_c$ . Thus, the absorption can be determined using the equation ( $\text{absorption} = 1 - L_c / L_b$ ) while the PL QY can be determined using the equation ( $\text{PL QY} = (P_c - (1 - A) \cdot P_b) / L_a \cdot \text{absorption}$ ).

In our case, the two step procedure (the first and the third one) is valid, since the impact of the sample on the reflectance of the sphere is negligible. The absorption intensity is determined by the difference of the integrated area at the laser excitation wavelength without and with the sample in the integrating sphere. The emission intensity is determined by the integration of the area of the photoluminescent emission spectrum. The laser power is measured using a wattmeter, and subsequently sent in the integrating sphere without any sample and detected for a short period of time. As the laser power and detection time are known, their product gives the laser energy. Thus, the relationship between the integration area at the laser excitation wavelength and the laser energy can be established. The reflectance of the integrating sphere depends on the wavelength. Normally, a white lamp of known and calibrated spectrum is used to determine it. This parameter is necessary to get the transfer function of the measurement set up. Here, since we did not possess the required calibrated white lamp, we have used three lasers: a UV laser (266 nm), a green laser (532 nm) and a red laser (632.8 nm) to obtain three correction factors. The correction factor is obtained by dividing the integrated area at the excitation wavelength by the laser energy. This procedure not only takes into account the spectral response of the integrating sphere at the specific wavelength, but also considers the influence of the components in the measurement setup (the loss of the light from the reflection at the entrance of the integrating sphere, at the entrance of the optical fiber and the CCD). The absorption intensity is corrected by the correction factor at 266 nm. The emission intensity is divided into three parts: 360-457 nm, corrected by the correction factor  $1.96 \times 10^8$  counts/J at 266 nm; 457-600 nm, corrected by the correction factor  $2.27 \times 10^8$  counts/J at 532 nm and 600-723 nm, corrected by the correction factor  $1.35 \times 10^8$  counts/J at 632.8 nm. The PL QY is the ratio of numbers of the emitted to absorbed photons, but the collected signal intensity is calibrated in energy. Since the photon energy is:

$$E = hv = hc/\lambda \quad (3.21)$$

the number of photons corresponding to the collected intensity  $I$  is readily written as:

$$N = I/E = I \cdot \lambda / hc \quad (3.22)$$

where,

$E$  is the energy of one photon,

$h$  is Planck's constant,  $6.626 \times 10^{-34}$  J·s,

$\nu$  is the frequency of the photon,

$c$  is the speed of light,  $2.998 \times 10^8$  m/s,

$\lambda$  is the wavelength of the photon,

I is the intensity of the detected light in energy,

N is the number of photons.

From **Equation (3.22)**, the PL QY can be written as:

$$\text{PL QY} = N_{em}/N_{ab} = \frac{I_{em} \cdot \lambda_{em}/hc}{I_{ab} \cdot \lambda_{ab}/hc} = \frac{I_{em} \cdot \lambda_{em}}{I_{ab} \cdot \lambda_{ab}} \quad (3.23)$$

where,

$N_{em}$  is the number of the emitted photons,

$N_{ab}$  is the number of the absorbed photons,

$I_{em}$  is the detected intensity of the PL emission of the sample expressed in energy,

$I_{ab}$  is the detected intensity of the absorption of the sample expressed in energy,

$\lambda_{em}$  is the wavelength of the emitted photons,

$\lambda_{ab}$  is the wavelength of the absorbed photons.

In (3.23),  $I_{em}$  and  $I_{ab}$  are measured directly and converted into energy using the different correction factors.  $\lambda_{ab}$  is the excitation wavelength (266 nm). For  $\lambda_{em}$ , as the calibration is done in three parts, the calculation is also divided into three parts, correspondingly. The integration of the product of the intensity and wavelength is also done in these three regions of the emission spectrum, respectively and divided by the product of the intensity and wavelength of the laser.

The PL QY was measured using an integrating sphere RTC-060-SF (Labsphere Company) and the same excitation and detection set up as for the PL measurements. The emission from the nanoparticles was collected by an optic fiber, dispersed by a spectrometer (iHR Triax 320 Jobin-Yvon) and detected by a liquid nitrogen-cooled Si CCD detector. The accuracy of this measurement is about 5 % [17].

#### 3.2.3.2.2. External quantum efficiency of solar cells

The external quantum efficiency (EQE) of a photosensitive device is the ratio of the number of charge carriers collected in an external circuit to the number of photons of a given energy shining onto the device photoactive surface (incident photons). From this measurement we can infer how good the solar cell is at converting sun-light to electricity for each wavelength range. In this work, our aim is to make the best use of UV light and to convert it into visible light, so we want to enhance the UV light part of the EQE of a solar cell and to maintain a high value of the EQE in the visible part of the spectrum.

In order to perform EQE measurements, we have first used commercially available photodiodes to replace solar cells, as these photodiodes can be quickly obtained in large

quantities and are more suitable for preliminary experiments. Their active surface is smaller, which permitted us to make more easily ZnO NPs depositions by LECBD method. LECBD gives circular layer of about 1 cm in diameter and the layer thickness can be considered as homogeneous over about 0.5 cm. We have used two different commercial Si photodiodes from Hamamatsu, on which the ZnO NPs were subsequently deposited by the LECBD. The first type of Si photodiodes has a high UV sensitivity and its quantum efficiency is of about 50 %, in the 370–400 nm spectral range before the ZnO layer deposition on their surface (Si photodiode series 1227 and 1337). The second type of photodiodes has much lower sensitivity in the UV (about 8 %), and their spectral response is high from 480 to 660 nm, with a peak sensitivity wavelength at 550 nm before the ZnO layer deposition (Si photodiode S7686). In parallel, we have completed this preliminary study by testing the effect of the ZnO NPs layer on a real monocrystalline Si solar cell with an antireflective SiN<sub>x</sub> layer on its top.

The EQE measurements were performed at room temperature and a xenon lamp was used as a light source. The lamp light was sent through a monochromator in order to choose a given excitation wavelength. The Oriel EQE measurement system operating in an AC chopped mode permitted the measurement of the spectral response of the photosensitive device in the UV-NIR spectral range. The reference input was used to compensate for the source drift and used to measure the photocurrent delivered by the photodetector under light illumination. The EQE response spectra were corrected from the spectral response of the system using a reference monocrystalline solar cell. The photocurrent measurements were performed over a large range of excitation wavelengths from 290 nm to 1200 nm. Afterwards, the EQE values were calculated, and we compared the EQE of each device before and after the deposition of the ZnO NPs layer on its top. It was used to estimate if there was an enhancement of the EQE in the UV/visible part of the spectrum via the down-shifting effect or in near IR spectral zone via the antireflection effect.

### 3.3. Conclusions

In this chapter, two different synthesis approaches of ZnO nanoparticles have been described. First, the purely physical fabrication method of ZnO nanoparticles, the so called Low Energy Cluster Beam Deposition (LECBD) was presented. It permits an easy control of the nanoparticle size and stoichiometry. Using LECBD, ZnO nanoparticles can be deposited on any substrate. However, this procedure requires high vacuum and a complex equipment. Moreover, the quantity of obtained nanoparticles is very small and only in the form of a film. The powders cannot be fabricated using this method. Thus, easy and inexpensive chemical methods should be used to produce large quantities of ZnO nanoparticles. Two different chemical methods have been proposed: the co-precipitation method and the hydrolysis method. In chemical methods, the synthesis conditions can be easily modified, so the physical and optical properties of the synthesized nanoparticles can be varied and optimized for the down-shifting applications. For comparison, the commercial ZnO nanoparticles have also been studied.

For the enhancement of visible photoluminescence in ZnO nanoparticles, the synthesis conditions in different chemical synthesis processes have been controlled to optimize the visible photoluminescent efficiency. In LECBD method, the oxygen pressure and the nozzle size have been controlled. In the co-precipitation method, the nature of the precursor, solvent and the alkaline hydroxide have been varied. In the hydrolysis method, the concentration and length of the surfactant and the reaction time have been optimized to increase the visible emission of the synthesized ZnO nanoparticles.

Afterwards, the ZnO nanoparticles produced with LECBD method have been deposited on photodiodes, serving as a preliminary study of the impact of the ZnO NPs film on the Si photodiode efficiency thanks to the down-shifting and the antireflection effect.

The physical, chemical, optical properties of the synthesized ZnO NPs were correlated with the synthesis parameters using the described characterization techniques.

### 3.4. References

1. Zhu Y., Apostoluk A., Liu S. B., Daniele S., Masenelli B., ZnO nanoparticles as a luminescent down-shifting layer for photosensitive devices. *Journal of Semiconductors*, 2013, vol. 34, no. 5, p. 053005/1-6.
2. Saji K. J., Joshy N. V., Jayaraj M. K., Optical emission spectroscopic studies on laser ablated zinc oxide plasma. *Journal of Applied Physics*, 2006, vol. 100, p. 043302/1-5.
3. Ishikawa Y., Shimizu Y., Sasaki T., Koshizaki N., Preparation of zinc oxide nanorods using pulsed laser ablation in water media at high temperature. *Journal of Colloid and Interface Science*, 2006, vol. 300, p. 612–615.
4. Morales-Flores N., Galeazzi R., Rosendo E., Díaz T., Velumani S., Pal U., Morphology control and optical properties of ZnO nanostructures grown by ultrasonic synthesis. *Advances in Nano Research*, 2013, vol. 1, p. 59-70.
5. Baruah S., Dutta J., Hydrothermal growth of ZnO nanostructures. *Science and Technology of Advanced Materials*, 2009, vol. 10, no. 1, p. 013001/1-18.
6. Rania S., Surib P., Shishodiak P. K., Mehra R. M., Synthesis of nanocrystalline ZnO powder via sol–gel route for dye-sensitized solar cells. *Solar Energy Materials & Solar Cells*, 2008, vol. 92, p. 1639–1645.
7. Djurišić A. B., Leung Y. H., Optical properties of ZnO nanostructures. *Small*, 2006, vol. 2, p. 944–961.
8. McCluskey M. D., Jokela S. J., Defects in ZnO. *Journal of Applied Physics*, 2009, vol. 106, 071101/1-13.
9. Perez A., Melinon P., Dupuis V., Bardotti L., Masenelli B., Tournus F., Prevel B., Tuillon-Combes J., Bernstein E., Tamoin A., Blanc N., Tainoff D., Boisron O., Guiraud G., Functional nanostructures from clusters. *International Journal of Nanotechnology*, 2010, vol. 7, p. 523-574.
10. Tainoff D., Masenelli B., Boisron O., Guiraud G., Melinon P., *The Journal of Physical Chemistry C*, 2008, vol. 112, p. 12623-12627.
11. Daniele S., Ghazzal M. N., Hubert-Pfalzgraf L. G., Duchamp C., Guillard C., Ledoux G. Preparations of nano-particles, nano-composites and fibers of ZnO from an amide precursor: photocatalytic decomposition of  $(\text{CH}_3)_2\text{S}_2$  in a continuous flow reactor. *Materials Research Bulletin*, 2006, vol. 41, p. 2210-2218.
12. Akhtar M. J., Ahamed M., Kumar S., Khan M. M., Ahmad J., Alrokayan S. A., Zinc oxide nanoparticles selectively induce apoptosis in human cancer cells through reactive oxygen species. *International Journal of Nanomedicine*, 2012, vol. 7, p. 845-857.
13. Malvern Instruments Technical Support Library, Available online at: <[www.malvern.com](http://www.malvern.com)> (accessed 25.07.2013).
14. WebBook de Chimie NIST (National Institute of Standards and Technology), Available online at <<http://webbook.nist.gov/cgi/cbook.cgi?ID=B6004648&Mask=80#Top>> (accessed 09.06.2015).

15. Kumar H., Rani R., Structural and optical characterization of ZnO nanoparticles synthesized by microemulsion route. *International Letters of Chemistry, Physics and Astronomy*, 2013, vol. 14, p. 26-36.
16. Yuvaraj D., Ra K. N., Optical and electrical properties of ZnO films deposited by activated reactive evaporation. *Vacuum*, 2008, vol. 82, p. 1274-1279.
17. Cuscó R., Alarcón-Lladó E., Ibáñez J., Artús L., Temperature dependence of Raman scattering in ZnO. *Physical Review B*, 2007, vol. 75, p. 165202/1-11.
18. Liu J. Z., Motta N., Lee S., Ultraviolet photodetection of flexible ZnO nanowire sheets in polydimethylsiloxane polymer. *Beilstein Journal of Nanotechnology*, 2012, vol. 3, p. 353-359.
19. Tachikawa S., Noguchi A., Tsuge T., Hara M., Odawara O., Wada H., Optical Properties of ZnO Nanoparticles Capped with Polymers. *Materials*, 2011, vol. 4, p. 1132-1143.
20. Wang X. F., Xie P. B., Zhao F. L., Wang H. Z., Wang Y. M., Spectra of ZnO nanoparticles under low photon energy excitation. *Particuology*, 2009, vol. 7, p. 496-500.
21. De Mello J. C., Wittmann H. F., Friend R. H., An improved experimental determination of external photoluminescence quantum efficiency. *Advanced Materials*, 1997, vol. 9, no. 3, p. 230-232.



## Chapter 4

### Strategies for ZnO nanoparticles with a high PL QY

A variety of physical, chemical and optical properties of ZnO nanoparticles (NPs) can be engineered as a function of the crystalline quality, size, morphologies, surface states, and composition, depending on their synthesis conditions. As it was mentioned in Chapter 2, slight changes in surface states can drastically alter optical behavior of ZnO NPs. The control of size and morphology allows tuning the concentration of defects. Furthermore, the interaction with a surfactant can be in the case of ZnO NPs an important factor permitting to obtain high photoluminescence quantum yield (PL QY).

In this chapter we make a comparison of the properties of ZnO NPs fabricated/synthesized by the different methods presented in Chapter 3: the LECBD method and the sol-gel (chemical) methods, along with the commercially available ZnO NPs. This comparison permits to choose the fabrication method giving ZnO NPs most adapted for the down-shifting process, i.e. having the visible emission as intense as possible compared to the UV emission and a very high PL QY.

In particular, two sol-gel methods have been used: co-precipitation and hydrolysis method. The physical, chemical and optical properties of these NPs have been studied. The effects of the crystalline quality, size, morphology and surface state on the optical properties of ZnO NPs will be presented. Finally, the influence of the surfactants on ZnO NPs optical properties will be described. The role of the confinement of charge carriers at the interface between the nanoparticle and the surfactant and the surface charge will be considered in order to design nanocomposites with specific optical properties.

#### 4.1. ZnO nanoparticles synthesized by LECBD method

At first, we will focus on the ZnO nanoparticles (NPs) synthesized by the LECBD method. One major interest of this deposition method is that, the nanoparticles can be deposited onto any given substrate. Another advantage is that the composition of the synthesized nanoparticles can be adjusted through the control of the partial pressure of O<sub>2</sub> in the plasma. The down-shifting layer consisting of ZnO NPs can be easily fabricated via this method and serve as a preliminary study on the influence of this layer on the solar cell efficiency.

At first, the study has been done on ZnO NPs films on Si substrates. Then a photoluminescent down shifting (LDS) layer made of ZnO NPs has been deposited onto Si solar cells and photodiodes directly, and the solar cells external quantum efficiency (EQE) has been measured and compared with the EQE of a solar cell without the LDS layer.

As we have mentioned in Chapter 3, in the LECBD method the ZnO aggregates are fabricated in the conditions of non-thermodynamic equilibrium, leading to an excess of Zn present in ZnO. The composition of the obtained ZnO NPs fabricated under different oxygen pressures has been examined by the Auger electron spectroscopy (AES) [1]. The AES spectra are presented in **Figure 4.1**. It is observed clearly that, with no oxygen introduction, Zn exists in the aggregates, while the oxidation of nanoparticles occurs with the oxygen introduction, since the characteristic Auger peak of the metallic zinc phase located at 495 eV decreases as the oxygen pressure in the buffer gas increases.

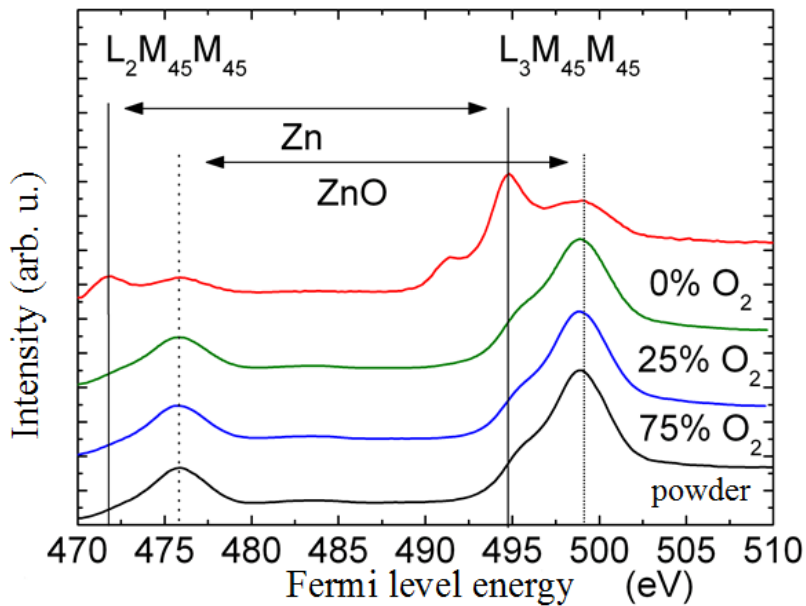


**Figure 4.1:** AES spectra of  $L_3M_{45}M_{45}$  transitions of aggregates of ZnO NPs synthesized by LECBD method with different oxygen pressures during the deposition and the target powder [1].

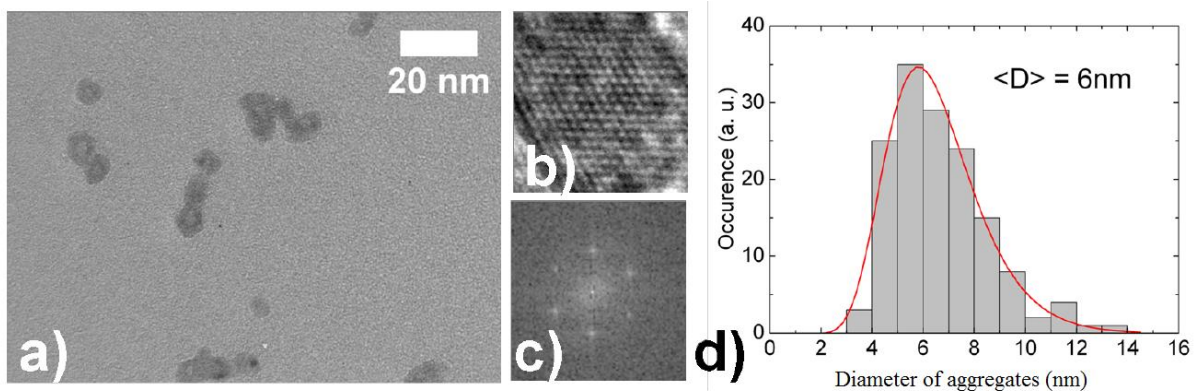


**Figure 4.2:** (a) TEM image of ZnO NPs synthesized by the LECBD method; (b) high-resolution TEM image of a particle; (c) Fourier transform of diffraction patterns taken at high-resolution and (d) size chart for NPs and the lognormal fit [1].

The transmission electron microscopy (TEM) images shown in **Figure 4.2** permit to estimate the size distribution and the crystallinity of the ZnO NPs. At an intermediate magnification, a size histogram has been made, after isolating the particles with a grey level thresholding. Here, this is particularly difficult, partly because of the aggregation of the nanoparticles in larger clusters, and partly because of the inherent low contrast in the low atomic mass of ZnO. For this study, it was considered that the "peanuts" shown in the TEM image in **Figure 4.1** were composed of several nanoparticles. The size distribution obtained from the analysis of more than one hundred NPs follows well the lognormal law with a peak located around 6 nm. The analysis of the Fourier transform of diffraction patterns taken at high resolution also permits to confirm the presence of ZnO nanoparticles well crystallized in the wurtzite phase.

The absorption spectrum of a 300 nm-thick film of ZnO NPs made by the LECBD method is shown in **Figure 4.3**. In the UV range, the absorption is important especially below 350 nm, where the absorption can be higher than 90 %. Thus we can say that ZnO NPs layer meets the basically required criterion for a down-shifting application. However, the absorption remains high (~ 60 %) at 500 nm, which could be detrimental to the down-shifting effect due to the reabsorption (the parasite absorption mentioned in Chapter 1).

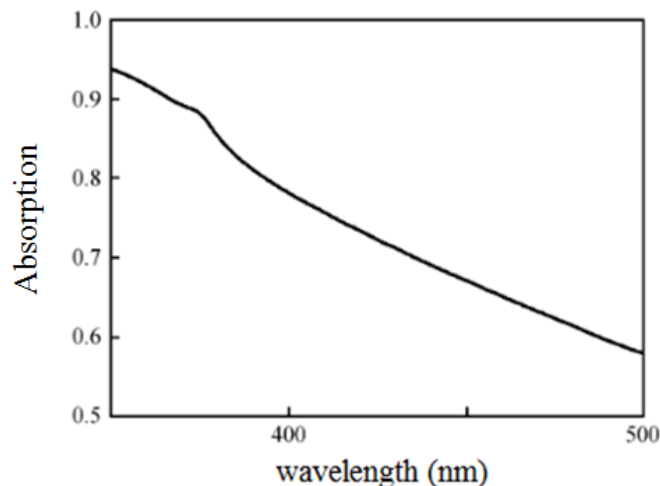


**Figure 4.3:** Absorption spectrum of a 300 nm-thick ZnO NP layer fabricated using the LECBD method.

**Figure 4.4** shows the PL spectra of ZnO NPs fabricated with different fractions of oxygen in the buffer gas. It can be noticed that using LECBD the fabricated ZnO NPs show two main emission bands: the excitonic emission in the UV range and the wide visible emission band. Even with 25 % of oxygen in the plasma which leads to stoichiometric ZnO NPs, the visible emission is still present, though it is weak, indicating that some defects still exist. The visible emission can be controlled through tuning the oxygen pressure in the plasma. Non-stoichiometric ZnO NPs synthesized with low oxygen content in the plasma (6.5 % and 12.5 %) show higher visible emission intensity, as compared to the stoichiometric ZnO NPs (fabricated with 25 % of oxygen

in the plasma). The highest visible emission intensity is attained with 12.5 % oxygen in the plasma. The ratio of visible emission intensity to UV emission intensity reaches 8.2. The PL quantum yield of the optimum ZnO NPs has been measured and calculated to be 0.5 %.

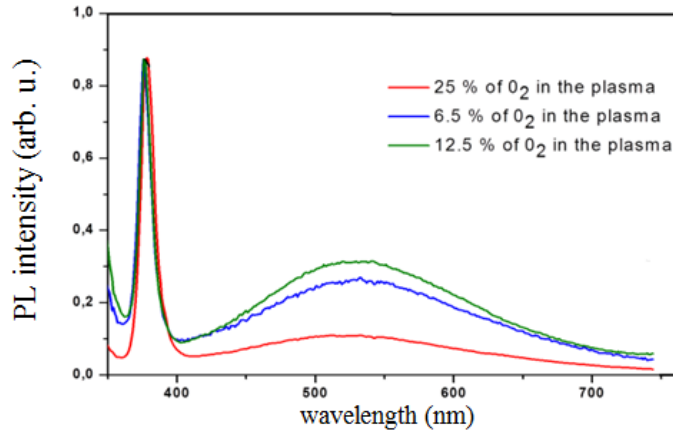


**Figure 4.4:** PL spectra of ZnO NPs fabricated by the LECBD method with different contents of oxygen in the plasma.

In order to confirm that the visible emission originates from the UV light absorbed by the ZnO NPs via the down-shifting effect, we also performed photoluminescence excitation (PLE) experiments on the ZnO NPs. We therefore measured the PL intensity of the visible emission in the range spanning from 400 nm to 800 nm as a function of the excitation wavelength provided by a tungsten (W) lamp. The PLE spectrum is shown in **Figure 4.5**. It is clear that the visible luminescence comes from the photons in the spectral range between 350-370 nm, which confirms the ZnO NPs absorb the UV light and re-emit at longer wavelength via the down-shifting process.

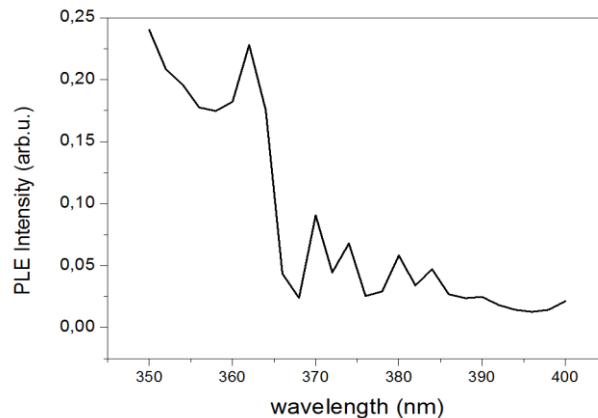


**Figure 4.5:** PLE spectrum of ZnO NPs fabricated by the LECBD method for the emission range from 400 nm to 800 nm.

In order to study the influence of the ZnO NPs layer on the EQE of a photoelectric device, ZnO NPs were deposited directly on two types of Si photodiodes. The results of the external

quantum efficiency (EQE) measurements are given in **Figure 4.6** (a), (b) and (c), respectively. Very thin ZnO NPs layers were deposited (a few nm thick) in order to minimize the parasite visible absorption in them.

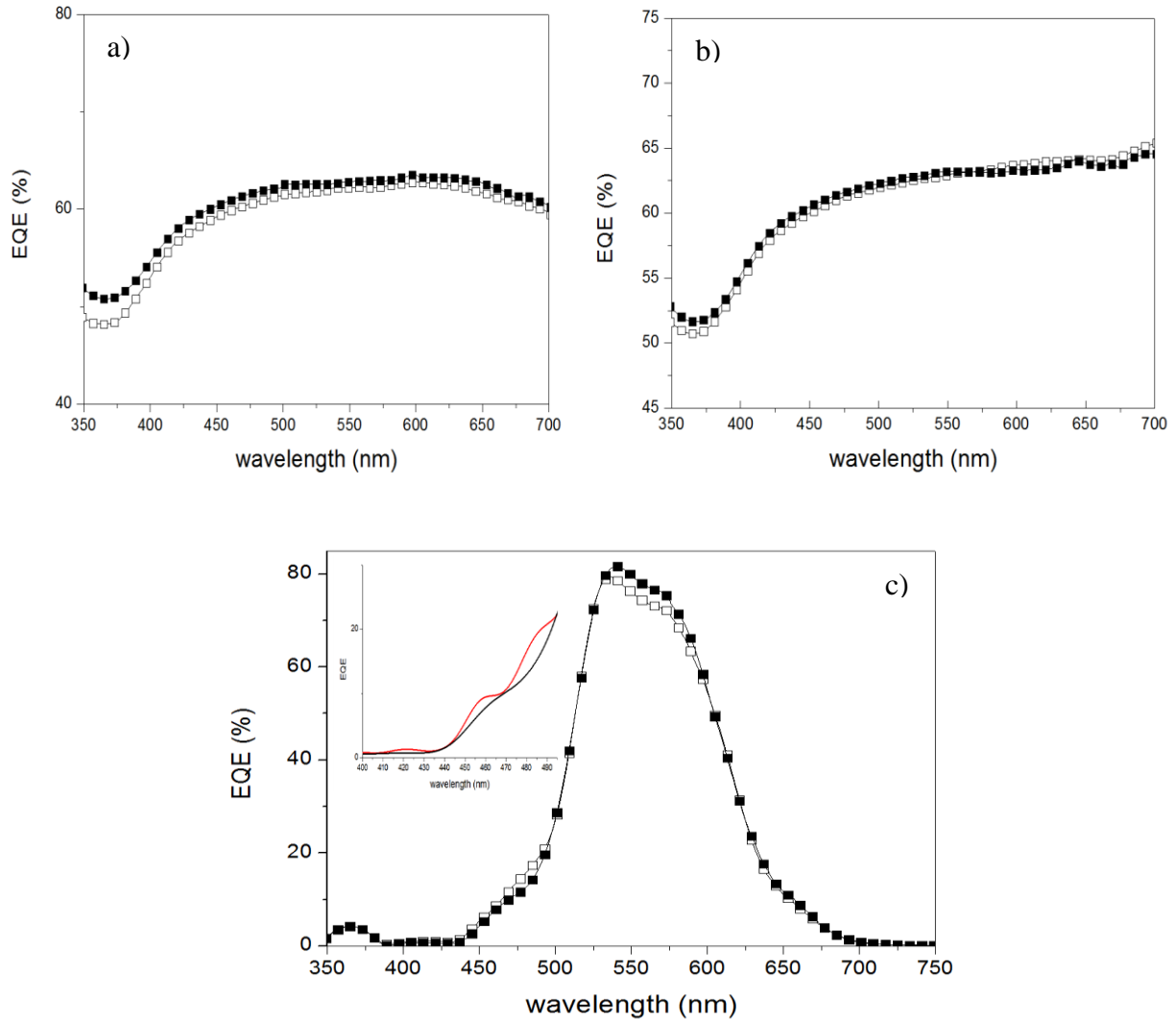


**Figure 4.6:** External quantum efficiency (EQE) of the (a) Si photodiode with initially high quantum efficiency in the UV before (solid squares ■) and after (empty squares □) the 5 nm-thick ZnO layer deposition on the front side of the device; (b) Si photodiode with initially high quantum efficiency in the UV before (solid squares ■) and after (empty squares □) the 10 nm-thick ZnO layer deposition on the front side of the device and (c) Si photodiode with initially low quantum efficiency in the UV before (solid squares ■) and after (empty squares □) the 2 nm-thick ZnO layer deposition on the front side of the device. Inset of (c) is the zoom around 400 nm from (c).

It can be clearly observed in **Figure 4.6** (a) that, for the photodiode with initially high quantum efficiency in the UV, the EQE in the 370-600 nm spectral zone decreases after the 5

nm-thick ZnO NPs layer deposition, while no change is observed for the same type of photodiode when 10 nm of ZnO NPs is deposited (see **Figure 4.6** (b)). On the contrary, a small EQE increase (of about 16.6 %) is observed in the spectral range between 350 and 500 nm for the photodiode with an initial low quantum efficiency in the UV, as presented in **Figure 4.6** (c), after a 2 nm-thick ZnO NP layer deposition.

To explain the observed behavior, it should be mentioned that, there are several key parameters which control the down-shifting efficiency. Two are of prime importance: the first one is the PL QY, the other one is the parasite absorption. As high-energy (UV and blue) photons pass through the ZnO NPs layer, they are absorbed and visible light is emitted via the down-shifting phenomenon. However, as the ZnO layer thickness increases, its transmittance in the visible range decreases. The EQE of the first type of photodiodes is already optimized in the UV and blue spectral range by the UV antireflection coating. Their EQE reaches 50 % (even higher) before the deposition of the ZnO NPs layer by LECBD. After the deposition of the ZnO NPs layer, the reflection and diffusion losses have a negative effect on the EQE of the photodiodes, which is not compensated by the down-shifting effect. As for the second type of Si photodiodes, before the ZnO NPs deposition, their EQE was just about 8 % in the UV spectral range. After we deposited the ZnO NPs layer on the front side of the photodiode, a slight increase of the EQE for wavelengths between 400 nm and 500 nm is seen, as shown in the inset of **Figure 4.6** (c). However, we cannot invoke a pure down-shifting effect to explain it since the absorption of the ZnO NPs layer is not as high as around 400 nm (the absorption spectrum in **Figure 4.3**) and the PL QY of these NPs is very low. We can thus expect some beneficial passive effects resulting from the thickness and morphology of the film. Consequently, to maximize the overall EQE of the whole device, the ZnO NPs layer thickness and morphology on the front side of the photodiode need to be optimized in order to control the reflection losses (and emission in the reverse direction). In parallel, we have completed this preliminary study by testing the effect of the ZnO NPs layer on a real monocrystalline Si solar cell with an antireflective SiN<sub>x</sub> layer on its top. The influence of the LDS layer thickness on the solar cell EQE is shown in **Figure 4.7**.

The effect of the thickness of the ZnO NPs layer on the EQE of the monocrystalline Si solar cell can be seen clearly in **Figure 4.7**. When the thickness is between 0 nm and 2 nm, there is an enhancement of the EQE characteristics. However, this is not the case for the thicker ZnO layers, as when the thickness goes beyond 8 nm, the EQE decreases. As was discussed for the Si photodiodes, this may be due to the reflection and diffusion losses induced by thicker ZnO NPs layers.

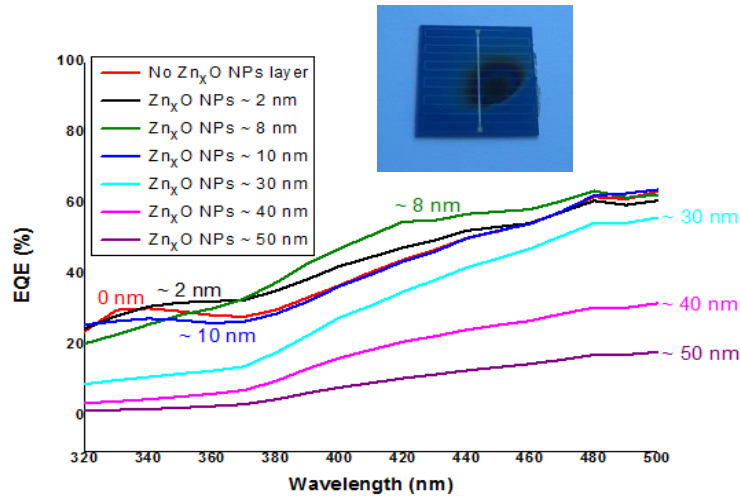


**Figure 4.7:** Spectral response measured on the monocrystalline Si solar cell, before and after the ZnO layer deposition on the front side of the solar cell. The inset is the picture of the solar cell: the black spot is the ZnO NPs deposited layer.

## 4.2. Commercially available ZnO nanoparticles

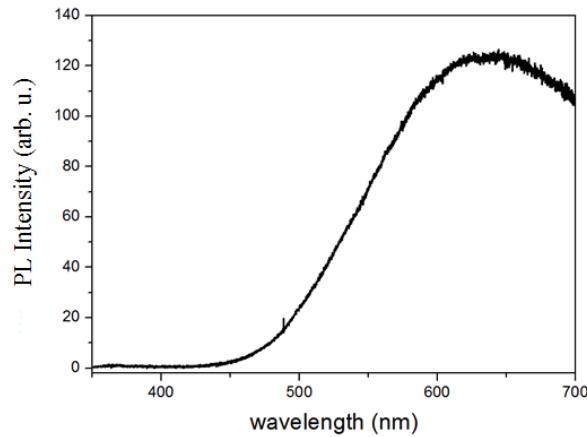


**Figure 4.8:** PL spectrum of commercially available ZnO NPs from Iolitec Company (the excitonic emission is very weak).

The decrease of the EQE of the studied photodiodes when the LDSL is deposited on their top may be caused by another problem: the low visible PL quantum yield of ZnO NPs synthesized by the LECBD method. Thus the solar cell EQE increase through the down-shifting effect induced by the ZnO NPs layer cannot compensate for the negative effect of reflection and diffusion losses. So in order to compare the behavior in terms of the PL QY efficiency, we have bought commercial ZnO NPs from Iolitec Company (Germany). The PL spectrum of these NPs is shown in **Figure 4.8**. The spectrum reveals a broad peak in the visible region between 450 and 700 nm,

which is profitable for the down-shifting, while no UV emission is observed. The PL QY is measured and calculated to be about 1%. Compared to the LECBD method, the visible emission efficiency has been improved, while the UV emission has been quenched. As the provider claims, the ZnO powder is stoichiometric, so we may attribute this PL to different intrinsic defects present in the crystalline structure of the ZnO NPs.

PLE measurement has also been done on the commercial ZnO NPs for the same emission range from 400 nm to 800 nm, and the result is presented in **Figure 4.9**. The PLE spectrum has a high intensity in the spectral range from 350 to 370 nm. It demonstrates that the visible luminescence of commercially available ZnO NPs comes from the photons absorbed in the range between 350-370 nm, confirming that ZnO NPs absorb the UV light and re-emit at longer wavelengths via the down-shifting process.

These commercial ZnO NPs exhibit an interesting emission spectrum, with no excitonic emission and a defect emission in the visible region. However, the PL QY is still low. So we should search other methods of fabrication of ZnO NPs in order to obtain ones with a high PL QY.

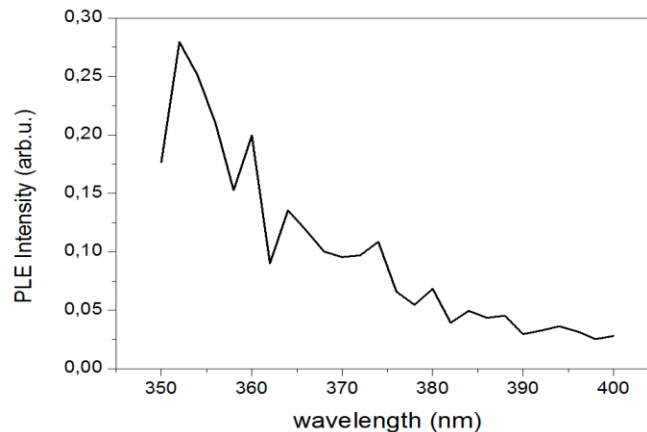


**Figure 4.9:** PLE spectrum of commercially available ZnO NPs (Iolitec, Germany) for the emission range from 400 nm to 800 nm.

### 4.3. Sol-gel methods

To obtain ZnO NPs with a high PL QY, two sol-gel methods were applied: the co-precipitation method and the hydrolysis method. In sol-gel method, the reaction takes place in ambient conditions and the reaction parameters are easy to control, so as to tune the optical properties of synthesized nanoparticles in order to optimize them. Thus, the highest PL QY can be achieved. Moreover, a scalable amount of nanoparticles can be synthesized using the sol-gel methods which are beneficial for the further industrial applications. Here, we first present the research results on the ZnO NPs synthesized with the commonly used co-precipitation method and then on the ZnO NPs synthesized with the hydrolysis method.

## 4.3.1. Co-precipitation method

## 4.3.1.1. Choice of the solvent

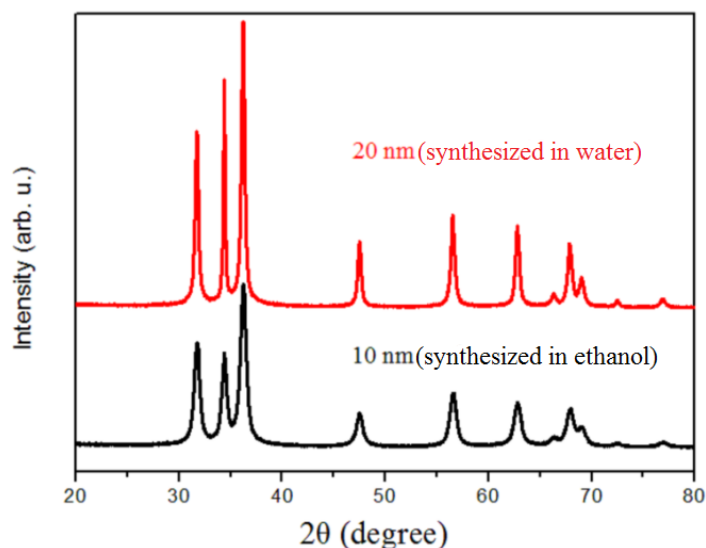


**Figure 4.10:** XRD diffractograms of ZnO NPs synthesized by the co-precipitation of the zinc acetate with KOH (4 KOH/Zn acetate) in ethanol (bottom) and in water (top). The curves are shifted along the y-axis for clarity.

The first parameter to control in the co-precipitation method is the nature of the solvent. We have chosen to investigate the solvent influence in function of its polarity. Therefore, water was used as a polar solvent and ethanol as a non polar one. Our study has proven that, the polarity of the medium impacts the size of the nanoparticles. Hexagonal wurtzite ZnO nanoparticles (JCPDS file no. 04-003-2106) were obtained with mean size increasing from about 10 nm in ethanol to around 20 nm in water, as deduced from the XRD diffractograms in **Figure 4.10**. The PL spectra of ZnO NPs synthesized in water and in ethanol have a similar shape, as can be seen in **Figure 4.11**. Moreover, a similar ratio of visible to UV emission intensity (marked as Vis/UV in **Figure 4.11**) is obtained. The PL QY of both types of ZnO NPs is the same - 2 %. Since water is a cheap and less hazardous product and, as far as industrial applications are concerned, the solvent nature does not make much difference, water has been chosen as the solvent to perform the nanoparticle syntheses in order to study the influence of the natures of the alkaline ion (LiOH or KOH) and the zinc precursor (acetate or sulfate) on the properties of ZnO.

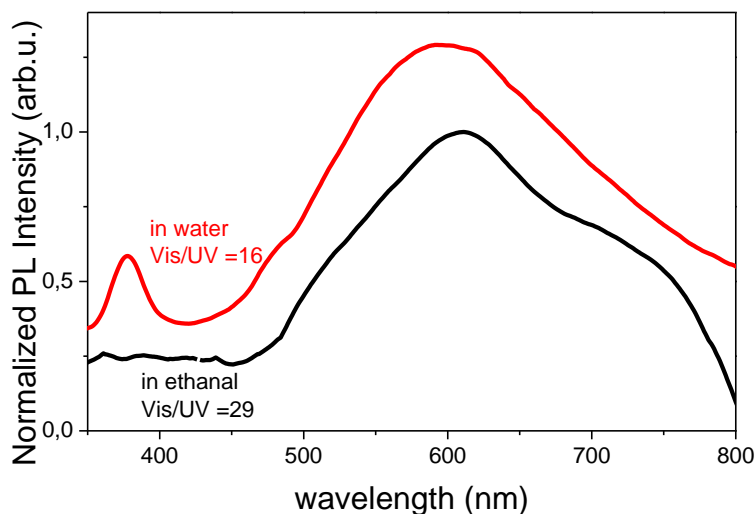


**Figure 4.11:** PL spectra of ZnO NPs synthesized by the co-precipitation of the zinc acetate with KOH (4 KOH/Zn acetate) in ethanol and in water.

#### 4.3.1.2. Crystalline structure characteristics

To study the effect of the alkaline hydroxide on the ZnO NPs, 4 equivalents of both alkaline hydroxide (KOH and LiOH) with respect to both zinc precursors (acetate and sulfate) were used in the co-precipitation synthesis. The XRD diffractograms presented in **Figure 4.12** demonstrate that with both zinc precursors and with both alkaline hydroxide solutions, wurtzite ZnO NPs of a good crystalline quality have been obtained. However, minor additional peaks can be seen in the spectra of ZnO NPs synthesized with LiOH, attributed to the presence of the tetragonal sweetite phase  $\text{Zn}(\text{OH})_2$  (JCPDS file no. 00-38-0356). The ratio between these two phases could not be quantified, since there exists only one file for the sweetite phase and none established structure. The sizes of the crystalline domains of the studied nanoparticles, estimated from the XRD diffractograms, are given in **Table 4.1**.

At this stage, we checked the influence of the quantity of LiOH and KOH used in the reaction on the final ZnO NPs. When reacting with zinc acetate, 2 equivalents of KOH gave mainly oligomeric  $\text{Zn}(\text{OH})_x(\text{OAc})_y$  species, while 2 equivalents of LiOH led to ZnO precipitate. The use of sulfate gave a mixture of wurtzite ZnO and wulffingite  $\text{Zn}(\text{OH})_2$  in a respective ratio 95:5 when reacting with 2 equivalents of LiOH. The estimation of the size of the ZnO crystalline domains using Sherrer's formula is given in **Table 4.1**.

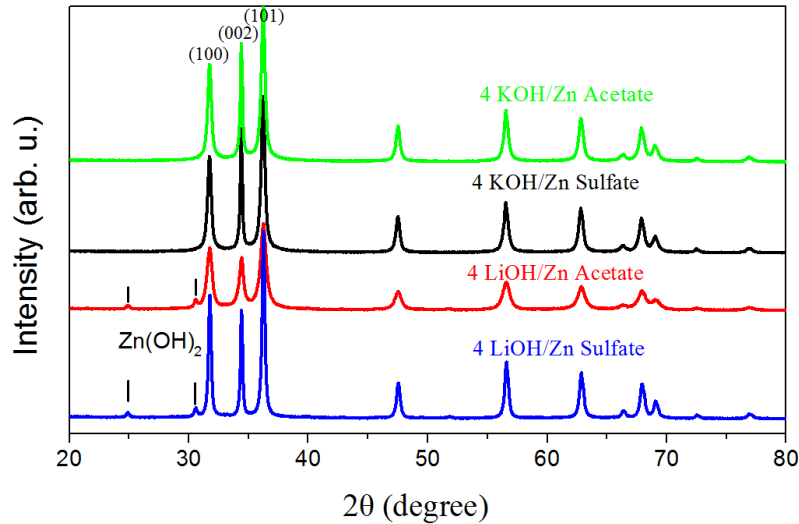


**Figure 4.12:** XRD diffractograms of ZnO NPs powders synthesized by the co-precipitation of the zinc acetate and zinc sulfate with KOH (4 KOH/Zn acetate and 4 KOH/Zn sulfate) and LiOH (4 LiOH/Zn acetate and 4 LiOH/Zn sulfate), from top to bottom. The curves are shifted along the y-axis for clarity.

**Table 4.1:** Estimated ZnO NPs crystalline domain sizes deduced from the XRD diffractograms presented in Figure 4.12.

Precursor	Alkaline hydroxide			
	KOH		LiOH	
	2 eq.	4 eq.	2 eq.	4 eq.
Zinc acetate		20 nm	21 nm	13 nm
Zinc sulfate		20 nm	23 nm	27 nm

As shown in the Raman spectra presented in **Figure 4.13**, with the zinc acetate as the precursor, all the as-prepared ZnO NPs show the typical peaks of the ZnO hexagonal wurtzite structure, located at around  $330\text{ cm}^{-1}$ ,  $385\text{ cm}^{-1}$ ,  $439\text{ cm}^{-1}$  and  $585\text{ cm}^{-1}$ , attributed to multiphonon modes,  $A_1(\text{TO})$  mode,  $E_2^{\text{high}}$  mode and  $E_1(\text{LO})$  mode, respectively [2]. However in the case of 4 LiOH/zinc acetate sample, the intensity of the polar  $A_1(\text{TO})$  mode is increased, when compared to two other curves shown in **Figure 4.13**, indicating the increase of the crystalline disorder.



## 4.3.1.3. Morphology characteristics

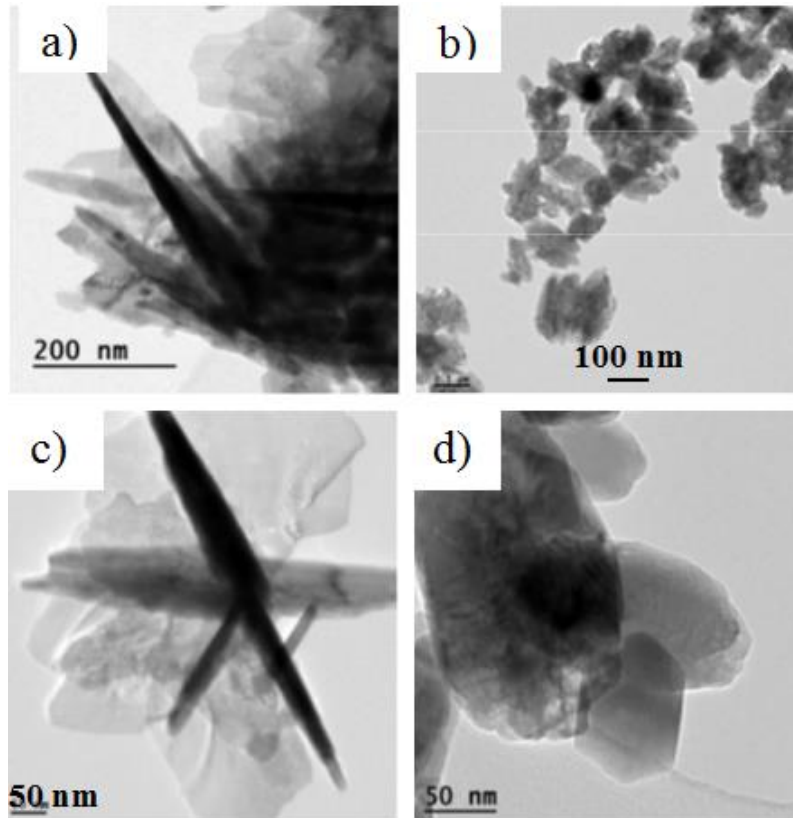


**Figure 4.15:** TEM images of the ZnO nanoparticles synthesized by the co-precipitation of the zinc acetate and the zinc sulfate with: (a) 4 KOH/Zn acetate, (b) 4 LiOH/Zn acetate, (c) 4 KOH/Zn sulfate and (d) 4 LiOH/Zn sulfate.

From TEM images in **Figure 4.15**, it can be noticed that the use of 4 eq. of KOH as the alkaline hydroxide resulted in needle-shaped ZnO NPs, while the use of 4 eq. of LiOH gave nanoplatelets. However, the mean crystalline domain size decreases from 20 nm (KOH) to 13 nm (LiOH) when acetate is used, while it increases from 20 nm (KOH) to 27 nm (LiOH) when sulfate is used. It demonstrates that the  $\text{Li}^+$  ions play a major role in the control of the morphology of ZnO NPs, while the nature of the precursor determines the crystalline domain size. The needle-like shape of particles obtained with KOH can be noticed also on the diffractograms in **Figure 4.12**, for which the contribution of the diffraction from the polar plane (002) is enhanced, as compared to that of ZnO NPs obtained with LiOH. However, neither the needles in **Figure 4.15** (a) and (c) nor the nanoplatelets in **Figure 4.15** (b) and (d) are monodomain crystals. Usually, the growth rate is the highest in the Zn-terminated (0001) plane resulting in the nanoneedle shape [3]. As  $\text{Li}^+$  is added, the adsorption of  $\text{Li}^+$  slows down the growth rate of (0001) plane and accelerates that of O-terminated (000 $\bar{1}$ ) plane and a non-polar (10 $\bar{1}$ 0) plane through changing the surface charge and the attachment of zinc-containing species [4], resulting in ZnO NPs in the form of nanoplatelets. The size variation is determined by the nature of both precursor and hydroxide. The size

reduction in the presence of LiOH compared to KOH and NaOH with Zn acetate has been reported previously [5] and was explained by the different growth kinetics between alkaline ions ( $K^+$ ,  $Na^+$  and  $Li^+$ ). For the  $K^+$  and  $Na^+$  ions, they interact weakly with the NP surface. They are easily replaced with  $OH^-$  groups, leading to the attraction of  $Zn^{2+}$  ions and the growth proceeds steadily, almost independent on the precursor's nature. Conversely, the  $Li^+$  ion has a smaller ionic radius, resulting in a stronger binding on the NP surface, resulting in the repulsion of  $Zn^{2+}$  ions and attraction of the precursor anions (acetate or sulfate ions). The acetate ion has a strong stabilizing effect on the nanoparticles [6]. Thus the ZnO NPs grown in this case are readily formed and stabilized in their final form. They remain small. On the contrary, sulfate ions have a lower stabilizing power. The growth of the NPs can proceed on a longer time scale, resulting in larger particles.

### 4.3.1.4. Optical properties

The relationship between the composition of the ZnO NPs powder and the photoluminescence properties/efficiencies were also investigated. **Figure 4.16** and **Figure 4.17** show the PL spectra of the ZnO NPs synthesized using zinc acetate and zinc sulfate as a precursor, respectively, and with different equivalents of KOH and LiOH. It can be seen that all spectra are dominated by a strong and broad visible emission band, sometimes accompanied by a weak UV emission band. The broad visible emission peak has been analysed by Gaussian fitting and the fitting results are presented in **Figure 4.16** and **Figure 4.17** and summarized in **Table 4.2**. For both precursors, the visible emission band is composed of two subbands: a yellow emission line (570-580 nm) and a red emission line (670-680 nm) marked as  $I_1$  and  $I_2$ , respectively.

The first observation which can be made is that the PL QY rises when the content of LiOH is increased, showing the same trend for ZnO NPs synthesized with both precursors. Therefore, we conclude that the presence of Li ions during the synthesis increases the concentration of the defects responsible for the visible emission. Moreover, the emission due to these defects not only prevails over the excitonic one, but it also starts to compete favorably with the non-radiative recombination channels. However, different behaviors are observed for the two precursors. For ZnO NPs fabricated with Zn acetate as a precursor, the ratio between visible and UV emission intensities (marked as Vis/UV in **Figure 4.16** and **Figure 4.17**) increases from 27 to almost infinite (i.e. there is no UV emission) and the ratio of integrated intensity of both subbands of the visible peak (the yellow emission to the red emission, marked as  $I_1/I_2$  in **Figure 4.16** and **Figure 4.17**) keeps almost the same value when the quantity of Li ions is increased. Contrary to Zn acetate, in the case of ZnO NPs synthesized with Zn sulfate, the ratios of Vis/UV and  $I_1/I_2$  are influenced by the content of  $OH^-$  ions, in addition to the content of  $Li^+$  ions. The ratios of Vis/UV and  $I_1/I_2$  follow the order  $4 LiOH > 4 KOH > 2 LiOH$ . When KOH or a low concentration of LiOH is used, the PL QY is higher with Zn sulfate than that with Zn acetate, however at high Li concentration, the PL QY increases and is identical for both precursors.

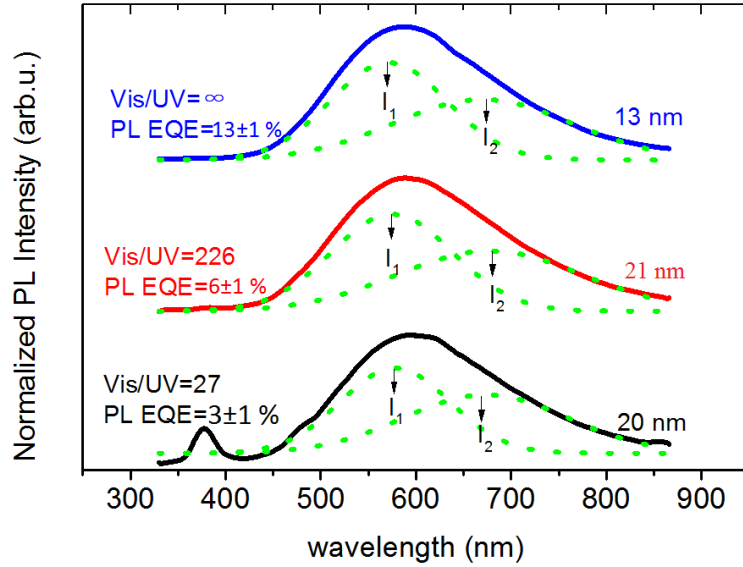


**Figure 4.16:** Normalized PL spectra of ZnO nanoparticles synthesized by the co-precipitation of the zinc acetate with KOH (4 KOH/Zn acetate, bottom curve) and LiOH (2 LiOH/Zn acetate, middle curve and 4 LiOH/Zn acetate, top curve). The experimental curve is shown as a solid line and the dotted curves are the fits of the visible emission peak. The plots are shifted along the y-axis for clarity.

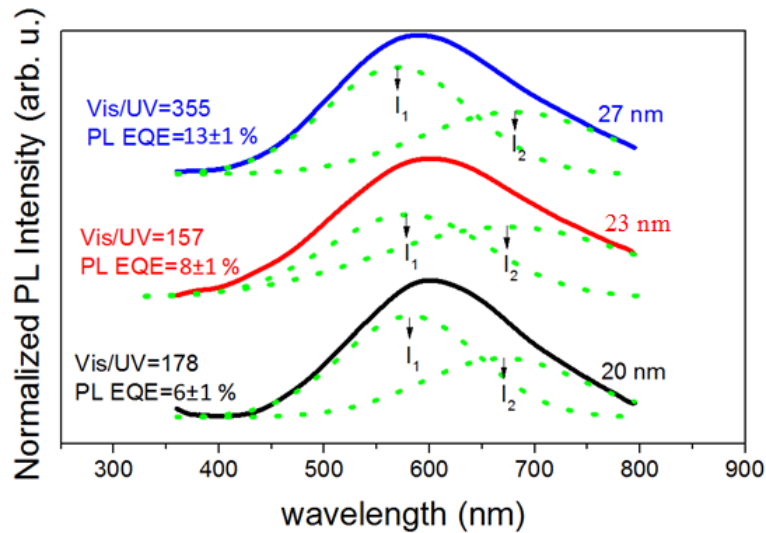


**Figure 4.17:** Normalized PL spectra of ZnO nanoparticles synthesized by the co-precipitation of the zinc sulfate with KOH (4 KOH/Zn sulfate, bottom curve) and LiOH (2 LiOH/Zn sulfate, middle curve and 4 LiOH/Zn sulfate, top curve). The experimental curve is shown as a solid line and the dotted curves are the fits of the visible emission peak. The plots are shifted along the y-axis for clarity.

**Table 4.2:** Summary of peak positions and the integrated intensity ratio of peak  $I_1$  and  $I_2$  of co-precipitation synthesized ZnO NPs with Zn acetate and Zn sulfate.

Sample synthesis condition	$I_1$ position (nm)	$I_2$ position (nm)	Integrated intensity ratio of $I_1/I_2$	Vis/UV	PL QY
4 KOH/Zn acetate	578	673	0.9	27	$3 \pm 1$ %
2 LiOH/Zn acetate	575	678	1.0	226	$6 \pm 1$ %
4 LiOH/Zn acetate	571	670	1.0	infinite	$13 \pm 1$ %
4 KOH/Zn sulfate	582	670	1.0	178	$6 \pm 1$ %
2 LiOH/Zn sulfate	579	673	0.7	157	$8 \pm 1$ %
4 LiOH/Zn sulfate	569	680	1.3	355	$13 \pm 1$ %

#### 4.3.1.5. Discussion

$\text{Li}^+$  ions are known to act as hole scavengers when they are in the interstitial sites [7] and to give rise to PL emission near 570 nm. However, they act as a deep acceptor when they are in substitution of Zn [8]. We have performed nucleation reaction analysis (NRA) on the samples synthesized with LiOH. No Li has been detected, indicating that its atomic concentration within the nanoparticles is smaller than the NRA detection limit of 0.5 %. Moreover, the relative intensity variation of the  $I_1$  visible emission component as illustrated by the ratio of  $I_1/I_2$  in **Table 4.2** for both precursors does not follow the variation in the  $\text{Li}^+$  concentration. Even though the  $I_1$  peak might be related to  $\text{Li}^+$  of interstitial site, this peak probably does not originate only from  $\text{Li}^+$  ions at interstitial sites. It can also be attributed to the intrinsic defects induced by the use of Li during the synthesis of NPs. The syntheses have been performed at ambient conditions in water, i.e., at the O-rich condition, in which  $V_{\text{Zn}}$  and  $\text{O}_i$  have the lowest formation energy, as mentioned in Chapter 2. Thus the most probable related defects to the visible emission are  $V_{\text{Zn}}$  and  $\text{O}_i$ . As was mentioned in Chapter 2, the sub-bandgap absorption under 532 nm excitation and red emission has been attributed to single defect -  $V_{\text{Zn}}$ . We have also performed the PL measurement using a 532 nm laser on ZnO NPs synthesized by the co-precipitation of the zinc acetate with LiOH (4 LiOH/Zn acetate), which has the optimum PL QY. The PL spectrum is shown in **Figure 4.18**. It can be seen that the ZnO NPs absorb the photons with energy lower than its bandgap and re-emit a red emission at about 630 nm. Hence, it confirms the existence of  $V_{\text{Zn}}$  in the ZnO NPs samples. However,  $V_{\text{Zn}}$  and its related complexes are preferentially located on the non-polar  $(10\bar{1}0)$  planes [9, 10]. For both precursors, the  $\text{Li}^+$  ions inhibit the  $(0001)$  plane growth rate while they increase the  $(10\bar{1}0)$  plane growth rate, resulting in the fraction of the non-polar  $(10\bar{1}0)$  plane decrease. Thus, the  $V_{\text{Zn}}$  concentration is decreased as the  $\text{Li}^+$  ion concentration increases. Thus the  $V_{\text{Zn}}$  is not the only defect responsible for the visible emission. D. Li *et al.* [11] have attributed both yellow and red emissions to  $\text{O}_i$ , located in the bulk and on the surface, respectively, which

also is most likely in our case. The defect responsible for the visible emission should be the  $V_{Zn}-O_i$  complex. After  $O_2$  adsorption on the ZnO NPs surface, a surface defect  $O_i$  is created, which is capable of diffusing easily and annihilating bulk O vacancies due to the low migration barrier [12]. The diagram of this mechanism is shown in **Figure 4.19**. When acetate is used as precursor, the ration between  $O_i$  at the surface and in the bulk remains fairly constant, thus the  $I_1/I_2$  ratio does not change with the nature of the alkaline hydroxide and their equivalent quantity variation, due to the strong stabilizing effect of the acetate. The size reduction caused by the  $Li^+$  ions attachment increases the overlap of the electron and hole wavefunctions and defect concentration, leading to an efficient tunneling of the hole to the trapped electron. The intensity of the visible luminescence is thus improved. However, when zinc sulfate is used as the precursor, the situation changes. Raman spectroscopy indicates that the crystal network is strongly perturbed by the LiOH. On the other hand, XRD indicates an increase in the mean size of the crystalline domain of the ZnO NPs synthesized with zinc sulfate and LiOH. In this case, despite the relatively large size, the presence of the radiative defects is increased. Hence, the PL QY increases with the  $Li^+$  content increase. Moreover, the introduction of the LiOH during the synthesis of ZnO nanoparticles has already been reported [13], and the role of  $Li^+$  ions in controlling the pH of the solution has been highlighted. Keeping the pH of the reaction medium at basic values maintains the oxidizing character of the solution and thus is expected to enhance the creation of O vacancies. Since the sulfate has weaker stabilizing effect than the acetate, the ZnO NPs synthesized in this case are much sensitive to the  $OH^-$  concentration, which influence the  $O_i$  creation and diffusion [14], resulting in the  $I_1/I_2$  ratio change. It can be concluded that the nanoparticle size matters (the smaller the better), but also that the fraction of the not well crystallized ZnO NPs facets have a significant influence on the intensity of the yellow-red luminescence of the NPs.

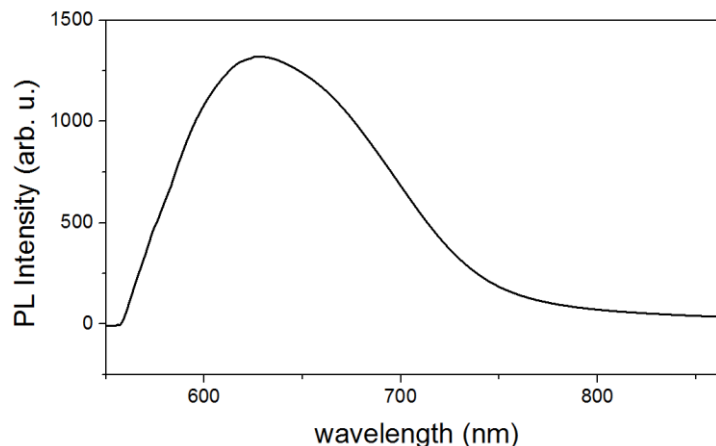


**Figure 4.18:** PL spectrum of ZnO NPs under the excitation of 532 nm synthesized by the coprecipitation of the zinc acetate with LiOH (4 LiOH/Zn acetate), which has the optimum PL QY.

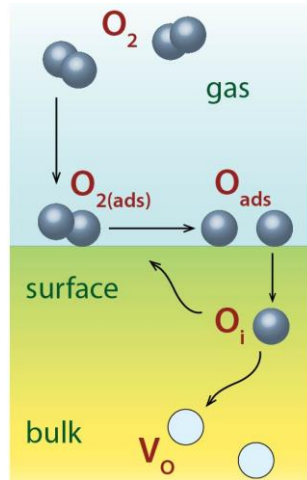


**Figure 4.19:** Diagram of the  $O_i$  creation and diffusion mechanism after the  $O_2$  adsorption on the ZnO NPs surface [12].

In order to further control the surface charge and prevent the aggregation of nanoparticles, a surfactant agent has been used. In this work, the polyacrylic acid (PAAH) was added in the reaction medium during the synthesis. The most interesting results were obtained when 4 LiOH/ Zn sulfate and 1 % of PAAH in weight with respect to ZnO were used. It can be noticed in the Raman spectrum presented in **Figure 4.20**, that a typical  $A_1(\text{TO})$  mode of hexagonal wurtzite ZnO has been found. Moreover, there are four peaks located at 215, 263, 481 and  $724\text{ cm}^{-1}$ , corresponding to  $\text{Zn}(\text{OH})_2$  phase [15]. Furthermore, no PAAH-related peaks are found in the Raman spectrum in **Figure 4.20**, which permits to conclude that PAAH is not attached to the surface of ZnO/ $\text{Zn}(\text{OH})_2$ . The inset in **Figure 4.20** (a) presents the Raman spectrum of the pure PAAH for comparison. This behavior is contrary to the one observed for other surfactants, which attach to the nanoparticle surface. Besides, it is not excluded that the amorphous ZnO and  $\text{Zn}(\text{OH})_2$  form during the synthesis of ZnO NPs, as the peaks related to the amorphous phase cannot be detected by the Raman spectroscopy.

**Figure 4.21** shows the corresponding PL spectrum and gives the values of the PL QY of ZnO NPs synthesized by the co-precipitation of the zinc sulfate with 4 LiOH/Zn sulfate with 1 % of PAAH in weight with respect to ZnO, together with the spectrum of the ZnO NPs synthesized in the same conditions but without PAAH, for comparison. The PL spectra and PL QY for both cases are identical. Thus the visible emission can originate from ZnO NPs present in both samples. The spectrum of ZnO without the  $\text{Zn}(\text{OH})_2$  emission presented in [16] shows a strong visible band at 2.16 eV (574 nm) similar to the PL spectra shown in **Figure 4.21**. Moreover, the presence of  $\text{Zn}(\text{OH})_2$  is reported to suppress the excitonic transition in the ZnO NPs [16], which may be the reason of the improved PL QY of about 13 %. Hence we conclude that the visible emission also probably comes from  $\text{Zn}(\text{OH})_2/\text{ZnO}$  phase present in both samples.

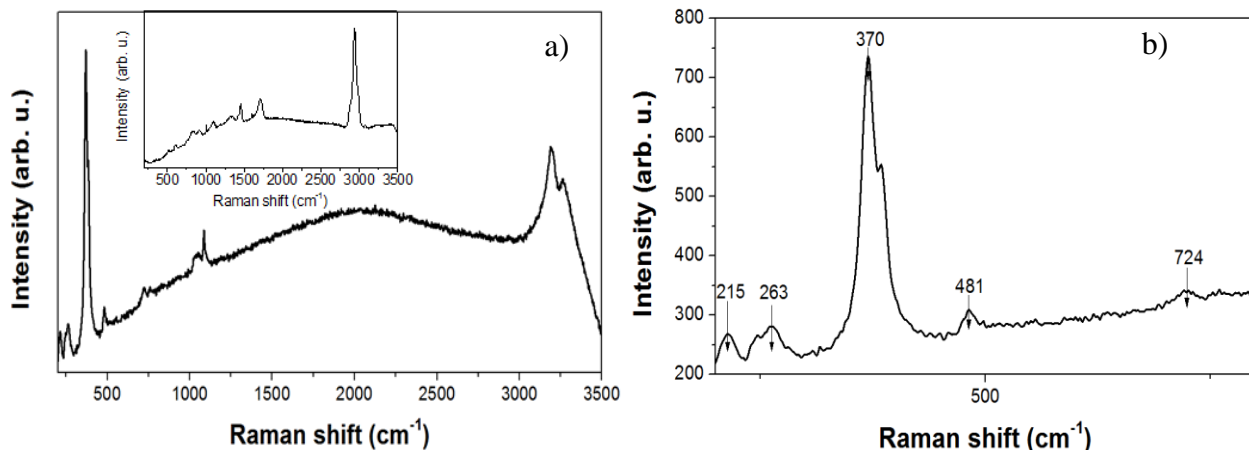


**Figure 4.20:** (a) Raman spectrum of ZnO NPs synthesized by the co-precipitation of the zinc sulfate with 4 LiOH/Zn sulfate and 1 % of PAAH in weight with respect to ZnO. The inset is the Raman spectrum of PAAH. (b) Zoom of Raman spectrum of ZnO NPs in the range 200-800  $\text{cm}^{-1}$ .

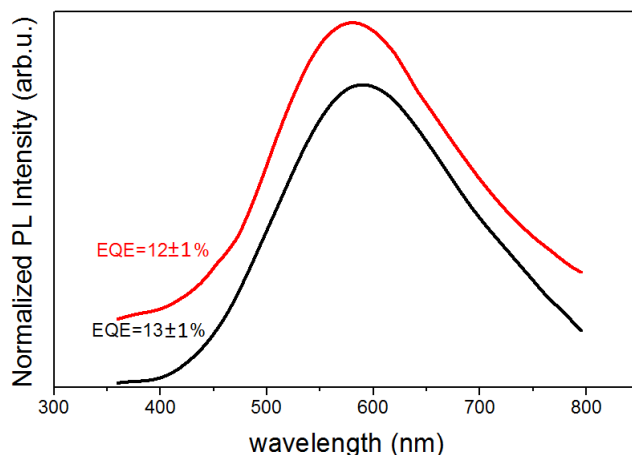


**Figure 4.21:** Normalized PL spectra of ZnO nanoparticles synthesized by the co-precipitation of the zinc sulfate with 4 LiOH/Zn sulfate with 1 % of PAAH in weight towards ZnO (top curve) and without PAAH addition (bottom curve). The plots are shifted along the y-axis for clarity.

#### 4.3.1.6. Conclusions

In the co-precipitation method, the ZnO NPs were synthesized using two zinc precursors: Zn acetate and Zn sulfate with two different alkaline hydroxides (KOH and LiOH) in water or ethanol. It is found that the size of the ZnO NPs synthesized in ethanol is smaller than the size of NPs synthesized in water for KOH, but the PL QY is the same. Since water is a cheaper and less hazardous compound and the solvent has no influence on the PL QY, water was used as solvent for further syntheses. By replacing KOH with LiOH in the synthesis process, when LiOH concentration increases, it was observed that the NPs size decreases with Zn acetate while it increases when ZnO sulfate is used. This can be explained by the stronger ability of acetate than

sulfate to protect the primary nanoparticle embryos from aggregating. In both kinds of ZnO NPs, the nanoparticle morphology changes from nanoneedles to nanoplatelets when KOH is replaced with LiOH in the synthesis process. Concomitantly, the intensity of the visible emission is enhanced as the concentration of LiOH is increased and the PL QY reaches 13 %. The visible emission is believed to originate from intrinsic defects rather than from the presence of the Li dopant. We relate this enhancement to the increase of the concentration of the intrinsic defects and the increase of the wavefunctions overlap of holes and trapped electrons at the defect sites due to the nanoparticle size reduction. Even more importantly, it is due to the increased fraction of not well crystallized facets on the surface of ZnO NPs.

For the two precursors used, the mechanisms of the enhancement of the defect-related emission are different. With acetate, it is only influenced by  $\text{Li}^+$  ion concentration, while it is also influenced by the  $\text{OH}^-$  concentration with sulfate, which confirms that acetate has a stronger surface stabilization power of the ZnO NPs during their growth than sulfate.

The effect of the PAAH used as a surfactant has also been studied. While the surface protection and the surface stabilization are observed for other surfactants, when PAAH is added during the synthesis, it behaves differently: no attachment on the surface of nanoparticles. Crystalline ZnO and  $\text{Zn}(\text{OH})_2$  have also been obtained, similar to that without PAAH addition. The formation of amorphous ZnO and  $\text{Zn}(\text{OH})_2$  cannot be excluded. The similar PL spectra and almost the same high value of PL QY for both ZnO NPs synthesized with PAAH and without PAAH indicate that the visible emission may originate from the ZnO or from  $\text{Zn}(\text{OH})_2/\text{ZnO}$  present in both samples.

### 4.3.2. Hydrolysis method

#### 4.3.2.1. Hydrolysis of $\text{Zn}[\text{N}(\text{SiMe}_3)_2]_2$

As first, the hydrolysis of  $\text{Zn}[\text{N}(\text{SiMe}_3)_2]_2$  in water was used to synthesize ZnO NPs. Two methods were used to deposit the synthesized ZnO NPs on the substrate: either pressing them on an indium foil or dispersing them in a polymer matrix (polyurethane, PU) and then depositing the mixture on a fused silica substrate. Then the PL spectra were measured for both types of samples. As can be observed in **Figure 4.22 (a)**, ZnO NPs fabricated by hydrolysis method and deposited on indium foil give mainly a visible and NIR emission (peaking at 700 nm), probably due to the surface states of the ZnO NPs. This statement is confirmed by the fact that this emission is quenched and blue-shifted in the case of the same nanoparticles dispersed in the PU matrix [17]. The PL emission spectrum of ZnO NPs fabricated by this sol-gel method dispersed in PU matrix is presented in **Figure 4.22 (b)** contains also some emission features of the polyurethane matrix, as can be seen by comparison in the PL spectrum of pure PU, shown in **Figure 4.23**.

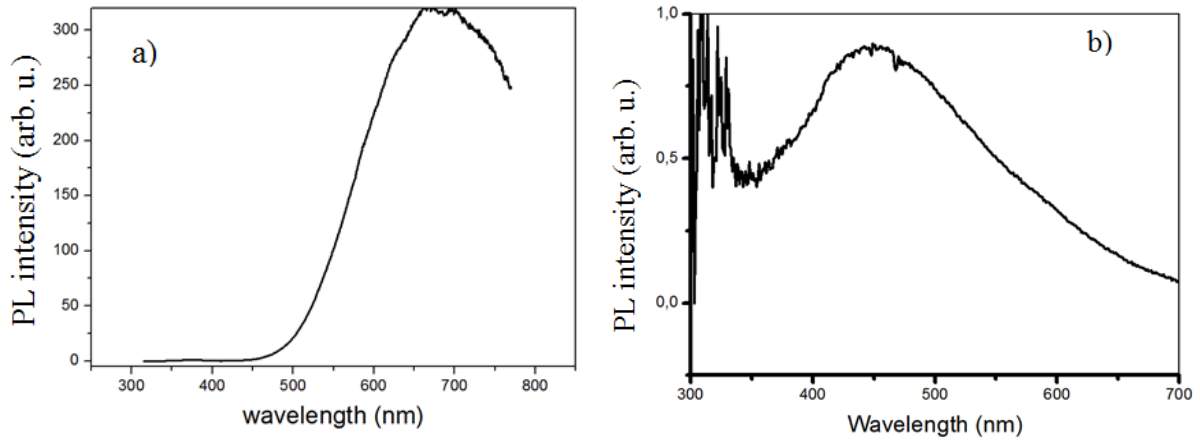


**Figure 4.22:** PL spectrum of the ZnO NPs synthesized by the hydrolysis method (a) deposited on the indium foil by pressing and (b) dispersed in PU matrix and deposited on fused silica substrate.

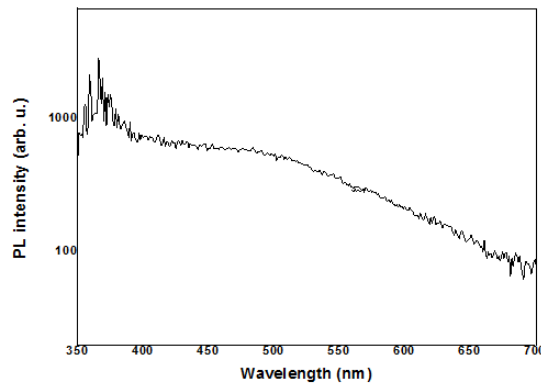


**Figure 4.23:** PL spectrum of the PU matrix alone, without the ZnO NPs.

The PLE spectrum of the ZnO NPs synthesized by the  $\text{Zn}[\text{N}(\text{SiMe}_3)_2]_2$  hydrolysis is also measured for the emission range from 400 nm to 800 nm and the result is presented in **Figure 4.24**. It also confirms that the visible luminescence of ZnO NPs synthesized by the hydrolysis of  $\text{Zn}[\text{N}(\text{SiMe}_3)_2]_2$  comes from the photons in the spectral range between 350-370 nm.

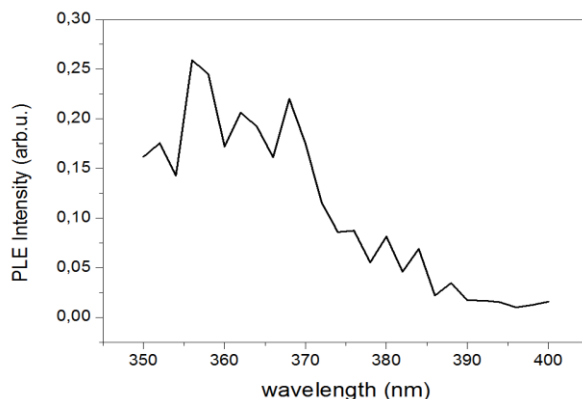


**Figure 4.24:** PLE spectrum of ZnO NPs synthesized by the  $Zn[N(SiMe_3)_2]_2$  hydrolysis for the emission range from 400 nm to 800 nm.

The corresponding PL QY is measured to be 2 %. Although it is already improved compared to the ZnO NPs synthesized by the LECBD method and the commercially available ones, it is still too low to make a dramatic enhancement of the UV-to-visible emission conversion efficiency and to compensate for the additional energy losses induced by the down-shifting layer.

#### 4.3.2.2. Hydrolysis of $ZnEt_2$

Though the ZnO NPs synthesized by the co-precipitation method have the visible emission efficiency of 13 %, much higher than that of ZnO NPs synthesized by the LECBD method and the commercially available ones, they are not dispersible in water or any other solvents, so it is difficult to make a down-shifting layer with homogeneously dispersed ZnO NPs. The addition of PAAH during their synthesis induced a structural change and the formation of  $Zn(OH)_2$ , but not the capping at the surface of ZnO NPs, so it was impossible to improve their dispersibility by the addition of the capping agent. Moreover, nanoparticle aggregation may destroy the high visible emission efficiency of ZnO NPs, so it should be avoided. As the hydrolysis method is performed in water and the surface of NPs can be easily modified using this method, it is expected that modifying the synthesis conditions, it will be possible to synthesize dispersible ZnO NPs. As the hydrolysis of  $Zn[N(SiMe_3)_2]_2$  gave ZnO NPs having a visible emission of only 2 %, another precursor was used - diethylzinc ( $ZnEt_2$ ) to perform the hydrolysis in water with the introduction of PAAH (polyacrylic acid) and PAANA (sodium polyacrylate) as stabilizing surfactant agents.

##### 4.3.2.2.1. Effect of the PAAH concentration

In the first step, PAAH of molecular weight  $M_w = 2000 \text{ g}\cdot\text{mol}^{-1}$  in different ratios (0, 0.063, 0.63, 6.3 wt%) in water has been added during the synthesis to control the surface states of the ZnO NPs. To ensure the PAAH actually interacts with the particles resulting from the hydrolysis of  $ZnEt_2$ , Fourier Transform IR (FTIR) spectroscopy has been carried out. The FTIR spectra are presented in **Figure 4.25**. In absence of PAAH, the stretching mode of the Zn-O bond [18, 19] can be seen in the range spanning from 540 to 570  $\text{cm}^{-1}$ . The broad feature around 3400  $\text{cm}^{-1}$

corresponds to the stretching mode of the O-H bond, indicating the presence of hydroxide groups OH in the sample.

When the PAAH concentration increases, the intensity of the Zn-O stretching mode is progressively reduced, being hardly distinguishable for the sample synthesized with 0.63 wt% of PAAH and absent for the sample with 6.3 wt % of PAAH. This demonstrates that the addition of PAAH during the synthesis tends to degrade the crystalline quality of the resulting ZnO particles. Concomitantly, additional peaks at  $2945\text{ cm}^{-1}$ ,  $1563\text{ cm}^{-1}$ ,  $1452\text{ cm}^{-1}$ , and  $1411\text{ cm}^{-1}$  related to PAAH appear. Their positions indicate that PAAH is mainly in its deprotonated form  $\text{PAA}^-$  in the sample. The peaks at  $1563\text{ cm}^{-1}$  and  $1411\text{ cm}^{-1}$  correspond to the asymmetric and symmetric modes of the carboxylate anion ( $\text{COO}^-$ ), respectively. The interaction between PAAH and ZnO occurs thus probably through chelation as evoked in [20]. However, with 0.063 wt% and 0.63 wt% of PAAH, a band at  $1743\text{ cm}^{-1}$  is observed. It shifts to  $1710\text{ cm}^{-1}$  with 6.3 wt% of PAAH. It corresponds to the C=O stretching mode of free carboxylic acid ( $\text{COOH}$ ) group and hydrogen-bonded  $\text{COOH}$  group, respectively [21]. We can first conclude that a minor part of PAAH is still in its protonated form for a low PAAH concentration and that it increases when the PAAH concentration reaches 6.3 wt%. Furthermore, we can infer that at high concentration, the excess of PAAH links to the rest of the PAAH or ZnO NPs through the H bond.

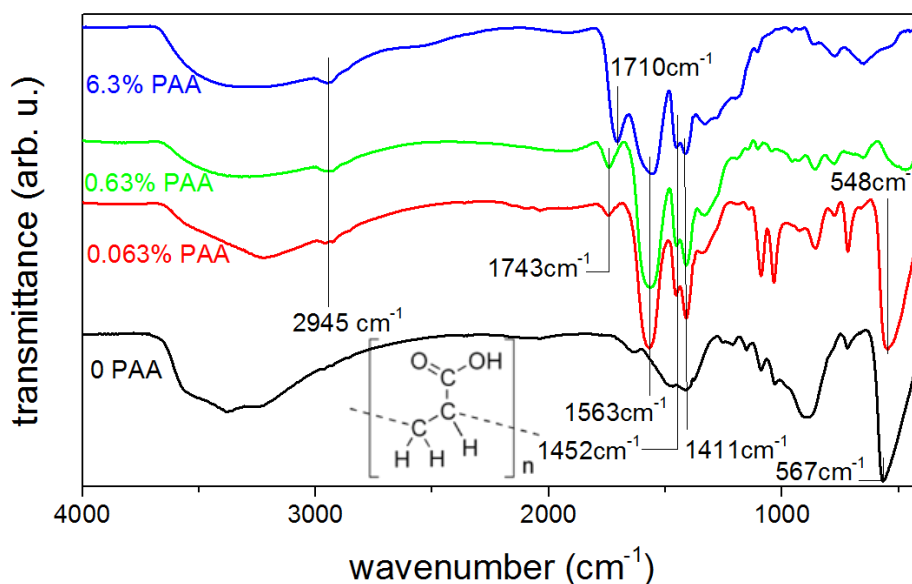


**Figure 4.25:** FTIR spectra of ZnO nanoparticles synthesized by the hydrolysis of  $\text{ZnEt}_2$  with different concentrations of PAA (0 wt%, 0.063 wt%, 0.63 wt% and 6.3 wt% from bottom to top). Inset: the chemical structure of PAAH. The plots are shifted along the y-axis for clarity.

To get more insight into the crystalline quality of the samples, we have performed Raman spectroscopy and X-Ray diffraction analysis (XRD). In the Raman spectrum of ZnO NPs synthesized without PAAH in **Figure 4.26**, ZnO NPs display the typical modes of ZnO hexagonal wurtzite structure, which are located at  $334\text{ cm}^{-1}$ ,  $440\text{ cm}^{-1}$ ,  $583\text{ cm}^{-1}$  attributed to

multiphonon modes,  $E_2^{\text{high}}$  mode and  $A_1(\text{LO})$  mode respectively [3]. This shows that the ZnO NPs synthesized with no PAAH have a good crystalline quality. XRD diffractograms of ZnO NPs synthesized with PAAH in different ratios are presented in **Figure 4.27**. As the PAAH concentration increases, the diffraction peaks associated with the ZnO wurzite structure diminish and eventually disappear at the highest concentration. This is in accordance with the FTIR results and confirms that the crystalline quality is degraded as the PAAH content increases. Consequently, more defects are gradually introduced in the ZnO nanoparticles and eventually lead to an amorphous material. Concomitantly, the size of the particles, estimated using Scherrer's equation, is reduced from 17 nm to 8 nm, as summarized in **Table 4.3**. Let us notice that at the concentration of 0.063 wt% and 0.63 wt%, some traces of  $\epsilon\text{-Zn}(\text{OH})_2$  (wulffingite) are present along with the wurzite ZnO phase [22].

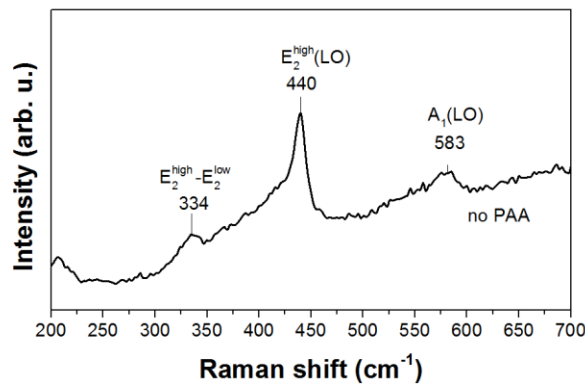


**Figure 4.26:** Raman spectrum of ZnO nanoparticles synthesized by the hydrolysis of  $\text{ZnEt}_2$  with no PAAH.

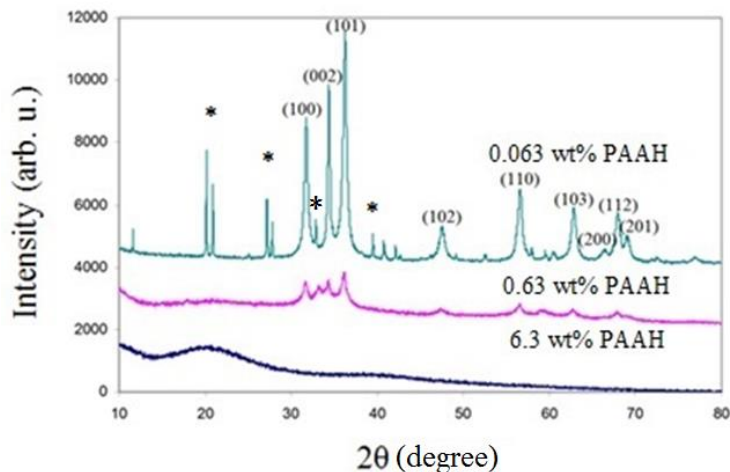


**Figure 4.27:** XRD diffractograms of ZnO nanoparticles synthesized by the hydrolysis of  $\text{ZnEt}_2$  with different concentrations of PAAH (0.063 wt%, 0.63 wt%, and 6.3 wt% from top to bottom). The plots are shifted along the y-axis for clarity. Peaks labeled with \* refer the  $\text{Zn}(\text{OH})_2$  wulffingite phase.

**Table 4.3:** Crystalline domain sizes of ZnO NPs synthesized with different concentration of PAAH estimated from XRD diffractograms.

Concentration of PAAH	crystalline domain size (nm)
0	17
0.063 wt%	15
0.63 wt%	8

The PAAH addition during the growth not only controls the size of the particles but also their shape as illustrated in the TEM images of **Figure 4.28**. When no or a little amount (0.063 wt%) of PAAH is added, crystalline platelets of about 20 nm are formed (as shown in **Figure 4.28** (a)). The actual dimension of these platelets is difficult to estimate accurately because of their superposition and gathering, but their apparent size seems in accordance with the crystalline domain size estimated from the XRD diffractograms of **Figure 4.27**. When 0.63 wt% of PAAH is added, spheres of about 200 nm in diameter are observed. As shown in the inset of **Figure 4.28** (b), these spheres are composed of dark small particles embedded in a matrix. The small particles are presumably made of ZnO and Zn(OH)<sub>2</sub>. Their size is in accordance with the crystalline domain size estimated from the XRD data. It thus seems that when the PAAH content increases during the synthesis, the resulting ZnO and Zn(OH)<sub>2</sub> nanoparticles turn from nanoplatelets to small nanoparticles dispersed in large polymeric spheres. At the highest PAAH concentration of 6.3 wt%, the nature of the material is hard to assess, but it is unlikely that it consists of ZnO nanoparticles in the PAAH matrix.

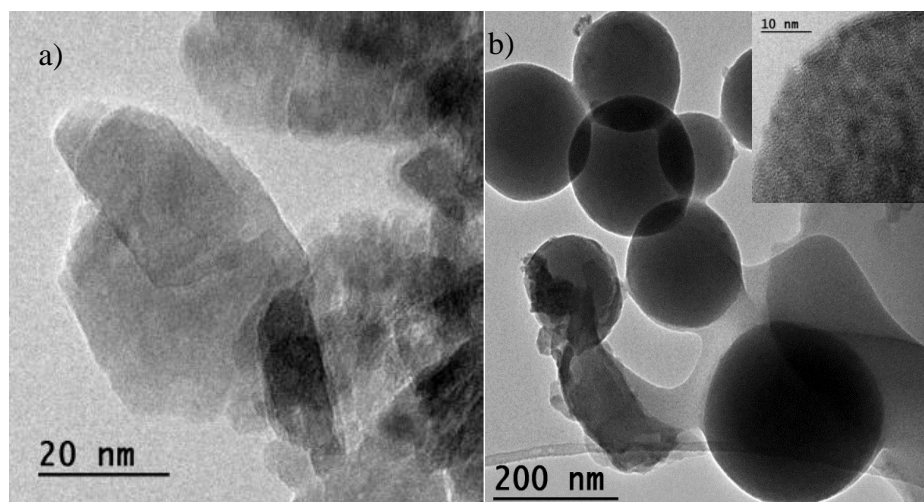


**Figure 4.28:** TEM images of ZnO nanoparticles synthesized by the hydrolysis of ZnEt<sub>2</sub> (a) with 0.063 wt% of PAAH and (b) with 0.63 wt% of PAAH (the inset is a zoom of the surface of a sphere).

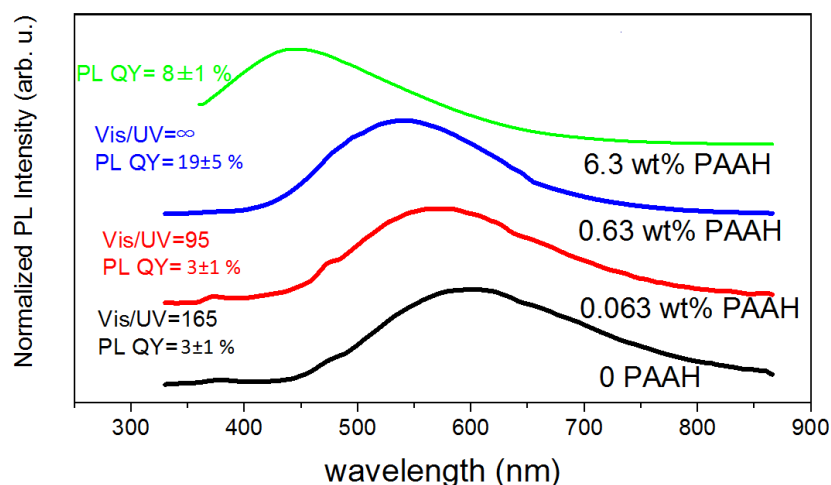


**Figure 4.29:** PL spectra of ZnO nanoparticles synthesized by the hydrolysis of  $\text{ZnEt}_2$  with different concentrations of PAAH (from bottom to top: 0 wt% of PAAH, 0.063 wt% of PAAH, 0.63 wt% of PAAH and 6.3 wt% of PAAH). The plots are shifted along the y-axis for clarity.

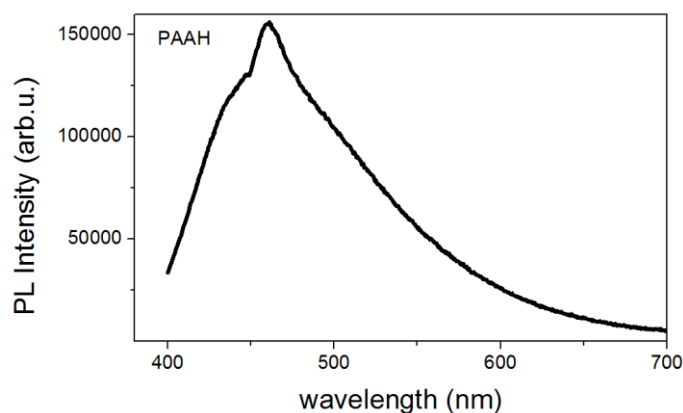


**Figure 4.30:** PL spectrum of PAAH.

Regarding the corresponding optical properties, as shown in the PL spectra of **Figure 4.29**, when the PAAH concentration increases from 0 to 0.063 wt%, both the visible/UV intensity ratio (marked as Vis/UV in **Figure 4.29**) and the PL QY remain low. The addition of PAAH at such a low content has almost no influence on any property of the resulting material. As it increases to 0.63 wt%, the Vis/UV ratio grows to almost infinite (i.e. the UV emission is suppressed) and the PL QY rises dramatically from 3 % to 19 % and then decreases to 8 % when the PAAH concentration increases to 6.3 wt%. The PL QY evolution is accompanied with a gradual blue-shift of the PL emission, from 600 nm to 540 nm at 0.63 wt% PAAH and eventually to 450 nm at 6.3 wt%. This blue-shift is not due to the appearance of the PL emission from the PAAH itself. As can be seen in **Figure 4.30**, the PL emission of PAAH is characterized by a sharp feature at  $\sim 460$  nm, which is not present in the spectra of the samples.

The dynamics of the PL emission has been studied by Time Resolved PL (TRPL) with the detection wavelength fixed at the emission spectrum peak wavelength of these NPs. The results are presented in **Figure 4.31** and summed up in **Table 4.4**. The PL emission consists of two components, a prominent rapid one and a minor slower one. With no or little PAAH, the rapid component has a decay time  $\tau_1$  of about 14 ns, while characteristic time of the slow one is one order of magnitude higher ( $\tau_2 \sim 284$  ns). When 0.63 wt% of PAAH is used, both decay times increase to 20 ns and 341 ns. This is in accordance with the increase in the PL QY and shows that there are less non-radiative centers in the structure of ZnO NPs for the case of the synthesis with 0.63 wt% of PAAH than in the case of lower PAAH concentrations.

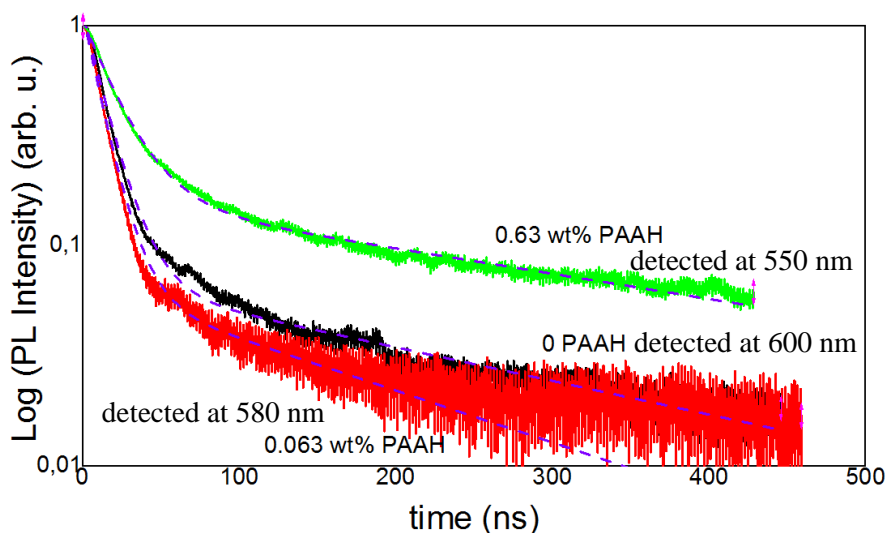


**Figure 4.31:** TRPL decay curves of ZnO nanoparticles synthesized by the hydrolysis of  $\text{ZnEt}_2$  with no PAAH, with 0.063 wt% and 0.63 wt% of PAAH as the detection wavelengths fixed at the peak positions of their emission spectra 600 nm, 580 nm and 550 nm, respectively. Corresponding biexponential fits (violet dash lines) results are summarized in **Table 4.4**.

**Table 4.4:** Time constants obtained by fitting TRPL spectra in **Figure 4.30** with the biexponential decay and the relative contributions of each exponential function.

Surfactants addition	Detection wavelength (nm)	Time constant 1 $\tau_1$ (ns)	Relative contribution	Time constant 2 $\tau_2$ (ns)	Relative contribution
No surfactants	600	14	0.93	284	0.07
0.063 wt% PAAH	580	12	0.96	184	0.04
0.63 wt% PAAH	550	20	0.84	341	0.16

PL excitation (PLE) spectroscopy has been performed to investigate the de-excitation channels. The results for the samples synthesized with 0.63 wt% of PAAH and no PAAH are shown in **Figure 4.32**. For the ZnO nanoparticles synthesized without PAAH, the excitation threshold corresponds to the gap of ZnO. The PLE signal becomes significant for photons of energy higher than 3.42 eV. However, for the particles synthesized with 0.63 wt% of PAAH, the global magnitude of the PLE signal is higher (in accordance with the higher PL QY), but a new feature is observed at around 340 nm (3.65 eV). This feature is not related to ZnO since, as shown in **Figure 4.33**, the bandgap of the nanoparticles is still situated at 3.42 eV (no quantum confinement is observed). This feature could be related to Zn(OH)<sub>2</sub>. However, only a weak peak in the XRD spectrum related to the crystalline zinc hydroxide compound has been detected in this sample (see Figure 4.27, peak at around 33°). Moreover, as shown in **Figure 4.34**, the PLE spectrum of PAAH actually presents a resonance at 343 nm. We thus conclude that this peak in the PLE spectrum is related to the presence of PAAH.

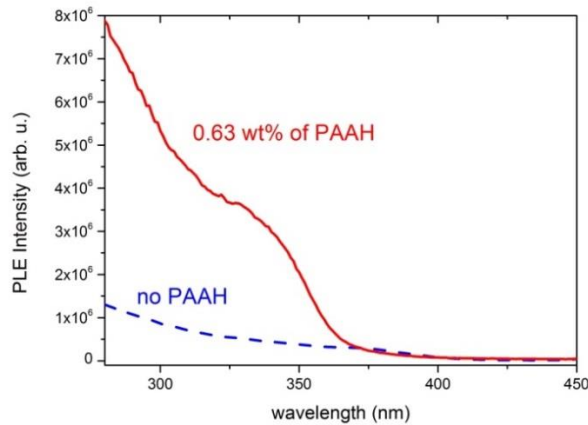


**Figure 4.32:** PLE spectra of ZnO nanoparticles synthesized by the hydrolysis of ZnEt<sub>2</sub> with no PAAH and with 0.63 wt% of PAAH measured at 550 nm.

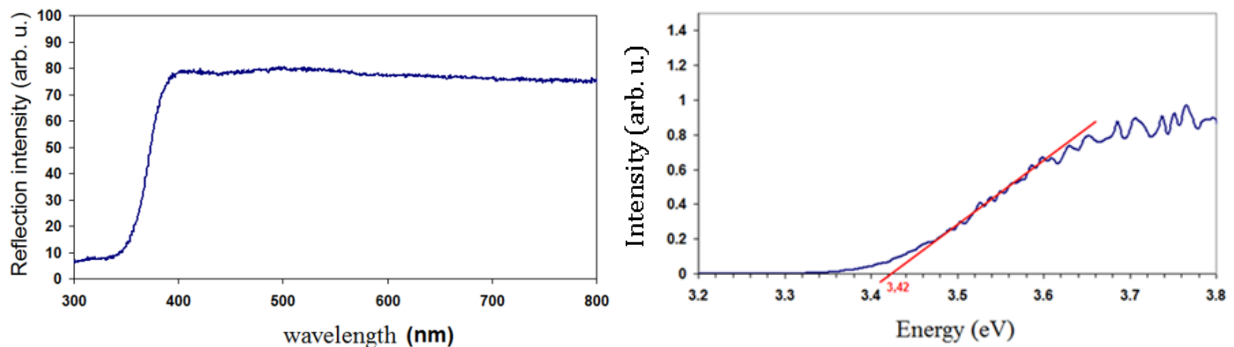


**Figure 4.33:** Reflection spectrum (left) and the bandgap estimation via Kubelka-Monk approximation (right) of ZnO nanoparticles synthesized by the hydrolysis of the diethyl zinc with 0.63 wt% of PAAH.

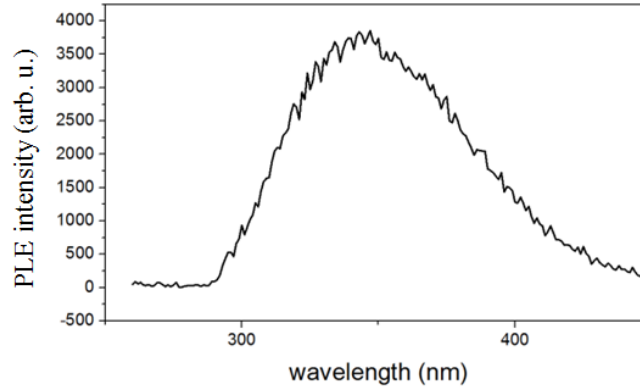


**Figure 4.34:** PLE spectrum of pure PAAH measured at 470 nm.

On the basis of these observations, we propose a model for the energy diagram of the ZnO/PAAH composite. **Figure 4.35** shows the energy diagram of the composite, with the conduction and valence band levels of ZnO and the HOMO (highest occupied molecular orbital) and LUMO (lowest unoccupied molecular orbital) of PAAH. The two materials form a type II heterojunction. When a high energy photon is absorbed either in the ZnO part or in the PAAH part, the electron readily thermalizes to the bottom of the ZnO conduction band, while the hole gets trapped at the HOMO of PAAH. This mechanism limits the formation of the exciton in ZnO if the two materials are intermixed on a length scale smaller than the exciton diffusion length. Next, the electron gets trapped at the defect level in the ZnO bandgap responsible for the visible emission. Eventually, the trapped electron and hole recombine to give rise to the visible emission. The emission efficiency is increased because of the strong overlap between the wavefunctions of the trapped electron and hole.

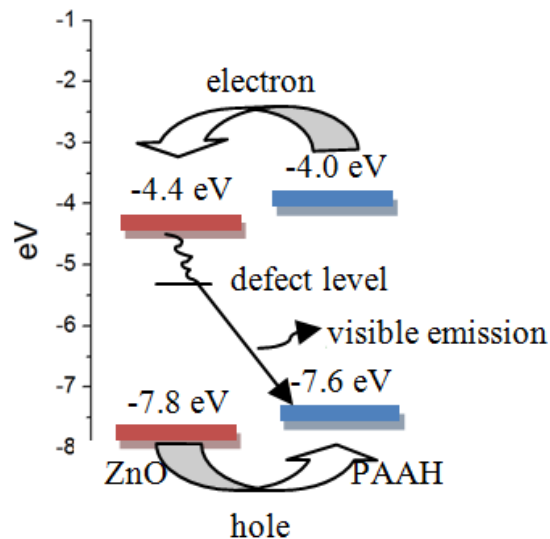


**Figure 4.35:** Schematic diagram of the energy levels for ZnO/PAAH nanocomposites and supposed mechanism of the PL QY enhancement.

To sum up the effect of the PAAH concentration on the synthesis of ZnO NPs, there exists clearly an optimum concentration at around 0.63%, which leads to small (~ 8 nm) ZnO nanocrystals embedded in large (~ 200 nm) polymeric spheres. The PL QY is maximum reaching almost 20 %. For lower PAAH content, almost no difference in PL spectrum shape and PL QY is observed with respect to the samples synthesized without PAAH. When the PAAH concentration is high (6.3 wt%), no indication of the presence of the crystalline ZnO is obtained and the PL emission is strongly blue-shifted and presents a reduced QY.

However, the reason of this PL QY enhancement for the synthesis with 0.63 wt% is not clear. It should be stressed that the effect of PAAH during the synthesis is at odd with its effect when added after the synthesis. Indeed, when added after the growth, PAAH acts a passivating capping agent [23, 24] leading to a reduced visible emission and an enhanced UV one. The adsorption scheme of PAAH on the surface of ZnO NPs is proposed in **Figure 4.36**. When PAAH concentration is low, it passivates the nanoparticle surface defects like other surfactants [25], but not enough to compete with the non-radiative recombination, so the Vis/UV ratio does not change much and the visible luminescence efficiency is low. Not only does the PAAH passivate the surface defects, but it is also expected to screen the surface hole traps (by controlling zeta potential) which are thought to play a major role in the subsequent recombination of holes with electrons at defects close to the ZnO surface. More detailed description of the PAAH adsorption on the surface of ZnO NPs is proposed in **Figure 4.37**, similar to the reaction between CdS quantum dots and PAAH proposed in [25]. We also measured the PL spectra of ZnO NPs synthesized with different concentrations of PAAH under a 532 nm excitation, as presented in **Figure 4.38**. They all show a red emission which demonstrates the existence of  $V_{Zn}$ , similar to the case of ZnO NPs synthesized by co-precipitation method. Moreover, the quantity of  $V_{Zn}$  increases as the PAAH concentration increases. When no PAAH is added, the orange emission with the maximum located at 596 nm is obtained, which is usually attributed to the oxygen interstitials ( $O_i$ ) [26]. With the addition of a small quantity of PAAH, the  $COO^-$  group on the surface creates  $O^{2-}\cdots Zn^{2+}\cdots OOC$  “bridge” between the ZnO and PAAH chain, as shown in **Figure 4.37** (a), similar to the reaction between CdS quantum dots and PAAH which lowers the density of the surface trap states [28]. Hence the Vis/UV ratio decreases and the recombination through defects not located on surfaces becomes dominant. This is consistent with the increase of the yellow emission in the sample synthesized with 0.063 wt% of PAAH, as it is typically related to  $O_i$  defects, which are located in the bulk [12]. Since we have proven the existence of  $V_{Zn}$ , but the PL QY did not show the same variation trend as the  $V_{Zn}$  quantity change in the case of no PAAH and 0.063 wt% of PAAH added, the defect responsible for the visible emission in these cases should be the complex of  $V_{Zn}-O_i$ . As the PAAH concentration increases, the PAAH molecules form a continuous monolayer on the ZnO NPs surface [27] marked as PAAH in **Figure 4.36**, inducing the morphology change to mesospheres when 0.63 wt% of PAAH is used. For this sample the highest PL QY has been obtained. The reason of this PL QY increase can be at first explained by the increase in the concentration of the crystalline defects responsible for the visible emission, or, as written above, by an efficient coupling between these defects and the

HOMO of PAAH. Second, it has also been reported in the literature that PAAH interacts more strongly with the non-polar facets of ZnO [28]. We can thus assume that PAAH favors their presence. The  $V_{Zn}$  which is more stable on the non-polar  $(10\bar{1}0)$  plane [29] increases its concentration with the PAAH concentration as shown in **Figure 4.38**. As the green emission is commonly attributed to the complexes containing  $V_{Zn}$ , the increase in the visible PL QY can also be partially attributed to this phenomenon. Third, we have demonstrated that the addition of PAAH reduces the size of the particles. In the generally accepted model, as mentioned previously, the size reduction is beneficial to the PL QY. However, this increase is significant only for very small sizes ( $\sim 2$  nm in diameter). In our case, the nanoparticles remain “large” with respect to the required dimension. So this size-related explanation of the PL QY increase is not valid in our case. Eventually, the fact that the ZnO particles are embedded in polymer spheres of a few hundreds of nm may also be beneficial for the PL QY. Such spherical structures, resulting from the aggregation of nanoparticles, has been reported several times [30] in sol-gel fabrication of ZnO nanoparticle based transparent electrodes for Dye Sensitized Solar Cells. In these studies, the hierarchical spherical aggregates are reported to increase the light scattering and thus its trapping and absorption in the film, which may also occur in the case of our spheres. Apart from the size reduction, the aforementioned mechanisms are likely to cooperate to lead to a high PL QY in the film synthesized with 0.63 wt% of PAAH.

When higher concentration (6.3 wt%) of PAAH is used, the H bonding forms between the ligand capping the nanoparticles and PAAH (see the FTIR spectrum in **Figure 4.25**), inducing ZnO/polyacrylic acid complexes formation, as shown in **Figure 4.37** (b). It is proposed to be responsible for the blue emission of ZnO NPs with a peak located at 446 nm similar to the ZnO/oleic acid complexes reported in [31].

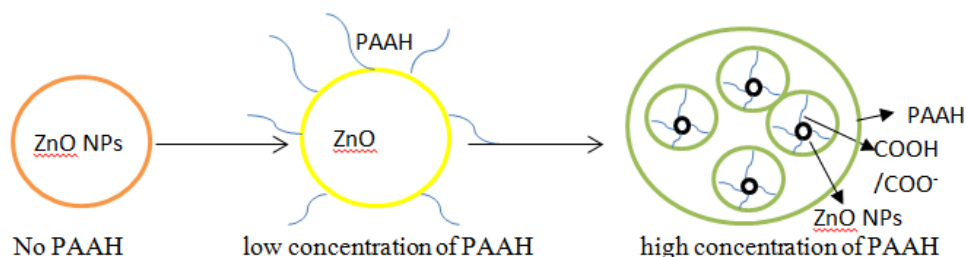


**Figure 4.36:** Adsorption of PAAH at the surface of ZnO NPs for various PAAH concentrations.

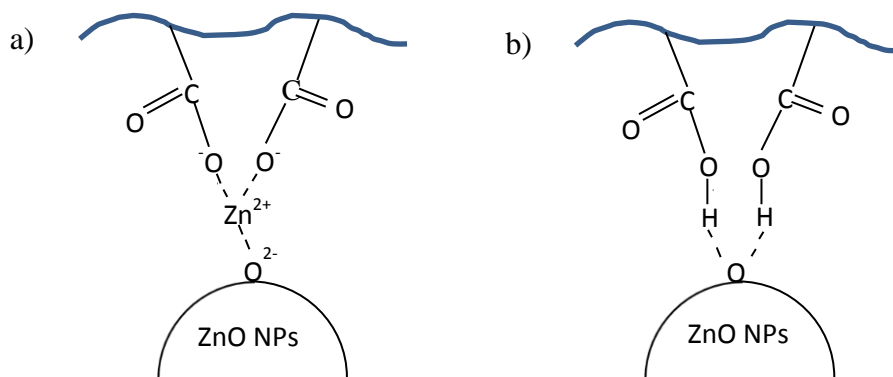


**Figure 4.37:** Scheme of the bidentate chelating structure of (a)  $\text{COO}^- - \text{Zn}^{2+}$  and (b) hydrogen bonding between ZnO NPs and PAAH layer.

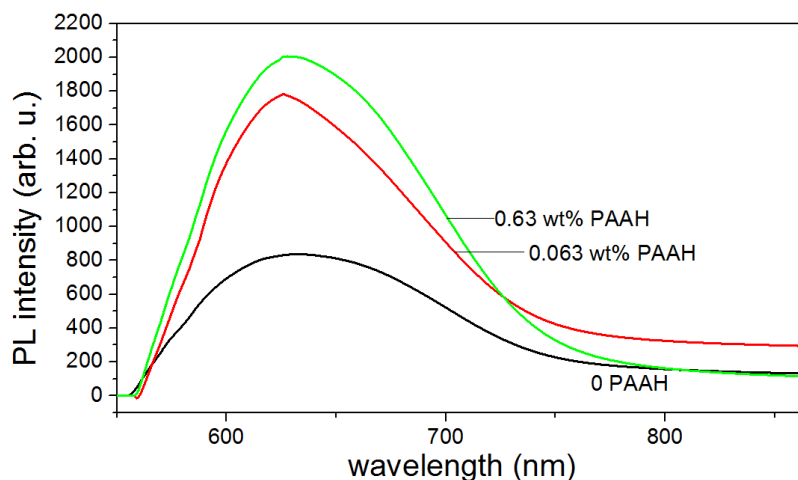


**Figure 4.38:** PL spectra of ZnO NPs under the excitation of 532 nm synthesized by the hydrolysis of  $\text{ZnEt}_2$  with different concentrations of PAAH (from bottom to top: 0 wt% of PAAH, 0.063 wt% of PAAH and 0.63 wt% of PAAH).

#### 4.3.2.2.2. Washing effect

Washing with ethanol the ZnO NPs powders synthesized by the hydrolysis of  $\text{ZnEt}_2$  with 0.63 wt% of PAAH and having the highest PL QY, permits to double the PL QY, reaching 36 %, while the PL spectrum remains unchanged. The morphology of the washed ZnO NPs was checked by SEM and the observed structures are shown in **Figure 4.39** (a). The mesospheres are still present, but the degree of the agglomeration decreases compared to the not washed ZnO NPs, (see the TEM images presented in **Figure 4.28** (b)). It is consistent with the observation reported in [32]. Thus, as the ZnO NPs agglomeration is decreased, the specific surface area increases. The crystalline quality of the washed ZnO NPs was also studied. The XRD diffractogram presented in **Figure 4.39** (b) demonstrates that the ZnO NPs have a low crystalline quality,

similar to the unwashed nanoparticles, as shown in **Figure 4.27**. The crystalline domain size deduced using Scherrer's formula is 8 nm, the same as in the case of non-washed NPs. Thus the enhancement is not due to the NPs size reduction, but most likely due to the fact that the washing removes from the sample some material responsible for the PL quenching.

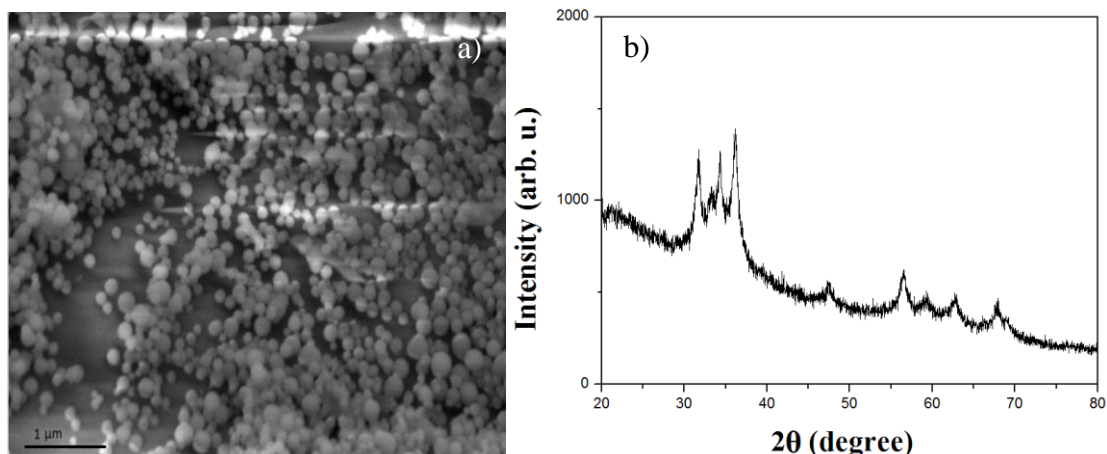


**Figure 4.39:** (a) SEM image and (b) XRD diffractogram of the ZnO NPs synthesized by the hydrolysis of  $\text{ZnEt}_2$  with 0.63 wt% of PAAH and then washed with ethanol.

#### 4.3.2.2.3. Effect of the polymer molecular weight

PAAH with different molecular weight (2000, 5000, 100 000 and 240 000  $\text{g}\cdot\text{mol}^{-1}$ ) has been added at the optimal concentration of 0.63 wt% during the synthesis to obtain ZnO/PAAH nanocomposites. The molecular weight of PAAH influences in an unusual manner the nanocomposite morphology and properties, as shown in the XRD diffractograms of **Figure 4.40**. The estimated ZnO NPs crystalline domain sizes deduced from the XRD diffractograms presented in **Figure 4.40** using Scherrer's formula are summarized in **Table 4.5**.

While a molecular weight of 2000  $\text{g}\cdot\text{mol}^{-1}$  leads, as already mentioned, to small ( $\sim 8$  nm) ZnO wurzite nanoparticles in polymer spheres, the use of chains of 5000  $\text{g}\cdot\text{mol}^{-1}$  leads to a diffractogram often seen in disordered ZnO or  $\text{Zn}(\text{OH})_2$  [22]. The two peaks at  $33.4^\circ$  and  $60^\circ$  are also found in the diffractograms of small hydrozincite particles ( $\text{Zn}_5(\text{OH})_6(\text{CO}_3)_2$ ) [33] but the latter phase is unlikely to occur in our synthesis process. The ZnO NPs size in the case of the synthesis with the chains of 5000  $\text{g}\cdot\text{mol}^{-1}$  estimated using Scherrer's equation is 5 nm. When the molecular weight of the PAAH is increased to 100 000  $\text{g}\cdot\text{mol}^{-1}$ , the wurzite structure is recovered and the corresponding size is about 8 nm. However, additional peaks corresponding to the  $\epsilon$ - $\text{Zn}(\text{OH})_2$  compound (wulfingite) are clearly seen. Eventually, for a molecular weight of 240 000  $\text{g}\cdot\text{mol}^{-1}$ , the sample is amorphous. Here again it is instructive to compare the XRD data to the TEM images, presented in **Figure 4.41**. As discussed previously, for a molecular weight of 2000  $\text{g}\cdot\text{mol}^{-1}$ , the sample consists of large polymer spheres embedding small ZnO nanoparticles. At a molecular weight of 5000  $\text{g}\cdot\text{mol}^{-1}$ , the general geometry is identical, but the polymer spheres look smaller and no ZnO particle is distinguishable. For a molecular weight of 100 000  $\text{g}\cdot\text{mol}^{-1}$ , the

crystalline ZnO nanoparticles are observed as dark zones in an extended bright polymer matrix. At the highest molecular weight of 240 000 g·mol<sup>-1</sup>, in agreement with the XRD data, no particle is observed and the polymer matrix appears stringy rather than spherical.

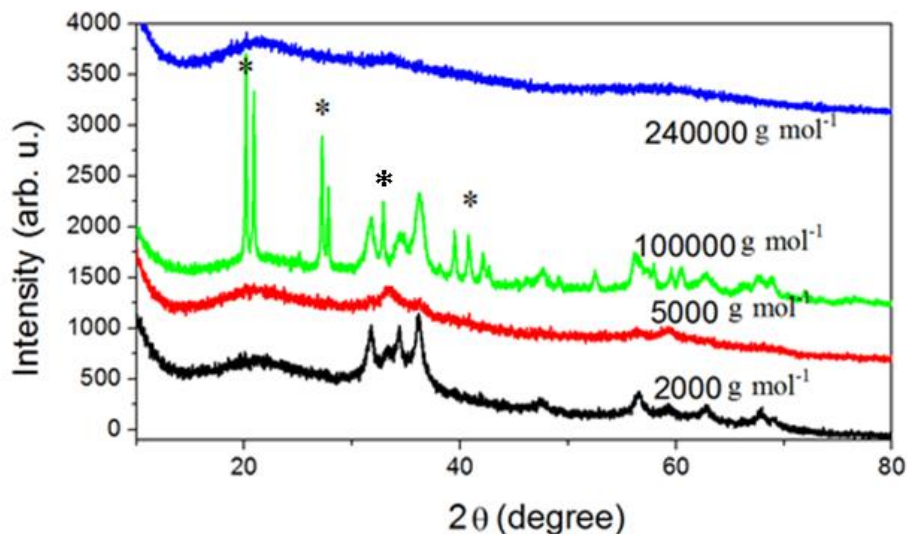


**Figure 4.40:** XRD diffractograms of ZnO nanoparticles synthesized by the hydrolysis of ZnEt<sub>2</sub> with different lengths of PAAH of 0.63 wt% (240 000, 100 000, 5000 and 2000 g·mol<sup>-1</sup> from top to bottom). The plots are shifted along the y-axis for clarity. Peaks labeled with \* refer the Zn(OH)<sub>2</sub> wulfingite phase.

**Table 4.5:** ZnO NPs crystalline domain sizes deduced from the XRD diffractograms presented in **Figure 4.40** using Scherrer's formula.

Molecular weight of PAAH (g·mol <sup>-1</sup> )	Crystalline domain size (nm)
2000	8
5000	5
100 000	8

The corresponding optical properties are obviously affected by the PAAH molecular weight, as can be seen in **Figure 4.42**. As the PAAH weight increases from 2000 to 5000 g·mol<sup>-1</sup>, the nanocomposite is made of mesospheres, but has an overall inferior crystalline quality than for 2000 g·mol<sup>-1</sup> and the PL QY rises from 19 % to 33 %. A UV emission appears at 363 nm, while the visible emission shifts from 540 nm to 516 nm. The excitonic emission peak is blue-shifted with respect to the bulk ZnO (~ 380 nm). This shift may be attributed to the quantum confinement effect. Assuming that this statement is true, we estimate the size of the quantum dots to be about 5 nm [34]. Then, the blue-shift of the visible emission can be explained, since it has been shown that the deep levels in the bandgap related to the visible emission are also subject to the quantum confinement effect [8]. When the PAAH weight increases to 100 000 g·mol<sup>-1</sup>, the

PL spectrum and PL QY (3 %) are identical to those of the ZnO nanoparticles synthesized without PAAH. In this case, the optical properties of ZnO/PAAH nanocomposites are not influenced by the presence of PAAH because the interaction between PAAH with longer carbon chains (corresponding to higher weight) and ZnO nanoparticles is weaker [35]. A much higher PAAH weight ( $240\,000\text{ g}\cdot\text{mol}^{-1}$ ) induces amorphous nanocomposites with a PL spectrum shifted to the blue range and a low PL QY (8 %), as in the case of a high concentration of the small chain PAAH ( $M_w = 2000\text{ g}\cdot\text{mol}^{-1}$ , **Figure 4.29**). At a high concentration of the small chain PAAH or at a low concentration of long chain PAAH, the steric hindrance caused by the PAAH is identical and limits the hydrolysis and the nucleation of ZnO particles. Consequently, as far the PL QY value is concerned, a low molecular weight of PAAH should be favored.

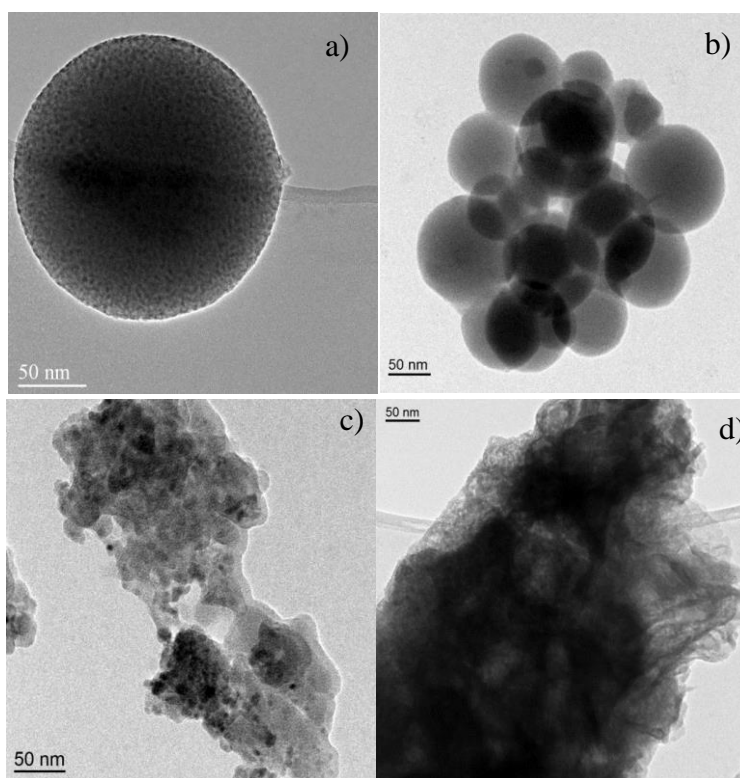


**Figure 4.41:** TEM images of ZnO nanoparticles synthesized by the hydrolysis of  $\text{ZnEt}_2$  with PAAH of 0.63 wt% of (a)  $2000\text{ g}\cdot\text{mol}^{-1}$ , (b)  $5000\text{ g}\cdot\text{mol}^{-1}$ , (c)  $100\,000\text{ g}\cdot\text{mol}^{-1}$  and (d)  $240\,000\text{ g}\cdot\text{mol}^{-1}$ .

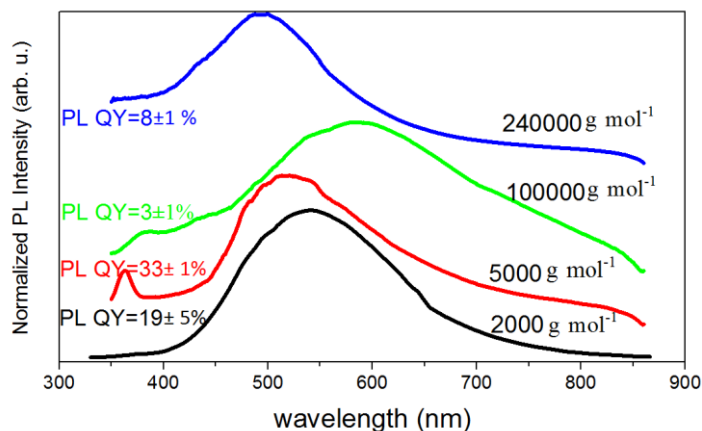


**Figure 4.42:** PL spectra of ZnO nanoparticles synthesized by the hydrolysis of  $ZnEt_2$  with different lengths of PAAH of 0.63 wt% (240 000, 100 000, 5000 and 2000  $g \cdot mol^{-1}$  from top to bottom). The plots are shifted along the y-axis for clarity.

#### 4.3.2.2.4. Effect of the polymer nature

To examine the ZnO/PAAH nanocomposites formation mechanism, PAAH has been substituted with 0.63 wt% of PAANa ( $M_w = 4000 g \cdot mol^{-1}$ ). The FTIR spectrum of the ZnO NPs synthesized with PAANa presented in **Figure 4.43** (a) shows the presence of deprotonated carboxylate groups ( $COO^-$ ) modes (at  $1568$  and  $1404 cm^{-1}$ ), but their amount is much smaller than that of the OH groups, when compared to the case of ZnO NPs fabricated with the PAAH. The broad feature around  $3400 cm^{-1}$  corresponds to the stretching mode of the O-H bond, indicating the presence of hydroxide groups OH in the sample. It can be noticed that the relative intensity of this band compared to the intensity of  $COO^-$  bands in **Figure 4.43** (a) is much smaller than in the case of the ZnO NPs fabricated with 0.63 wt% of PAAH (see **Figure 4.25**), that is why we conclude that the quantity of  $COO^-$  with respect to  $OH^-$  is lower for the 0.63 wt% PAANa sample than for the 0.63 wt% PAAH sample.

Also, the ZnO stretching mode can be clearly noticed, indicating a good crystallinity. This is confirmed by the Raman spectrum of the sample presented in **Figure 4.43** (b), which shows the usual modes of the ZnO wurtzite structure. In fact, the Raman spectrum, PL spectrum and PL QY of the ZnO/PAAH nanocomposite synthesized using PAANa as shown in **Figure 4.43** (c) are similar to those of the ZnO NPs synthesized without any surfactant. In both cases, the ZnO NPs have the wurtzite crystalline structure [3]. Consequently, the presence of H (in PAAH) is beneficial to the synthesis of highly luminescent disordered nanocomposites. We can also notice that the difference in wavenumber of the  $COO^-$  modes is larger in the present case than in the case of PAAH addition. This reveals that the interaction of the carboxylate group is closer to a mono-dentate bond in the present case whereas it adopts a bi-dentate (or bridging) interaction when PAAH is used. The nature of PAAX (X =H or Na) therefore controls the surface of the ZnO particles.

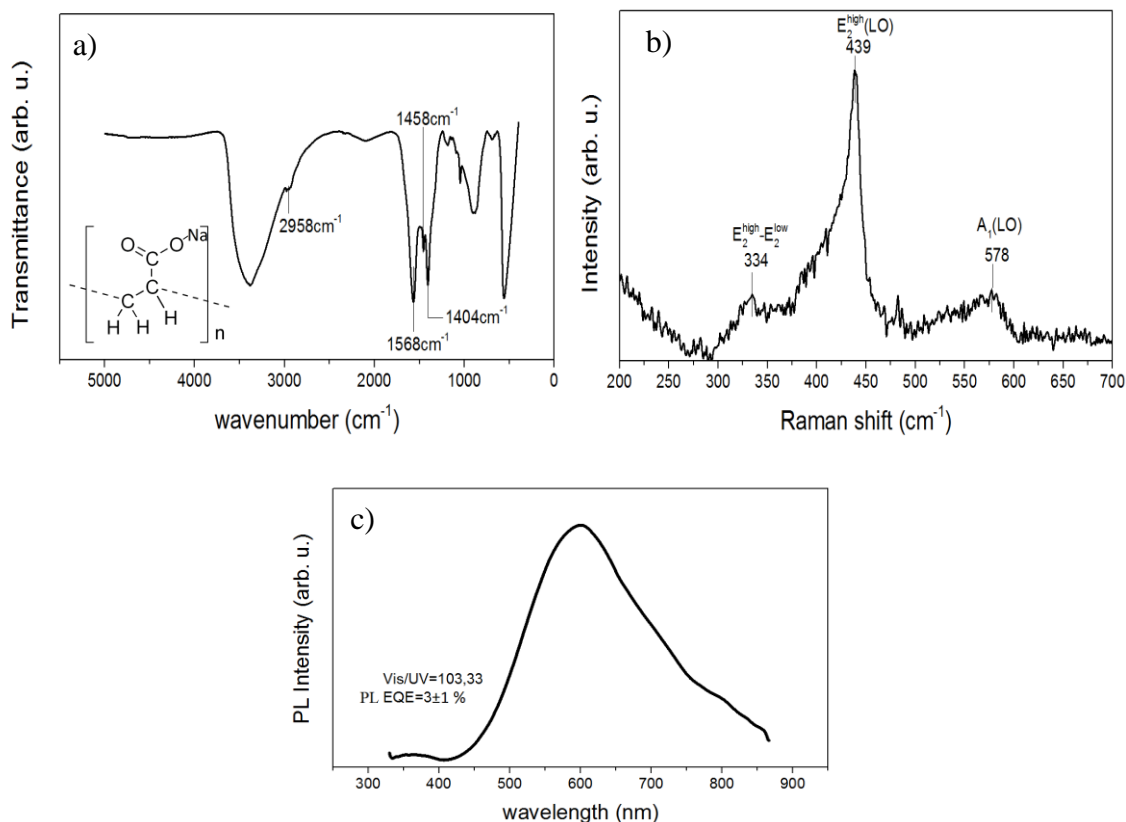


**Figure 4.43:** (a) FTIR spectrum; (b) Raman spectrum and (c) PL spectrum of ZnO NPs synthesized by the hydrolysis of ZnEt<sub>2</sub> with 0.63 wt% of PAANa. Inset: chemical formula of PAANa.

Mixing PAANa with PAAH (volume ratio of 25:75) at optimal 0.63 wt% is found to be highly beneficial for the visible emission. While the PL spectrum does not change when compared to the sample synthesized with 0.63 wt% of PAAH, the PL QY is increased to 50 % and even higher to 70 % after a one month exposure to air, as shown in **Figure 4.44** (a). The QY increase over one month can be explained by the OH group adsorption at the ZnO NPs surface and the diffusion into the sample. Such an effect has already been reported [8] and the presence of OH groups is known to increase the visible emission of ZnO. However, no synergetic effect such as the one of PAAH and PAANa put together has been reported to the best of our knowledge. The XRD spectrum of the sample synthesized with 75:25 PAAH and PAANa does not reveal the presence of any wurzite phase. On the contrary, as for the sample synthesized with pure PAAH of  $M_w = 5000 \text{ g}\cdot\text{mol}^{-1}$ , it points to the presence of highly disordered Zn(OH)<sub>2</sub> or, less likely, the hydrozincite particles in an amorphous material (cf. **Figure 4.44** (b)). The exact interaction between PAAH and PAANa and ZnO is not easy to describe, but it can be said that adding PAANa modifies the dissociation of PAAH described by the equation (4.1) and shifts the equilibrium to the left hand side term. As stated above, this will impact the shape of the nanoparticles, the nature of the planes constituting the particles as well as their crystalline quality.

It thus seems that the interaction of the protonated form PAAH with the precursor ( $\text{ZnEt}_2$ ) is beneficial as far as luminescence quantum yield is concerned.

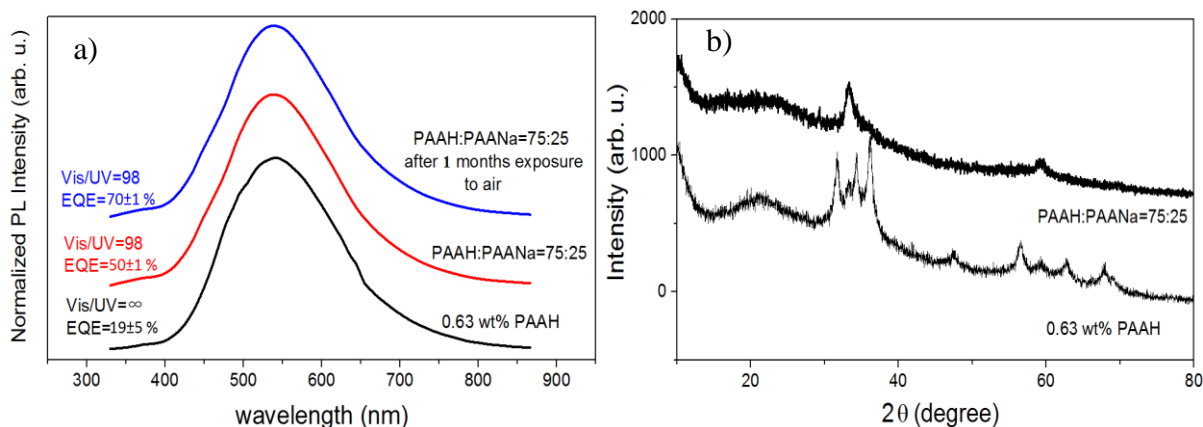


**Figure 4.44:** (a) PL spectra of ZnO nanoparticles synthesized by the hydrolysis of  $\text{ZnEt}_2$  with 0.63 wt% of PAAH only (bottom curve) and with PAAH and PAA<sub>N</sub>a of 75:25 (middle curve) and after 1 month exposure to air (top curve). (b) XRD diffractograms of ZnO nanoparticles synthesized by the hydrolysis of  $\text{ZnEt}_2$  with 0.63 wt% of PAAH only (bottom curve) and with PAAH and PAA<sub>N</sub>a of 75:25 (top curve). The plots are shifted along the y-axis for clarity.

TRPL measurement has been performed on this sample with the detection wavelength fixed at the peak position of its emission spectrum of 540 nm, and the PL decay and the results of the fitting procedure are shown in **Figure 4.45**. Like for the sample synthesized with 0.63 wt% of PAAH, also for this sample, two contributions can be distinguished. The prominent fast component is now characterized by a decay time  $\tau_1$  of 65 ns while the minor slow component has a decay time  $\tau_2$  of 787 ns. Both decay times are increased, indicating a reduced effect of the non-radiative centers. In the literature, three components with decay times differing by at least one order of magnitude have been reported. Typically, a fast component ( $< 10$  ns) is observed for the emission in the blue. The green visible emission is characterized by an extremely long decay time between 1340 ns and 1850 ns [36]. Eventually, as mentioned above, a third intermediate component is reported with a decay time of 60 ns, but it has not been assigned definitely. In our case, we observe only two components (no blue emission) with a decay time of a few tens of ns and a longer one of several hundred ns. The first one is largely dominant and may correspond to the unassigned contribution reported in the literature which would be specific to the surface states induced by the presence of an organic acid.

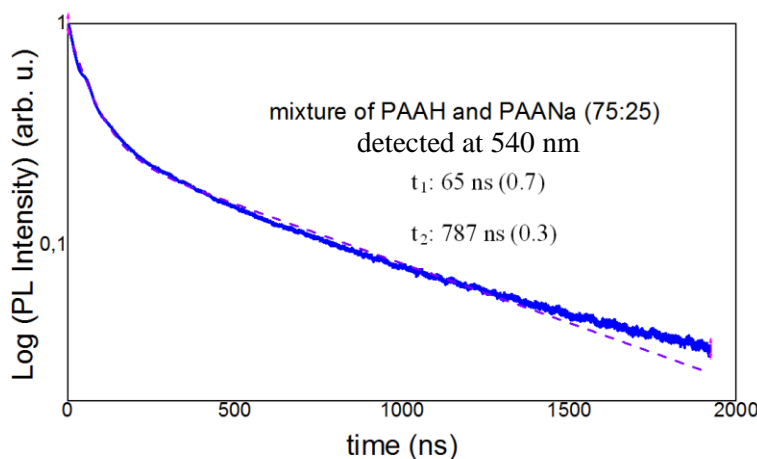


**Figure 4.45:** TRPL decay curves and corresponding biexponential fits (violet dash lines) results of ZnO nanoparticles synthesized by the hydrolysis of  $\text{ZnEt}_2$  with the mixture of PAAH with PAANa (0.63 wt%, 75:25 in volume) as the detection wavelength fixed at the peak position of its emission spectrum 540 nm.

#### 4.3.2.2.5. Conclusions

We have reported on the hydrolysis of  $\text{ZnEt}_2$  in the presence of PAAH. The addition of PAAH during the synthesis instead of after it proves to be a cost effective method to synthesize scalable amounts of highly luminescent ZnO/PAAH nanocomposites. The effects on the ZnO luminescence of the PAAH addition during the synthesis are opposite to those of PAAH used as a capping agent on ZnO NPs. In particular, the UV emission is suppressed while the intensity of the visible emission is increased. The key parameter lies in the control of the degree of crystalline disorder of the ZnO nanoparticles embedded in the composite. Surprisingly, a rather large degree of disorder is required to obtain a high PL QY. This control can be obtained by tuning the PAAH concentration. Below the optimum concentration of 0.63 wt%, the addition of PAAH has no significant effect on the PL QY of the synthesized ZnO NPs. Over the optimum concentration too large a disorder is induced, leading to a completely amorphous material. At the optimum concentration of 0.63 wt%, the PL QY approaches 20 % and remains stable over weeks. The molecular weight of the PAAH molecules used also has a major influence. Low molecular weights (i.e. small chains) are more efficient to achieve a high PL QY. Eventually, a mixture of PAAH and PAANa (75:25 in volume) is extremely favorable for high photoluminescence efficiency. The PL QY rises up to 50 % and even to 70 % after one month, making this nanocomposite an interesting alternative to existing high QY luminescent nanomaterials. To explain this enhancement, a model based on the type II heterostructure formed by ZnO/PAAH is proposed.

## 4.3.2.2.6. Problem of the dispersion of ZnO NPs

The ZnO NPs synthesized with the addition of 0.63 wt% of PAAH ( $2000 \text{ g}\cdot\text{mol}^{-1}$ ) in the hydrolysis method were used to prepare a colloidal dispersions to be used for the deposition of the down-shifting layer. These nanoparticles in a form of powder have been dispersed in an aqueous solution containing different amounts of PAAH used as a surfactant. It has been demonstrated that these ZnO NPs can be homogeneously dispersed, which is due to their high zeta potential value as shown in zeta potential distribution spectrum in **Figure 4.46**. Usually, a colloidal dispersion with its zeta potential value close to  $\pm 30 \text{ mV}$  or the absolute zeta potential value higher than  $30 \text{ mV}$  is considered as stable and homogeneous [37]. The average zeta potential of the dispersion system containing 0.63 wt% of PAAH ( $2000 \text{ g}\cdot\text{mol}^{-1}$ ) in an aqueous solution with 31.5 wt% of PAAH is estimated to be  $-19 \text{ mV}$  over the measured range shown in **Figure 4.46**, so it is expected to be a relatively good and stable dispersion.

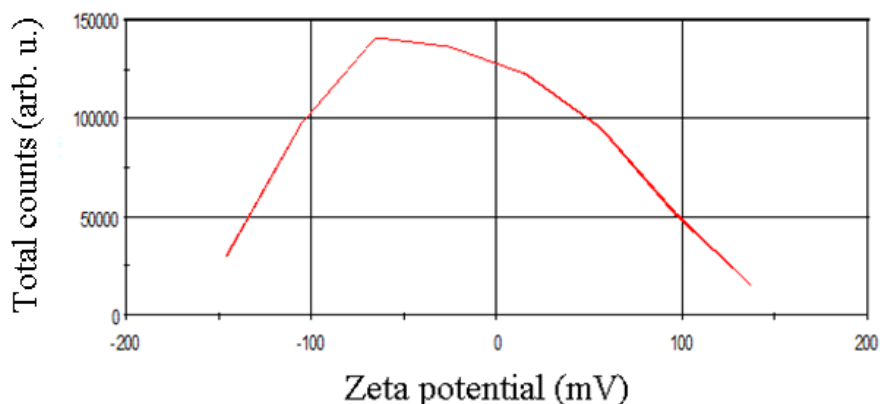


**Figure 4.46:** Zeta potential distribution spectrum of ZnO nanoparticles synthesized by the hydrolysis of  $\text{ZnEt}_2$  with 0.63 wt% of PAAH and of  $M_w = 2000 \text{ g}\cdot\text{mol}^{-1}$ , dispersed in an aqueous solution containing 31.5 wt% of PAAH.

**Table 4.6:** Dispersion quantity and fraction of ZnO nanoparticles in different concentrations of PAAH in aqueous solution.

PAAH concentration (wt%)	Mass of ZnO NPs put in the solution (mg)	Mass of ZnO NPs in the suspension (mg)	Weight fraction of the dispersed ZnO NPs with respect to the total weight of the solution
3.15	150	84	0.84%
6.3	330	184.8	1.85%
12.6	600	327	3.27%
21	810	441.45	4.41%

31.5	950	522.5	5.23%
------	-----	-------	-------

The quantity of ZnO NPs dispersed in 10 mL PAAH solution is also determined by the concentration of the PAAH, as shown in **Table 4.6**. The higher the PAAH concentration, the more ZnO NPs can be dispersed in the solution. This can be easily observed in the diagram showing the quantity of ZnO NPs in suspension as a function of PAAH solution concentration presented in **Figure 4.47**.

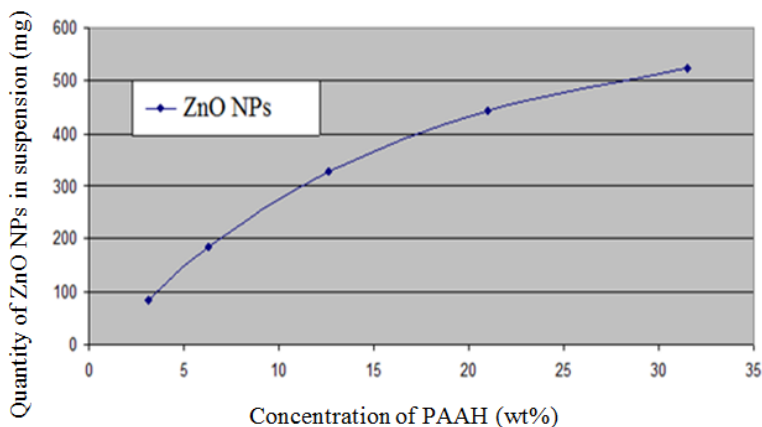


**Figure 4.47:** Diagram of the quantity of ZnO NPs dispersed in 10 mL suspension in function of PAAH concentration.

However, there is a problem with the dispersion of the ZnO NPs synthesized by hydrolysis method in which PAAH is added during the synthesis. These ZnO NPs can only be dispersed in solutions containing high amount of PAAH, but cannot be dispersed in water, ethanol or other common solvents, so the subsequent fabrication of a luminescent down-shifting (LDS) layer is limited. Moreover, after the dispersion in the solution of PAAH, the green emission from the ZnO NPs is suppressed. Instead, the solutions emit blue light, which degrades the down-shifting effect efficiency.

As a preliminary study, the ZnO NPs synthesized with the addition of 0.63 wt% of PAAH with a molecular weight of  $2000 \text{ g}\cdot\text{mol}^{-1}$  in the hydrolysis method have been dispersed in PAAH solutions with different concentrations, then deposited on fused silica or freeze-dried. Such prepared samples were then studied by the PL and their PL spectra are presented in **Figure 4.48**. A blue shift of the PL can be clearly observed. It is obvious that the blue shift of the PL spectra is caused by the capping of the PAAH added after the synthesis. It may be due to the passivation of the green emission related defects, while the ZnO/polyacrylic acid complexes are formed by the H bonding which are responsible for the blue emission, as discussed previously.

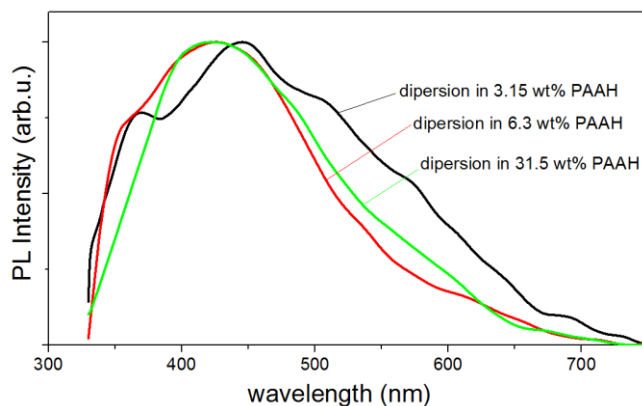


**Figure 4.48:** PL spectra of ZnO nanoparticles synthesized by the hydrolysis of  $\text{ZnEt}_2$  with 0.63 wt% of PAAH at  $2000 \text{ g}\cdot\text{mol}^{-1}$ , dispersed in the solution with different concentrations of PAAH.

It is also interesting to mention that the PAAH added during and after the synthesis of the ZnO NPs will influence their optical properties in different ways. The addition of the PAAH after the ZnO NPs synthesis simply passivates the NPs surface, while the addition of the PAAH during the ZnO NPs synthesis not only passivates the NPs, but also influences the chemistry of the synthesis reaction, according to the concentration of PAAH added. In conclusion, we can control the ZnO NPs emission not only through the size, morphology and surfactant concentration, but also tune it via the surfactant addition procedure.

Since the obtained ZnO NPs are difficult to disperse in common solvent solutions, we have tried to deposit the solution containing ZnO NPs in PAAH matrix on a fused silica glass and then deposit a PMMA layer on its top, as shown in **Figure 4.49**. We have measured the PL spectra of different part of this structure including the fused silica glass, pure PMMA, the layer containing ZnO NPs in PAAH and the PMMA layer on the top of ZnO NPs layer. The results are shown in **Figure 4.50**, the lines adopt the colors of the corresponding region where the signal comes from in **Figure 4.49**.

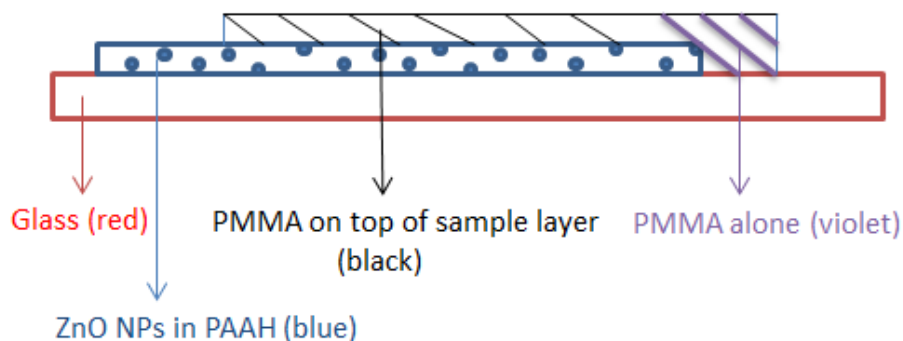


**Figure 4.49:** Diagram of the process of the deposition of one layer containing ZnO NPs in PAAH matrix and then another layer of PMMA on its top.

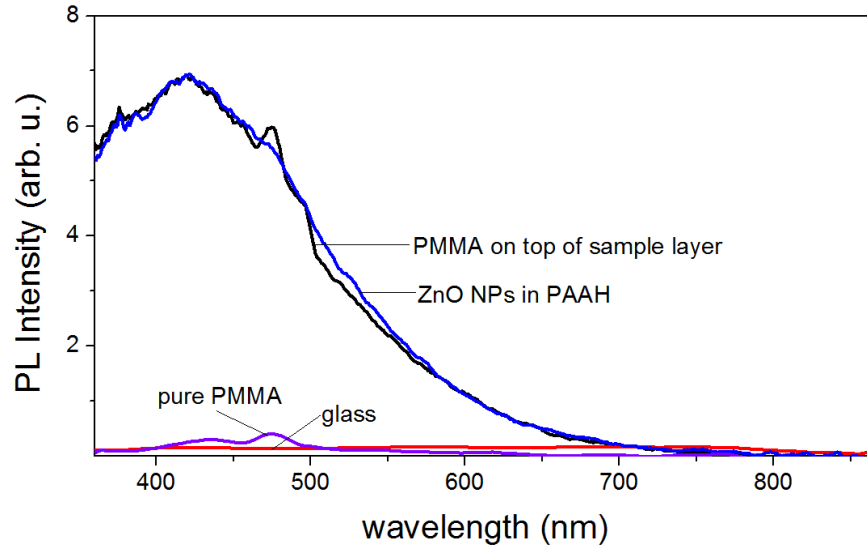


**Figure 4.50:** PL spectra of different parts of the structure shown in Figure 4.49, including the fused silica glass, the pure PMMA, the layer containing ZnO NPs in PAAH matrix and the PMMA layer on the top of the ZnO NPs layer.

As can be seen in **Figure 4.50**, the fused silica glass and the pure PMMA show a weak emission in the spectral range between 350 and 850 nm and the PL spectra are almost the same before and after the PMMA layer deposited on the ZnO + PAAH layer. It paves a way for the deposition and stabilization of ZnO NPs as a down-shifting layer on the front side of the photovoltaic devices. Even though we can't disperse ZnO NPs in a PMMA solution, if we can fabricate dispersible ZnO NPs in another solvent or find another solvent which can disperse them and meanwhile will not be detrimental to their visible emission (not like PAAH), we can deposit the solution containing ZnO NPs as one layer and deposit a PMMA solution on its top to stabilize it. Thus it can make the ZnO NPs layer stable while not influencing its optical properties.

## 4.4. Conclusions

In this chapter, we have presented the results of the structural and optical studies of ZnO NPs synthesized by different methods: the LECBD and the sol-gel methods. Some commercially available ZnO nanoparticles were also studied for comparison.

The preliminary study of the down-shifting layer containing ZnO NPs placed on the front side of solar cells or photodiodes has been presented. A potential increase in the external quantum efficiency of the photovoltaic devices in the UV range with the down-shifting layer was demonstrated, when the initial efficiency in the UV of the photodiode is low. This EQE increase was assumed to be due not to the down-shifting effect of ZnO NPs but rather to the anti-reflection effect of the down-shifting layer. However, the external quantum efficiency of the photovoltaic devices in the total studied spectral range was reduced. The parasite absorption was not compensated due to the low PL QY of the ZnO NPs. The LECBD deposited nanoparticles, as well as the commercial ones exhibited very low PL QY, which made them virtually useless for down-shifting applications.

Secondly, we have focused on the sol-gel methods. Two sol-gel methods have been studied with the purpose to improve the PL QY of ZnO NPs, i.e. the co-precipitation method and the hydrolysis method. The results of the physical, chemical and optical characteristics have been present in detail.  $\text{Li}^+$  ions and PAAH have been found to have a beneficial effect on the green emission efficiency with the PL QY increase to 13 % and 19 % when added to co-precipitation and hydrolysis reaction milieu, respectively. The concentration of  $\text{Li}^+$  ions and the concentration and the molecular weight of PAAH affected the size, morphology and optical properties of ZnO NPs. The use of 0.63 wt% of PAAH ( $5000 \text{ g}\cdot\text{mol}^{-1}$ ) was found to be optimal for the green emission, with the PL QY enhanced to 33 %. More interestingly, washing the ZnO NPs with ethanol proved further improvement of the ZnO NPs PL QY. Mixing PAAH with PAAH with the ratio 25:75 increased the PL QY of the green emission dramatically to 50 %. It increased up to 70 % after the exposure to air after one month. The mechanisms of the improvement of the visible emission efficiency in the two sol-gel methods have been proposed and discussed.

Finally, the problem of the dispersion of the ZnO NPs synthesized with the hydrolysis method has been stated. The ZnO NPs functionalized by PAAH could be dispersed in a PAAH solution, but not in other solvents like water or ethanol. Furthermore, the dispersion of ZnO NPs induced another problem: the dispersion in the PAAH solution quenched the green emission, and instead, led to a blue emission. Thus, the dispersion in the PAAH solution is not good for the fabrication of the down-shifting layer for photovoltaic devices. We should search for other ways to prepare ZnO NPs dispersible in common solvents like water for example, for the further applications, while maintaining a high PL QY in the visible range. We also proved that the PMMA layer deposition on the top of ZnO NPs layer did not influence its optical properties, which paved a way for the down-shifting layer preparation. We do not need to disperse the ZnO NPs in PMMA solution, we can deposit layer by layer to fabricate the down-shifting layer.

## 4.5. References

1. Taïnoff D., Influence des défauts sur les propriétés optiques et électroniques de nanoparticules de ZnO. PhD thesis, Université Claude Bernard - Lyon 1, 2009. (Accession Order No. 259-2009).
2. Damen T. C., Porto S. P. S., Tell B., Raman Effect in Zinc Oxide. *Physical Review*, 1966, vol. 142, p. 570-574.
3. Lin W. W., Chen D. G., Zhang J. Y., Lin Z., Huang J. K., Li W., Wang Y. H., Huang F., Hydrothermal Growth of ZnO Single Crystals with High Carrier Mobility. *Crystal Growth & Design*, 2009, vol. 9, p. 4378–4383.
4. Dem'yanets L. N., Kostomarov D. V., Kuz'mina I. P., Chemistry and Kinetics of ZnO Growth from Alkaline Hydrothermal Solutions. *Inorganic Materials*, 2002, vol. 38, p. 171–179.
5. Singh J., Mittu B., Chauhan A., Sharma A., Singla M. L., Role of alkali metal hydroxide in controlling the size of ZnO nanoparticles in non-aqueous medium. *International Journal of Fundamental and Applied Sciences*, 2012, vol. 1, p. 91-93.
6. Pourrahimi A. M., Liu D., Pallon L. K. H., Andersson R. L., Martínez Abad A., Lagarón J. -M., Hedenqvist M. S., Ström V., Gedde U. W., Olsson R. T., Water-based synthesis and cleaning methods for high purity ZnO nanoparticles – comparing acetate, chloride, sulphate and nitrate zinc salt precursors. *RSC Advances*, 2014, vol. 4, p. 35568-35577.
7. Felbier P., Yang J., Theis J., Liptak R. W., Wagner A., Lorke A., Bacher G., Kortshagen U., Highly Luminescent ZnO Quantum Dots Made in a Nonthermal Plasma. *Advanced Functional Materials*, 2014, vol. 24, p. 1988-1993.
8. McCluskey M. D., Jokela S. J., Defects in ZnO. *Journal of Applied Physics*, 2009, vol. 106, p. 071101/1-13.
9. Leung Y. H., Chen X. Y., Ng A. M. C., Guo M. Y., Liu F. Z., Djurišić A. B., Chan W. K., Shi X. Q., Van Hove M. A., Green emission in ZnO nanostructures—Examination of the roles of oxygen and zinc vacancies. *Applied Surface Science*, 2013, vol. 271, p. 202– 209.
10. Li M., Xing G., Wu B., Wu T., Zhang X., Sum T. C., Origin of green emission and charge trapping dynamics in ZnO nanowires. *Physical Review B*, 2013, vol. 87, p. 115309/1-8.
11. Li D., Leung Y. H., Djurišić A. B., Liu Z. T., Xie M. H., Shi S. L., Xu S. J., Chan W. K., Different origins of visible luminescence in ZnO nanostructures fabricated by the chemical and evaporation methods. *Applied Physics Letters*, 2004, vol. 85, p. 1601-1603.
12. Gorai P., Seebauer E. G., Surface-Based Defect Engineering of Metal Oxides. Center for Nanoscale Science and Technology, UIUC (2013).
13. Lv Y., Xiao W., Li W., Xue J., Ding J., Controllable synthesis of ZnO nanoparticles with high intensity visible photoemission and investigation of its mechanism. *Nanotechnology*, 2013 vol. 24, no. 17, p. 175702/1-10.
14. An W., Wu X. J., Zeng X. C., Adsorption of O<sub>2</sub>, H<sub>2</sub>, CO, NH<sub>3</sub>, and NO<sub>2</sub> on ZnO Nanotube: A Density Functional Theory Study. *The Journal of Physical Chemistry C*, 2008, vol. 112, no. 15, p. 5747–5755.
15. Morales-Flores N., Galeazzi R., Rosendo E., Díaz T., Velumani S., Pal U., Morphology control and optical properties of ZnO nanostructures grown by ultrasonic synthesis. *Advances in Nano Research*, 2013, vol. 1, p. 59-70.
16. Zhou H., Alves H., Hofmann D. M., Kriegseis W., Meyer B. K., Kaczmarczyk G., Hoffmann A. Behind the weak excitonic emission of ZnO quantum dots: ZnO/Zn(OH)<sub>2</sub> core-shell structure. *Applied Physics Letters*, 2002, vol. 80, p. 210-212.

17. Guo L., Yang S. H., Yang C. L., Yu P., Wang J. N., Ge W. K., Wong G. K. L., Highly monodisperse polymer-capped ZnO nanoparticles: Preparation and optical properties. *Applied Physics Letters*, 2000, vol. 76, no. 20, p. 2901-2903.
18. Yuvaraj D., Ra K.N., Optical and electrical properties of ZnO films deposited by activated reactive evaporation. *Vacuum*, 2008, vol. 82, p. 1274–1279.
19. Nesakumar N., Rayappan J. B. B., Jeyaprakash B. G., Krishnan U. M., Influence of pH on Structural Morphology of ZnO Nanoparticle. *Journal of Applied Sciences*, 2012, vol. 12, p. 1758-1761.
20. Jones F., Farrow J. B., van Bronswijl W., An Infrared Study of a Polyacrylate Flocculant Adsorbed on Hematite. *Langmuir*, 1988, vol. 14, p. 6512-6517.
21. Zhang B. B., Kong T., Xu W. Z., Su R. G., Gao Y. H., Cheng G. S., Surface Functionalization of Zinc Oxide by Carboxyalkylphosphonic Acid Self-Assembled Monolayers. *Langmuir*, 2010, vol. 26, p. 4514–4522.
22. Lin B. C., Shen P., Chen S. Y., ZnO and  $\epsilon$ -Zn(OH)<sub>2</sub> Composite Nanoparticles by Pulsed Laser Ablation on Zn in Water. *The Journal of Physical Chemistry C*, 2011, vol. 115, p. 5003–5010.
23. Zhang J. H., Dong G. J., Thurber A., Hou Y. Y., Gu M., Tenne D. A., Hanna C. B., Punnoose A., Tuning the Properties of ZnO, Hematite, and Ag Nanoparticles by Adjusting the Surface Charge. *Advanced Materials*, 2012, vol. 24, p. 1232-1237.
24. Richters J. -P., Voss T., Wischmeier L., Rückmann I., Gutowski J., Influence of polymer coating on the low-temperature photoluminescence properties of ZnO nanowires. *Applied Physics Letters*, 2008, vol. 92, p. 011103/1-3.
25. Du X. W., Fu Y. S., Sun J., Han X., Liu J., Complete UV emission of ZnO nanoparticles in a PMMA matrix. *Semiconductor Science and Technology*, 2006, vol. 21, p. 1202-1206.
26. Liu X., Wu X. H., Cao H., Chang R. P. H., Growth mechanism and properties of ZnO nanorods synthesized by plasma-enhanced chemical vapor deposition. *Journal of Applied Physics*, 2004, vol. 95, p. 3141-3147.
27. Tian X. Q., Xu J. B., Xie W. G., Controllable Modulation of the Electronic Structure of ZnO (10 $\bar{1}0$ ) Surface by Carboxylic Acids. *The Journal of Physical Chemistry C*, 2010, vol. 114, p. 3973–3980.
28. Kunze C., Valtiner M., Michels R., Huber K., Grundmeier G., Self-localization of polyacrylic acid molecules on polar ZnO(0001)-Zn surfaces. *Physical Chemistry Chemical Physics*, 2011, vol. 13, p. 12959-12967.
29. Leung Y. H., Chena X. Y., Nga A. M. C., Guo M. Y., Liu F. Z., Djurišić A. B., Chan W. K., Shi X. Q., Van Hoved M. A., Green emission in ZnO nanostructures—Examination of the roles of oxygen and zinc vacancies. *Applied Surface Science*, 2013, vol. 271, no. 15, p. 202–209.
30. Xu F., Sun L. T., Solution-derived ZnO Nanostructures for Photoanodes of Dye-sensitized Solar Cells. *Energy & Environmental Science*, 2011, vol. 4, p. 818-841.
31. Fu Y. S., Du X. W., Kulinich S. A., Qiu J. S., Qin W. J., Li R., Sun J., Liu J., Stable aqueous dispersion of ZnO quantum dots with strong blue emission via simple solution route. *Journal of the American Chemical Society*, 2007, vol. 129, p. 16029-16033.
32. Shen Y., Ding D. F., Deng Y. Z., Fabrication and Characterization of Polycrystalline WO<sub>3</sub> Flocky Microspheres induced by ethanol. *Powder Technology*, 2011, vol. 211, p. 114-119.
33. Yang J., Guan Y. J., Verhoeven T., Santen R. V., Li C., Hensen E. J. M., Basic metal carbonate supported gold nanoparticles: enhanced performance in aerobic alcohol oxidation. *Green Chemistry*, 2009, vol. 11, p. 322-325.

34. Viswanatha Ranjani, Sapra S., Satpati B., Satyam P. V., Devb B. N., Sarma D. D., Understanding the quantum size effects in ZnO nanocrystals.
35. Chang J., Waclawik E. R., Experimental and theoretical investigation of ligand effects on the synthesis of ZnO nanoparticles. *Journal of Nanoparticle Research*, 2012, vol. 4, p. 1012/1-14.
36. Kahn M. L., Cardinal T., Bousquet B., Monge M., Jubera V., Chaudret B., Optical Properties of Zinc Oxide Nanoparticles and Nanorods Synthesized Using an Organometallic Method. *ChemPhysChem*, 2006, vol. 7, p. 2392 – 2397.
37. Ikono R., Maulana N. N., Dewinggih T., Effendi M., Widayanto W. B., Sukarto A., Rochman N. T., Effect of Polyacrylic Acid Addition to Improve Nano Zinc Oxide Dispersion Stability. *International Journal of Engineering & Technology*, 2012, vol. 12, no. 6, p. 95-99.



## Chapter 5

## Dispersion of ZnO nanoparticles

Even though ZnO nanoparticles (NPs) with high photoluminescence quantum yield (PL QY), reaching 50 % (or even 70 %) have been synthesized, the remaining challenge is to obtain their homogeneous and stable dispersion. Although these NPs can be dispersed in PAAH, the PL spectrum is drastically modified and it will be difficult to fabricate an efficient down-shifting layer as dispersing the required concentration of ZnO NPs, necessary to have a strong PL, is not possible (it is too high, over the limit of the dispersibility of ZnO NPs in the PAAH solution). So we should search a method to fabricate dispersible ZnO NPs in water which permits a high concentration of ZnO NPs as well as an easier layer fabrication.

### 5.1. ZnO nanoparticles dispersible in water

For ZnO NPs synthesized by the hydrolysis method with the addition of PAAH, the obtained NPs are not dispersible in water. Due to this fact, these NPs are not appropriate for the further integration in the industrial PV systems.

PAAH has hydrophilic groups (OH groups). It is a weak acid which is partially ionized according to the **Reaction 5.1**. On the contrary, sodium polyacrylate (PAANa) is a salt which is fully ionized, as described by the **Reaction 5.2**.



**Figure 5.1:** Picture of ZnO NPs synthesized by the hydrolysis of  $\text{ZnEt}_2$  with a mixture of PAAH and PAANa with the ratio of 50:50 in volume, the concentration of 0.63 wt% and the reaction time of 1h.

According to the equilibrium reactions 5.1 and 5.2, it can be noticed that by adding PAANa in PAAH solution, the ionized  $\text{PAA}^-$  concentration increases, so the equilibrium state in **Reaction 5.1** will be shifted in favor of the left hand side product. It results in more PAAH adsorption on the ZnO NPs and thus induces more hydrophilic groups on the NPs surface, which is beneficial for the dispersion in water. So as a first try, the surfactant in the hydrolysis method is changed from PAAH to the mixture of PAAH of  $2000 \text{ g}\cdot\text{mol}^{-1}$  and PAANa of  $4000 \text{ g}\cdot\text{mol}^{-1}$  with 0.63 wt% concentration, which is proven to be the optimum for obtaining a visible PL efficiency, as shown in Chapter 4. This mixture of PAAH and PAANa with a ratio of 50:50 in volume was added during the hydrolysis synthesis of ZnO NPs. In this case, the reaction time was reduced from 24 hours to 1 hour. From the picture in **Figure 5.1**, it can be seen that the solution containing the ZnO NPs synthesized using the mixture PAAH:PAANa is transparent, which indicates that ZnO NPs dispersible in water have been obtained.

From the size distribution spectrum in **Figure 5.2**, it can be concluded that the hydrodynamic diameter of these ZnO NPs is mainly in the 4-30 nm range. There are no crystalline wurtzite domains present, as illustrated in the corresponding XRD diffractogram (cf. **Figure 5.3**), probably because the reaction time of 1h is too short to form the crystalline nanoparticles. However, two small peaks at about  $33^\circ$  and  $60^\circ$ , already observed in XRD spectrum in section 4.3.2.2, are present also for ZnO NPs synthesized using the mixture PAAH:PAANa. As already mentioned, these features are often observed for amorphous samples containing a fraction of  $\text{Zn}(\text{OH})_2$ .

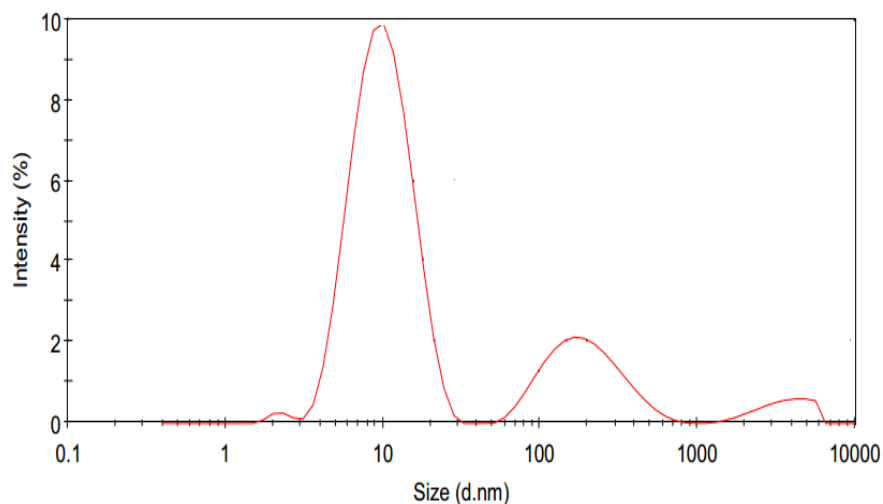


**Figure 5.2:** Size distribution measured by DLS measurement of ZnO NPs synthesized by the hydrolysis of  $\text{ZnEt}_2$  with a mixture of PAAH and PAANa at the ratio of 50:50 in volume, the concentration of 0.63 wt% and the reaction time of 1h.

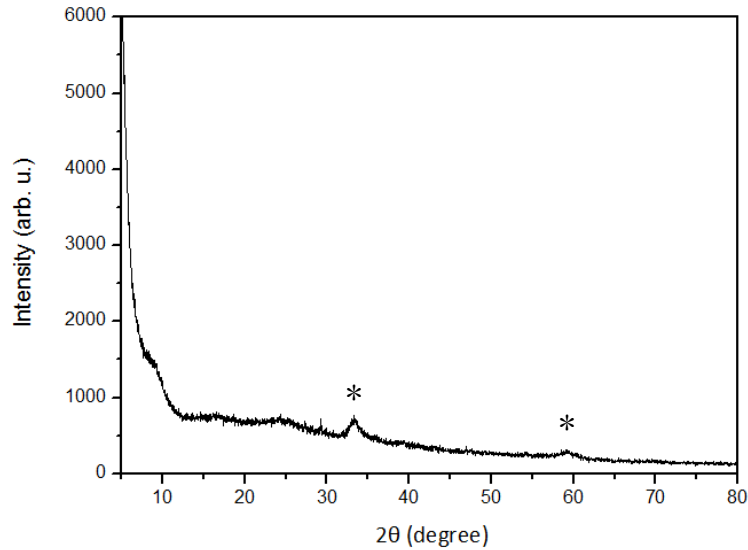


**Figure 5.3:** XRD diffractogram of ZnO nanoparticles synthesized by the hydrolysis of  $\text{ZnEt}_2$  with a mixture of PAAH and PAA Na at the ratio of 50:50 in volume, the concentration of 0.63 wt% and the reaction time of 1h. Peaks labeled with \* are often present in XRD diffractograms of badly crystallized samples containing Zn hydroxide.

Interestingly, the dispersible ZnO NPs emit in the green range, as can be seen in the PL spectrum in **Figure 5.4**. This is beneficial for the down-shifting. Furthermore, the PL QY remains relatively high, at 22 %.

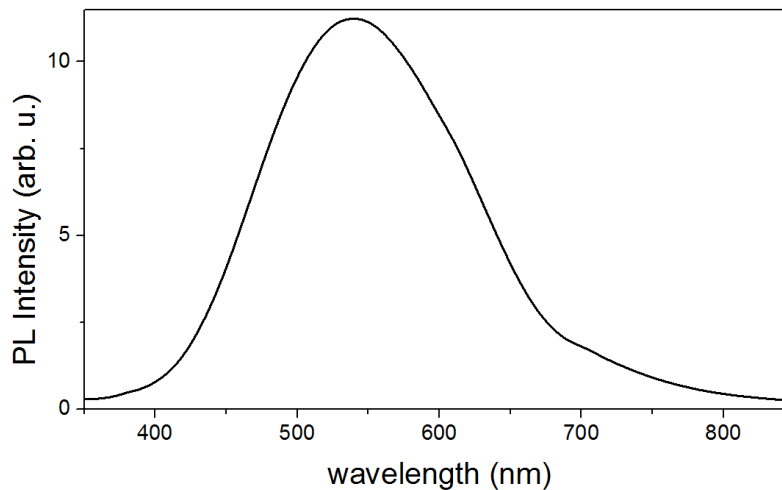


**Figure 5.4:** PL spectrum of ZnO nanoparticles synthesized by the hydrolysis of  $\text{ZnEt}_2$  with a mixture of PAAH and PAA Na at the ratio of 50:50 in volume, the concentration of 0.63 wt% and the reaction time of 1h.

## 5.2. Effect of the mixture ratio of PAAH and PAANa

It was demonstrated that with the addition of the mixture of PAAH and PAANa at the ratio of 50:50 in volume during the hydrolysis of Zn acetate, within one hour dispersible nanoparticles with a relatively high PL QY can be obtained. Different mixture volume ratios of PAAH and PAANa have then been added during the synthesis to check if the visible emission efficiency can be further improved, while keeping the dispersibility in water. When the mixture volume ratio of PAAH and PAANa is too high (75:25) or too low (25:75), the ZnO NPs are not dispersible in water, whereas the ZnO NPs synthesized with mixture volume ratios in between these two extremal values are dispersible. Thus it confirms the importance of the co-existence of the acid form and the deprotonated form of PAAH/PAANa for the dispersibility of ZnO NPs in water. When a too high fraction of the acid in the mixture form is introduced to react with ZnO NPs, ZnO/polyacrylic acid complexes via H bonding are formed, as was described in Chapter 4, when a high concentration or a long chain length of PAAH has been used. The blue emission from the ZnO NPs synthesized with the mixture volume ratio of PAAH and PAANa of 75:25 is also similar to the case when a high concentration or a long chain length of PAAH has been used, which confirms the assumption that the ZnO/PAAH complexes are formed in the case of 75:25 mixture used in the reaction (cf. **Figure 5.5**).

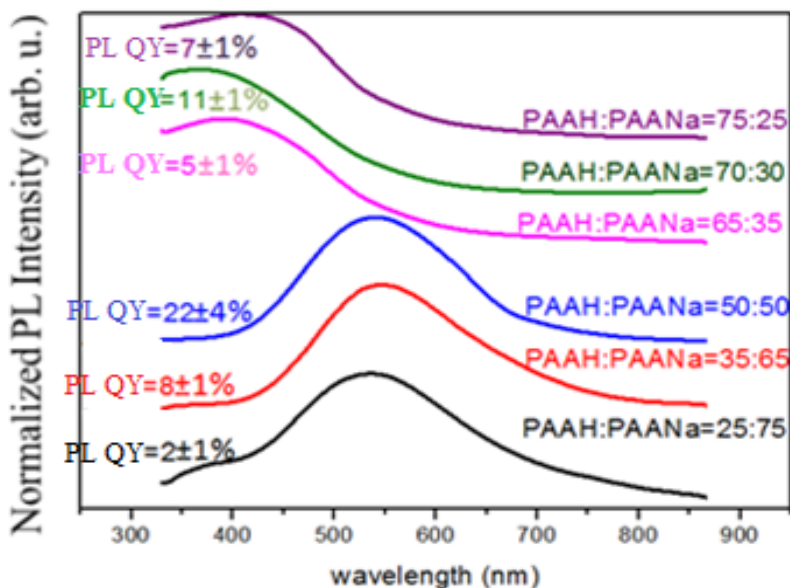


**Figure 5.5:** PL spectra of ZnO nanoparticles synthesized by the hydrolysis of  $\text{ZnEt}_2$  with different ratios of PAAH and PAANa and the reaction time of 1h. The plots are shifted along the y-axis for clarity.

The XRD diffractograms of the ZnO NPs synthesized with different mixture volume ratios of PAAH and PAANa have been measured and are not presented here, since they are all similar to that shown in **Figure 5.3**, as it turns out that all ZnO NPs have an amorphous structure. The PL

spectra and PL QY of the ZnO NPs synthesized with different mixture volume ratios of PAAH and PAANa have been measured and are presented in **Figure 5.5**. As it can be seen, when the PAAH volume ratio is below 50 %, the PL emission is in the green range and both the PL QY and the ratio of the visible to UV emission intensity (marked as Vis/UV in **Figure 5.5**) increase with the PAAH volume fraction in the mixture. The maximum PL QY is obtained when the PAAH and PAANa volume ratio is 50:50. When a volume fraction of PAAH higher than 50 % has been used, the PL spectra shift to the UV-blue range and the PL QY remains low.

The importance of the reaction time should be mentioned here. ZnO NPs synthesized with the mixture volume ratio of PAAH and PAANa of 75:25 and with the reaction time of 1 hour show blue emission and low PL QY of 7 %, as can be seen in **Figure 5.5**. However, ZnO NPs synthesized with the same mixture volume ratio, but with a reaction time of 24 hours show green emission and a high PL QY of up to 50 %, as shown in **Figure 4.44** (a). Compared to a long reaction time of 24 hours, which induces a formation of the ZnO/PAAH nanocomposite with an ionic-covalent bond, a short reaction time of 1 hour may just induce simpler complexes of ZnO and PAAH/PAA<sup>-</sup> at the first stage of the adsorption of the PAAH on the ZnO NPs surface. Even though both kinds of samples are amorphous, the chemical states of the polymer shell are quite different, inducing major changes in the dispersibility and optical properties. Although the highest PL QY is obtained after 24h of reaction, a compromise should be reached between the PL QY, the dispersibility and the reaction time.

At this point, given the constraints related to the fact that NPs for the down-shifting need a high PL QY for an emission in the 500-800 nm spectral range, along with a high dispersibility, the best compromise is to use a PAAH/PAANa volume ratio of 50:50 with the reaction time of 1h to fabricate ZnO NPs.

### 5.3. Effect of the mixture concentration of PAAH and PAANa

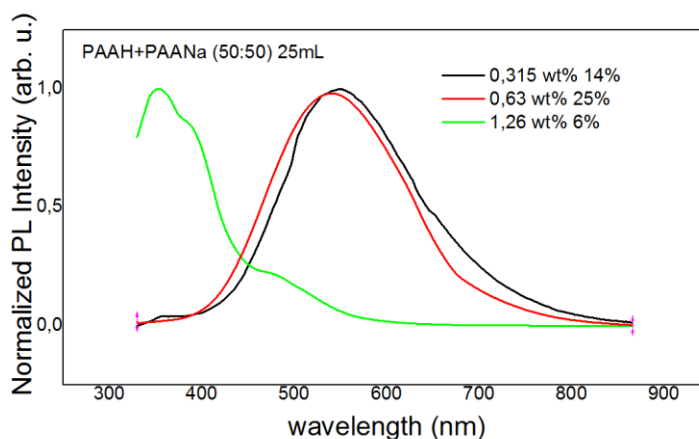


**Figure 5.6:** PL spectra of ZnO nanoparticles synthesized by the hydrolysis of  $ZnEt_2$  with different concentrations of the mixture of PAAH and PAANa (50:50 in volume) and with the reaction time of 1h.

As the optimal mixture volume ratio of PAAH and PAANa regarding the dispersibility in water and a high PL QY in the visible spectral range has been determined to be 50:50, the volume ratio was kept at this value to synthesize ZnO NPs, but the concentration of the mixture was varied to determine the optimal concentration of PAAH and PAANa mixture added during the synthesis.

It can be seen from the PL spectra and PL QY of ZnO NPs synthesized with different mixture concentrations of PAAH and PAANa (cf. **Figure 5.6**), that the optimal optical behavior is obtained at the concentration of 0.63 wt%. A lower mixture concentration results in a lower PL QY with the PL emission in the green spectral range, while a higher mixture concentration results in a blue emission with a low PL QY.

**Table 5.1:** PL spectra peak positions and PL QY of ZnO NPs synthesized by the hydrolysis of  $ZnEt_2$  with the mixture of PAAH and PAANa (50:50 in volume) with different individual concentrations of PAAH and PAANa (i.e. the concentration of PAAH and PAANa was varied independently) and with the reaction time of 1h.

PAAH (2000 g·mol <sup>-1</sup> )	PAANa (4000 g·mol <sup>-1</sup> )		
	0.63 wt%	0.8 wt%	1 wt%
0.63 wt%	PL peak @ 524 nm	PL peak @ 524nm	
	PL QY 21 ± 1 %	PL QY 22 ± 1 %	
0.8 wt%	PL peak @ 483nm	PL peak @ 484nm	
	PL QY 10 ± 1 %	PL QY 10 ± 1 %	
1 wt%			PL peak @ 499nm PL QY 11 ± 1 %

Moreover, the effects of the individual PAAH and PAANa concentration variation have also been checked. The results are listed in **Table 5.1**. When compared to the PAANa concentration change, the concentration of PAAH plays a major role and determines the shape of the PL spectra and PL QY value. 0.63 wt% of PAAH is the optimal concentration for attaining a high green

emission efficiency. The higher concentrations of 0.8 wt% and 1wt% reduce the PL QY and cause the blue-shift of the PL spectra. On the contrary, if the PAAH concentration is fixed, the PL spectra and the PL QY are not influenced by changes in the PAANa concentration. So it is confirmed that the optimum mixture concentration of the PAAH and PAANa solution is 0.63 wt% to synthesize the ZnO NPs, the value used in previous sections.

#### 5.4. Effect of the length of individual chains of PAAH and PAANa

*Table 5.2: PL spectra peak positions and PL QY of ZnO NPs synthesized by the hydrolysis of ZnEt<sub>2</sub> with the mixture of PAAH and PAANa (50:50) with different molecular weights of PAAH and PAANa of 0.63 wt% and with the reaction time of 1h.*

PAAH (g·mol <sup>-1</sup> )	PAANa (g·mol <sup>-1</sup> )				
	2 000	4 000	5 000	100 000	240 000
2 000	550 nm PL QY: 16 %	550nm PL QY: 22 %	560 nm PL QY: 8 %	540 nm PL QY: 18 %	545 nm PL QY: 16 %
5 000	536 nm PL QY: 10 %	545 nm PL QY: 23 %	550 nm PL QY: 16 %	559 nm PL QY: 7 %	547 nm PL QY: 7 %
100 000	556 nm PL QY: 17 %	438 nm PL QY: 6 %	532 nm PL QY: 7 %	406 nm PL QY: 5 %	541 nm, PL QY: 6 %
240 000	550 nm PL QY: 34 %	452 nm PL QY: 6 %	517 nm PL QY: 2 %	504 nm PL QY: 9 %	545nm, PL QY: 10 %

Next, we have investigated the effect of the chain length (molecular weight) of both PAAH and PAANa on the resulting nanoparticles. As was observed for the ZnO NPs synthesized with only PAAH, the interaction between PAAH with long carbon chains (corresponding to higher weight) and ZnO NPs becomes weaker (see section 4.3.2.2.3) [1]. Consequently, if either PAAH or

PAANa has a long carbon chain, it is expected to shift the ZnO NPs PL to the blue and reduce the PL QY, which is not interesting for the down-shifting process.

In order to check the influence of the carbon chain length on the final ZnO NPs, the mixture of PAAH and PAANa with a volume ratio of 50:50 and a concentration of 0.63 wt% was used and the individual lengths of both PAAH and PAANa were tuned. Then the PL spectra and PL QYs of these ZnO NPs were measured. The peak positions of the PL spectra and the PL QYs are summarized in **Table 5.2**.

As can be seen in **Table 5.2**, from a general point of view, ZnO NPs synthesized with a short chain length of either PAAH or PAANa or with short lengths of both of them, have a high green emission efficiency (as marked in green in the table). For ZnO NPs synthesized with long chain lengths of PAAH or PAANa, ZnO NPs have a low PL QY and most of them emit in the blue spectral range, which is marked in orange in the table. It is consistent with our previous assumption that short chain lengths are necessary for a high PL QY. In conclusion, to obtain a high visible emission efficiency, at least one short chain length of PAAH and PAANa should be used in the synthesis.

To get more insight into the reason of the high green emission efficiency for ZnO NPs synthesized with small molecular weight of either PAAH or PAANa, the time resolved photoluminescence (TRPL) spectra have been measured. **Figure 5.7** presents TRPL for nanoparticles synthesized with  $2000 \text{ g}\cdot\text{mol}^{-1}$  PAAH and  $4000 \text{ g}\cdot\text{mol}^{-1}$  PAANa on one hand and  $240\,000 \text{ g}\cdot\text{mol}^{-1}$  PAAH and  $2000 \text{ g}\cdot\text{mol}^{-1}$  PAANa on the other hand, for comparison. The corresponding spectra are shown in **Figure 5.7**. The decay time constants deduced from the fitting of the TRPL spectra of **Figure 5.7** are listed in **Table 5.3**. As we have mentioned in Chapter 4, since the decay time in ZnO nanostructures is dependent on their size and morphology, it is difficult to attribute them to specific defects. However, the lifetime enhancement indicates the improvement of the radiative recombination efficiency [2]. The values of decay times presented in **Table 5.3** indicate that compared to the short decay time of the ZnO NPs synthesized with the molecular weight of PAAH and PAANa of  $2000 \text{ g}\cdot\text{mol}^{-1}$  and  $4000 \text{ g}\cdot\text{mol}^{-1}$ , respectively, the PL of ZnO NPs synthesized with PAAH and PAANa of  $240\,000 \text{ g}\cdot\text{mol}^{-1}$  and  $2000 \text{ g}\cdot\text{mol}^{-1}$ , respectively, has a much longer decay, which is consistent with the higher radiative recombination efficiency observed.

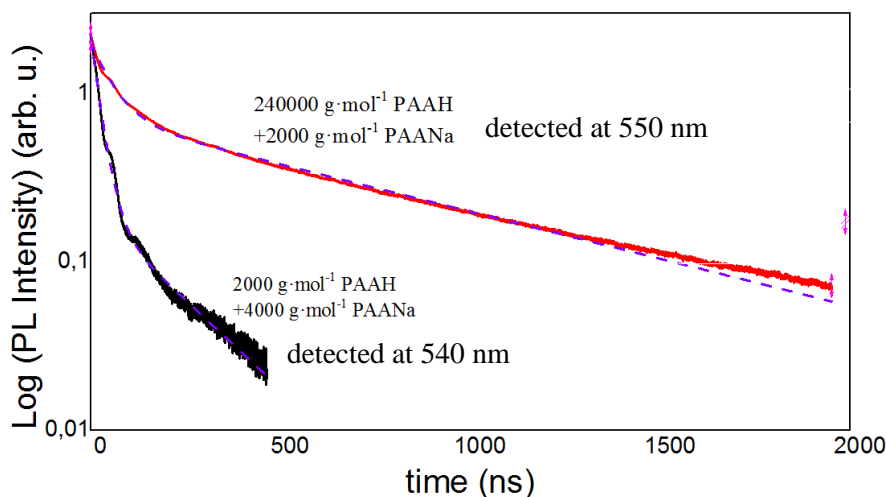


**Figure 5.7:** TRPL decay curves of ZnO nanoparticles synthesized by the hydrolysis of  $\text{ZnEt}_2$  with a mixture of PAAH ( $2000 \text{ g}\cdot\text{mol}^{-1}$ ) and PAANa ( $4000 \text{ g}\cdot\text{mol}^{-1}$ ) and a mixture of PAAH ( $240\,000 \text{ g}\cdot\text{mol}^{-1}$ ) and PAANa ( $2000 \text{ g}\cdot\text{mol}^{-1}$ ) (50:50 in volume and the concentration of 0.63 wt%) as the detection wavelength fixed at the peak position of their emission spectra 540 nm and 550 nm, respectively. Corresponding biexponential fits (violet dash lines) results are summarized in **Table 5.3**.

**Table 5.3:** Time constants obtained by fitting TRPL spectra in **Figure 5.7** with a biexponential function and relative contributions of each exponential function.

Surfactants addition	Detection wavelength (nm)	Time constant 1 $\tau_1$ (ns)	Relative contribution	Time constant 2 $\tau_2$ (ns)	Relative contribution
2000 $\text{g}\cdot\text{mol}^{-1}$ PAAH +4000 $\text{g}\cdot\text{mol}^{-1}$ PAANa	540	23	0.91	207	0.09
240 000 $\text{g}\cdot\text{mol}^{-1}$ PAAH +2000 $\text{g}\cdot\text{mol}^{-1}$ PAANa	550	55	0.65	774	0.35

We can notice, however, that when low weight chains of both PAAH and PAANa are used, the decay is almost monoexponential. This indicates that the emission comes from a homogeneous population of radiative defects. The decay time of 23 ns is close to that measured in the previous chapter for samples having identical PL QY ( $\sim 20\%$ ). On the contrary, when PAAH with a high molecular weight is used, the decay is composed of two significant contributions. The corresponding decay times, of 55 ns and 774 ns, are here again close to those measured in the previous chapter for samples with high PL QY ( $\sim 50\%$ ). We can thus infer that when the PL QY is high, the emission originates from two distinct defect populations and as the PL QY is high, the reported decay times become close to the radiative time of the studied defects.

Hence we can estimate the radiative decay time of the responsible defects to be of the order of 50 ns (or higher) for the first defect population and of the order of 700 ns (or higher) for the second defect population.

### 5.5. Effect of the type of the polyacrylate cation salt ( $\text{Li}^+/\text{Na}^+$ ) in the mixture

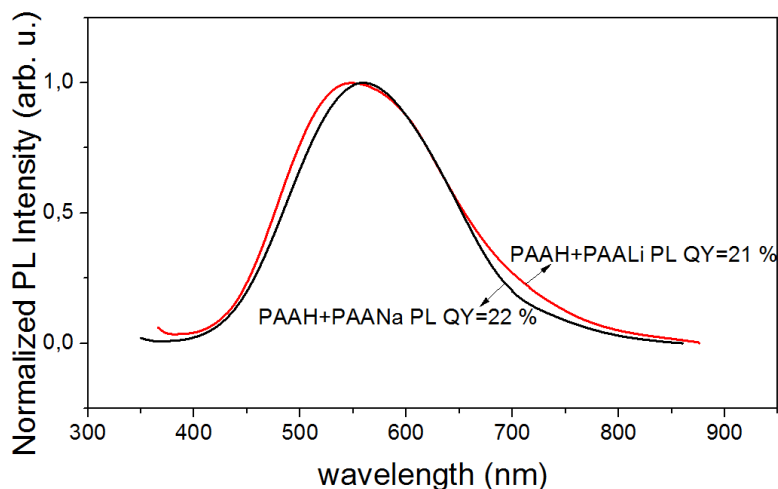


**Figure 5.8:** Normalized PL spectra and PL QYs of ZnO nanoparticles synthesized by the hydrolysis of  $\text{ZnEt}_2$  with 0.63 wt% of PAAH and 0.63 wt% of PAALi (50:50 in volume) and with 0.63 wt% of PAAH and 0.63 wt% of PAANa (50:50 in volume), with the reaction time of 1h.

To further investigate the effect of PAAH and PAANa mixture added during the hydrolysis process on the dispersibility and the visible emission efficiency of the ZnO NPs, PAANa was replaced with PAALi of identical molecular weight and at the same concentration of 0.63 wt% and with the same mixture volume ratio with PAAH of 50:50. The PL spectrum and PL QY were then measured. They are presented in **Figure 5.8**. For comparison, the PL spectrum and PL QY of ZnO NPs synthesized with the same parameters of PAAH and PAANa mixture are also shown in **Figure 5.8**. It can be clearly seen that the PL spectra of ZnO NPs synthesized with the mixture of PAAH and PAALi have similar spectral shapes and PL QYs similar to those of the ZnO NPs synthesized with the mixture of PAAH and PAANa. Thus it can be concluded that the PL spectra and PL QY are not influenced by the cation type of the polyacrylate salt ( $\text{Li}^+/\text{Na}^+$ ). On the contrary, it seems that only the presence of  $\text{PAA}^-$  is necessary to obtain a high PL QY and the PL emission in green-yellow-red spectral range.

## 5.6. Effect of the volume of the reaction precursor and the added PAAH and PAANa (or PAALi) mixture

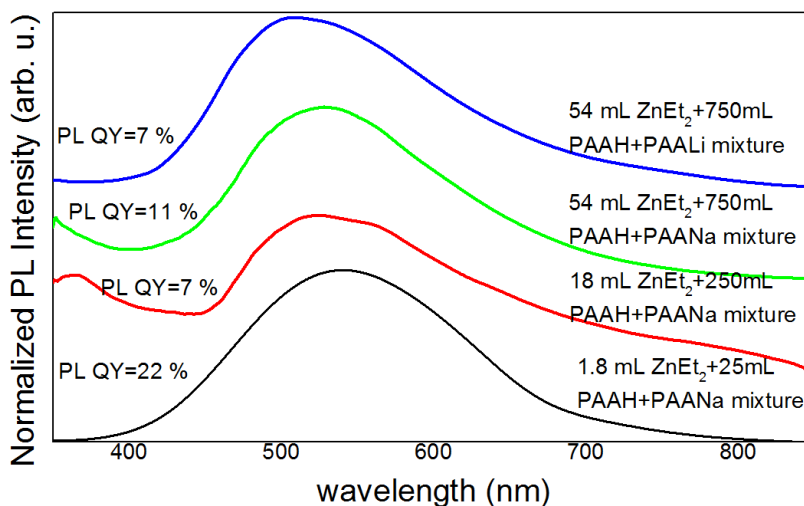


**Figure 5.9:** Normalized PL spectra and PL QYs of ZnO nanoparticles synthesized by the hydrolysis of different volumes of  $\text{ZnEt}_2$  with different volumes of 0.63 wt% of PAAH and 0.8 wt% of PAANa (or 0.63 wt% of PAALi) (50:50 in volume) mixture and with the reaction time of 1h.

Finally, the volumes of the precursor and the added PAAH and PAANa (or PAALi) surfactant solution have been increased concomitantly by 10 times and 30 times, compared to those added in the first stage of the study. The goal here was to investigate the ability to produce scalable amount of colloidal solution in a reasonable (1h) time. This study is important for the next step of this work, beyond this thesis, which will aim at the industrial application of the investigated products. The PL spectra and PL QYs of the ZnO NPs synthesized with these large volumes have been measured and compared with the ones measured for the previously synthesized ZnO NPs. The results are shown in **Figure 5.9**.

From the PL spectra and PL QYs shown in **Figure 5.9**, increasing the reaction volumes of the precursor and the surfactant mixture by 10 times or 30 times slightly affects the emission spectra but dramatically reduces the PL QY. When the volume increases, the quantity of ZnO NPs obtained is naturally increased. It seems that keeping the reaction time at 1h is not appropriate when large quantity of colloidal solution is used, as the reaction conditions are changed – the temperature distribution is not identical for large volumes as in the case of small volumes as it is harder to attain a homogeneous temperature distribution in large pots. Moreover, in the case of a small reaction volume, a magnetic stirrer is used to mix the solution, while in the case of large reaction volumes, palettes are used for mixing, which changes the reaction conditions, though it is, at this point, difficult to ascertain in which manner. More study has to be made in order to optimize the reaction time in the case of higher reaction volumes.

## 5.7. Conclusions

In this chapter, we have investigated the reaction parameters to obtain dispersible ZnO NPs with a high PL QY of the visible emission. Since the addition of PAAH alone does not allow the dispersibility in water, while maintaining the desired optical properties, another salt (PAANa or PAALi) has been added simultaneously to the reaction milieu. Different ratios, concentrations and carbon chain lengths (related to the molecular weight) of PAAH and PAANa have been used to check their influence on the dispersibility and visible emission efficiency of the ZnO NPs. It was found that, by adding during the hydrolysis 0.63 wt% of PAAH and 0.63 wt% of PAANa mixture with a volume ratio of 50:50 and with at least one of them having a short chain length and simultaneously reducing the reaction time to 1 hour, the obtained ZnO NPs were dispersible in water and the green emission efficiency was between 22 % and 34 %. The effects of the PAAH and PAANa mixture on the reaction mechanisms have been discussed. Finally, the volumes of the precursor ( $\text{ZnEt}_2$ ) and of the surfactant mixture of PAAH and PAANa have been increased by 10 times and 30 times, inducing a reduction in the visible emission efficiency without any change in the shape of the PL spectrum. At this stage, it can be concluded that to keep the high visible emission efficiency of dispersible ZnO NPs, the optimal volume for  $\text{ZnEt}_2$  and the surfactant mixture are 1.8 mL and 25 mL, respectively.

It was also confirmed that the addition of PAANa increases the concentration of the  $\text{PAA}^-$  form in the solution. This limits the deprotonation of PAAH and thus enhances the reaction between ZnO and PAAH. It seems that for the desired optical properties, the protonated PAAH form is required. On the other hand, the deprotonated form  $\text{PAA}^-$  is necessary to get a high zeta potential and, consequently, a good dispersibility. The finely tuned mixture of PAAH:PAANa allows to concomitantly attain these two characteristics. The fact that PAAH has a determining influence on the optical properties of ZnO NPs, influences was confirmed by the replacement of PAANa with PAALi. The optical properties of the resulting samples are identical with those synthesized using PAANa, showing that the salt cation ( $\text{Na}^+$  or  $\text{Li}^+$ ) has no importance and that only  $\text{PAA}^-$  anions play a role on the optical properties of the obtained ZnO NPs.

From a practical point of view, as far as industrial manufacturing of these colloids is concerned, the PAAH/PAANa mixture has a beneficial effect allowing the reduction of the synthesis time from 24h to 1h. However, at such a short reaction time, increasing the reaction volume by 10 times or 30 times degrades the optical properties, despite the fact that the amount of synthesized NPs is naturally increased.

## 5.8. References

- 
1. Chang J., Waclawik E. R., Experimental and theoretical investigation of ligand effects on the synthesis of ZnO nanoparticles. *Journal of Nanoparticles Research*, 2012, vol. 14, p. 1012/1-14.
  2. Zhong Y. C., Djurišić A. B., Hsu Y. F., Wong K. S., Brauer G., Ling C. C., Chan W. K., Exceptionally Long Exciton Photoluminescence Lifetime in ZnO Tetrapods. *The Journal of Physical Chemistry C*, 2008, vol. 112, p. 16286- 16295.



## Chapter 6

### Simulation of the efficiency of solar cells with a luminescent down-shifting layer of ZnO nanoparticles

In the previous chapters ZnO nanoparticles with a high photoluminescence quantum yield (PL QY) of up to 70 % which are only dispersible in PAAH and ZnO NPs dispersible in water with a relatively high PL QY of 22 % have been presented. The next step is to deposit the ZnO NPs layer on solar cells to determine the influence of down-shifting effect on the final solar cell efficiency. The previously obtained colloidal dispersion is meant to be used as a precursor for an ink that will be sprayed onto solar cells. Before the complete realization of the solar cell with a sprayed down-shifting layer (DSL), we wish to estimate the down-shifting effect of the ZnO NPs layer by simulation.

#### 6.1. Determination of the optical indices of the down-shifting layer

To simulate the influence of a down-shifting layer containing ZnO NPs on the final performance of a solar cell, the refractive index  $n$  and the absorbance  $k$  of ZnO NPs and of the matrix are to be known. As previously mentioned, the best ZnO nanoparticles dispersible in water are those with PAAH/PAANa shell. The DSL resulting from the colloidal solution spray will consist mainly of PAAH. Thus in this part of the study in order to determine the optical indices of PAAH and ZnO NPs by performing the spectroscopic ellipsometry measurement, the layers have been made from pure PAAH solution and PAAH solution containing ZnO NPs. For obtaining an accurate result from the spectroscopic ellipsometry, the layer should be homogeneous at least within the zone of measurement and its thickness less than 1 micrometer. Hence, the spin-coating technique has been used to produce the layers for the spectroscopic ellipsometry measurement.

##### 6.1.1 Layer preparation – spin-coating technique

Spin-coating is a commonly used technique to prepare relatively uniform and thin layers with thickness of the order varying from nano- to micrometers. A typical spin-coating process involves depositing a small amount of a liquid material in the center of a substrate and then spinning the substrate at a desired speed. The centrifugal force will cause most of the solution to spread towards (and eventually off) the edge of the substrate, leaving a thin film of the material on the surface. Excess solution is removed through the evaporation and annealing, resulting in a relatively uniform film with the thickness reduced to the critical value. The key stages of spin-coating process are shown in **Figure 6.1** [1]. The final film thickness and other properties will depend on the nature of the fluid (viscosity, drying rate, surface tension, etc.) and the parameters chosen for the spinning process. Factors such as the final rotation speed, acceleration, and the

rotation time affect the properties of the coated films. One of the most important factors in spin-coating is repeatability, as subtle variations in the parameters that define a spin-coating process can result in drastic variations in the coated film. To solve this problem, it was necessary to look more precisely on the theory of spin-coating and the various adjustable parameters during the deposition of thin layers in an attempt to obtain thicknesses of less than one micrometer.

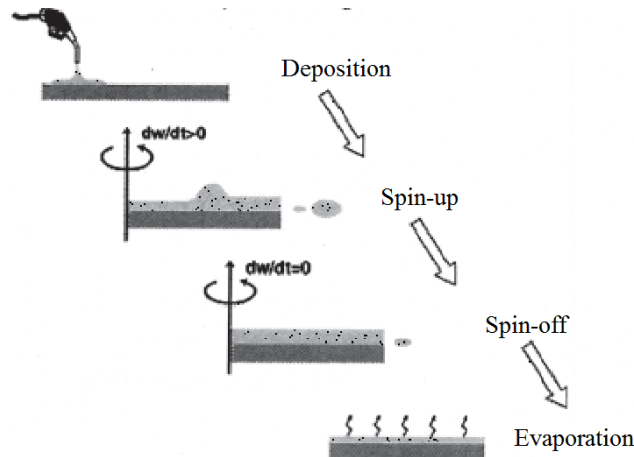


**Figure 6.1:** Key stages of spin-coating process.

Although there have been many theoretical works on the calculation of the layer thickness fabricated by spin-coating process [1], the thickness is hard to control in the real process. In order to solve the problem of the control of the thickness, we first thought to vary the parameters related to the rotation of the spin-coater, that is to say, the speed, acceleration and the operation time. The higher the speed, acceleration and the operation time, the thinner the resulting layer should be. However, even if we have gained a little bit of finesse on the level of the thickness, we have not managed to get the samples with sufficiently low thickness by increasing the speed and acceleration. Moreover, too high acceleration results in swirling patterns and streaks forming. Thus conversely, we lost in the homogeneity by increasing the acceleration and speed of the spin-coater.

The second category of parameters that we could vary is related with the compound to be deposited. Indeed, the higher viscosity of the compound, the harder it is to spread. With this in mind, we decided to reduce the dose of PAAH in water and we were able to obtain samples of a suitable thickness. The film made with a lower concentration of 5.25 wt% of PAAH solution had a thickness of about 70 nm, against the thickness of more than 1  $\mu\text{m}$  for samples fabricated with the concentration higher than 90 wt% of PAAH solution. Thus we were able to make PAAH solutions containing ZnO nanoparticles of optimum optical properties which are synthesized by hydrolysis of  $\text{ZnEt}_2$  with 0.63 wt% of PAAH (emitting in green spectral range, PL QY of  $\sim 20\%$ ). The decreasing of the PAAH solution concentration permitted to obtain thinner layers, but one of the disadvantages associated with it is that the amount of dispersible ZnO nanoparticles in PAAH decreases and thus the luminescence intensity drops as well.

The following parameters were used for spin-coating: acceleration:  $a = 1000$  rpm/s, duration:  $t = 600$  s, speed:  $s = 10000$  rpm. The only solvent used is water. The annealing was carried out at  $200^{\circ}\text{C}$  for 15 minutes. The samples used had a mass concentration of 5.25 % PAAH, which permits to disperse about 150 mg of ZnO NPs in 10 mL solution, as can be seen in **Figure 4.47** and **Table 4.6**. The very small amount of ZnO present in the samples was problematic, because the values of the optical indices of the layers containing NPs were very close to those obtained for pure PAAH. Indeed, we sometimes manage to fine fit the ellipsometry data of PAAH + ZnO sample using the parameters  $(n, k)$  of the sample containing pure PAAH.

### 6.1.2. Spectroscopic ellipsometry measurement

Spectroscopic ellipsometry is an optical technique primarily used to determine film thickness and optical constants  $(n, k)$ . The ellipsometry measurement is based on the change in polarization as the light is reflected on the material surface or transmitted through the material. The light polarization change is represented as an amplitude ratio,  $\Psi$ , and the phase difference,  $\Delta$ . The measured response depends on optical properties and thicknesses of individual materials constituting the sample. It is also applied to characterize the composition, crystallinity, roughness, doping concentration and other material properties associated with a change in the optical response. Since the 1960s, the interest in ellipsometry has grown steadily, since this method is able to provide the sensitivity necessary to measure nanometer-scale layers used in microelectronics.

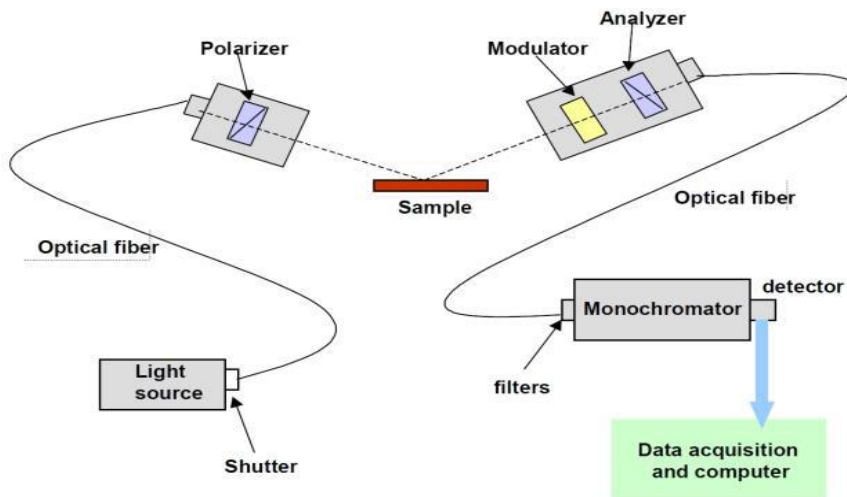


**Figure 6.2:** Schematic diagram of different components of an ellipsometric set up [2].

The measurements were performed using a Jobin-Yvon UVISSEL ellipsometer. It permits measurements in the spectral range from 1.5 to 5 eV (260-830 nm). **Figure 6.2** [2] shows different components of the ellipsometric setup. A polarized light beam is directed onto the sample. After reflection on the sample surface, the polarization of the beam is changed and this change is then analyzed using a modulator and an analyzer. The acquisition is carried out step by

step and controlled by a monochromator. Our acquisitions were conducted with a step of 0.05 eV between two measurement points.

To fit the curves measured by ellipsometry on a PAAH layer, we used the New Amorphous model. This is a dispersion formula derived from the Forouhi-Bloomer model [3]. This model is known to be often used in the modeling of various polymer layers, including some resins used in photolithography. The model is based on the following equations [2]:

$$n(\omega) = n_{\infty} + \frac{B(\omega - \omega_j) + C}{(\omega - \omega_j) + \Gamma_j^2} \quad (6.1)$$

$$k(\omega) = \begin{cases} \frac{f_j(\omega - \omega_g)^2}{(\omega - \omega_g) + \Gamma_j^2} & \omega > \omega_g \\ 0 & \omega < \omega_g \end{cases} \quad (6.2)$$

where,

$$B = \frac{f_j}{\Gamma_j} [\Gamma_j^2 - (\omega_j - \omega_g)^2],$$

$$C = 2f_j \cdot \Gamma_j (\omega_j - \omega_g)$$

with the following 5 fitting parameters:

$n(\infty)$  represents the value of the refraction index when the frequency tends to infinity,

$f_j$  (eV) is between 0 and 1, connected to the peak amplitude of the extinction coefficient,

$\Gamma_j$  (eV) is related to the absorption peak width. The higher the value, the broader the peak, but the lower the amplitude,

$\omega_j$  (eV) is the energy (approximately) at which the extinction coefficient is maximum,

$\omega_g$  (eV) is the energy gap of the material.

We also tried to model the PAAH layer with the Tauc-Lorentz model [4]. However, the results were worse than those obtained with the New Amorphous model.

As for ZnO NPs, the values of the refractive indices of bulk ZnO that can be found in the literature [5] were taken and they were not varied in the fitting procedure.

The models built to describe our samples for the adjustment of the ellipsometry measurements data were very simple. **Figure 6.3** shows the two models used: the simpler on the left side and the more complex one on the right side. The more complex model took into account the presence of thermal oxide (SiO<sub>2</sub>) at the surface of the silicon substrate (a few nanometers) and the presence of a roughness at the interface air/PAAH+ZnO NPs.

In the end, the results of the fitting of the experimental data using both models were very similar. We decided, for the sake of simplicity, to work primarily with the simpler model presented in the left side of the **Figure 6.3**. When the results of the adjustments were not good, it made no sense to refine them with a more sophisticated model.

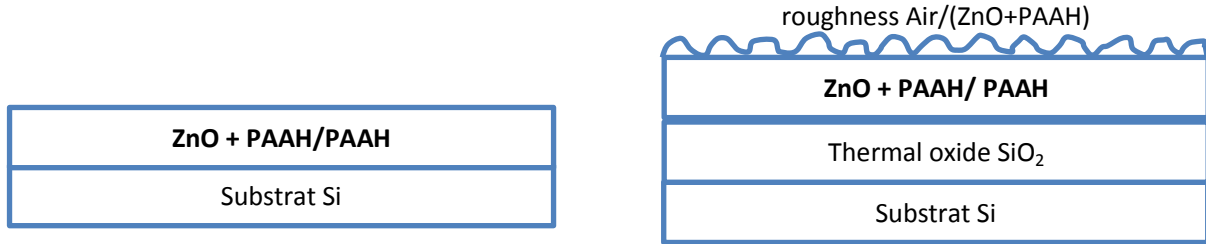


**Figure 6.3:** Model structures for samples: (left) the simple model and (right) the more elaborated model.

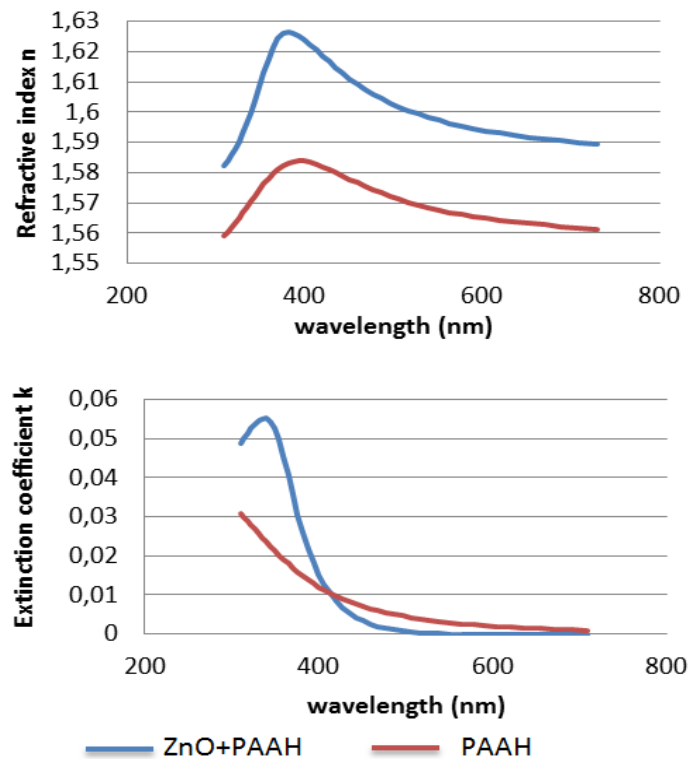


**Figure 6.4:** Comparison of optical indices of pure PAAH and of the mixture of PAAH + ZnO NPs (emitting in the green spectral range, PL QY of ~ 20 %).

The curves shown in **Figure 6.4** correspond to the ellipsometric measurements performed on the samples of PAAH and ZnO + PAAH mixture layers of best optical quality. Regarding refractive indices, it is observed that those of ZnO NPs + PAAH mixture are superior to those of pure PAAH. It can be attributed to the higher value of the refractive index of ZnO, which is

approximately 2. For the extinction coefficient of the hybrid compound, the values appear to decrease for wavelength greater than 350 nm. However, it seems surprising that for wavelengths greater than 400 nm the extinction coefficient of ZnO + PAAH is zero while that of pure PAAH is not.

Using the Jobin-Yvon UVISEL ellipsometer, we have been able to work in the wavelengths range between 300 nm and 730 nm. Indeed, experimental values outside this spectral range did not permit to obtain a good match with the model used to describe our samples. This is due to two reasons: first, in the UV, that is to say for wavelengths below 300 nm, the absorption increases so much that the signal acquisition in this range is no longer possible. The increase in the absorption is caused largely by the ZnO nanoparticles. On the other hand, for longer wavelengths in the near infrared spectral range, around 1.5-1.6 eV (775 nm - 830 nm), there also exists a problem in the data acquisition, which subsequently prevents good correspondence between the experimental values and the model used. This may be due to the absorption of ZnO/PAAH complex. Moreover, for wavelengths longer than 830 nm, we cannot measure any signal due to the setup limitation. In order to work in a reasonable range of wavelengths for the simulations of the influence of the down-shifting layer on our samples, we needed to obtain the values of  $n$  and  $k$  in the range between 300 nm and 1200 nm. Due to the incapacity to experimentally obtain the ellipsometric data in this broad spectral range, we decided to extrapolate the values of  $n$  using Cauchy polynomial equation. The result of this extrapolation is shown in **Figure 6.5**. The equation used in this extrapolation is given by:

$$n = \frac{A}{\lambda^4} + \frac{B}{\lambda^2} + C \quad (6.3)$$

With A, B and C are constants.

For the extinction coefficient, since it becomes zero from 590 nm for the PAAH + ZnO NPs mixture, we assume it to be zero for longer wavelengths.

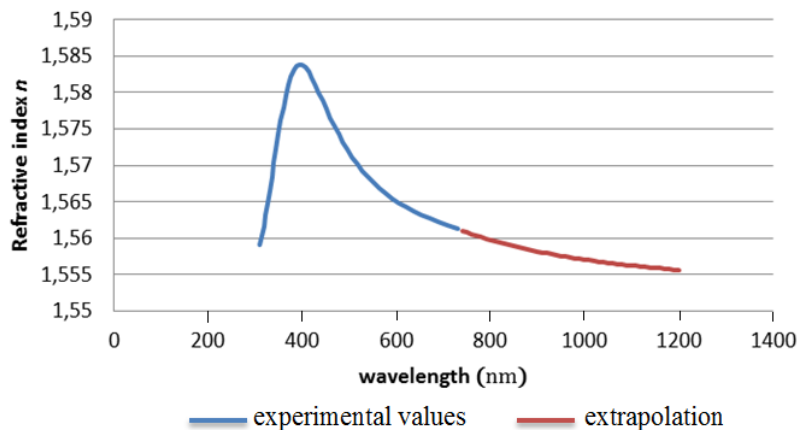


**Figure 6.5:** Extrapolation of the refractive index in the range 730 - 1200 nm.

### 6.1.3. Effective medium theory

In order to describe the effective physical properties of mixture of different materials, i.e. the mixture composed of many materials, several theoretical models can be used, depending on the treated medium. These models permit to estimate the effective properties of the mixture based on the properties of each constituent material and on the interaction between them and the contribution of different constituents in the case of mixture. Nowadays the most commonly models used are the Bruggeman and the Maxwell-Garnett models. It is important to mention that these theoretical models do not give a precise evaluation of the properties of the studied materials, but rather an approximative description.

#### 6.1.3.1. Bruggeman model

The Bruggeman model is the most commonly used one. It permits to calculate certain physical properties for a mixed medium consisting of two or more constituents [6]. The model has been initially developed for the approximation of the conductivity of a mixed medium. But the formula is also valable for the dielectric permittivity approximation and thus for the optical refractive index, since these quantities are linked according to:

$$\varepsilon = (n - i * k)^2 \quad (6.4)$$

where,

$\varepsilon$  is the dielectric permittivity of the material,

$n$  is the refractive index of the material,

$k$  is the extinction coefficient of the material.

In the Bruggeman model, the different constituents are considered to be randomly mixed. The Bruggeman model is well adapted for mixtures where a percolation path exists for each constituent. Therefore it does not describe appropriately the structure of our materials in which there is no percolation between ZnO nanoparticles. The Maxwell-Garnett model, which is a derivation of the Bruggeman model used to describe mixed mediums with dilute inclusions, is thus more interesting.

#### 6.1.3.2. Maxwell-Garnett model

In the Maxwell-Garnett model, the medium consists of spherical inclusions of one or more materials dispersed in a host matrix. It corresponds to the description of our medium (ZnO NPs dispersed in PAAH). ZnO NPs are thus considered as the inclusion spheres, while the PAAH is the host matrix. In this hypothesis with one single type of inclusion, the relative effective permittivity of the materials can be calculated using the following formula [7]:

$$\frac{\varepsilon_{eff}-\varepsilon_h}{\varepsilon_{eff}+2\varepsilon_h} = f_i \frac{\varepsilon_i-\varepsilon_h}{\varepsilon_i+2\varepsilon_h} \quad (6.5)$$

where,

$\varepsilon_{eff}$  is the effective permittivity of the mixtures,

$\varepsilon_h$  is the permittivity of the host matrix,

$\varepsilon_i$  is the permittivity of the inclusion material (inclusion spheres),

$f_i$  is volume fraction of the inclusion spheres material with respect to the total volume of the mixture.

The use of the Maxwell-Garnett model as described by **Equation 6.3** requires a number of assumptions concerning our material:

1. the volume fraction of the inclusion material should be small because they must not be in contact with each other,
2. the volume fraction of the inclusions should be constant throughout the material,
3. there is no size dispersion of the inclusion nanoparticles,
4. the inclusions are spherical.

**Figure 6.6** [8] shows the schematic representation of different effect mediums adapted to Bruggeman model and Maxwell-Garnett model, respectively.

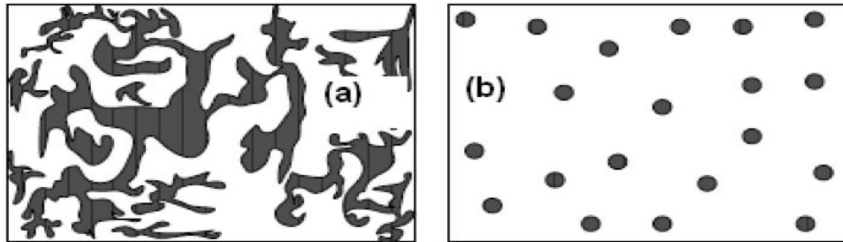


**Figure 6.6:** Schematic representation of the effective mediums by: (a) Bruggeman model and (b) Maxwell-Garnett model [8].

There is a fairly rich literature about the refinements that can be made to the Maxwell-Garnett model to take into account the size dispersion of nanoparticles and the fact that they are perhaps not quite spherical but rather elliptical [9]. However, we have not studied these detailed models, not to make the simulations more complicated at the first stage, however in the future it will be worthwhile to add some refinements to the model used. Regarding the hypothesis of the

low volume fraction, our samples contain less than 10 % in volume of nanoparticles and one can consider that the low volume requirement is fulfilled.

### 6.1.3.3. Comparison with the ellipsometry results

The objective here was to compare the results obtained from ellipsometry with the Maxwell-Garnett model for determining the optical indices of the composite materials. To make this comparison, we used the PAAH data previously obtained by ellipsometry measurement and for ZnO, we used the values found in the literature [5]. Indeed, insofar as the nanoparticles used have a radius of about twenty nanometers, much bigger than the exciton Bohr radius of ZnO (2.3 nm), there is no quantum confinement effect, so we assumed that the refractive indices are almost identical to those of the bulk zinc oxide.

We wished to obtain the effective indices for several concentrations of nanoparticles in the PAAH, but due to the constraints related to the limit of the concentration of the dispersed ZnO NPs mentioned earlier, necessary for obtaining a sufficiently thin film, we were able to fabricate a restricted (in terms of the NPs concentration) series of samples.

In **Figure 6.7** are presented the refractive indices of ZnO + PAAH obtained via the ellipsometric measurement and those calculated using the Bruggeman and the Maxwell-Garnett model. It can be noticed that the theoretical curve calculated using the Maxwell-Garnett model is in qualitative agreement with the experimental curve. Surprisingly, in the theoretical calculation of refractive indices, even the Bruggeman model gave satisfactory results, even if the extinction coefficient  $k$  was neglected. Similarly, the comparison between the values of  $n$  calculated according to the Maxwell-Garnett model taking  $k$  as non-zero, and the values of  $n$  calculated neglecting  $k$  (taking it as zero), shows that the curves are almost identical. The maximum difference between the values of  $n$  calculated with and without  $k$  is 0.1 %. The correspondence is optimal between 350 and 550 nm, however, it can be noticed in **Figure 6.7** that in the UV, the values of the effective refractive index obtained by the ellipsometry are at maximum 2 % smaller than the values obtained from the Maxwell-Garnett model. The value of the volume fraction of the ZnO nanoparticles used in the calculations according to the Maxwell-Garnett model that best fits the experimental curve is 6.3 %. It corresponds very well to the value of the volume fraction introduced during the sample preparation (about 6 %).

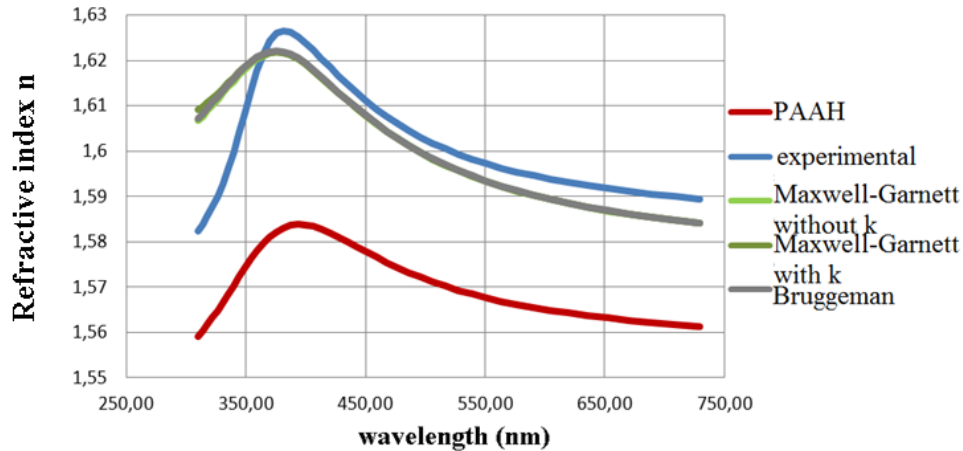


**Figure 6.7:** Comparison of refractive indices  $n$  obtained for the ZnO NPs + PAAH film experimentally and calculated theoretically using the Maxwell-Garnett model (with and without  $k$  for simplification) and the Bruggeman model, and the experimental values of  $n$  obtained for pure PAAH. The theoretical curves calculated using the Maxwell-Garnett model with and without  $k$  ( $k = 0$ ) are superposed.

On the other hand, for the extinction coefficient, the experimental data and the values calculated using the Maxwell-Garnett model do not match (see **Figure 6.8**). For wavelengths below 400 nm, it can be observed that the experimental extinction coefficient of the composite film is higher than that calculated using the Maxwell-Garnett model. However, it seems surprising that the extinction coefficient is zero beyond 550 nm because even for pure PAAH this coefficient is non-zero. This is even more astonishing, as our composite material is composed of more than 90 wt% of PAAH. This may be related to the measurements and models used to fit the experimental data. More precisely, the use of bulk data to model the ZnO nanoparticles is a rather rough approximation.

In the following simulations, however, we will assume that the extinction coefficient of the composite material follows the Maxwell-Garnett law.

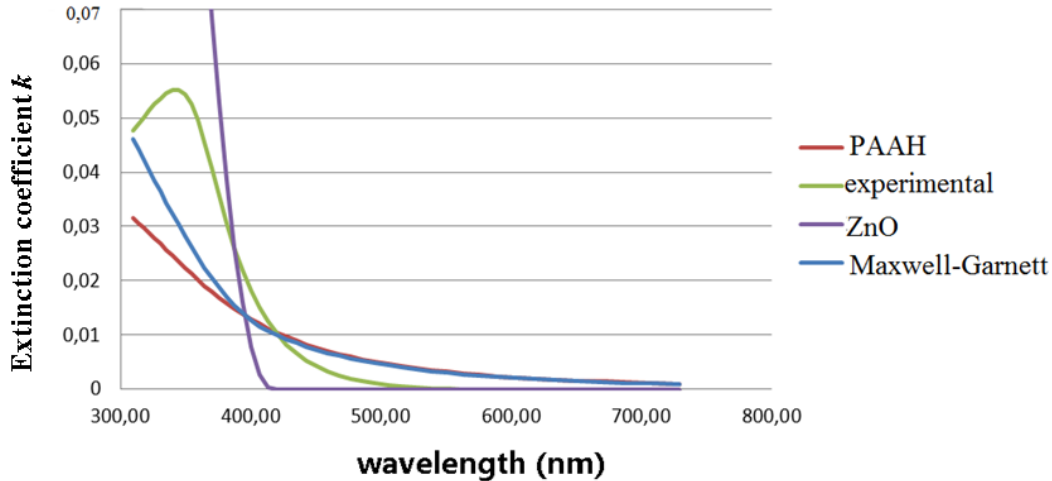


**Figure 6.8:** Comparison of extinction coefficients  $k$  between different materials (ZnO, PAAH and the ZnO NPs + PAAH mixture – marked as experimental in the legend) obtained by the ellipsometry measurement and the theoretical curves calculated using the Maxwell-Garnett model for ZnO NPs + PAAH mixture.

## 6.2. Simulations

The simulations presented in this part have been done by our PFE (Projet Fin d'Etude) student, Mr. Victor Goutorbe. Obtaining optical indices of constituent materials in the down-shifting layer opens the door to the realization of different simulations necessary to evaluate the performance of the down-shifting layer and its influence on the final efficiency of the solar cell. To quantify this impact, the simulations were divided into two parts. At first, the anti-reflective behavior of the ZnO NPs layer is quantified. In the second part, the gain in the solar cell performance provided by the down-shifting of ZnO NPs layer, i.e. transferring photons in the UV into the visible is calculated. The simulations are carried out using three programs: (X-ray Oriented Programs) XOP, (Solar Cell Capacitance Simulator) SCAPS and Excel. XOP permits to simulate the optical properties of a stack of layers, while SCAPS manages the electrical properties of studied solar cells [10]. Finally, Excel is used to treat the data generated by the other two programs.

### 6.2.1. Anti-reflective behavior

To perform the simulations on anti-reflective (AR) behavior of the down-shifting layer, the XOP software which provides the values of the reflectance (R), the transmittance (T) and the absorbance (A) of a stack layer in function of optical indices and thicknesses of different layers constituting the stack was used. The values of R, T and A obtained correspond to the effective values of the whole stack. All simulations were performed on the range of wavelengths 300 - 1200 nm. It should be precised that the following materials used in different stacks: Ethylene Vinyl Acetate (EVA),  $\text{Si}_3\text{N}_4$  and  $\text{MgF}_2$  do not absorb in this wavelength range. Thus the absorbance obtained using the XOP program corresponds directly to the absorbance of the down-

shifting layer (ZnO NPs + PAAH). This has facilitated the task, in particular in calculating the number of photons converted from the UV to the visible by the down-shifting process. All simulations were performed for the two presented types of solar cells (cf. **Figure 6.9**): copper indium gallium selenide (Cu(In,Ga)Se<sub>2</sub>, CIGS) solar cell and the amorphous Si (a-Si) solar cell.

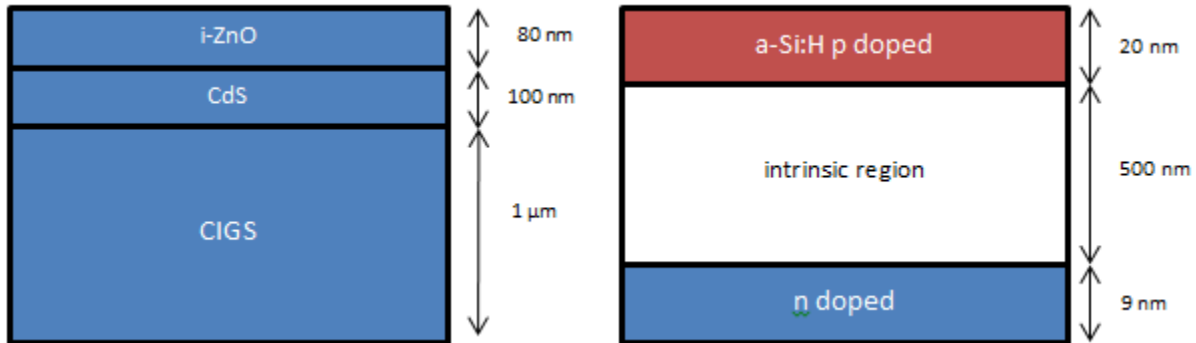


**Figure 6.9:** Structure of the studied copper indium gallium selenide (CIGS) solar cell (left) and the amorphous Si (a-Si) solar cell (right).

In the SCAPS software, the required input data is already implemented in the program with for each material constituting the studied solar cell. An exponential absorption law is assumed for all layers. AM1.5G standard illumination spectrum is implemented by default.

Thus the values of the external quantum efficiency (EQE) of these two types of cells in the desired wavelength range from 200-1200 nm without ZnO NPs layer on the top of the cell can be retrieved. The results are shown in **Figure 6.10**. It can be observed that the EQE of the studied solar cells is lower for wavelengths below 400 nm than the EQE around 500-600 nm, in the spectral range where the ZnO NPs have the maximum photoluminescence intensity. Note however that in the case of amorphous silicon (a-Si), a strong decrease of the EQE is observed after a peak at 600 nm. Beyond 670 nm values are lower than those of the range 200-400 nm.

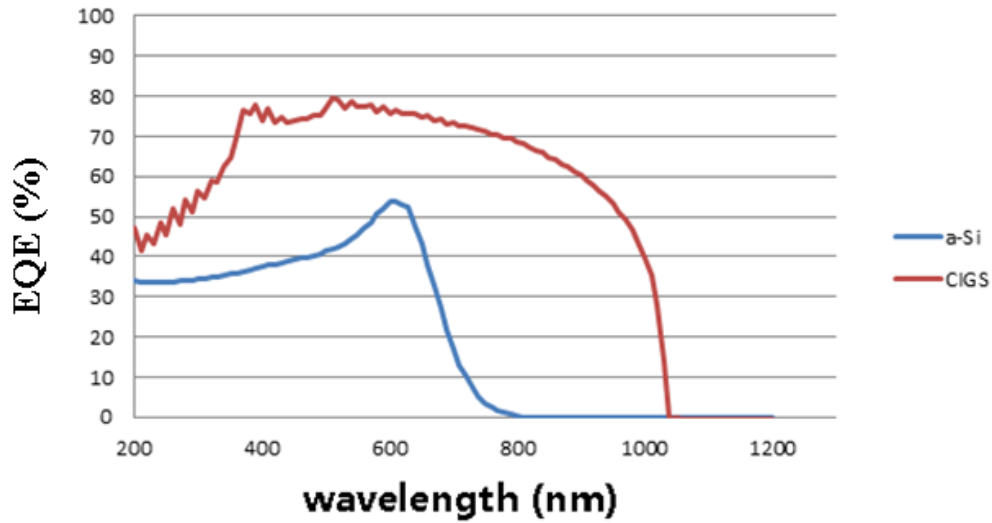


**Figure 6.10:** Comparison of the EQE of the CIGS and amorphous silicon (a-Si) solar cells made by simulations with SCAPS software.

The principle of the anti-reflective layers used in the structure of solar cells is obviously to reduce the light reflected at the solar cell's surface, so as to make it penetrate maximum of it within the solar cell. For this purpose, it is necessary that the refractive index of the material used as an AR layer is appropriate and that the thickness of the AR layer is "quarter-wave" for obtaining the constructive interference on one side of the solar cell and destructive interference on the other side. The refractive index of optimum AR layer is given by [11]:

$$n_{ARL} = \sqrt{n_{upp} * n_{low}} \quad (6.6)$$

where,

$n_{upp}$  is the refractive index of the upper layer,

$n_{low}$  is the refractive index of the lower layer.

With regard to the interference, to obtain the constructive interference on one side of the solar cell, the thickness of the layer must follow the law:

$$d = ((2k + 1) \lambda) / (4 * n) \quad (6.7)$$

$\lambda$  is the wavelength at which a minimum reflection is desired (in the case of photovoltaic solar cell, this value is preferentially fixed in between 550-600 nm, corresponding to the maximum of the incident solar power),

$n$  is the refractive index of the layer,

$k$  is an integer (generally 1, 2 or 3 ...).

### 6.2.1.1. Amorphous silicon solar cell

For the amorphous silicon solar cell, different structures of the stack were considered, with silicon nitride ( $\text{Si}_3\text{N}_4$ ) used as an antireflection layer.

**Figure 6.11** shows different structures studied in the simulations. In this first series of simulations the thickness of the EVA is set to 0.1 mm and that of  $\text{Si}_3\text{N}_4$  to 70 nm (the standard value used in the fabrication technology of this type of cells). However, the thickness of the ZnO NPs + PAAH layer was varied in order to find an optimum. First, for a rough simulation, the thickness was varied with a step of 25 nm between 0 and 500 nm. Then, if necessary, some values have been refined with a smaller step.

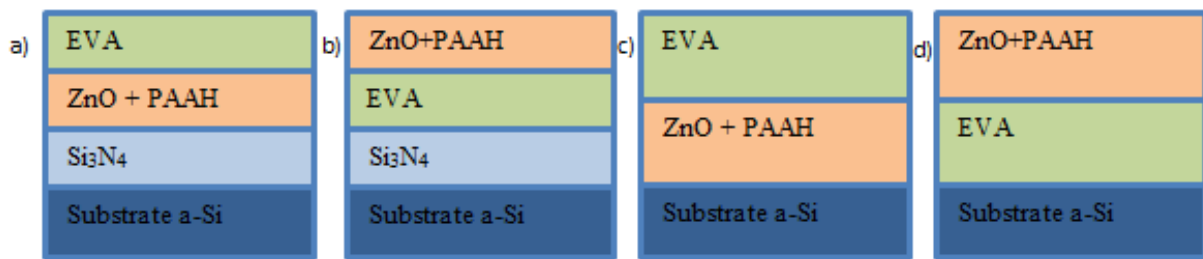


**Figure 6.11:** Schematic diagrams of different stack structures for amorphous silicon solar cells with a ZnO NPs+PAAH layer.

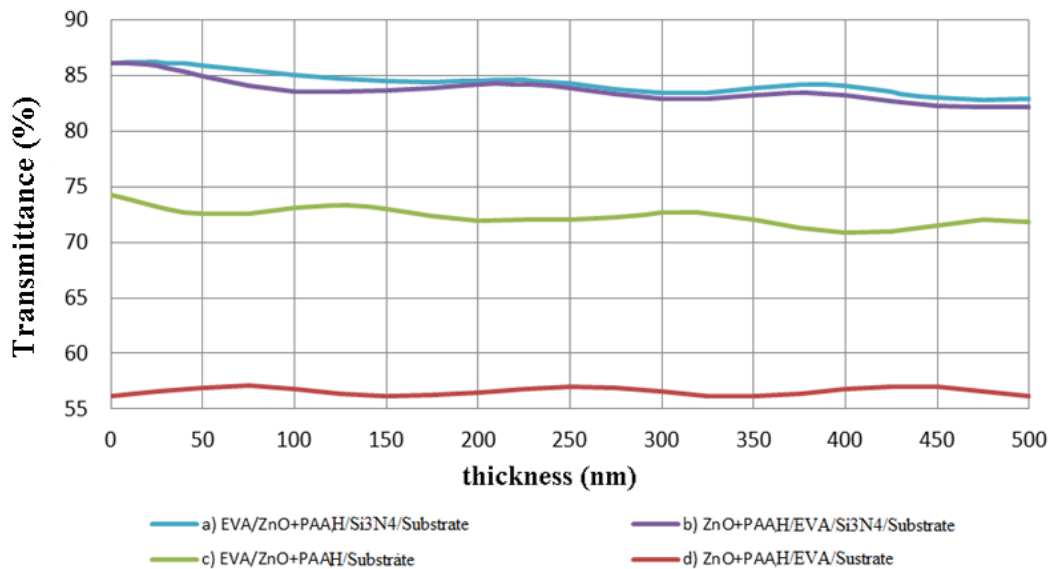


**Figure 6.12:** Evolution of the transmittance at 600 nm in function of the down-shifting layer thickness for different structures presented in **Figure 6.11** by simulations with SCAPS software.

As it can be noticed in the graph presented in **Figure 6.12**, the structure with the best anti-reflective behavior is the one shown in **Figure 6.11** (a). It has the highest transmittance among all

the structures in the studied thickness range. Indeed, it seems consistent because the refractive index of ZnO + PAAH mixture is between that of the EVA and that of silicon nitride as recalled in **Table 6.1**. Although the refractive indices vary with wavelength, the anti-reflective behavior can be predicted by comparing the values for a given wavelength. It also can be seen in **Figure 6.12** that the structures (a) and (b) are quite similar in terms of the performance. In contrast, for the structures (c) and (d) in which there is no layer of the silicon nitride, the performance is poor and, in the worst case, the transmittance of only about 55 % is obtained. Thus these two structures will not be considered in further studies, because the reflection losses would be far too high and anyway, the down-shifting will not be able to compensate for these losses.

**Table 6.1:** Refraction index values at 600 nm for different materials used in the simulations.

Material	a-Si	Si <sub>3</sub> N <sub>4</sub>	ZnO	ZnO + PAA	EVA
Refractive index $n$ at 600 nm	4.3	2.02	2.0	1.59	1.51

**Figure 6.13** shows the results obtained only for the structure with the best AR behavior. Several peaks can be observed in the transmission curve. However, although the simulations for thicknesses smaller than 100 nm have been made, such thin down-shifting layers cannot be realized in practice due to technical reasons. The 25 nm-thick down-shifting layer, for which the maximum transmittance is obtained, cannot be fabricated, because the ZnO nanoparticles themselves are approximately 20 nm in diameter. The optimum thickness seems thus to be 225 nm, while the transmittance is 84.5 %. Hence this thickness of the down-shifting layer will be taken into account in the simulations of the EQE of a-Si solar cells with the DS layer on their top.

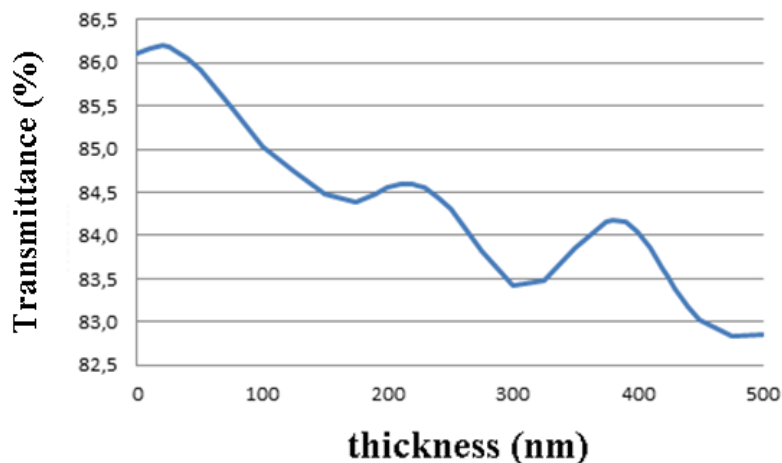


**Figure 6.13:** Transmittance at 600 nm of the structure in **Figure 6.11** (a) in function of the down-shifting layer thickness.

After determining which stack structure is the most favorable to have a minimal reflection, the thickness of the EVA encapsulation layer of the amorphous silicon solar cell was varied. Six different thicknesses for EVA, between 0.1 mm and 0.6 mm were studied, with a down-shifting layer having a thickness between 100 and 400 nm. The EVA layer having this order of the thickness is generally presented on commercially available solar cells, but in some cases it may be even thicker, up to 1 mm. It may therefore be interesting to broaden the range of the studied values, however, as shown in **Figure 6.14**, the results are hard to visualize in parallel on the same graph.

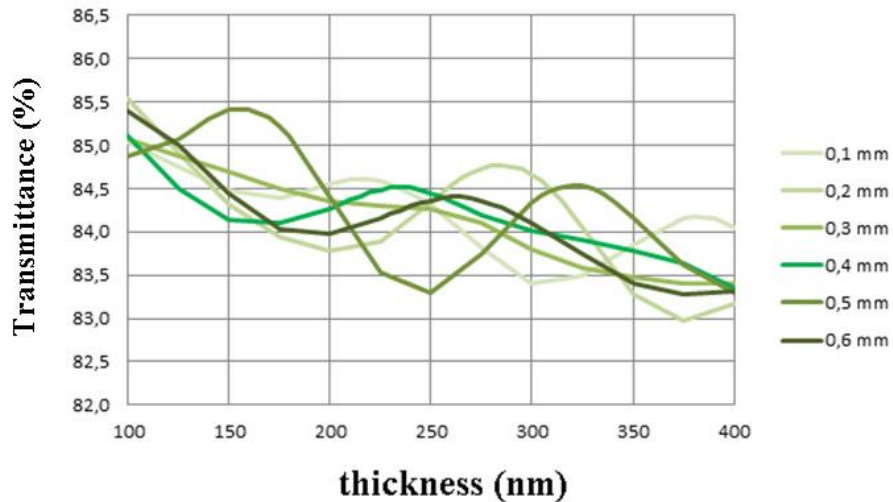


**Figure 6.14:** Evolution of the transmittance at 600 nm in function of the thickness of the down-shifting layer for various thicknesses of the EVA layer.

It is observed that several "couples" of thicknesses (down-shifting layer and EVA) could be chosen to maximize the transmittance of the layer stack on the top of the solar cell. The two most favorable couples are  $d_{\text{eva}} = 0.1$  mm with  $d_{\text{down-shifting}} = 100$  nm or  $d_{\text{eva}} = 0.5$  mm with  $d_{\text{down-shifting}} = 160$  nm. In order to maximize the number of nanoparticles (and thus to have a higher intensity of the luminescent emission) present in the layer to maximize the down-shifting efficiency, it would be more interesting to work with the second pair of values.

#### 6.2.1.2. CIGS solar cell

In the case of the CIGS solar cell, three different layers stack structures were studied, as shown in **Figure 6.15**. Moreover, the outermost layer of the solar cell is a ZnO layer which also serves as the top electrode. The layer being electrically active, it is supported by SCAPS software and it will not be integrated in the simulations. This ZnO electrode will be considered as the "substrate" when using XOP software, to obtain the transmittance, the absorbance and the reflectance of the whole stack if layers on the top of the solar cell. In the case of solar cells which are not encapsulated by the glass, a magnesium fluoride layer ( $\text{MgF}_2$ ) is deposited on the ZnO. The

refractive index of this layer is about 1.38 at 600 nm. This layer plays an anti-reflective and a protective role.

The results of these three structures in terms of transmittance are very good. The best structure is the structure (c) in **Figure 6.15**. As shown in **Figure 6.16**, the transmittance reaches 96.3 % for a down-shifting layer of thickness of about 100 nm. It will be recalled that in our case a down-shifting layer with the thickness of 100 nm is very difficult to fabricate using the spin-coating, however, the simulations were carried out just for an indication of the eventual gain of the solar cell performances.

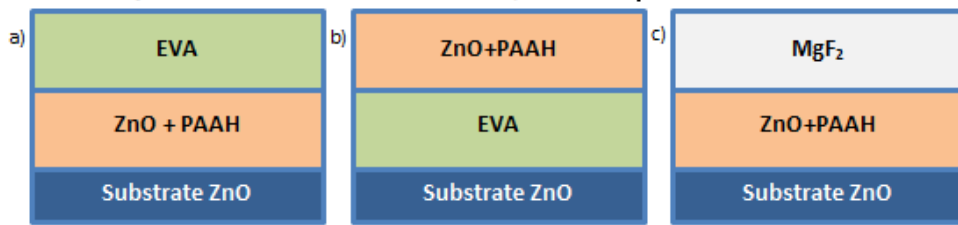


**Figure 6.15:** Schematic diagrams of the different top layer stack structures to be applied to the CIGS solar cells.

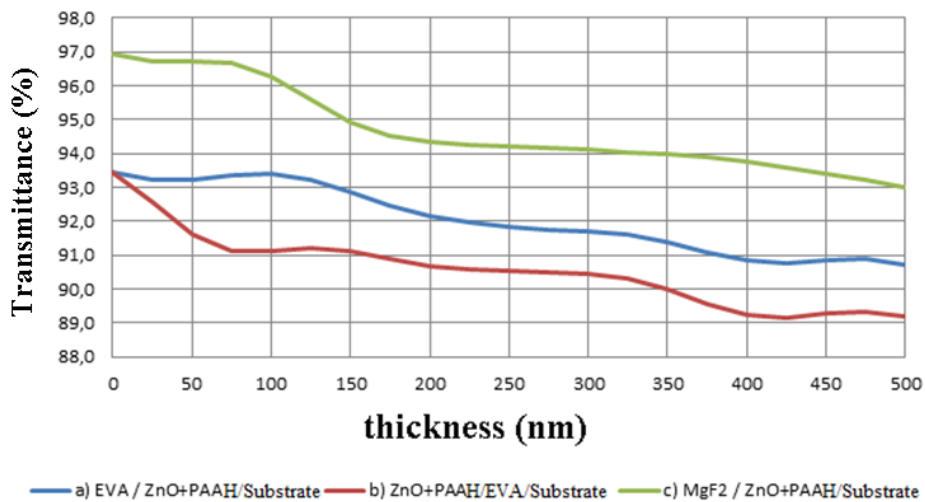


**Figure 6.16:** Evolution of the transmittance at 600 nm in function of the down-shifting layer thickness for 3 different structures presented in **Figure 6.15**.

Structures (a) and (b) contain an EVA layer, so the simulations were performed by varying the thickness of this layer, similarly to what has already been done for the amorphous silicon solar cells. The results are presented in **Figure 6.17**.

In the case of the CIGS solar cell, there are less fluctuations of the transmittance in function of the thickness of the down-shifting layer than in the case of the a-Si solar cell. Indeed, among

the 6 tested thicknesses of EVA layer in these simulations, there are no distinguishable differences between them, except for the 0.5 mm of EVA and the 250 nm-thick down-shifting layer. All the transmittance values are generally high, but as no oscillations are observed, but rather an almost continuous drop, as far as only the transmittance is concerned, the 100 nm-thick DS layer seems the most interesting.

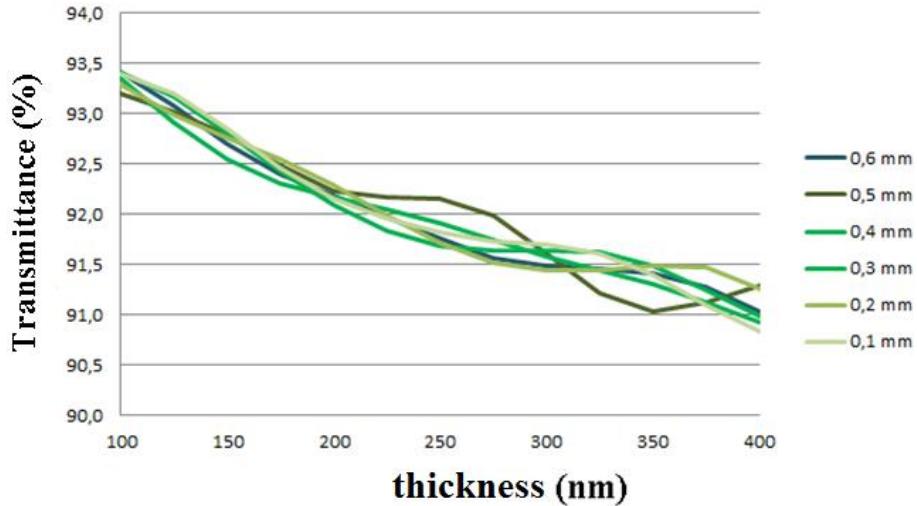


**Figure 6.17:** Evolution of the transmittance at 600 nm in function of the down-shifting layer thickness for various thicknesses of EVA layer.

### 6.2.2. Down-shifting effect

After making the simulations of the anti-reflective behavior of different layer stack structures for the two studied types of solar cells (a-Si and CIGS), a number of optimal structures and thicknesses must be chosen, in order to then calculate the contribution of the down-shifting effect to the final efficiency of solar cells. The investigations were restricted to 5 configurations for each studied type of solar cell, to limit the number of simulations to perform.

For the amorphous silicon cell, the following structures are considered:

- I. Structure (a) 0.1 mm of EVA and 220 nm of the down-shifting (DS) layer
- II. Structure (a), 0.5 mm of EVA and 160 nm of the DS layer,
- III. Structure (a), 0.5 mm of EVA and 320 nm of the DS layer,
- IV. Structure (a), 0.2 mm of EVA and 100 nm of the DS layer,
- V. Structure (a), 0.2 mm of EVA and 285 nm of the DS layer.

All selected points belong to structure (a) because it offers an anti-reflective performance far superior than other structures. Regarding the selected thicknesses of the DS layers, they are more

or less big in order to study the influence of the number of the luminescent nanoparticles which contribute to the down-shifting effect on the final efficiency of the given solar cell.

For the CIGS cell, the following structures are considered:

VI. Structure (c), 100 nm of the down-shifting (DS) layer,

VII. Structure (c), 350 nm of the DS layer,

VIII. Structure (a), 0.1 mm of EVA and 100 nm of the DS layer,

IX. Structure (a), 0.1 mm of EVA and 200 nm of the DS layer,

X. Structure (a), 0.5 mm of EVA and 250 nm of the DS layer.

To quantify the solar cell performance, I-V simulations using SCAPS software have been performed. As this software does not support the layers located on the solar cell which have a non-electrical behavior, the incident spectrum was modified in function of the electrically non-active layers which constituted the stack (in terms of their reflectivity, the absorbance and the transmittance) on the solar cell. To account for the photoluminescence of ZnO nanoparticles, the number of photons absorbed by the DS layer was calculated, thanks to the absorbance obtained with XOP software. Though the absorbance was calculated with the effective index of the layer, as the extinction coefficient of ZnO NPs is more than one order of magnitude higher than that of PAAH, it was assumed that all the photons were absorbed by the ZnO NPs. The number of the photons re-emitted by the DS layer is calculated as follows:

$$\text{nb(Photons reemitted)} = \text{nb(Photons absorbed)} * \text{PL QY} * 1/2 \quad (6.8)$$

where,

PL QY is the photoluminescence quantum yield of ZnO NPs,

1/2 a factor introduced since the photoluminescence is isotropic and only half of the photons is emitted in the direction of the solar cell and the other half is emitted in the opposite direction.

The photoluminescence spectrum of ZnO NPs was taken into account to determine the wavelength of each down-shifted photon. The following formula gives the total number of the incident photons at each wavelength:

$$\text{nb(incident photons)} = \text{nb(transmitted photons)} + \text{nb(down-shifted photons)} \quad (6.9)$$

Once the number of incident photons at each wavelength is known, it was converted into energy, with the relationship between the energy of a photon and its wavelength  $\lambda$  ( $E = hc/\lambda$ ). The energy values for each wavelength thus correspond to the new incident spectrum, after passing through the down-shifting layer. This spectrum was used in each case to perform I-V simulations using SCAPS software.

In summary, two important assumptions we made are: 1. all photons absorbed by the DS layer are absorbed by ZnO NPs; 2. only half of the re-emitted photons by the ZnO NPs arrive to the solar cell.

To get an idea of the potential evolution of the performance of solar cells having on their top a down-shifting layer based on ZnO nanoparticles, simulations with different PL QY of ZnO NPs were made. Five different cases of the modification of the illumination spectrum were considered:

1. The AM1.5G illumination spectrum modified by the absorption and reflexion in the stack without the DS layer,

2. The illumination spectrum amended by the absorption and reflexion of the incorporated the DS layer, but not taking into account the down-shifting effect,

3. The illumination spectrum taking into account the down-shifting effect with a PL QY = 3.23 % (ZnO NPs currently used)

4. The illumination spectrum taking into account the down-shifting effect with PL QY = 70 % (ZnO NPs existing but not used at present due to the dispersion problem in a solution for preparing a layer),

5. The illumination spectrum taking into account the down-shifting effect with a PL QY = 100 % (NPs ideal in terms of photoluminescence).

Four parameters provided by the simulations of the I-V curves are: the short-circuit current  $J_{sc}$ , the open circuit voltage  $V_{oc}$ , the fill factor FF and the efficiency  $\eta$ . These parameters characterize the performance of a solar cell. The results are shown in the tables numbered from I to X (corresponding to the simulated samples presented in the early part in this chapter). When the boxes are dark pink, this means that the parameter value is lower than that obtained without the DS layer, in other words when the results show that the application of a down-shifting layer in the solar cell structure is disadvantageous for the final solar cell performance. When the boxes are green, this means that, on the contrary, the application of a down-shifting layer in the solar cell structure is advantageous.

6.2.2.1. Amorphous Si solar cells

		<b>I)</b>	EQE 3.23 %	EQE 70 %	EQE 100 %	without DS	AM1.5G
220 nm	$V_{oc}$ (V)		1.290	1.294	1.295	1.290	1.277
	$J_{sc}$ (mA/cm <sup>2</sup> )		7.334	7.400	7.430	7.330	7.093
	FF (%)		43.355	43.261	43.219	43.359	43.697
	$\eta$ (%)		5.782	5.806	5.817	5.781	5.847

		<b>II)</b>	EQE 3.23 %	EQE 70 %	EQE 100 %	without DS	AM1.5G
160 nm	$V_{oc}$ (V)		1.293	1.296	1.297	1.275	1.278
	$J_{sc}$ (mA/cm <sup>2</sup> )		7.382	7.432	7.454	7.046	7.113
	FF (%)		43.278	43.208	43.177	43.777	43.666
	$\eta$ (%)		5.763	5.781	5.789	5.851	5.848

		<b>III)</b>	EQE 3.23 %	EQE 70 %	EQE 100 %	without DS	AM1.5G
320 nm	$V_{oc}$ (V)		1.286	1.291	1.293	1.268	1.278
	$J_{sc}$ (mA/cm <sup>2</sup> )		7.262	7.354	7.395	6.929	7.113
	FF (%)		43.455	43.326	43.269	43.957	43.666
	$\eta$ (%)		5.727	5.760	5.775	5.826	5.848

		<b>IV)</b>	EQE 3.23 %	EQE 70 %	EQE 100 %	without DS	AM1.5G
100 nm	$V_{oc}$ (V)		1.291	1.293	1.294	1.271	1.272
	$J_{sc}$ (mA/cm <sup>2</sup> )		7.346	7.381	7.397	6.974	7.004
	FF (%)		43.323	43.274	43.253	43.878	43.834
	$\eta$ (%)		5.723	5.736	5.741	5.778	5.787

		<b>V)</b>	EQE 3.23 %	EQE 70 %	EQE 100 %	without DS	AM1.5G
285 nm	$V_{oc}$ (V)		1.287	1.291	1.293	1.267	1.272
	$J_{sc}$ (mA/cm <sup>2</sup> )		7.273	7.356	7.393	6.915	7.004
	FF (%)		43.441	43.323	43.271	43.978	43.834
	$\eta$ (%)		5.720	5.750	5.764	5.795	5.787

All the results obtained are not very positive. Indeed, even considering ZnO nanoparticles having PL QY of 100 %, all four parameters never increase in the same time. It can be observed that for all the simulations, the open circuit voltage and the short circuit current increase, while the fill factor and the efficiency are reduced. It should be mentioned, however, that the values of these parameters change a little only, as the relative difference is in the range of 1 to 4 %.

6.2.2.2. CIGS solar cells

<b>VI)</b>		EQE 3.23 %	EQE 70 %	EQE 100 %	without DS	AM1.5G
100 nm	$V_{oc}$ (V)	0.558	0.558	0.558	0.558	0.558
	$J_{sc}$ (mA/cm <sup>2</sup> )	31.192	31.271	31.307	31.188	31.469
	FF (%)	61.228	61.230	61.231	61.228	61.317
	$\eta$ (%)	13.176	13.185	13.188	13.176	13.227

<b>VII)</b>		EQE 3.23 %	EQE 70 %	EQE 100 %	without DS	AM1.5G
350 nm	$V_{oc}$ (V)	0.558	0.558	0.558	0.558	0.558
	$J_{sc}$ (mA/cm <sup>2</sup> )	30.803	31.043	31.147	30.802	31.469
	FF (%)	61.106	61.112	61.115	61.106	61.317
	$\eta$ (%)	13.313	13.338	13.349	13.313	13.227

<b>VIII)</b>		EQE 3.23 %	EQE 70 %	EQE 100 %	without DS	AM1.5G
100 nm	$V_{oc}$ (V)	0.557	0.557	0.557	0.557	0.556
	$J_{sc}$ (mA/cm <sup>2</sup> )	30.303	30.384	30.419	30.303	30.209
	FF (%)	61.228	61.230	61.231	61.228	61.279
	$\eta$ (%)	13.162	13.171	13.175	13.162	13.108

<b>IX)</b>		EQE 3.23 %	EQE 70 %	EQE 100 %	without DS	AM1.5G
200 nm	$V_{oc}$ (V)	0.556	0.556	0.556	0.556	0.556
	$J_{sc}$ (mA/cm <sup>2</sup> )	29.946	30.096	30.160	29.946	30.209
	FF (%)	61.173	61.177	61.179	61.173	61.279
	$\eta$ (%)	13.168	13.184	13.191	13.167	13.108

<b>X)</b>		EQE 3.23 %	EQE 70 %	EQE 100 %	without DS	AM1.5G
250 nm	$V_{oc}$ (V)	0.556	0.557	0.557	0.556	0.557
	$J_{sc}$ (mA/cm <sup>2</sup> )	30.011	30.190	30.267	30.011	30.290
	FF (%)	61.162	61.167	61.169	61.162	61.282
	$\eta$ (%)	13.201	13.221	13.229	13.201	13.117

Again, the results indicate that the gain in terms of the performance of the solar cells having a down-shifting layer in their structure is generally low. In most cases, the final parameters of the solar cells are not positively influenced by the down-shifting layer. The results of the simulation VI) are the worst. Indeed, none of the parameters evolves towards higher values, even when studied nanoparticles have PL QY of 100 %. On the contrary, the simulation VIII) is quite encouraging because, with the exception of the fill factor, all parameters improve favorably even for a low PL QY. However, even in the simulation VIII), the parameters increase very little even

if in the cases of the NPs with a PL QY of 100 %, which is not a good forecast for the final performance of the real devices.

### 6.3. Conclusions

In this chapter, the simulations of the influence of the ZnO nanoparticle layer deposited on the front side of the solar cells have been performed, taking into account the anti-reflective effect and the down-shifting effect. First, the optical indices of the down-shifting layer containing ZnO NPs and PAAH matrix have been determined by spectroscopic ellipsometry measurements. The experimental results were adjusted using the Bruggeman and the Maxwell-Garnett models and the refractive index and the extinction coefficient of the constituent ZnO NPs and PAAH were obtained.

Then the obtained optical indices have been used to simulate the anti-reflective effect of the ZnO NPs + PAAH layer on the front side of two types of solar cells: the amorphous Si solar cell and the CIGS solar cell. The effect of the anti-reflection layer is estimated through the transmittance simulations for different layer stack structures. For a-Si solar cells, the reflection losses are relatively low (about 10 %). For CIGS solar cells, the results are also good, in the best case the reflection loss is smaller than 5 %. However, it is important to notice that in all the studied structures, the addition of the down-shifting layer increases the reflection losses, which maybe one reason of the negative results (in terms of the enhancement of the efficiency of solar cells with the DS layer on their top) obtained in the I-V simulations.

The I-V simulations realized with SCAPS software permit to estimate the influence of the down-shifting effect on the final solar cell efficiency. These simulations have been performed on the most efficient layer stack structures in terms of the transmittance. The results are not very encouraging. It may be due to two reasons. On one hand, the volume fraction of ZnO NPs in the down-shifting layer is low (6 %). It is related to the ellipsometry measurement constrains (the layer cannot be too thick, as mentioned before) and the dispersibility limit of ZnO NPs in PAAH matrix. On the other hand, to simplify the calculations, we have assumed that just a half of the re-emitted photons by ZnO NPs arrive on solar cells while the others are lost. The fraction of the lost photons may be lower. Moreover, the use of the Maxwell Garnett model may not reproduce the real properties of the fabricated layers. Thus in the future work, establishing a more elaborated model is important for giving a more accurate estimation of the down-shifting effect on the final efficiency of the studied solar cells structures.

## 6.4. References

---

1. Sahu N., Parija B., Panigrahi S., Fundamental Understanding and Modeling of Spin Coating Process : A Review. *Indian Journal of Physics*, 2009, vol. 83, no. 4, p. 493-502.
2. Horiba Jobin Yvon. Spectroscopic Ellipsometry - User Guide.
3. Forouhi A. R., Bloomer I., Optical properties of crystalline semiconductors and dielectrics. *Physical Review*, 1988, vol. 38, no. 3, p. 1865-1874.
4. Jellison G. E., Modine F. A., Parameterization of the optical functions of amorphous materials in the interband. *Applied Physics Letters*, 1996, vol. 69, p. 371-373.
5. PV Lighthouse. Refractive index library PV lighthouse. (online) Accessed in March 2015. <http://www.pvlighthouse.com.au/resources/photovoltaic%20materials/refractive%20index/refractive%20index.aspx>.
6. Niklasson G. A., Modeling the optical properties. SPIE Newsroom- The international society for optical engineering. 2006, DOI: 10.1117/2.1200603.0182.
7. En Naciri A., Ellipsométrie : Principes de base et application aux nanocristaux. Ecole thématique GDR-NACRE, 2014.
8. Mansour M., Étude des propriétés optiques de nanoparticules de semiconducteurs : Application de l'ellipsométrie aux silicium et germanium nanostructurés. PhD thesis, l'Université Paul Verlaine-Metz, 2006, DOI : <http://docnum.univ-lorraine.fr/public/UPV-M/Theses/2006/Mansour.M.SMZ0612.pdf>.
9. Keita A. -S., En Naciri A., Size distribution dependence of the dielectric function of Si quantum dots described by a modified Maxwell-Garnett formulation. *Physical Review B*. 2011, vol. 84, p. 125436/1-11.
10. M. Burgelman, P. Nollet, S. Degraeve, Modelling polycrystalline semiconductor solar cells, *Thin Solid Films* (2000), vol. 361-362, p. 527-532.
11. Honsberg C., Bowden S., Anti-reflection coating. PVEducation. (online) Accessed in March 2015. <http://www.pveducation.org/pvcdrom/design/anti-reflection-coatings>.



## General conclusions

This thesis has been devoted to the study of ZnO nanoparticles as potential down-shifter for photovoltaic solar cells. Among the different parameters to optimize, the greatest effort has been paid to obtain the nanoparticles with a high photoluminescence quantum yield (PL QY). Two different approaches for ZnO nanoparticles fabrication/synthesis have been described. First, the structure and the properties of the ZnO NPs fabricated by the Low Energy Cluster Beam Deposition (LECBD) method were presented. In this method, the stoichiometry of ZnO NPs can be controlled during the synthesis by tuning the pressure of the buffer gas  $O_2$ . The synthesized ZnO NPs can be directly deposited on photodiodes or solar cells for an estimation of the influence of the down-shifting effect on the final EQE of the photodevice. However, as the obtained ZnO NPs have a low photoluminescence quantum yield, the achieved gain from the down-shifting effect cannot compensate for the optical losses. Moreover, only a film of the material can be obtained using this method, rather than a powder containing the nanoparticles. This procedure requires high vacuum and the deposition is possible only on small areas. Hence, it is not practical for further study and industrial applications. Commercially available ZnO NPs have then been chosen as a candidate for the down-shifter, but the optical properties were not better than those of the ZnO NPs fabricated by the LECBD method. Thus sol-gel synthesis methods have been used. They not only permit to get scalable amounts of ZnO NPs but also allow achieving a high PL QY.

The first studied sol-gel method is the commonly used co-precipitation method using different Zn precursors and alkaline hydroxides. The optical properties of the synthesized nanoparticles in function of the size and the morphology have been investigated using either Zn acetate or Zn sulfate as the precursor and adding or  $Li^+$  or  $K^+$  cations. The largest influence is observed on the properties of ZnO NPs synthesized with  $Li^+$  ions. Their presence changes the growth mechanism, whatever the precursor nature. They control the morphology of the particles, blocking the growth along the  $c$  axis and thus changing the balance between the polar and non-polar planes. Consequently, since the presence of the native defects in ZnO responsible for the visible emission is related to this balance, the PL QY is enhanced and reaches 13 %. A little amount of  $Zn(OH)_2$  is also present, which is believed to be beneficial for the PL QY. If the role of  $Li^+$  ions is reinforced when Zn acetate is used as a precursor, their role is reduced when Zn sulfate is used as a precursor in the co-precipitation reaction. The presence of other species (such as  $OH^-$  ions) in the structure of the ZnO NPs plays also a role.

The second studied sol-gel method is the hydrolysis of  $ZnEt_2$ . By adding polyacrylic acid (PAAH) in the appropriate volume ratio, the appropriate concentration and the suitable chain length during the synthesis, the PL QY can be increased to 20 %. Instead of a simple nanoparticle capping effect, as when PAAH is added after the ZnO NPs synthesis, the chemical environment is strongly influenced by presence of PAAH, forming a hybrid ZnO/PAAH nanocomposite. In particular, the nanocomposite structure, size, composition and morphology have to be characterized in order to understand their influence on the PL spectra and the PL QY

enhancement. The enhancement of the PL QY due to the addition of PAAH during the NPs synthesis is related to the increase of the crystalline disorder and has been attributed to the improvement of the electron-hole wavefunction overlapping within the hybrid composite, to the spherical morphology of the nanostructure and to the creation of a type II heterostructure. It turned out that the presence of  $\text{Zn}(\text{OH})_2$  phase positively influences the PL QY. PAAH/PAANa mixture with a volume ratio of 75:25 was used to synthesize the ZnO NPs with PL QY increased to 50 % and even to 70 % after one month of exposure to the air. It remains stable even after 1 year. Such a high and stable PL QY is reported for the first time to the best of our knowledge.

After obtaining the ZnO NPs having a high PL QY, our efforts were dedicated to the preparation of a stable colloidal suspension based on the ZnO/PAAH hybrid composite. Although the obtained ZnO NPs in the hybrid composite have a high PL QY, they are not dispersible. For the fabrication of the down-shifting layer on the front side of solar cells, a solution with homogeneously dispersed ZnO NPs is necessary. Thus PAAH/PAANa mixture has been added during the ZnO NPs synthesis with a reaction time reduced from 24h to 1h. Dispersible ZnO NPs in water have been successfully synthesized with an optimal PL QY of 22 % - 34 %.

The influence of the down-shifting layer containing ZnO NPs in the PAAH matrix on the performances of a-Si and CIGS solar cells has been eventually estimated using XOP and SCAPS programs for simulations. ZnO NPs layer is not only a down-shifter but also has anti-reflective properties. However, the simulation results demonstrate a negative effect on solar cells considering both the anti-reflection and the down-shifting effect. It is assumed to be due to the low volume fraction of ZnO NPs in the PAAH matrix and the models used in the simulations.

As a first perspective of this work, since it was demonstrated that a weak organic acid added during the ZnO NPs synthesis leads to an efficient and bright photoluminescence in the ZnO-based hybrid nanocomposite, this study should be generalized to other acids. Oleic acid has been investigated in the literature and turned out to have a positive influence on the final PL QY. These hybrid systems with high PL QY can be applied not only in the down-shifting layers, but also in white light LEDs. Currently, lanthanide based phosphors are used as the down-shifters in white light LEDs. However, lanthanides which are rare elements are economically controlled by a few countries, are expensive and are, on the other hand, hard to recycle. Contrary to them, ZnO is abundant and cheap. Therefore, with a high PL QY, the hybrid ZnO/PAAH nanoparticles could represent a promising alternative.

As far as their use as a down-shifting layer in solar cells is concerned, further improvement of the modelization should be carried out to optimize the structure of the solar cell in order to obtain the highest enhancement of the solar cells with a DS layer on their top. Indeed, other numerical studies in the literature devoted to CdTe particles with high PL QY used as a DS layer in CIGS solar cells have shown that a significant improvement of the solar cell efficiency can be achieved. It would be interesting to verify how these simulations differ from the ones performed on our structures.

Eventually, as far as industrial applications are concerned, the research effort should now concentrate on the parameters which allow for the synthesis of large amount of colloidal suspension in a short period of time. In particular, the role of the reaction volume is not clear and it would be worth carrying deeper studies concerning this issue.